Interaction laser plasma dans le régime relativiste : Application à la production de sources ultrabrèves de particules énergétiques.

Mauro Manclossi

Thèse présentée à l'École Polytechnique

pour obtenir le grade de

DOCTEUR DE L'ÉCOLE POLYTECHNIQUE
ET DE L'UNIVERSITÀ DI MILANO-BICOCCA

Spécialité : Lasers et Matière

par

Mauro MANCLOSSI

Ultra High Intensity laser produced fast electron transport in under-dense and over-dense matter

soutenue publiquement le 19 Avril 2006
devant le Jury composé de :

M. Dimitri BATANI	Università di Milano Bicocca, Italie	Directeur de thèse
M. Tom HALL	University of Essex, Angleterre	
M. Maurizio LONTANO	Istituto di Fisica del Plasma "Piero Caldirola", Italie	Rapporteur
M. Victor MALKA	École Polytechnique, France	Directeur de thèse
M. Vladimir TIKHONCHUK	Université de Bordeaux I, France	Président du Jury
M. Claes-Goran WAHLSTROM	Lund Institute of Technology, Suéde	Rapporteur

Thèse préparée au Laboratoire d'Optique Appliquée UMR 7605
ENSTA – École Polytechnique – CNRS

¿Para que sirve la utopía? Para eso sirve: para caminar.
Eduardo Galeano (1940-)

"Man muss noch Caos in sich haben, um einen tanzenden Stern zu gebähren"

Friedrich Nietzsche (1844-1900)

Ai miei genitori,
Egidio e Maria Rosa

Remerciements

Je tiens d'abord à remercier Danielle Hulin et Gérard Mourou, successivement directeurs du laboratoire LOA, commun à l'École Polytechnique et à l'ENSTA, pour m'avoir accueilli et permis d'effectuer ce travail de thèse dans d'excellentes conditions.

Je remercie chaleureusement les membres du jury de thèse de m'avoir honoré de leur présence et de l'intêret qu'ils ont manifesté bien avant la soutenance.

Je remercie notamment Vladimir Tikhonchuk qui a accepté la présidence du jury ainsi que Tom Hall pour son point de vue original et critique.

Je remercie spécialement Maurizio Lontano et Claes Goran Wahlstrom d'avoir accepté la charge ingratte de rapporteurs à partir de la version non finie du manuscrit que je leur avais remis.

Je tiens bien évidemment à remercier Victor Malka, responsable de ce travail de thèse, qui m'a introduit dans le laboratoire. Victor m'a donné sa confiance en me proposant un sujet de thèse original et en se battant pour me trouver un financement. Victor est un chercheur avec des intuitions brillantes et une grande puissance pédagogique, capable avec une attitude toujours positive d'obtenir le meilleur de chacun. Au cours de ces années, j'ai apprecié son pragmatisme, sa rigueur et sa capacité à mettre la pression quand il faut *bosser* et l'ambiance de rigolade lorsqu'on peut ou lorsqu'il faut se détendre un peu.

Je le remercie pour m'avoir toujours fait confiance, encouragé et poussé à acquérir autonomie et détermination dans mon travail. Je remercie énormement Victor pour sa disponibilité et son humanité qui vont bien au-delà des devoirs d'un directeur de thèse: Victor a été beaucoup plus.

Je suis ensuite très particulièrement reconnaissant a Dimitri Batani qui a co-dirigé cette thèse. Dimitri rappresenta per me la vera essenza di un ricercatore: sempre appassionato ed entusiasta, incredibilmente aperto, mai scientificamente autoritario (anche se sempre autorevole) e soprattutto sempre disponibile alla discussione e a rimettersi in causa in prima persona. Dimitri mi ha aperto la porta del mio primo laboratorio (LULI dell'École Polytechnique) e mi ha in seguito dato voglia e incoraggiato a continuare con un dottorato. Dimitri mi ha introdotto nella comunitá scientifica internazionale e mi ha permesso di partecipare a numerose conferenze, spesso in luoghi da favola.....Vorrei ringraziare Dimitri per essersi cosí tanto implicato nella

mia tesi, soprattutto per quanto concerne l'analisi e l'interpretazione dei risultati e per avere infine assolto l'ingratissimo compito del primo revisore della primissima versione del manoscritto. Grazie Dimitri per la tua disponibilitá assoluta (compresa la vigilia di Pasqua), per la tua umanitá, per la fisica scritta dietro gli scontrini della trattoria cinese a Bicocca (memore dell'insegnamento del sommo Fermi secondo il quale la fisica di un problema deve sempre poter essere scritta sul retro di una busta...), per avermi fatto ripetere il discorso della conferenza SIF sulla rer B, accompagnato da "Sono un italiano" di Toto Cotugno. A questo proposito il mio unico rimpianto é di non avere avuto diritto (come qualcuno piú fortunato di me) ai cerchi esplicativi scritti con un bastone sulla sabbia nel parco vicino a casa tua, come il grande Archimede al centurione romano: "Noli tangere circulos meos". Grazie di cuore, grazie per essere Dimitri.

Je tiens à remercier de manière particulière Joao Santos, un bon ami, avec qui j'ai partagé des longues journées et des longues nuits de manip. Joao a été en effet le responsable d'une grande partie des expériences menées pendant ce travail de thése. Cette dernière est pour une bonne partie, et c'est peu dire, la logique continuation d'une thématique et d'un long travail que Joao avait déjà entamé. Joao est un chercheur scientifiquement généreux dont j'ai beaucoup appris, d'un point de vue de la conduite d'une expérience, des techniques expérimentales ou de la méthodologie d'analyse. Pour tout cela, ma gratitude est énorme: "Obrigado" Joao!!

Je tiens également à exprimer ma reconnaissance à Jérôme Faure qui même si engagé principalement dans une autre thématique du groupe, a toujours fait tout son possible pour être impliqué, en me donnant souvent des conseils précieux pendant nos manips, et surtout en participant activement à la très longue phase d'analyse et d'interpration des résultats.

Je tiens encore à remercier Vladimir Tikhonchuk et Arnaud Debayle pour m'avoir accueilli plusieurs fois au sein du laboratoire CELIA à Bordeaux.

Cette thèse est loin d'être un travail exclusivement personnel et je souhaite remercier les différentes équipes de chercheurs, ingénieurs, techniciens, administratifs des laboratoires LOA et LULI où les expériences ci décrites ont eté realisées. Merci a Alain pour son aide et disponibilité pendant les experiences en "Salle Jaune" et aux autres etudiants (thesards et post docs) du LOA, par leur accueil et leur soutien professionnel ou amical.

Un ringraziamento particolare a Federico e Thomas per la complicitá nelle nostre sventure, per i mille favori, per essere stati piú volte coinvolti in loschi traffici di libri, vestiti, salami, pacchi del terrone etc...Grazie Fede per tutti i Nespresso ("what else?") e per l'atmosfera di "little Italy" all'LOA...."pohhpopoppopopohhpo.....CAMPIONI DEL MONDO!!!!"

Grazie a Petit e soprattutto a Osvi e Piedo per la compagnia durante la fase di redazione.

E per concludere, un grazie di cuore a Thomas per troppe cose e a Lisi....Per ancora di piú.....!

Grazie!

Contents

Part I

Introduction

Chapter 1

Research framework

The continuous development of laser technology since its invention in the '60s allowed the concentration of light/luminous energy in increasingly narrow domains of wavelength (monochromaticity), space (spatial coherence) and time (temporal coherence).

In last years such evolution produced an enormous increase of the laser intensity available for laser-matter interactions. Thanks to the development at the end of the '80s, of the technique of amplification by frequency shift (also called *Chirped Pulse Amplification* or CPA) [1], laser power in the Petawatt regime has became possible. This type of lasers, ultra-intense lasers (also called *Ultra-High Intensity* or UHI lasers) reach intensities on target higher than 10^{18} W/cm^2 with temporal duration shorter than the picosecond.

1.1 High power lasers

An increase of on-target laser intensities can be obtained *a priori* in three different ways. The first one consists in decreasing the focal spot size, but we are finally constrained by beam diffraction. Another possibility would be the increase in energy but this implies bulkier amplifiers. The last option consists in decreasing the pulse duration, which produces the following problems:

- The pulse duration shortening is obtained by increasing its spectral width ($\tau\Delta\nu \approx 0.5$, where τ is the duration and $\Delta\nu$ the spectral pulse width), which implies an amplifier medium with large band-width.
- The pulse duration shortening also results in increasing the pulse intensity I_0 in the amplifier medium. Above a certain threshold, non-linear effects become

important and deform the space and temporal pulse profiles. We can quantify these non-linear effects by the integral:

$$B = \frac{2\pi}{\lambda_0 N_0} \int_0^l N_2 I_0(z) dz \ ,$$

where N_0 and N_2 are respectively, the linear and the non-linear part of the index of refraction of the optical medium, l is its length and λ_0 the laser wavelength. In practice, one must be limited to $B \leq B_{crit} \approx 1 - 2$. Otherwise the high space frequencies are preferentially amplified, producing beam filamentation and subsequently the medium breakout.

The easy way to circumvent all these problems consists in stretching in time the laser pulse before its amplification and in allowing for its final recompression. Fig. 1.1 summarizes the various stages of such **Chirped Pulse Amplification** technique:

1. An initial large band pulse ($\sim 10^{-9}$ J, 100 fs) delivered by an oscillator (usually titanium-sapphire) is stretched (one says also *chirped*) in time by a dispersive optical system, in general made up of one afocal and two diffraction gratings laid out in an anti-parallel configuration: the various pulse wavelengths are diffracted at different angles and follow different optical paths. A second passage in the stretcher eliminates the transverse space shift introduced during the first passage, producing a pulse $10^3 - 10^4$ time longer than the initial pulse and with the spectral components temporally ordered, the long wavelengths before the shorter ones. The peak pulse intensity is thus lowered below the damage threshold of the amplifier materials.

2. The "chirped" pulse is amplified in several steps by a factor $10^8 - 10^{10}$ in amplifiers with adequate band-width, remaining below the damage threshold of the crossed optical mediums.

3. Then a dispersive system, symmetrical to the strecher, compresses the beam. The shorter wavelengths follow an optical path shorter than the longer wavelenghts in order to compensate for the relative delays introduced by the stretching.

Focusing the obtained pulse with an energy of a few joules and a duration lower than 1 ps, in a focal spot of ten microns diameter, leads to an on-target intensity higher than 10^{18} W/cm^2. The experiments described in this thesis work were realized on two ultra high intensity lasers. The first one is a Nd:glass system delivering pulses ranging between $10 - 20$ J, with a wavelength of 1.06 μm, in $300 - 400$ fs (100 TW

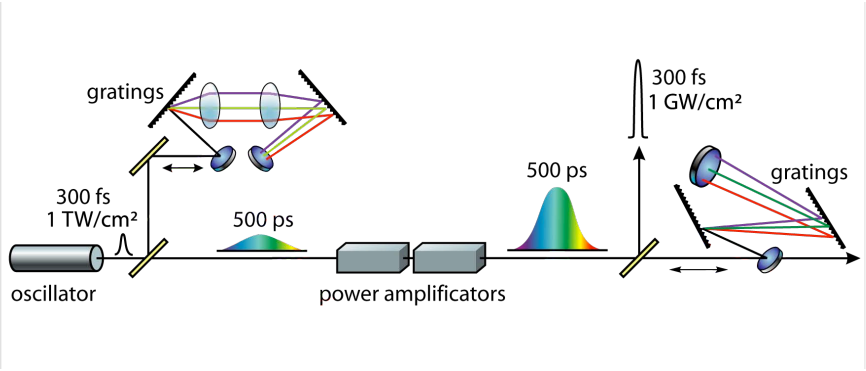

Figure 1.1: CPA technique line out.

laser at LULI); the second one use Ti:Saphire as amplifier medium and delivers pulses ranging between $1-2$ J, with a wavelength of 815 nm, in $30-40$ fs ("Salle jaune" laser at LOA),

This kind of installations is nowadays becoming current and the continuous search for increasing the interaction power is already leading soon to petawatt systems, where the intensity can approach or exceed the $10^{21}\mathrm{W/cm^2}$. Such projects are launched at LOA and CEA in France, at RAL in UK, at GSI in Germany, at ILE in Japan, at INRS in Canada, at CUOS and UNL in USA.

1.2 Laser-matter interaction in the UHI regime

The development of such lasers is mainly justified by the extreme physical conditions which they make possible to reach. Indeed the electric field corresponding to a linearly polarized laser pulse is

$$E[\mathrm{Vm^{-1}}] = 2.7 \times 10^{12}\, I_{18}^{1/2} \ ,$$

where I_{18} is the laser intensity expressed in units of $10^{18}\mathrm{W/cm^2}$. For $I_{18} = 1$, the laser field corresponds to approximately 5 times the field binding in an electron to an hydrogen atom ($E_H \approx 5 \times 10^{11}\,\mathrm{Vm^{-1}}$). Any atom subject to such a field is thus ionized practically instantaneously.

Immediately after ionization the electron oscillation velocity in the laser electric field is very close the speed of light c, and plasma thus created becomes relativistic. In this relativistic regime, we observe (cf. Chap. 2 for more details):

- The conversion of a large fraction ($\sim 0.1-0.5$) of the laser energy into very energetic particles (until tens and even hundreds of MeV). The currents and

densities of current in the target can reach extreme values, of about 10^7 A and 10^{12} Acm^{-2}.

- The laser wave propagation beyond the critical density n_c, as a consequence of the reduction of the effective plasma electron frequency due to the relativistic increase in the electron mass,

$$\omega'_{pe} = \frac{\omega_{pe}}{\gamma^{1/2}}$$

where γ is the Lorentz factor. This phenomenon is called *induced transparency* [2]. The refraction index ($n < n_c$) is also modified, supporting the collimated propagation of the laser pulse on distances longer than the Rayleigh length, a phenomenon called *relativistic self-focusing*.

- The electromagnetic pressure of such UHI laser pulse is very high and can exceed 1 Gbar:

$$P_{rad} = 2I_0/c \approx 600\, I_{18} \text{ Mbar}$$

By comparing this expression with the thermal pressure of a plasma with a mass density ρ and of temperature T:

$$P_{Th}[\text{Mbar}] \simeq 480\, \rho[\text{gcm}^{-3}]\, T[\text{keV}]$$

it is seen that a pulse with $I_{18} \sim 1$ is able to contain the thermal expansion of an ionized solid with a temperature of 1 keV and thus to ensure its confinement. The modification of the target surface and the creation of shock waves take place for $P_{rad} > P_{th}$ [3].

A short pulse duration ($\sim$ ps) limits the hydrodynamic expansion of the target surface and the interaction conditions are very different from those obtained in the nanosecond regime, where the phenomena of absorption take place in a wide region of subcritical and critical plasma. In the ultra-intense regime, the interaction zone has dimensions often smaller than the laser wavelength λ_0 and is much denser than in the nanosecond case: the interaction almost occurs with a solid. In practice, however, the density profile is determined by the pedestal of the UHI pulse, which can last few nanoseconds. For an intensity of $I = 10^{18} - 10^{19}$W/cm^2, a temporal contrast of $1 : 10^8$ is sufficient to produce a coronal plasma with a gradient length (cf. Sect. 2.1.2 and Eq. 2.7)

$$L_{grad} \equiv \frac{n_e}{(dn_e/dz)} \sim \lambda_0$$

1.3 Applications of laser-matter interaction in the relativistic regime

The development of UHI laser systems, able to produce new physical phenomena, allowed the development of original research in a large number of fields. The results described in this PhD work are limited however to the interaction of intense and short pulse laser with solid and gas targets and to the study of the intense laser-generated relativistic electron currents in matter. Among other applications which I will briefly evoke, this research is more deeply related to the Fast Ignition concept in the Inertial Confinement Fusion context, which will be described below.

1.3.1 Fast Ignitor

Fast ignition is an alternative approach to Inertial Confiment Fusion. This approach, suggested in 1994 [4], benefits of UHI lasers technology. Before entering in the Fast Ignition specificities, let us place ourself in the more general context of thermonuclear fusion and, in particular, of the Inertial Confiment Fusion.

Thermonuclear fusion

One of the current major scientific challenges consists in finding a new source of energy, able to compensate the future exhaustion of fossile fuels (oil, gas), and, at the same time, to avoid the problems of nuclear waste reprocessing, resulting from the fission of heavy atoms. A possible way is the controlled thermonuclear fusion of light nuclei. The most effective reaction is

$$ {}^{2}_{1}\mathrm{D} + {}^{3}_{1}\mathrm{T} \longrightarrow {}^{4}_{2}\mathrm{He}\,(3.5\,\mathrm{MeV}) + {}^{1}_{0}\mathrm{n}\,(14.1\,\mathrm{MeV}) $$

The goal is to confine a Deuterium-Tritium plasma (DT) during a sufficient long time with a rather high density and with a *thermonuclear* temperature ($10^8\,\mathrm{K} \sim 10\,\mathrm{keV}$) in order to satisfy the *Lawson criterion*:

$$ n_e \tau > 10^{14}\,\mathrm{cm}^{-3}\mathrm{s}\ , $$

where τ is the length of time of plasma confinement and n_e its electronic density. Two ways are studied in parallel: magnetic confinement fusion, where we exploit the confinement time, and inertial confinement fusion (ICF), where we exploit the plasma electronic density. We are interested in this second way where the compression and the heating of a small mass of overdense DT are carried out using very powerful laser

beams (or particle beams, in the next future). The implosion is determined by the target hydrodynamics and the inertia of the medium.

Inertial Confinement Fusion

Fusion could be obtained according to the following steps:

1. Focusing light beams on the target.
2. Ionization of the surface of a microballon ablator which contains DT
3. Ablation due to the increase in the laser heating
4. Because of the conservation of the momentum, propagation of a centripetal shock wave towards the interior of the target.
5. Ignition of the nuclear fuel in a central hot spot which satisfies the conditions of the necessary temperature and pressure
6. Combustion of the DT gradually carried out by the propagation of the particles α which maintain the reaction (thermonuclear burn wave).

Two different approaches are being studied to carry out the implosion. The direct attack consists in imploding the microballon of DT by laser beams directly focused on the target. This technique is very sensitive to the inhomogeneities of irradiation at the origin of hydrodynamic instabilities (Rayleigh-Taylor, Richtmeyer-Meshkov, ...). In the scenario of indirect attack, the implosion is ensured by the X-radiation emitted by the interior walls of high atomic number cavity, on which the laser beams are focused. The microballon of DT is inside this cavity. The principal constraints of this approach relate to the X-radiation: the conversion rate of laser energy into X-radiation must be as high as possible and the thermalisation of the radiation in the cavity must be optimized to obtain an isotropic compression. Another uncertainty concerns the laser beams propagation in the cavity: to avoid plasma filling out the cavity entries, the cavity is filled with a light gas which is ionized by the lasers. The produced plasma, transparent to the laser, constitutes a medium favorable for the growth of parametric instabilities, potentially detrimental to the laser beams propagation.

The lasers under consideration for implosion have an intensity peak of the order of 10^{15} W/cm^2, a pulse duration of 10's nanoseconds and a wavelength of 0.35 μm. Two projects aiming at the demonstration of the ICF concept are currently being developed: the *National Ignition Facility* (NIF) at the *Lawrence Livermore National Laboratory* (LLNL) in the United States with 48 groups of 4 beams delivering an energy higher than 1.5 MJ, and the laser *MégaJoule* of CEA/DAM in Bordeaux with 60 groups of 4 beams delivering an energy between 1.6 and 2 MJ.

The concept of the Fast Ignition: an alternative

In the fast ignition approach the phases of compression and heating of the DT capsule are decoupled. The last one is done by means of UHI lasers while compression is realized with conventional ICF lasers.

In its original formulation, the process consists of four steps (see Fig. 1.2):

1. The compression must be done as adiabatically as possible but without the goal of creating a central hot spot. The target core passes from a density $\rho = 0.3\,\mathrm{gcm}^{-3}$ to $\rho = 300\,\mathrm{gcm}^{-3}$. A millimetre-length under-dense crown of plasma surrounds the target core.

2. A first ultra-intense pulse (intensity $\sim 10^{18}$ W/cm^2; duration ~ 100 ps) bores a channel in the subcritical corona, and pushes the critical surface towards the dense core of the capsule.

3. The channel is used as guide for a second shorter ultra-intense laser pulse ($\gtrsim 10^{20}$ W/cm^2; $\tau \sim 1$ ps) which must approach the compressed core as much as possible ($n_e \sim 10^{26}\mathrm{cm}^{-3}$) to generate a supra-thermal electron beam able to penetrate in the dense fuel.

4. These particles travel over a few hundreds microns before reaching the inner region of the core where they deposit their energy. Those particles, whose energy is about $\sim 1\,\mathrm{MeV}$, have a mean free path close to that of the α particles of 3.5 MeV and can create a "lateral" hot spot where ignition conditions are met: temperature $T \sim 5 - 10\,\mathrm{keV}$ and areal density $\rho R \sim 0.3 - 0.5\,\mathrm{gcm}^{-2}$ [5].

The interest for this concept comes from, first of all, the decoupling of the fuel compression and heating, which minimizes the constraints of irradiation uniformity and of implosion symmetry. This should allow a greater tolerance to hydrodynamic instabilities. In addition, the hot spot is created in an isochoric way, (i.e. much faster than the typical hydrodynamic time scales). This theoretically produces an higher gain than the usual isobar model [6]. Taking into account the changes in the ignition conditions and the influence of the lateral position of the hot spot, numerical simulations of Atzeni & Ciampi [7] lead to the following conditions on the additional energy source, which moderate by a factor 5 the initial optimistic estimate:

$$\begin{cases} E[\mathrm{kJ}] \geq 18\,(\rho/300\,\mathrm{gcm}^{-3})^{-1.85} \\ P[\mathrm{PW}] \geq 2900\,(\rho/300\,\mathrm{gcm}^{-3})^{-1} \\ I[\mathrm{Wcm}^{-2}] \geq 9\,10^{18}\,(\rho/300\,\mathrm{gcm}^{-3})^{0.9} \end{cases}$$

where ρ is the target core density. However, these estimates result from hydrodynamic simulations where the energy is delivered in the form of a beam of ions and not of an

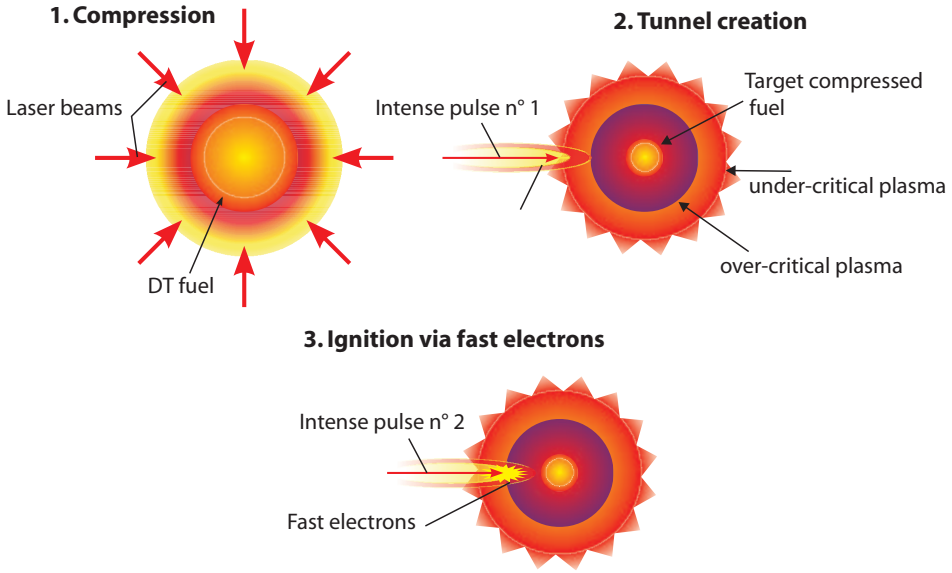

Figure 1.2: Fast Ignition concept: **1.** Target compression. **2.** Creation of a density channel. **3.** Fast electrons generation and transport and fuel ignition. A *zoom* is done on the third point to which this thesis is more particularly devoted.

ultra-short laser pulse. The phenomena suitable for the electronic transport are thus not taken into account, nor the conversion rate of laser energy into "useful" electrons, which can be appreciably lower than unity. Nevertheless it should be noted that the initial compression causes, with the stagnation, a central hot spot involving a density variation. In this case a modified isobaric model can be more realistic [8].

Other uncertainties remain upstream of ignition, and I have tried in my thesis to clear up a part of them:

1. **The propagation of an UHI pulse in a long plasma and the possibility of guiding a second pulse**. This point exceeds the objectives of this thesis but we can however report some encouraging experimental results:

   (a) A strong illumination/or high intensity supports the propagation in subcritical plasmas and the formation of density channels [9, 10].

   (b) Strong magnetic fields due to currents of electrons collinear to the laser beam ($\sim 10\,\mathrm{MG}$) are generated in subcritical plasmas. The electronic propagation may be positively assisted by these fields [11, 12].

   (c) The effective guiding of a second pulse in a preformed channel was observed [13, 14].

   (d) The penetration of a UHI pulse in supercritical regions is allowed by combined mechanisms of ponderomotive push and induced transparency.

2. **Fast electron generation in over-dense plasmas**. During the interaction of a laser with an overcritical plasma, the laser wave can penetrate only over a short distance, the skin depth. In this thickness, a large part ($\sim 30\,\%$) of the laser energy is transferred to the plasma electrons in the form of kinetic energy. The various mechanisms of generation of the relativistic electrons, functions of the interaction geometry, the plasma density and temperature gradients where this interaction occurs, are discussed more in detail in Chap. 2.

3. **Electronic transport in dense matter**. In the context of the fast ignitor, electrons of some MeV, accelerated at the surface of an overcritical plasma must propagate towards the target core and deposit their energy therein. The transport of this suprathermic electronic population is ruled by two kinds of mechanisms:

   - The collisions with the electrons and the ions of the crossed medium. In this case, each electron interacts individually with the medium. These interactions cause the angular diffusion (elastic collisions) and the deceleration

(inelastic collisions [1]) of the electrons.

- The *spontaneous* generation of electromagnetic fields. They are collective effects insofar as they depend on the density of the electronic beam current. These effects can contribute to beam guiding and thus compensate angular diffusion, but also induce a transport inhibition if compared to a purely collisional model. The collective effects are also associated with the development of instabilities.

Since this thesis aims precisely to the characterization of the electronic transport in the dense matter, several related theoretical concepts will be introduced in Chap. 2.

1.3.2 Other applications

Ion beam acceleration

The interaction and the propagation of the fast electrons through solid targets can lead to the acceleration of ions in two distinct regions. At the surface irradiated by the laser, electrons are pushed through the interior of the target by the ponderomotive force. This produces a field of space charge able to accelerate towards the interior of the target also the ions close to the surface [15, 16, 17]. After having crossed the target thickness, the fast electrons escape from the back surface. Therefore, a very intense space charge field, associated an electrostatic potential of the order of the average energy of the electrons, appears and accelerates the rear surface ions [18, 19, 20, 21, 22, 23]. An ionic expulsion occurs also at the front surface because certain electrons are accelerated towards the vacuum, directly or after being reflected by the space charge field [15]. The accelerated ions are generally protons, coming either from the material itself, or from the absorption of some water or oil on the surface. The maximal ion energy measured until now is of a few tens of MeV with a typical "temperature" of about some MeV [19, 15, 23]. Heavier ions as Pb^{46+} up to 430 MeV [15] were also observed. The total transfer of energy between laser energy and ionic kinetic energy can reach 10% with a number of accelerated protons ranging between 10^{12} and some 10^{13} for laser powers of $100\,\mathrm{TW} - 1\,\mathrm{PW}$ [19]. Because of the geometry of the acceleration mechanism, preferentially normal to the surface of the target, the angular divergence of these ion beams can be very low. They can thus be used for probing dense plasmas [24, 25, 26, 22], or even for replacing the electrons in the fast ignitor scheme [27].

[1] While moving through the material, the electrons can take part to various inelastic scattering events corresponding to excitation of surface and bulk plasmons, interband electron transitions from core to empty levels.

Electron acceleration in under-dense plasmas

High intensity laser beams, having enormous electric fields, can be used for their capacity to effectively accelerate particles. Plasmas are ideal accelerator media because, contrary to the non-ionized matter, they can support very strong electric fields. However, they require the conversion of the laser transverse electric field into a longitudinal field able to trap and accelerate the particles. Acceleration of electrons to high energies can be achieved by:

- The excitation of intense plasma waves [28].
- The electromagnetic pressure of the laser, i.e., the action of ponderomotive force [3, 29, 30].
- The direct interaction with the laser (*Direct Laser Acceleration*, DLA) [31, 32].

In the first method, a plasma wave with a phase velocity very close to c is excited. This method produces the highest energies, because the maximum energy of the accelerated electrons depends on the phase velocity of the accelerating wave. An optimal acceleration requires a volume of under-dense plasma. This condition is satisfied in the interaction with a gas jet, or, in the case of a solid target, by means of a pre-pulse creating a pre-plasma in front of the target surface before the arrival of the main pulse. Various accelerating mechanisms using the generation of plasma waves are possible, like the **beat waves acceleration** [28, 33, 34], the **laser wake field acceleration** [28, 35] and the self-modulated **acceleration** [36, 37, 38]. Until now electrons accelerated at energies up to $\sim 200\,\mathrm{MeV}$ [39] have already been observed. The development of these techniques, following the development of the laser technology towards increasingly more intense irradiation, makes it possible to consider applications in many domains [40]: high-energy physics [41], medicine [42], material science [43].

Sources of coherent radiation

Coherent X-radiation produced in the laser-plasma interaction with very high brightness can be used to probe a number of biological processes with a unique temporal resolution [44]. To probe organic matter, X-rays need to be in a particular frequency band, called the water window, extending from 23.3 Å to 43.6 Å. The radiation must be, moreover, very bright, well orientable and of a certain coherence. Two ways are currently studied to produce such radiation using plasmas:

- X-ray lasers based on the atomic properties of the plasmas created by UHI laser-solid interaction containing multi-charged ions which are natural sources of XUV emission [45].

- Non-linearities, in gaseous medium or in a plasma. The movement of electrons in an ultra-intense laser wave produces the radiation of harmonics of the initial laser wavelength [46]. This phenomenon can easily be used in a subcritical plasma, or in the skin depth during the interaction with a solid, to produce coherent X-radiation. In the case of solids, the coupling of the incident wave with surface modes can also produce harmonics of the laser wave [47, 48].

Sources of incoherent radiation

A dense and hot plasma, produced by the interaction of an UHI laser with a solid target, is an excellent source of incoherent X-radiation. This results either from radiative recombinations (transition free-bound) or from atomic excitations or de-excitations (bound-bound). During the deposition of laser energy, the plasma emits photons in a range of energy going from some eV to some keV. After the interaction, the plasma cools and does not emit any more radiation.

Moreover, X-radiation in the field of MeV is generated by the suprathermic electrons created during the interaction at the plasma surface. Their propagation in the dense matter is accompanied by a radiation which is the series of a number of lines due to the ionization of the medium (bound-free transition: stripping of electrons from the atomic shell K) and a continuous of Bremsstrahlung emission arising from electron-ion collisions (free-free transition). The distribution in energy and angle of this radiation depends on the electronic distribution, the type of material considered and the thickness of the crossed target. If the electrons are rather energetic, we can expect γ radiation with the emission of photons with similar energies [49]. This radiation can be used as probe beam for experiments of radiography of very dense media with fast evolution [18].

Source of neutrons

Deuterium material irradiated by UHI lasers can produce neutrons by the ions accelerated at the target surface [50, 51, 52, 53], according to the reaction

$$\mathrm{D} + \mathrm{D} \longrightarrow {}^{3}\mathrm{He} + \mathrm{n}$$

These neutrons can be used to infer plasma properties (ion temperature, plasma evolution). Photoneutrons are also produced by the interaction of the γ radiation described above with the target atoms [54].

Astrophysics studies

Laser-matter interactions with intensities exceeding 10^{20} W/cm^2 could allow to reproduce astrophysical conditions in the laboratory. We can thus imagine studying nuclear reaction rates in the dense matter, the physics of metals at ultra-high pressures (phase transition, metallization and hydrogen crystallization), or the physical mechanisms controlling the supernovas, stars and nebulas [55, 56].

Part II

Theoretical considerations

Chapter 2

Ultra High Intensity laser-matter interaction

In this chapter we give some theoretical informations on the laser-matter interaction, essential for the comprehension of our experimental results, obtained with laser intensity between 10^{18} and 10^{20} Wcm^{-2}. The principal points are related to the production of relativistic electrons and their transport in the dense matter.

2.1 Conversion of laser energy and production of relativistic electrons

The generation of suprathermic electrons constitutes the process of laser energy absorption dominating in the relativistic interaction regime (5×10^{19} Wcm^{-2}).

It is interesting to compare this regime of UHI laser-matter interaction with the nanosecond regime. In fact, an UHI laser pulse is often accompanied by a pedestal, with an intensity definitely weaker and which precedes by a few nanoseconds the intense part. This pedestal, related to the ASE (Amplified Spontaneous Emission) of the laser chain, cannot be completely removed and interacts with the target, creating a pre-plasma which expands towards the vacuum before the arrival of the principal peak. The interaction condition seen by this peak are thus determined by the pre-plasma gradient length, which depends on the pedestal duration and intensity. A laser pulse of $\sim 10^{13}$ Wcm^{-2} characterized by a contrast in intensity between the pedestal and the intense part of about 5×10^{-7} produces a pre-plasma length L_{grad} of few hundreds of microns.

2.1.1 Interaction in the nanosecond regime

When an intense laser beam irradiates a solid target, the matter is ionized very quickly. In the laser focal spot the atomic electrons are torn stripped by multiphotonic ionization and accelerated by the laser electric field. A plasma is generated by the collisions between these first electrons and the remaining material.

The heated and ionized matter slackens towards the vacuum (*ablation*) and the plasma created presents a density gradient from the solid until the vacuum. The laser wave with the wavelength λ_0 penetrates until an electronic density limit, the critical density

$$n_c = \frac{m\epsilon_0\omega_0^2}{e^2} = \frac{1.1\,10^{21}}{\lambda_0[\mu\mathrm{m}]^2}\,\mathrm{cm}^{-3}\ , \tag{2.1}$$

for which the plasma frequency

$$\omega_{pe} = \sqrt{\frac{n_e e^2}{\epsilon_0 m_0}} \tag{2.2}$$

is equal to the laser radiation frequency $\omega_0 = 2\pi c/\lambda_0$. Three distinct zones are defined in this plasma (see Fig. 2.1-a):

- The **corona**, with a density lower than n_c, is the zone where laser absorption occurs. There the electronic temperature reaches values of the order of keV.
- The **conduction region**, density ranging between n_c and the solid density n_s, is the zone where the laser energy absorbed in the corona is transported by thermal conduction, X-rays or fast particles towards the high densities. The temperature here lies between 10 eV and 1 keV.
- The **shocked region**, of density higher than n_s, is the zone where the relaxation of plasma towards the vacuum suddenly produces, by rocket effect, a setting in motion of the matter in the direction of the laser. This generates a shock wave which propagated towards the major parts of the target compressing it. The temperature reaches some eV and a density of 3-4 times n_s.

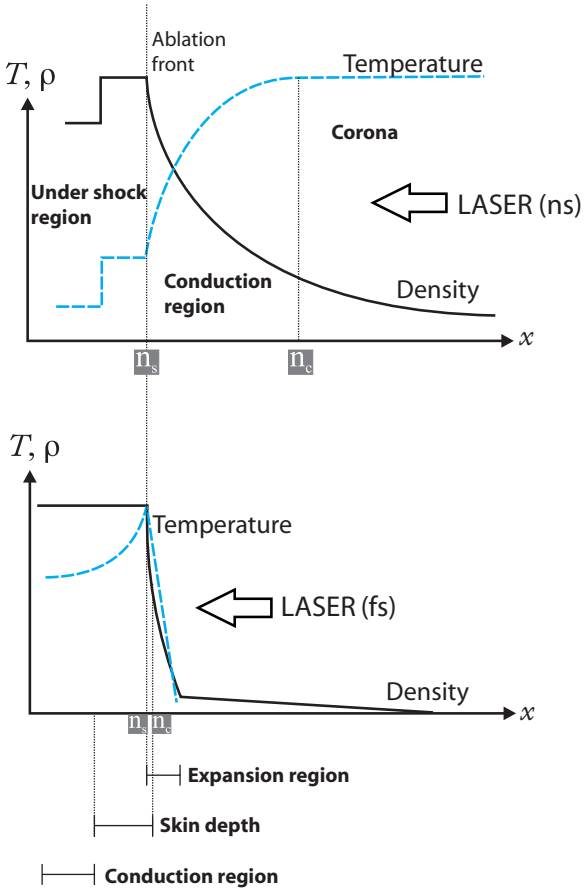

Figure 2.1: Representation of the density ρ and temperature T profiles of the target irradiated by the laser beam in both interaction regimes: **a)** nanosecond regime, **b)** femtosecond regime.

2.1.2 Interaction in the femtosecond regime

In UHI laser-matter interaction, at intensity which can reach $10^{18} - 10^{20}$ Wcm^{-2}, the mechanisms of laser absorption and the characteristics of generated plasma are modified if compared to the nanosecond case. This is related to the strong electromagnetic field associated to the laser wave and, on the other hand, to the short pulse duration ($\leq$ ps).

Thus, the high intensity of the electromagnetic field associated to the laser wave causes a substantial development of the nonlinear laser-target coupling, the dynamics of the electrons becomes relativistic. An electron subject to such a field is quickly stripped from the atom and moves under the Lorentz force associated with the laser field:

$$\frac{d\mathbf{p}}{dt} = -e(\mathbf{E} + \mathbf{v} \times \mathbf{B}) \tag{2.3}$$

Since in vacuum $B = E/c$, the electron will start, in the case of a moderated intensity, to oscillate collinearly with the transverse electric field of the wave. Its maximum oscillation speed is then given by

$$\frac{v_\perp}{c} = a_0 = \frac{eE}{m\omega c} = 0.85(I_{18}\lambda_\mu^2)^{1/2}$$

When $I_{18}\lambda_\mu^2 \sim 1$, the electron becomes relativistic and the magnetic component of the Lorentz force cannot be neglected any more. Consequently, the electron, in addition to its transversal movement, acquires a longitudinal movement. Under these relativistic conditions, the momentum, $\mathbf{p} = \gamma m\mathbf{v}$, and the energy of an electron initially at rest interacting in the vacuum with a wave planes are [57]

$$\frac{p_z}{mc} = a_0^2/2 \qquad \frac{p_\perp}{mc} = a_0 \qquad \frac{E_{kin}}{mc^2} = \gamma - 1 = \frac{a_0^2}{2}$$

For example, for a laser pulse intensity $I \sim 10^{19}$ W/cm^2 and $\lambda \sim 1\,\mu$m, corresponding to our experimental parameters, we will be able to obtain electrons with a kinetic energy $E_{kin} \sim 1.8$ MeV.

In reality, during the interaction of a laser pulse with a target, the electron is not insulated, but rather drowned in a plasma or in a solid. As we will see further in this chapter, the adiabacity of the electron movement can then be broken by several mechanisms, so that at the end of the laser pulse the electron preserves the energy gained during the interaction, on the contrary to what occurs in the case of the interaction of a plane wave in vacuum.

The relativistic regime is characterized by several effects due to the increase of the electron mass, $m = \gamma m_0$. Among these, the change of the electronic plasma frequency

$$\omega'_{pe} = \frac{\omega_{pe}}{\gamma^{1/2}} \ ,$$

where ω_{pe} is given by the Eq. 2.2.

The transparent maximum density for the laser wave is thus increased at strong intensities. The propagation in the range $\omega'_{pe} < \omega < \omega_{pe}$, made possible by the relativistic effects, is called *induced transparency* [2] and corresponds to a normaliized amplitude

$$a_0 > \sqrt{\frac{n_e^2}{n_c^2} - 1} \ ,$$

where n_c is the critical density given by the Eq. 2.1.

The modification of the plasma frequency also affects the refraction index

$$N = \sqrt{1 - \frac{\omega_{pe}^2}{\gamma\omega^2}} \tag{2.4}$$

It is maximum on the beam axis whose radial profile satisfy the condition $a_0(0) > a_0(r)$, which induces a curve of the wave front which, in its turn, causes the convergence of the beam. If this focusing effect compensates the diffraction, the pulse can be propagated in a collimated way in under-dense plasmas over distances quite longer than the Rayleigh length [58, 9]. This mechanism, called *relativistic self-focusing*, requires a total power higher than the critical power $P_c(\mathrm{GW}) = 17(\frac{\omega}{\omega_{pe}})^2$ [59, 60].

The principal consequence of the short duration of the laser pulse is the weak hydrodynamic expansion of the plasma during the interaction time. The coronal subcritical plasma, characteristic of the nanosecond interaction, does not have time to be constituted and the conditions for the generation of the shock wave are not satisfied.

To have an idea about the subcritical region dimensions it is necessary to estimate the velocity of the ablation front (defined as the plane where the matter is ejected towards the vacuum). We can, in first approximation, suppose that plasma behaves like a perfect gas expanding isothermal. By this assumption, the ablation velocity is given by the ionic sound velocity

$$v_{abl} \sim c_s \approx (Z^* T_e / m_i)^{1/2} \ , \tag{2.5}$$

where Z^* is the average ionization state, m_i the ionic mass and T_e the electronic temperature. We took into account that in our case the electronic temperature is much larger than the ionic temperature. Let us consider that thermodynamic balance

is established and take the approximation of perfect gas. For laser intensities higher than 10^{17} Wcm^{-2} Rozmus and Tikhonchuk [61] obtained the following scaling-law, relating the plasma temperature to the laser intensity

$$T_{plasma}[\text{keV}] = 16\, Z^{-5/8} \left(\frac{\lambda_0}{\mu\text{m}}\right)^{-1/2} \left(\frac{I_0}{10^{18}\ \text{Wcm}^{-2}}\right)^{3/4} \tag{2.6}$$

In this model, the local electronic temperature is determined by the balance between the rate of the laser energy absorption and the efficiency of thermal transport towards the interior of the target. The reduction of the hydrodynamic expansion led to a restriction of the thermal conduction region (if compared to the *ns* case), which as a consequence produced a much faster increasing of the temperature with laser intensities.

Under these conditions we can estimate that in the UHI regime the plasma ablation velocity is of the order of $5 \times 10^{6-7}$ cm/s, values comparable to those obtained in the nanosecond case. During the interaction, the plasma expansion is very weak, often reduced to dimensions lower than the laser wavelength. The interaction occurs almost with a solid, in areas much denser than in the case of the nanosecond interaction. This is even truer for laser intensities larger than 10^{18} Wcm^{-2}, where the radiation pressure may be sufficiently high to balance the plasma expansion (cf. Chap. I) and thus may induce a strong steepening of the density profile. A indentation of the critical surface inside the target can even take place, changing the interaction geometry. The temperature profile of the interaction plasma is also very different from that one of the nanosecond case and largely modifies the mechanisms of laser absorption, as we will see further in the text.

In Fig. 2.1-b) the spatial profiles of laser-plasma density and temperature in the femtosecond regime are represented. There are three different zones:

- the **expansion region**, of density lower than n_s, corresponds to the plasma in expansion in front of the target. The density decreases towards vacuum with a typical scalelength *gradient length* $L_{grad} \equiv \frac{n_e}{\partial n_e/\partial z}$, of the order of

$$L_{grad} \approx \tau c_s \ , \tag{2.7}$$

  where τ is the laser pulse duration. Its dimensions lie between 10 nm and a few μm (in the nanosecond regime, it varied from several tens to several hundreds of microns).

- the **skin depth**, beyond the critical density. This zone is delimited by the profile of the evanescent part of the laser wave, which diminishes over a typical length

defined by

$$L_{skin} = \frac{c}{\omega_{pe}} \tag{2.8}$$

Its dimension, for a solid density plasma, is about ten nanometers. Because of the weak hydrodynamic expansion, the critical density is spatially very near to the solid density and, for gradient lengths of $L_{grad} < L_{skin}$, the laser electric field is directly coupled with the solid particles.

- the **thermal conduction zone** in which the energy, as in the case of the nanosecond interaction, is transported by the thermal electrons towards the deeper regions of the target. This zone is classically described by the Spitzer theory [62], which supposes that the electrons mean free path is lower than the characteristic length of the heat gradient. For strong laser intensities ($> 10^{17}$ Wcm^{-2}) the Spitzer theory is not valid any more and the thermal transfer must be treated differently [63, 64].

For a raised intensity, even in the presence of a pre-plasma, the electrons play a dominating part, as well as for the plasma relaxation as for the heating of the dense region. The coupling between the intense laser field and the electrons as well as the charge migration and the kinetic effects which result from it, dominate if compared to the fluid behaviour of plasma. In particular, considering that the electrons are heated very quickly by the laser field and that the electron-ion relaxation time, of the order of the picosecond, is lower than the interaction duration, the plasma is far from the thermodynamic equilibrium. The in-depth heating is primarily due to the fast electrons. The mechanisms associated with its generation are detailed in the continuation.

2.1.3 Fast electron generation

Let us consider the laser wave as a plane wave which initially gives a kinetic energy $a_0^2/2$ to an electron initially at rest. It is shown that the electron canonical momentum, $P_\perp = p_\perp - eA$, where $p_\perp$ is the electron transverse momentum and A is the wave potential vector, is preserved during the interaction (Woodward's law):

$$p_\perp(t) - eA_\perp(x,t) = p_{\perp 0} - eA_{\perp 0} = 0$$

The movement of the electron then stops as soon as the laser pulse disappeared. It is impossible to accelerate an electron in a plane wave except if the adiabacity is broken, i.e., if the electron escapes from the laser wave before the laser pulse finishes, carrying away a certain energy. There are various ways to do it:

- Through collisions with the plasma ions. The electrons lose their coherence in the wave and can leave the interaction zone with a non-zero momentum
- By means of the interaction of the electrons with a standing wave (two plane waves being propagated in opposite directions). For a weak laser intensity, the electrons oscillate around the nodes of the field. For a higher intensity, the movement of the electrons becomes chaotic, being the acceleration larger for larger laser intensity [65]
- Because of the laser wave has a finite transverse width. Thanks to the transverse oscillations in the laser field, the electrons can leave the wave before its end and with a momentum different from the initial one. The oscillation energy is then transformed into drift energy. In other words, the Gauss equation imposes that the transverse width of the laser pulse reveals a longitudinal field, breaking the assumption of the plane wave plane [66]
- In a plasma where the space charge forces act as recall forces. Then a longitudinal field appears and it's able to break the Woodward's law. The electron will not remain any more at rest after the end of the laser pulse [67].

The mechanisms of collisional absorption are characteristic of the interaction in the nanosecond regime but play a minor role at the higher intensities because of the decrease of the collision frequency with the oscillation velocity. Thus, collective phenomena of absorption become dominant. A significant part of irradiated laser energy is then transferred to the plasma electrons which are strongly accelerated.

Collisional absorption (inverse bremsstrahlung)

During the collisions between the electrons and the ions of the plasma, the oscillation energy of the electrons in the laser field is locally converted into thermal energy. The absorption rate is given by [68]:

$$A_{coll} = \frac{\omega_0}{\omega_{pe}} \left(\frac{8\nu_{ei}}{\omega_0} \right)^{1/2} \tag{2.9}$$

For a Maxwellian plasma the collision frequency, ν_{ei} averaged over the distribution function and assuming Spitzer's collisions, is given by [69]

$$\nu_{ei} = 3\,10^{-6} \frac{Z^* n_e \ln \Lambda_{ei}}{T[\mathrm{keV}]^{3/2}} \ , \tag{2.10}$$

where Z^* is the ionization state and $\ln \lambda_{ei}$ is the Coulomb logarithm. Absorption grows with the electronic density and reaches its maximum near the critical density.

However, in order to make collisional absorption effective over several laser periods, it is forth-seeing to work with a density gradient not too steep ($L_{grad}/\lambda_0 > 1$). Collisional absorption dominates at weak laser intensity, where collective effects are negligible, but becomes negligible above 10^{15} W/cm^2: here the increase in the temperature reduces the collision frequency ($\nu_{ei} \propto 1/v_{th}$) until the oscillation velocity v_{osc} equalizes or exceeds the thermal velocity $v_{th} = (K_B T_e/m)^{1/2}$, reducing a little more the frequency of effective collision

$$\nu'_{ei} \approx \nu_{ei} \frac{v_{th}^3}{(v_{th}^2 + v_{osc}^2)^{3/2}} \ ,$$

this finally becomes independent on the thermal velocity [70] for high oscillation velocities (i.e. high intensities).

Absorption by anomalous skin effect

At high temperatures, the electron mean free path v_{th}/ν_{ei} increases and can exceed the skin depth $L_{skin} = c/\omega_{pe}$. If the average distance travelled during one laser period also satisfies the condition $v_{th}/\omega_0 > L_{skin}$, the laser field is transported in-depth in the plasma beyond the skin depth and the absorption stops being local. The effective collision frequency becomes $\nu_{eff} = v_{th}/l_{anom}$ where the anomalous skin depth is given by [71]:

$$L_{anom} = \left[\frac{v_{th}}{c} \left(\frac{\omega}{\omega_{pe}} \right) \right]^{1/3}$$

The absorption rate associated to this mechanism, for pulses shorter than a few 100 fs, interacting with a stiff density gradient ($L_{grad}/\lambda_0 < 1$), is given by [72] :

$$A_{anom} = \left(\sqrt{\frac{2}{\pi}} \frac{\omega_0^2 v_{th}}{w_{pe}^2 c} \right)^{1/3} \tag{2.11}$$

Resonance absorption

The resonance absorption, the first collisionless process to be identified [73, 74, 75], supposes a laser wave with p polarization, interacting in oblique incidence with an inhomogenous plasma (i.e. incident at an angle θ with respect to the target normal). The laser propagates up to the maximal density $n_e = n_c \cos\theta$ and it is then reflected. It can however penetrate by tunnel effect up to $n_e = n_c$ where its electric component E_z, normal to the target, may excite a longitudinal plasma wave (evanescent wave). The growth of the plasma wave is limited by thermal convection but especially by wave

breaking which takes place when v_{osc} approaches the wave phase velocity v_ϕ [76, 77]. This involves the loss of periodicity of the electronic trajectories and the electrons can be accelerated to high energies. The absorption rate due to this mechanism is [78]:

$$A_{reson} = \frac{1}{2}\left[2.3\left(\frac{2\pi L_{grad}}{\lambda_0}\right)^{1/3}\exp\left(-\frac{4\pi L_{grad}}{3\lambda_0}\right)\right]^2 \tag{2.12}$$

The absorption is maximum for the incidence angle $\theta \approx \arcsin(\lambda_0/2\pi L_{grad})^{1/3}$.

Numerical simulations at laser intensities $\sim 10^{16}$ W/cm^2 showed that the population of electrons accelerated by resonance absorption may be well described by a Maxwellian distribution of temperature [79, 80]

$$T_h[\text{keV}] \sim 10\big(T_e\, I_{16}\, \lambda[\mu\text{m}]^2\big)^{1/3}$$

The preminence of resonance absorption was verified in experiments for a laser pulse of $\sim 10^{16}$ W/cm^2, 120 fs and $\frac{L_{grad}}{\lambda} \sim 0.2$ [81]. This mechanism however weakens in the case of very steep density gradients $\frac{L_{grad}}{\lambda_0} < \frac{v_{osc}}{2\pi c}$, i.e. when the oscillation amplitude of the electrons exceeds the gradient scalelength [82]. In this case, speaking about plasma wave does not make any sense, since these are excited during each laser period.

Vacuum heating

Vacuum heating, also called *Brunel effect* [83], can also occur in the case of a target with a stiff edge (we always consider a laser pulse with p polarization interacting with oblique incidence). The electrons are torn off from the skin depth towards the vacuum by the longitudinal component E_z of the laser field E_0, during its first half-period. Since the skin depth electronic density is very high, such electrons are sufficiently numerous so that the space charge electric field thus formed may shield the E_z field. The electrons reinjected towards the target are decoupled from the laser at each laser period, carrying the energy acquired in the longitudinal oscillation, $\propto v_z^2$. The rate of absorbed energy is

$$A_{vh} = \frac{1.75(1+2\frac{v_{th}}{v_z})}{2\pi}\,\frac{v_z^3}{v_0^2 c\cos\theta}\ , \tag{2.13}$$

where θ is the incidence angle, $v_0 = \frac{eE_0}{m\omega_0}$ and $v_z = \frac{eE_z}{m\omega_0}$[1].

[1]This model, neglecting the effect of the magnetic term of the Lorentz's force, is no more valid in the relativistic case.

Vacuum heating is more effective than the resonance absorption for $\frac{v_{osc}}{\omega} > L_{grad}$. This fact has been in particular observed in numerical simulations if $\frac{L_{grad}}{\lambda} < 0.1$ and $I \sim 10^{14-18}$ W/cm^2 [84]. The average energy of the accelerated electrons is $\propto \left(I\lambda^2[\mu\text{m}]\right)^{\alpha}$, where α is between 1/3 and 1/2.

J × B (or ponderomotive acceleration)

The previous mechanisms are related to "moderate" laser intensities. At intensities higher than 10^{18} W/cm^2 (and certainly above 10^{19} W/cm^2), nonlinear effects related to the space gradients of the laser pulse begin to dominate the interaction. These effects appear in the form of a force able to push the critical surface towards the interior of the target macroscopically. This force is called *ponderomotive force*. The laser pulse presents space gradients in the transverse direction, because of its radial profile, and also in the longitudinal direction, because of its temporal profile and its damping inside the target, beyond critical surface. Let us consider a laser pulse frequency ω_0 normally focused on the target surface. Classically, an oscillating electron in an inhomogenous laser field $\left(\mathbf{E} = \mathbf{E_0}(\mathbf{r})\cos(\omega_0 t)\right.$ and $\left.\mathbf{B} = \mathbf{B_0}(\mathbf{r})\cos(\omega_0 t)\right)$ is subject to a non linear force [85] :

$$\mathbf{F}_{nl} = -\frac{e^2}{2m_e\omega_0^2}\left[\nabla(|\mathbf{E_0}(\mathbf{r})|^2)(1+\cos(2\omega_0 t))\right] \tag{2.14}$$

This force is made up of a slowly time dependent part (if compared to the laser frequency ω_0) and of a part oscillating at $2\omega_0$ frequency. In the relativistic regime [86] it becomes:

$$\mathbf{F}_{nl} = \nabla(\gamma - 1)m_e c^2 \ , \tag{2.15}$$

where γ is the electron relativistic factor. The value of the Eq. 2.14, averaged over the laser period constitutes the ponderomotive force:

$$\begin{aligned} \mathbf{F}_p \equiv \langle \mathbf{F}_{nl} \rangle &= -\frac{e^2}{4m_e\omega_0^2}\nabla(|\mathbf{E_0}(\mathbf{r})|^2) \\ &= -\frac{1}{n_c}\nabla\frac{I_0}{2c} \end{aligned} \tag{2.16}$$

It drives out the particles from the areas of strong field, but acts only slightly on the ions because of their larger mass (the ions follow the electrons under the effect of the space charge in time scale of about few picoseconds). The ponderomotive force causes the indentation of the target surface (called *hole boring*) [3, 87]. However, it is the oscillating part which, combined with the recall electrostatic force of ions, is at the

origin of the heating: the electrons in the skin depth (widened in the relativistic regime because of the reduction of the plasma frequency) are initially expelled radially and accelerated longitudinally towards the interior of the target by a force with constant direction but variable amplitude. The space charge then recalls them towards the vacuum. As we saw at the beginning of this chapter, the magnetic component of the Lorentz's force (Eq. 2.3) which acts on the electrons, in this interaction regime, has the same order of magnitude of the electric component and cannot be neglected. Then it enters in competition with the space charge forces producing an oscillating *8*-shaped movement, over-imposed on a drift which depends on the non-uniformity of the laser field in the skin layer. The electrons cannot be any more adiabatically coupled with the oscillations. The heating, produced by their dephasing is called $\mathbf{J} \times \mathbf{B}$ *heating*. Every half-cycle, trains of electrons are accelerated towards the target, as already observed in several PIC simulations [88, 89, 20]. According to Wilks *et al.* [3], these electrons present a Maxwellian distribution in energy whose temperature follows the ponderomotive potential associated with a purely transverse movement:

$$\begin{aligned} T_h &\approx \phi_p = (\gamma_\perp - 1) m_e c^2 \\ &\approx 511\,\mathrm{keV} \left[\sqrt{1 + 0.7 \left(\frac{I_0}{10^{18}\ \mathrm{Wcm}^{-2}} \right) \left(\frac{\lambda_0}{\mu\mathrm{m}} \right)^2} - 1 \right] \end{aligned} \tag{2.17}$$

For gradient lengths $L_{grad} \sim \lambda_0$, this scaling law has been confirmed numerically, by 1D numerical simulations performed by several authors [88] and experimentally [90].

Parametric absorption

The interaction of an intense laser pulse with a large subcritical plasma (such as the pre-plasma formed before the arrival of the main pulse by the low pedestal) may produce several parametric instabilities, via non-linear mechanisms supplied by the inhomogeneities of plasma, $\delta n_e / n_e$. They result from the coupling of the laser wave (*pump* wave) to diffused electrostatic and electromagnetic waves. The most effective mechanism for the acceleration of electrons is the stimulated Raman scattering, where a plasma electronic wave is amplified, due to the heating of the incident and scattered waves. The electrons can be trapped in this longitudinal wave and can be accelerated until wave breaking. Their final velocity depends on the phase velocity of the plasma wave (close to the group velocity of the laser pulse), which decreases with the density of the (pre)-plasma. The maximum energy gained by the electron is given by [91]

$$\Delta\gamma = 4\gamma_{ph}^2 \frac{\delta n_e}{n_e}$$

Where γ_{ph} is the relativistic factor associated to the phase velocity of the plasma wave. This acceleration takes place over a de-phasing distance of $l_d \approx \lambda_0 \gamma_{ph}^3$. Energies of the order of one hundred MeV were observed for very subcritical plasmas ($n_e \sim 10^{-2} n_c$) [36, 92].

In the classical regime, this instability is circumscribed to densities $n_e < n_c/4$. At high intensities, the induced transparency makes parametric instabilities possible, even for overcritical densities, (even if then all instabilities merge in a new regime [93]). However, its efficiency in heating the electrons is still definitely lower than other mechanisms presented before.

Synthesis about the acceleration and characteristic of the electrons source

In conclusion, various mechanisms of electronic heating are possible according to the considered interaction regime. The majority of them operate simultaneously. The most important parameters are on one side the laser intensity, which determines the oscillation velocity of the electrons and the importance of the non-linear and relativistic phenomena, and on the other side the gradient length which determines the typical density and the plasma thickness where the interaction develops.

However, the presence of a long slope plasma, favorable to the parametric instabilities, does not exclude the $\mathbf{J} \times \mathbf{B}$ heating because the surface of the target can be steepened by the ponderomotive effects. On another side, normal incidence does not inevitably invalidate the resonance absorption. The focusing of the laser wave on the target is indeed accompanied by a longitudinal electric component. Moreover, the deformation of the target surface makes it possible the laser locally interacting in oblique incidence.

A good characterization of the accelerated fast electron beam means determining its total energy, its distribution in energy and its angular divergence. Because of the complexity of the physics involved, it is here necessary to recall a summary of the experimental results and numerical simulations (PIC or others).

2D Simulations are able to describe all the processes presented above. For laser intensities $I \sim (3-50) \times 10^{18}$ W/cm^2 and maximum densities of $10-50\ n_c$ they predict values of conversion rate and temperature respectively equal to [94]

$$\begin{aligned} f_{abs} &\sim 40-70\% \ , \\ T_h &\sim 100-1000\,\mathrm{keV} \end{aligned}$$

These values grow with laser intensities and decrease with the density of overcritical plasma. The source of fast electrons, at the level of irradiated surface, can be described

by a Maxwellian distribution in energy [3]

$$f(\gamma, T_h) \sim \exp\left(-\frac{m_0 c^2(\gamma - 1)}{T_h}\right) \tag{2.18}$$

This makes possible to define a characteristic "temperature", T_h, of the suprathermal distribution. It can be some orders of magnitude higher than the temperature of the bulk plasma from which this population results. Experimental and numerical estimates for the temperature of the electrons were obtained for intensities ranging between 10^{17} and 10^{19} W/cm^2. By comparing the measurements carried out by three different kinds of diagnostics in the same experiment, Beg *et al.* obtained a scaling law for the temperature of the accelerated electrons T_h *vs.* laser intensity [95]:

$$T_h[\text{keV}] = 100\left[\left(\frac{I_0}{10^{17}\ \text{Wcm}^{-2}}\right)\left(\frac{\lambda_0}{\mu\text{m}}\right)^2\right]^{1/3} \tag{2.19}$$

This experiment was undertaken with an incidence angle of the pump laser on target of 30°, undoubtedly supporting accelerating mechanisms (resonance absorption or the anomalous skin absorption, dependending on the laser intensity) different from those which are probably dominant in our experiments, carried out in normal incidence. In our case, we estimate that the principal heating mechanism is the $\mathbf{v} \times \mathbf{B}$ heating[2], for which Wilks' simulations [3] and Beg's law [95] established heuristically scaling laws for temperature of the electrons previously produced (Eq. 2.17).

Fig. 2.2 shows the temperature *vs.* the laser intensity predicted by the two scaling laws. Calculation have been made for the laser wavelength $\lambda_0 = 1.057\,\mu$m. For moderated intensities, we see that the temperature from Beg's law (Eq. 2.19), associated to a resonance acceleration process, is slightly higher than that from the Wilks' law (Eq. 2.17). On the other hand, for larger intensities (10^{18} W/cm^2), the Wilks' law dominates, revealing the prevalence of the ponderomotor mechanisms. In our experimental conditions ($I_0 \gtrsim 10^{19}$), the Beg's law predicts an electronic temperature of about few hundreds of keV and the Wilks' law a temperature higher than MeV. Experimentally, irregularities of the target surface and nonuniformities of laser irradiation (*hot spots*) can simultaneously support a large variety of accelerating mechanisms in different zones of the laser focal spot, producing an electronic population characterized by distinct temperatures. Tikhonchuk [96] estimates that the spectrum in energy of the electron beam accelerated in the interaction of an UHI laser with a solid target can have two components:

[2]However this does not exclude mechanisms rather related to an oblique incidence, because of, especially, the awaited deformation of the target surface

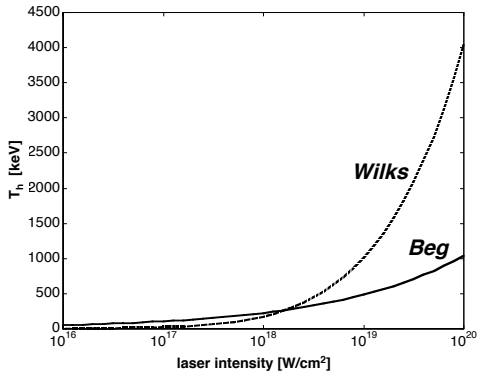

Figure 2.2: Temperature of the accelerated fast electron population as a function of the laser intensity. Solid curve: estimation according to Beg *et al.* [95] (Eq. 2.19). Dashed curve: estimation according to Wilks *et al.* [3] (Eq. 2.17).

- A not very dense part, $n_f \sim 10^{18-19}$ cm^{-3}, with an average kinetic energy of about $\langle E_{kin} \rangle \sim 5 - 10$ MeV. Its total energy is about only less than the 1% of the laser energy in the focal spot. This component arises from acceleration by plasma waves excited in the pre-plasma formed at the front target surface.

- A denser part, $n_f \sim 10^{21}$ cm^{-3}, with $\langle E_{kin} \rangle$ of about few hundreds of keV, probably due to ponderomotive acceleration.

The electronic distribution will change in time during the propagation in matter under the effect of deceleration processes discussed in the following section. The first in time and the more energetic electrons will travel in the target without being disturbed by the remaining part. Because of the weak energy content of this part of the electronic distribution, it disturbs the medium only very slightly and will then have almost no influence on the propagation of the bulk of fast electrons. At least, this is true for metal targets characterized by densities of free electrons largely higher than the beam density. Instead, in an insulator, the first and very energetic electrons have the considerable effect of ionizing the material. The bulk of fast electrons then travel in a sensible changed medium.

2.2 Fast electron transport in matter

The propagation in solid matter of a beam of charged particles is a complex process which involves several mechanisms, related at the same time to the background material and to the particles energy.

Since in laser-matter interaction experiments the accelerated electrons come from the target itself, the local neutrality of the medium is affected, giving place to important collective effects. In general the propagation of an electron beam in matter is accompanied by angular deflection and energy loss. The fundamental physical processes which take place are:

- Collisional effects, due to the elastic and inelastic scattering between fast electrons and ions and free electrons of the crossed medium;
- Electric and magnetic effects (collective) due to the fields induced in the target during the propagation.

2.2.1 Collisional effects: fast electron scattering

The high density of the propagation medium forces us to take into account the Coulomb collisions of the suprathermal electrons with the elements which constitute the propagation medium (ions, electrons). Such "individual" interactions can be elastic or inelastic. They lead to an angular deflection and a loss of energy of the electron beam. Inelastic collisions with atomic electrons are the principal responsible for energy loss. The energy lost by fast electrons is transferred to the medium in the form of excitation, ionization or radiation emission, and it can cause the change of the atomic states of the medium. On the contrary, the elastic collisions take place with the ions of the medium: a small part of the primary electron energy is yielded to the atom as recoil energy without its state being affected. The large difference in mass between the two particles justifies the fact that elastic collisions play a minor part in energy transfer, but they are those which contribute more to the angular diffusion of the electron beam.

Angular scattering

The angular scattering due to a coulomb collision can be described by Rutherford's theory. In an ionized solid this is limited on one side by the shielding effects of the atomic nucleus, and on the other side by the Debye length, which define "individual" interaction and therefore limits the scattering angle. Thanks to the long range of the Coulomb force, the collisions with small angles are much more frequent than the

collisions with great angles. The cumulative effect of many small scattering becomes more important than the effect of a few individual scattering events at great angles.

The scattering angular range is thus divided into three regions:

- A "simple scattering region", with large scattering angles;
- A "multiple scattering region", with small scattering angles;
- An intermediate "plural scattering region", which is very difficult to model.

We are especially interested in the multiple scattering region and the physical quantity of interest is the average quadratic angle

$$< \theta^2 >= \frac{\int \theta^2 \, d\sigma}{\int \, d\sigma} \ ,$$

where $d\sigma$ is the scattering cross section. According to Rutherford's formula, we can calculate the scattering average quadratic angle for solids or plasmas. For a penetration dz, we obtain (in CGS units):

- For a solid [97]:

$$\frac{d\langle\theta^2\rangle}{dz} \simeq \frac{16\pi}{m_e^2 c^4} \frac{n_i Z(Z+1)e^4}{\gamma^2\beta^4} \ln(204Z^{-1/3}) \ ,$$

  where n_i is the volume density of the ions and Z is the ion charge.

- For a plasma [98]:

$$\frac{d\langle\theta^2\rangle}{dz} \simeq \frac{8\pi}{m_e^2 c^4} \frac{n_i Z^2 e^4}{\gamma^2\beta^4} \ln\Lambda \ ,$$

  where $\ln\Lambda$ is the Coulomb logarithm.

Since successive collisions are independent phenomena, the theorem of the central limit states that for a rather larger number of collisions the angular distribution will roughly be Gaussian around the direction of propagation of the beam with an average quadratic angle $\langle\theta^2\rangle$ given by the previous formulas. Other statistical models, known as multiple scattering models, describe the angular distribution resulting after many collisions. In particular, we are interested in *Molière's theory*, adapted to a strongly collisional case, as in solids [99]. This theory converges to a Gaussian distribution for small angles and roughly reproduces the Rutherford scattering for larger angles. It is valid only for a sufficiently large number of collisions (≥ 5), and can be used only in solids, while at the moment is not adapted to plasmas.

Collisional deceleration

As we saw before, the energy loss during an elastic electron-ion collision is several orders of magnitude lower than that in electron-electron collisions. The exchanged maximum energy (which corresponds to the case of an head-on collision, much less probable than a collision at small angle) is given by

$$(\Delta\mathscr{E}_{max})_e \simeq \frac{\mathscr{E}_0(\mathscr{E}_0 + 2m_e c^2)}{918 m_e c^2 A} \ ,$$

where A is the nucleus atomic mass and $\mathscr{E}_0$ is the initial energy of the incident electron. In aluminium ($A \simeq 27$), material frequently used in our experiments, the fraction of maximum energy lost in one elastic collision varies between 0.009% and 0.048% for energies ranging from 100 keV and 5 MeV. This energy loss is, in general, much lower than the average loss associated with an inelastic collision. Nevertheless, during its propagation, the electron undergoes a great number of elastic collisions and thus the energy effectively lost can become considerable. From solid samples with atomic numbers Z varying from 4 to 50, an expression was found for the relationship between the inelastic and elastic cross sections [100]:

$$\frac{\sigma_{inel}}{\sigma_{el}} = \frac{20}{Z}$$

therefore only in the heaviest elements we cannot neglect the energy loss due to elastic collisions in relation to inelastic collisions. For aluminium ($Z = 13$), $\frac{\sigma_{inel}}{\sigma_{el}} \approx 1.5$, we will consider that the fast electrons energy loss is mainly due to the collisions with the electrons of the medium. Thereafter, we will consider only the contribution of the inelastic collisions to the fast electrons deceleration inside the target. To quantify this aspect, we introduce the concept of range $\langle S \rangle$ and of average energy loss during the trajectory $\langle \frac{d\mathscr{E}}{ds} \rangle$. This quantity, called *stopping power*, is a function of the incident electron energy and of the material characteristics, and takes into account the various mechanisms of energy exchange during collisions. We will approach the cases where the propagation medium is a cold solid or a hot plasma.

Propagation in a cold solid The principal mechanisms responsible for the energy loss by collisions in a cold solid are:

- The ionization or the excitation of the material atoms.
- The radiation emission by bremsstrahlung due to the interaction with the nuclear electric field.

The total stopping power will be the sum of two terms corresponding to these two contributions:

$$\left(\frac{d\mathscr{E}}{ds}\right)_{tot} = \left(\frac{d\mathscr{E}}{ds}\right)_{ion} + \left(\frac{d\mathscr{E}}{ds}\right)_{rad}$$

The first term is expressed [101]:

$$\begin{aligned}\left(\frac{d\mathscr{E}}{ds}\right)_{ion} &= -\frac{2\pi n_i Z e^4}{mc^2\beta^2}\left[\ln\left(\frac{(\gamma^2-1)(\gamma-1)}{2(I_p^Z/mc^2)^2}\right)\right. \\ &+ \left.(1-\beta^2) - \frac{2\gamma-1}{\gamma^2}\ln 2 + \frac{1}{8}\left(\frac{\gamma-1}{\gamma}\right)^2 - \delta\right], \end{aligned} \tag{2.20}$$

where n_i and I_p^Z are the atomic density and the material average ionization potential, respectively. The latter depends on the atomic number according to the following empirical formula [102]:

$$I_p^Z\,[\mathrm{eV}] = 9.76Z + 58.8Z^{-0.19} \tag{2.21}$$

This expression reproduces, for Z much beyond 13, the experimental values of the average ionization potential coming from measures of α particles penetration length, such those published in the ICRU report [103].

The *ionization* stopping power (Eq. 2.20) is composed of two factors: the first, decreasing function of the electron velocity, is important above all at low energy ($\lesssim$ 1 MeV); the second, grows more slowly with energy, and becomes important at high energies. This growth is slowed down by the corrective parameter δ representing the density effect acting for large impact parameters if compared to atomic dimensions, when the perturbation of the atomic scattered field (induced by the close atoms) is no longer negligible. Under these conditions, the interaction shows a collective behaviour [104, 105]. Also let us note that Eq. 2.20 supposes an incident electron energy larger than that of atomic electrons. It is valid only for kinetic energies higher than the ionization potential of the K-shell background material. The *ionization* stopping power is represented in Fig. 2.3 for cold aluminium according to the kinetic energy of the incoming electron.

On the contrary to the "ionization" stopping power, the "radiative" stopping power is proportional to the incoming energy and to Z^2. It can then become very high for heavy elements. The relationship between the two energy losses is approximate [106]:

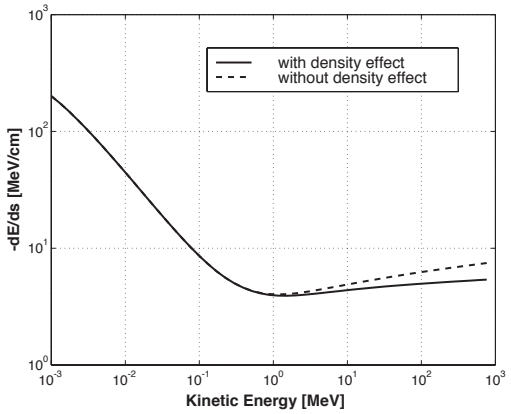

Figure 2.3: Ionization stopping power in cold aluminium *vs.* the electron kinetic energy: with density effect (line) and without density effect (dashed).

$$\frac{(d\mathscr{E}/ds)_{rad}}{(d\mathscr{E}/ds)_{ion}} \simeq \frac{Z\mathscr{E}_0}{1600mc^2}$$

The radiative mechanism prevails in the deceleration of the incoming particles when the energy is larger than a critical value: $\mathscr{E}_0 > 1600mc^2/Z$. In the case of heavy elements like lead ($Z = 82$), this limit is $\mathscr{E} \simeq 9.8\,\mathrm{MeV}$. In the case of aluminium, it is $\mathscr{E} \simeq 63\,\mathrm{MeV}$. We can thus neglect the energy loss by bremsstrahlung in our experimental conditions. Only a tiny fraction of the electrons will have a sufficient energy to effectively produce bremsstrahlung radiation, while crossing the propagation layer.

Propagation in a hot plasma In the case of a heated solid, which becomes a plasma with an ionization state Z^*, in addition to the contribution of the bound electrons, it is necessary to take into account the contribution of the free electrons and the plasmons (excitation of plasma waves).

The ionization and radiative stopping powers are modified by the presence of two types of electronic populations (free and bound) whose relative importance is determined by the average charge of the ionic population. In particular, the ionization stopping power decreases when the plasma temperature increases. This comes from simultaneous effects. First, the number of bound electrons decreases and the stopping power becomes

$$\left(\frac{d\mathscr{E}}{dx}\right)_{ion}^{Z^*} = \frac{Z - Z^*}{Z}\left(\frac{d\mathscr{E}}{dx}\right)_{ion} \tag{2.22}$$

$(d\mathscr{E}/dx)_{ion}$ is given by the expression 2.20 where we neglect the δ term due to the density effect. Second, the average ionization potential increases because of the reduction in the nuclear shielding. A scaling law for the average ionization potential was proposed by More [107]:

$$I_p^{Z^*}[\mathrm{eV}] = 10\,Z\frac{\exp\left[1.29\left(\frac{Z^*}{Z}\right)^{0.72-0.18Z^*/Z}\right]}{\left(1-\frac{Z^*}{Z}\right)^{1/2}} \tag{2.23}$$

Such a shielding reduction also causes the increase of the radiative stopping power with the temperature. The contribution to the total energy loss remains however negligible.

In addition to these changes, it is necessary to take into account the mechanisms of deceleration, due to the presence of a free electrons population:

- The noncollective interaction with the plasma free electrons, for impact parameters lower than the Debye length ($b < \lambda_D$).
- The interaction with the plasma collective modes (plasmons) for impact parameters greater than the Debye length ($b > \lambda_D$).

The $non-collective$ contribution of the free electrons to the plasma stopping power is [108]:

$$\left(\frac{d\mathscr{E}}{ds}\right)^{Z^*}_{free} = -\frac{2\pi Z^* n_i e^4}{mc^2\beta^2}\left[\ln\frac{1}{4\epsilon_{min}} + 1 - \frac{2\gamma-1}{\gamma^2} + \frac{1}{8}\left(\frac{\gamma-1}{\gamma}\right)^2\right] \tag{2.24}$$

here $\epsilon_{min} = (\lambda_{db}/D)^2$ where λ_{db} is the De Broglie length and D is the effective Debye length, defined as the maximum of the traditional Debye length and of the interatomic radius $r_i = (3/4\pi n_i)^{1/3}$, in order to take into account the effects of ionic correlation at low temperature and high density. More in general, the contribution of the free electrons (Eq. 2.24) increases with the temperature because of its linear dependence on the ionization state Z^*, and the increasing of Debye length, in particular at low density. On the other hand, it decreases, with the plasma density, because of the Debye length reduction.

To finish, the contribution to deceleration from excitation of plasma waves is given by:

$$\left(\frac{d\mathscr{E}}{ds}\right)^{Z^*}_{plasmons} = -\frac{2\pi Z^* n_i e^4}{mc^2\beta^2}\ln\left[1+\left(\frac{v}{\omega_{pe}D(3/2)^{1/2}}\right)^2\right]\,, \tag{2.25}$$

where ω_{pe} is the plasma electron frequency of the ionized plasma and $n_e = Z^* n_i$.

2.2.2 Collective effects

Beyond the collisional effects, of individual nature, previously presented, the propagation of an intense beam of electrons in dense matter is also ruled by a range of effects of collective nature due to the electric and magnetic fields induced by the beam itself.

For instance, the beam self interaction may lead to its magnetic pinching - and thus be able to partially compensate the angular divergence associated to the multiple scattering. The electromagnetic response of matter is determined by a return current, resulting from the acceleration of a part of the free electrons in the medium, in order to neutralize the current of the incoming suprathermal electrons. Such a return current, necessary to allow the propagation of currents exceeding the Alfvén limit, can be nevertheless at the origin of instabilities, potentially harmful to the fast electron propagation.

Neutralization

Propagation in conductors Let us consider the injection of an intense electron beam in a conducting medium. The beam density is much lower than the medium electronic density. The beam propagation could be limited by its Coulomb explosion if a reallocation of the medium charges does not neutralize the beam space charge: however the local overdensity of negative charge, due to the presence of the beam, produces an electrostatic field which pushes back the exceeding electrons[3], out of the beam region. The neutralization characteristic time depends only on the nature of the crossed medium and it is about:

- Case of a **noncollisional medium (hot plasma)**

$$\tau_{neut} \sim \frac{1}{\omega_{pe}} \ ,$$

  It corresponds to a time during which a plasma, subjected to a disequilibrium in charge, reacts with a recall force.

- Case of a **very collisional medium** (ohmic material)

$$\tau_{neut} \sim \frac{\epsilon_0}{\sigma} \qquad \text{or} \qquad \sim \frac{\nu}{\omega_{pe}^2} \ ,$$

  where ϵ_0 is the vacuum dielectric permitivity, σ is the medium conductivity and ν is the electron-ion collisions frequency. In Aluminium $\sigma \gtrsim 10^6\,\Omega^{-1}\mathrm{m}^{-1}$,

[3]Those of the medium, because the beam electrons are almost inert according to their relativistic nature.

this time is about 10^{-17} s. The collective process of neutralization, logically, is slowed down by the collisions. The more important the collisions are, the more neutralization is difficult.

Another limitation related to the transportable current is due to magnetic effects. If the current is very intense, the self-generated magnetic field can even reverse the electron motion with respect to their initial propagation direction. According to Alfvén [109], the maximal propagating current is given by

$$I_A \simeq \frac{\beta_f \gamma_f m c^3}{e} \simeq 1.7 \times 10^4 \mathrm{A}\, \beta_f \gamma_f \tag{2.26}$$

I_A is called *Alfvén limit* and physically corresponds to the situation where the beam magnetic field is sufficiently intense to reverse the propagation direction of the electrons in the beam edge. In their expression β_f and γ_f are respectively the normalized velocity and the relativistic factor of the beam electrons. If the current is higher than this limit, it will stop propagating, unless the medium can provide a *return* current which lowers the total current value below the Alfvén limit. When the plasma depth is much lower than the beam radius, this neutralization in current takes place locally, even inside beam. Depending on the medium conductivity, this inductive electric field can considerably decrease the total current, and thus the total magnetic field. This allows the propagation of beam currents higher than the Alfvén limit. The current neutralization characteristic time is of the order of the magnetic diffusion time, an increasing function of the medium conductivity

$$\tau_B = \frac{\sigma r_f^2}{\epsilon_0 c^2} \tag{2.27}$$

where r_f is the beam radius. This time is very long (10 ps) in the case which interests us.

Propagation in neutral gases and insulators The necessity of current neutralization as well as charge neutralization explains the dramatic effect on the propagation of the density of free electrons in the medium. In insulators and gases, in opposition to conductors, the beam density is greater than the medium free electron density and free electrons need to be created by field or impact ionization, processes which require time and energy and could be highly nonstationary. This results in stronger fields and a more inhibited motion. As for the nature of fields producing inhibition, Bell *et al.* [110] considering an electrostatic field (cf. Ref. [96]), explicitly calculates charge separation and electrostatic fields through Poisson equation in the insulator case. However, most computer models [111] neglect electrostatic fields; inductive fields play the main role, a reasonable assumption in conductors but probably not in insulators and neutral gases, as we will see later in the next chapters.

Instabilities

In the description of the injection of an intense electron beam in a medium, we should not only hold into account the medium reaction, but also the way in which this reaction can affect or disturb the initial beam distribution.

During the propagation, the return current cancels the incident current almost completely (i.e. the net current will be below the Alfvén limit). This quasi stationary state, where the self-induced fields act little on the electrons of the beam, is however favorable to the development of various instabilities, either microscopic (on a scale much lower than the beam radius) and macroscopic (on a scale of the order of the beam radius or larger).

Microscopic Instabilities Because of the coupling of the beam with the plasma particles, instabilities develop through the local generation of electrostatic and electromagnetic fields. The interplay of the incoming beam and the return current, with opposed velocities, gives place to an axial or transversal beam velocity dispersion, which can be negative for the fast electrons transport. This kind of instabilities, known as microscopic or kinetic, develop on a temporal scale of the order of the plasma frequency (of the beam or of the plasma). For example we can distinguish:

- the **two-stream instability** [112], where the electrostatic disturbance induced by the intense beam (much less dense than the plasma) can excite natural plasma oscillations.
- the **Weibel instability** [113] (also known as *electromagnetic filamentation instability*), which is produced by the magnetic repulsion between currents of opposite directions which reinforce any initial displacement. It tends to break the local current neutralization of the incoming beam, by splitting it up in filaments. This modulation of the current density profile is accompanied by the creation of a similarly modulated electromagnetic field, accentuating the pinching of the filaments.

Macroscopic instabilities Because of the limited conductivity of the propagation medium, instabilities also develop on the scale of the radius of the incidental beam. The macroscopic instabilities characteristic time is comparable to the magnetic diffusion time, hence their growth is much slower than the microscopic mechanisms. We can evoke:

- **hollowing instability**, which leads to a minimum of current on the beam axis. The limited conductivity of the medium results in a non-completely achieved current neutralization. This produces the focusing of the incoming beam, and the

current over-density on the axis implies in turn a localized plasma heating. This process is unstable since the ohmic heating due to the return current will further lower the resistivity on axis, amplifying the initial perturbation accentuate the initial disturbance by still lowering the resistivity. The incoming and the return currents reject each others and the local over-density of this last one will induce a digging of the first current.

- the **hosing instability** is an hydromagnetic instability which results in a snaking movement of the beam following a transverse displacement. Even if small, a beam displacement involves a magnetic field for a duration of the order of the magnetic diffusion time τ_b, in order to preserve the total current before the displacement. A recall force, due to the interaction between the longitudinal beam current and the perpendicular component of the residual magnetic field, pushes the beam towards its original position. In the presence of a limited conductivity, beam displacements and the recall forces can be dephased leading to an instability[4].

- the **sausage instability** is a symmetrical deformation of the beam envelope. An unstable mode can then develop, associated to a self-similar expansion and contraction of the beam section, without affecting the radial beam profile.

- the **ionization instability**, which occurs as a high intensity electron beam propagates through an insulator [114, 115]. In insulators, the charge separation at the edge of the propagating intense electron beam produces a strong electrostatic field [96, 116], which very rapidly ionizes the material. Moreover, even if the bulk of the fast electron beam propagates in a dense plasma (the conductivity of which is only marginally different from the conductivity of a metal) the ionization front becomes unstable because its velocity increases with the electron beam local density. This enhances small corrugations of the ionization front which grow in time.

The instabilities described above can lead to plasma heating and limit the energy which a beam can transport through the medium.

Material collective heating

In addition to the collisional effects, of individual nature, collective effects in electronic transport in dense matter can largely increase the beam energy deposition and thus the material heating.

[4]In the non-collisional case the plasma is a perfect conductor ($\tau_b \to \infty$), and the beam magnetic field is frozen in the plasma. In this limit the fast electrons will oscillate at the betatron frequency.

The magnetic neutralization of the incoming current is primarily done by the means of an electromotive magnetic field which accelerates the return current and slows down the beam. The energy lost by this mechanism simultaneously contributes to heat the plasma and to generate a magnetic field.

In the Lovelace & Sudan's model [117], somewhat modified by Gremillet [118], an important fraction of the beam energy is converted into plasma thermal energy. In this model, the energy lost by a Gaussian beam is obtained by integration in time and space of the power density $\mathbf{j}_f \cdot \mathbf{E} = \eta j_f j_p$ (η is the medium resistivity), which leads to the expression:

$$W_f = \left(e\pi r_f^2 n_f \beta_f\right)^2 \ln\left(1 + \frac{2t}{\tau_B}\right) , \tag{2.28}$$

the energy provided to plasma (ohmic heating), resulting from the integration of $\mathbf{j}_p \cdot \mathbf{E} = \eta j_p^2$, is given by:

$$W_p = \frac{1}{2}\left(e\pi r_f^2 n_f \beta_f\right)^2 \ln\left(1 + \frac{4t}{\tau_B}\right) \tag{2.29}$$

The heating per unit length of plasma can be obtained by taking a perfect gas model:

$$\frac{3}{2} n_p k_B T = W_p \tag{2.30}$$

The temperature, in practical units, is given by the approximation:

$$T[\mathrm{eV}] \approx 400\, \beta_f^2 \left(\frac{Z^* n_i}{6 \times 10^{22}\,\mathrm{cm}^{-3}}\right)^{-1} \left(\frac{n_f}{10^{20}\,\mathrm{cm}^{-3}}\right)^2 \left(\frac{\eta}{10^{-6}\,\Omega\mathrm{m}}\right) \left(\frac{t}{500\,\mathrm{fs}}\right) \tag{2.31}$$

Left panel of Fig. 2.4 shows the heating induced by this ohmic effect in an Aluminium plasma, for two different monokinetic beams. Even if this estimation neglects the beam dynamics and the variation of the resistivity with the temperature, as well as the effect of possible instabilities, the obtained result, predicting temperatures of about a few tens of eV, shows the importance of the heating due to ohmic mechanisms only, with "usual" experimental parameters. For this calculation, we considered the ionization state Z^* as a function of the temperature according to the approximate More's formula, deduced from the Thomas-Fermi's theory [107] for an ionic aluminium plasma density $n_i \approx 6 \times 10^{22}\mathrm{cm}^{-3}$ (cf. right panel of Fig. 2.4).

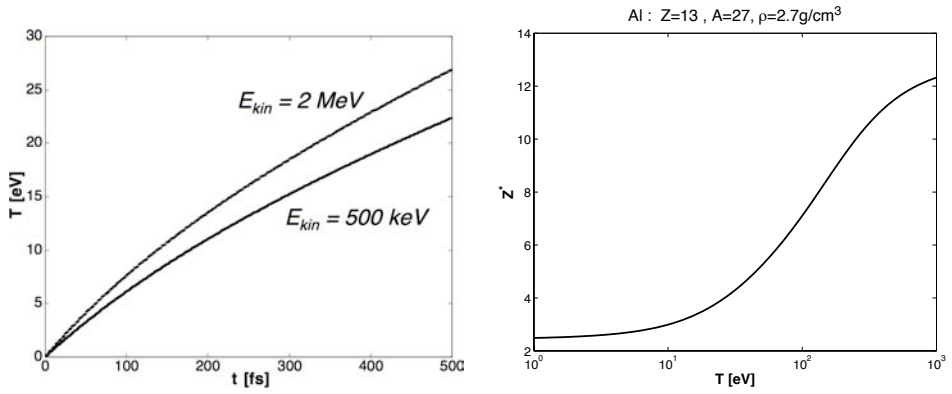

Figure 2.4: An ohmic heating of an Aluminium plasma as a function of time for two Gaussian monokinetic beams of electrons. Beam parameters: ray $r_0 = 4\,\mu$m and electron density $n_f = 5.3 \times 10^{19}\,\mathrm{cm}^{-3}$. The medium resistivity is $\eta = 10^{-6}\,\Omega$m. On the right-hand side, Aluminium ionization state as a function of the temperature.

2.2.3 Competition between collisional and collective effects

The upper limit of collisional heating is obtained by neglecting the angular scattering. Energy per unit length provided to plasma by collisions is thus written as:

$$W_p^{collision} = \pi a^2 n_f \beta_f c t \left(\frac{dE}{ds}\right) \ , \tag{2.32}$$

where, dE/ds is given by the formula 2.20[5], if we take into account (for the sake of simplicity) only the logarithmic term (other terms have only a corrective nature). The relationship between the energy yielded by collisional and collective effects is then written, in practical units [118]:

$$\begin{aligned} \frac{W_p^{collision}}{W_p} &\approx 6.4\,10^{-4}\,\frac{1}{\beta_f^3}\left(\frac{Z n_i}{6\,10^{22}\,\mathrm{cm}^{-3}}\right)\left(\frac{n_f}{10^{20}\,\mathrm{cm}^{-3}}\right)^{-1}\left(\frac{\eta}{10^{-6}\,\Omega\mathrm{m}}\right)^{-1} \\ &\times \ln\left(\frac{(\gamma^2-1)(\gamma-1)}{2(I_p^Z/mc^2)^2}\right) \ , \end{aligned} \tag{2.33}$$

where we used the fact that $4t/\tau_B \ll 1$. As expected, the relative importance of the ohmic effects is proportional to the medium resistivity and the density of the incoming

[5]The expression 2.20 corresponds to the case of the ionization losses in a cold solid. More rigorously, for the calculation of 2.32 we should consider a hot solid, but the collisional stopping power presents only a weak dependence with the temperature [118]

current. Fig. 2.5 shows the evolution of this ratio as a function of the kinetic energy of the incoming beam. We can then conclude that with our typical experimental parameters, target heating is mainly of Ohmic origin

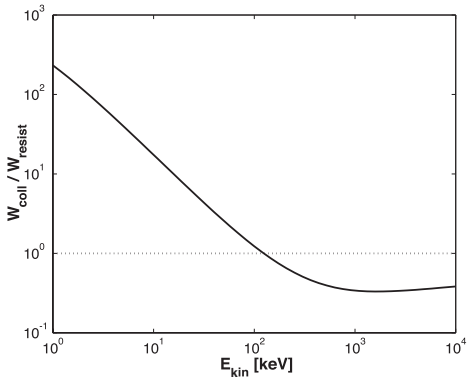

Figure 2.5: Ratio of the heating induced by collisional effects and ohmic heating, as a function of the kinetic energy of the incoming population. Parameters are identical to Fig. 2.4.

Part III

Experiments and experimental results analysis

Chapter 3

Fast electron Propagation in gas jets: Experimental results

Until now, many experiments were performed using optical diagnostics in order to study the fast electrons propagation in solid targets and more particularly the heating they induce. These experiments were often based on shadowgraphy diagnostics [119, 120] or reflectometry [121] aiming to detect the ionization front propagation inside transparent targets. For limited laser intensity ($10^{14} - 10^{17}$ W/cm^2), it was possible to associate the ionization front velocity to a thermal conduction wave or to a radiative wave. However, these have velocities almost two orders of magnitude lower than the propagation velocity of suprathermal electrons. A similar shadowgraphy experiment, carried out at the LULI laboratory at higher laser intensity (10^{19} W/cm^2) [122, 123] showed a ionization front propagated in a silica target at $c/3$ surmounted by even faster ($c/2$) narrow jets ($10 - 20$ μm). These velocities cannot be explained by a diffusion model and unveil non local effects like suprathermic electrons or hard X-rays. Specific tests made it possible to exclude the possibility of hard X-rays. The observed velocities can thus be associated only to the fast electrons propagation: a larger isotropic cloud transporting the major part of the electron energy at $c/2$ and collimated jets of fast electrons, justified by the focusing effect of self-induced magnetic fields. This experiment showed that the fast electrons can propagate and ionize a solid target over several hundred microns.

The effect of target density on electron propagation has been evidenced in experiments using K_α spectroscopy and foam targets [124]. This was related to the difference in conductivity for different heatings induced by the fast-electron propagation [124, 116]. The necessity of current neutralization as well as charge neutralization explains the dramatic effect on the propagation of the density of free electrons in the

medium. This qualitatively explains the differences observed between insulators and conductors: in insulators, free electrons need to be created by field or impact ionization, processes which require time and energy. This results in stronger fields and a more inhibited motion. As for the nature of fields producing inhibition, Bell *et al* consider an electrostatic field [110]. Tikhonchuk [96] explicitly calculates charge separation and electrostatic fields through Poisson equation. However, most computer models [111, 125, 126] neglect electrostatic fields; inductive fields play the main role, a reasonable assumption in conductors but probably not in insulators. A recent experiment [127, 128] gave other indications on the the fast electrons transport: a gas jet, at the back of a solid target, was probed transversely using a shadowgraphy diagnostic. Fast electrons, created in the solid target, emerged in the jet and, thanks to snap shots images taken at closer delays ($1 - 5$ ps), a filamented ionization front could be observed. This ionized front comes from the target back surface and then propagates into the gas. The initial size of the filamented area is ~ 100 μm for a target thickness of 50 μm. The goal of the experiments described in [127, 128] was the study of the fast electron propagation in a regime where the beam density approaches the density of the background plasma. They showed a small-scale filamentation instability using a large magnification but neglecting the global electron propagation on a larger spatial scale. Also, some filamentation may be present at the front edge (as already observed in [127]) but it could be related to an ionization instability, rather than Weibel, and in any case it does not seem to be the main element in driving the fast electron dynamics which appears instead to be governed by electrostatic fields. On the other side, the presence of strong electromagnetic fields in the material has been inferred through the observation of electric inhibition of the propagation of fast electrons in insulators [129] and foams [124], but they have not been directly evidenced. From this point of view, the propagation of fast electrons in gas targets is most promising: indeed due to the low electron density of the background material, it is particularly difficult establish a return current, bringing to a large charge separation and very strong electrostatic fields.

Moreover, since the gas is also transparent to light probe, in the same experiment we used chirped shadowgraphy to follow fast electron dynamics. This is another novel diagnostics, which allows the evolution to be followed on a single-laser shot, unlike the 2D classical shadowgraphy used in [130], thereby getting rid of the shot-to-shot fluctuations. The diagnostics is quite similar to that used in [131] with the exception that there the probe beam was reflecting on a perturbed solid target, while here it transversally probes the gas.

In order to investigate the dynamic of the fast electrons at such low densities where electric inhibition is maximized and directly show the existence of such huge electrostatic fields, we performed few experiments using two complementary, temporal and spatial resolved diagnostics:

- *Classical* and *chirped* shadowgraphy: since the gas is transparent to light probe, we used the shadowgraphy diagnostic (in two different configuration) to follow fast electron dynamics. In its *chirped* scheme, this is a novel diagnostics, which allows the evolution to be followed on a single-laser shot, unlike the 2D classical shadowgraphy thereby getting rid of the shot-to-shot fluctuations. The *chirped* shadowgraphy diagnostics is quite similar to that used in [131] with the exception that there the probe beam was reflecting on a perturbed solid target, while here it transversally probes the gas.

- *The proton imaging*: depending on the experiment being performed, laser - generated protons can be used to measure a mass difference in the crossed material [22]. However, since protons are charged particles, they are sensitive to electric and magnetic fields, allowing the direct measurement of such fields [132]. Let's notice that such possibility is limited to quasi static fields only, which is our case, since rapid oscillating fields are averaged out. Indeed the gas medium is practically non-collisional for the probe protons (as well as for the propagating fast electrons) due to its low density. Therefore any deviation of protons can only be due to electric and magnetic fields.

In this context, we first generate fast electrons by irradiating a thin metallic (Ti) target with a high-intensity short-pulse laser, before propagating them in a gas jet (Ar or He) at different densities. Advantages of using a gas are: (i) density can be easily changed by adjusting the pressure; (ii) gases are optically transparent so that optical shadowgraphy can be used as a diagnostic tool; (iii) a gas, as foams, fused silica and plastic, is an insulator, implying the need for ionization; (iv) very low densities can be used, thus maximizing inhibition; this offers a unique possibility of studying inhibition when it is not marginal. Also, the gas medium is practically noncollisional for fast electrons, hence the main effect on propagation is due to self-generated fields.

Finally, it should be noted that, in fast ignition, the deposition of 10 kJ in ∼10 ps over ~ 10 μm [4] implies fast-electron densities $n_b \sim 10^{23}\mathrm{cm}^{-3}$. While at present it is not clear how these can be generated, still such densities are much larger than in typical coronal plasmas ($n_e \sim 10^{21}\mathrm{cm}^{-3}$). Hence the study of the limit $n_b \geqslant n_e$ is also of practical importance for fast ignition. This limit is indeed also met in our experiment: we recall that typical fast-electron energy of ~ 1 MeV, and conversion efficiencies from laser energy to fast electrons up to $15 - 25\%$, have been measured with our setup [129, 133, 134]. Since the electron beam is produced from a region comparable to the focal spot in a time of the order of the laser pulse duration, we get $n_b \sim 5 \times 10^{20}\mathrm{cm}^{-3}$ (as expected, of the order of the laser critical density), while the atomic gas densities used in the experiment are $n_e \sim 3 \times 10^{19}\mathrm{cm}^{-3}$, as we will show later.

3.1 Laser facility and experimental configuration

3.1.1 LULI's 100 TW laser

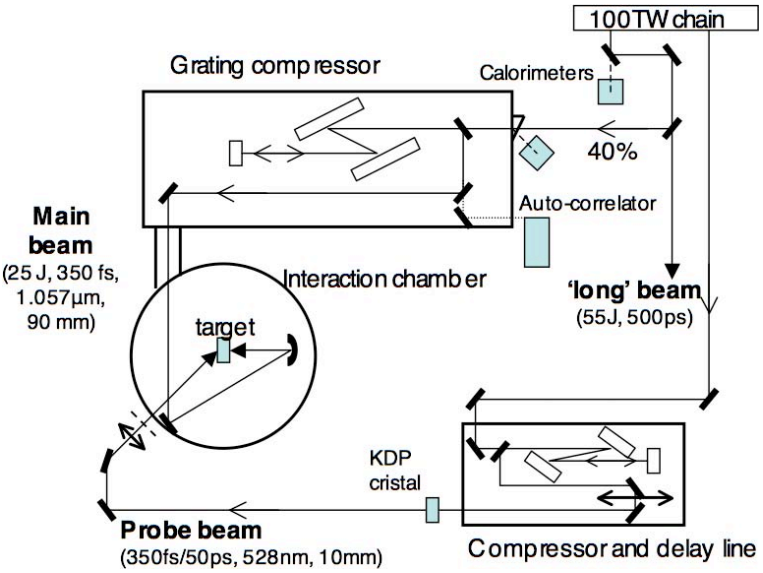

Figure 3.1: Diagram of the beams in the interaction room of 100 TW laser chain at LULI.

The experiment was realized on the LULI's 100 TW laser facility, based on the Chirped Pulse Amplification technique [1]). The pulse of 100 fs and 1 nJ resulting from a Ti:Sa (*Tsunami*) oscillator is initially temporally stretched to $\sim$ 2 ns and injected into a Ti:Sa regenerative amplifier, which works at 10 Hz and is characterized by a gain of $\sim 10^6$. The resulting pulse with mJ energy (also used as alignment and synchronization beam in the experimental room) is then sent in an amplifying chain of mixed glasses (phosphate and silicate) doped with neodymium, where it reaches its final energy of $\sim$ 90 J, with a duration of 500 ps, a diameter of 90 mm and a spectral width of 6 nm. At the entry of the interaction room, a beam splitter $R \approx 40\%$ divides the laser beam into two beams (see Fig. 3.1 for the facility setup in the interaction room):

- One, of approximately 35 J, is injected into a 4-loop grating compressor under vacuum and is temporally compressed to 350 fs (FWHM) with a conversion efficiency of 65%. This main "interaction" beam[1] is sent to the interaction chamber through a vacuum passage (10^{-3} mbar) and focused on the target, placed at the center of the chamber.

[1]The maximum energy injected into the compressor is determined by the damage threshold of these diffraction gratings.

- The second beam, can be used either compressed, by an in air-compressor (< 10 J, 400 fs) or not compressed (55 J, 500 ps). The laser beam is equipped with an adjustable delay line and can be used to create a pre-plasma or like heating beam. In the long pulse configuration this beam is focused after crossing a random phase plate, making possible to obtain a moderate intensity ($\sim 10^{13}\,\mathrm{Wcm^{-2}}$) but with high uniformity.

There is also a third beam (the *probe* beam), with an energy of ~ 100 mJ and a diameter of 20 mm, taken along the amplification chain and also compressed by a compressor in air with small size gratings. The duration of this pulse lies between the hundred of ps and a minimum of 350 fs, depending on the distance between the diffraction gratings. This beam is also equipped with an adjustable delay line and was used in various optical diagnostics to probe, with a temporal resolution close to the principal laser pulse duration ($\sim$ ps), the passage and the heating induced by the fast electrons in the target. As we will explain in the next section, in our experiments the probe beam was always doubled in frequency (528 nm) with a KDP crystal.

Furthermore in the experimental campaign during which we use the proton imaging diagnostic, after amplification, the main pulse was also split into two CPA1 and CPA2 pulses. CPA1 was always re-compressed down to a duration of 300 fs in a double-pass grating compressor while CPA2 pulse was re-compressed in a separate, twin compressor. While the CPA1 compressor is enclosed in a vacuum chamber directly connected to the target chamber. On the contrary in the CPA2 compressor the pulse propagates in air and is injected into the target chamber through an anti-reflection coated dielectric window, having a minimum transmission efficiency of 95%. The window partially degraded the beam spatial quality, leading to poorer focusing properties. The vacuum level during a laser shot was set by the level inside the CPA1 compressor, and was typically in the range $\approx 10^{-5} - 10^{-4}$ mbar.

3.1.2 Interaction chamber and installed diagnostics

The interaction chamber (working in a primary vacuum of some 10^{-5} mbar) is shown in Fig. 3.2.

The main pulse is focused on the target front surface, at normal incidence, by an off-axis $f/3$ dielectric parabolic mirror of 300 mm focal length and a 77.5 mm off-axis. Approximately 50% of the laser energy is focused in a Gaussian focal spot of $\approx 20\,\mu$m FWHM. The parabola alignment as well as the focusing quality of the main pulse were checked by an imaging system at ω_0 installed along the laser axis. This imaging system is focused on a geometrical point representing the chamber center and defined using a microball with a diameter of $\approx 100\,\mu$m. Its position was controlled by three high magnification alignment cameras, imaging the microball at various angles. The

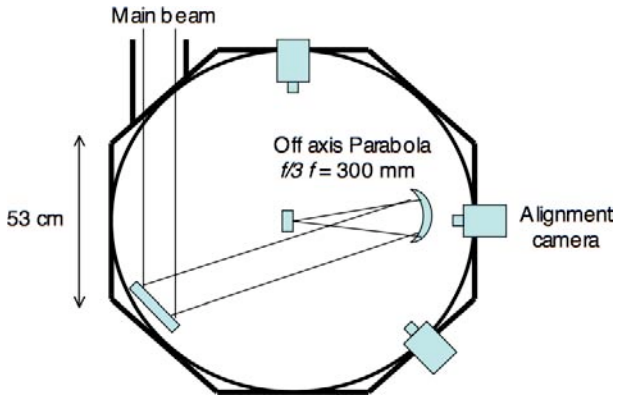

Figure 3.2: Diagram of the LULI's 100 TW interaction chamber. The target is in the center. The interaction beam is focused by an off axis parabola, on the right of the target. It is possible to see three alignment cameras, related to three normal directions (depth, height, laterality).

alignment procedure consists in moving the parabola in a systematic way in order to minimize the focal spot and to reduce the spherical astigmatism produced by an imperfect angular adjustment.

Moreover, the probe beam, when used, is perpendicular to main beam. The details of the diagnostics will be given in the following paragraphs.

3.1.3 Energy and temporal duration measurements

The energy delivered by the laser chain was measured during each shot by means of two calorimeters respectively placed behind the mirror at the entry of the experimental room (meaning the mirrors leakage) and on "parasite" reflection of the compressor entry pin-hole (Fig. 3.1). Each day a verification shot was done. The whole beam was sent in an absolute calorimeter. The gain of the compressor and the under-vacuum optics were calibrated at the beginning of the experiment, by placing an absolute calorimeter in the interaction chamber in order to determine the energy incident on the target. The pulse duration ($\sim$ 350 fs) was measured several times during the experiment using a single-shot 3ω auto-correlator. In the proton imaging configuration, also the second CPA2 pulse duration was measured in the same way.

3.1.4 Target configurations

The composite target configuration for the shadowgraphy experiments is constituted of a first front foil of solid material and a gas jet. The shadowgraphy target outline is

shown in Fig. 3.3.

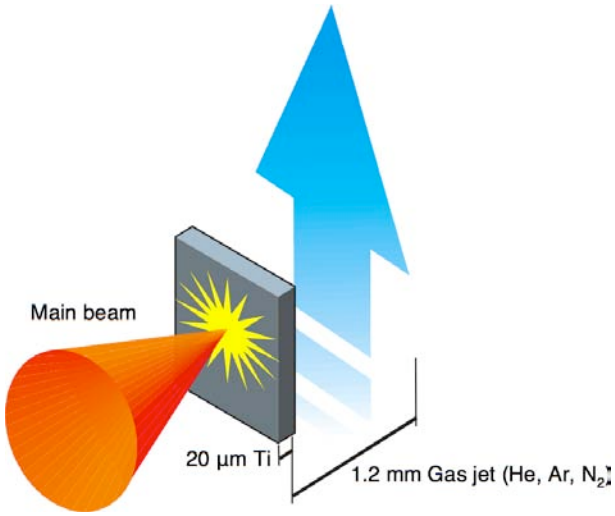

Figure 3.3: Composite target configuration for the shadowgraphy experiments.

The foils have been constructed starting from ultra-thin foils, glued on a support and then controlled with a microscope. Usually the foil target was titanium and its thickness was maintained constant in order to have the same interaction conditions in every shoot. The surface rugosity and undulations of these two layers are not completely dismissible and constitute a cause of non-homogeneous absorption of the laser energy (depending on the effective incoming angle). Concerning the gas jet, we used three kinds of gas (He, Ar, N_2) respectively at 30, 80 bars, at 30, 70 bars and at 15, 30, 100 bars. The thickness of the gas jet was the same in all shots. In order to accurately mesure the gas jet atomic density at different pressures, I used an interferometric system in conditions close to the experiment, at the gas jet laboratory (see Appendix A).

The deduced bi-dimensional neutral atom profiles in the position where the CPA laser beam was focused (1.2 mm from the nozzle) are shown in Fig. A.11.

We can observe that the gas jet density changes from 0 (at the edge of the gas jet) to peak values of $8\times10^{18}\text{cm}^{-3}$, $1.7\times10^{19}\text{cm}^{-3}$, $2.7\times10^{19}\text{cm}^{-3}$, $3\times10^{19}\text{cm}^{-3}$, respectively for pressures of 30, 50, 70 and 80 bars at the nozzle exit.

Finally, in the proton radiography experiment, we also used an additional thin (15 μm) gold or tungsten foil (perpendicular to the previous ones) on which we focused a second most intense laser beam in order to produce a point-like source of protons. The proton imaging target outline is shown in Fig. 3.5.

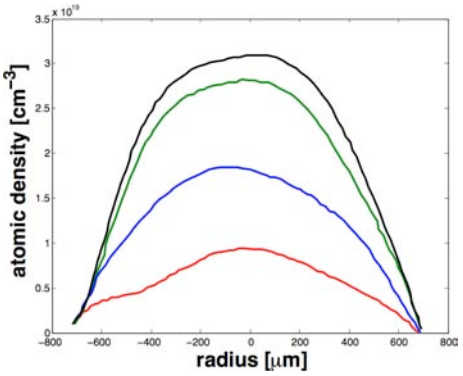

Figure 3.4: Density profile in the gas jet: atomic density (cm^{-3}) *vs.* distance from gas jet centre (μm).

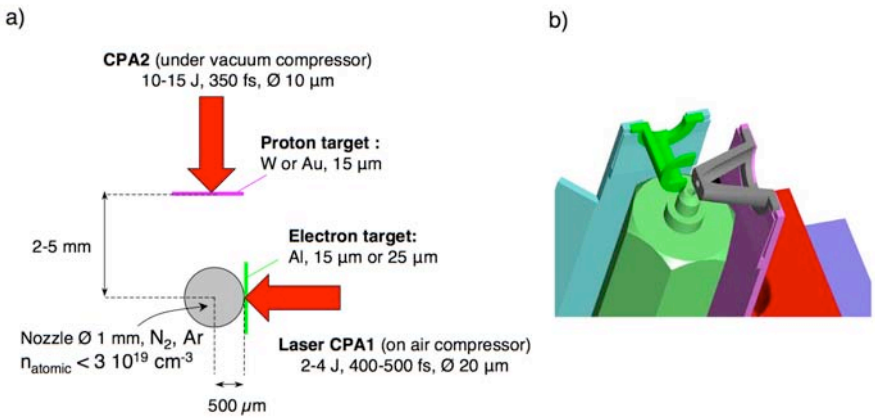

Figure 3.5: a) Target lineout for the proton imaging experiment. b) Detail of the target support/nozzle system for the the proton imaging experiment.

3.2 Shadowgraphy diagnostic

3.2.1 Shadowgraphy principle

The shadowgraphy principle is very simple. As it shown in Fig. 3.6, a not focused, low energy probe beam is sent onto the gas jet, perpendicularly to the main beam.

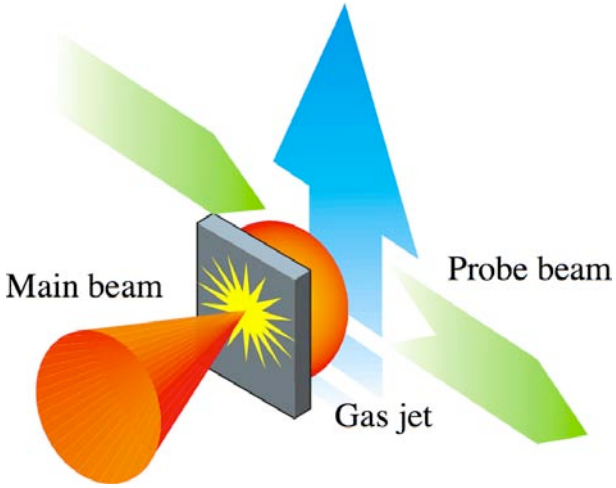

Figure 3.6: Sketch of the shadowgraphy principle.

The crossed material (interaction surface + gas jet) is in a state of thermal plasma in the interaction region (frontal part of the interaction surface) and in a state of a warm matter, at lower temperature, in the deeper region of the gas jet, thanks to heating produced by the fast electrons. Furthermore the electron density gradient and the local density variation due to the ionization phenomenon, will act like lenses, curving the probe beam and refracting the rays in different directions[2].

[2]For a wave with a frequency ω travelling with an angle θ through a plasma with a wave vector k, a plasma refraction index $\mu = \frac{ck}{\omega}$ and a refraction gradient $\nabla\mu$, it's easy to demonstrate the following relation:

$$\frac{d\theta}{dy} = \frac{1}{\mu}\frac{d\mu}{dz}, \tag{3.1}$$

where the angle and the direction refers to Fig. 3.7.

After crossing a plasma thickness l:

$$\theta = \int_0^l \frac{1}{\mu}\frac{d\mu}{dz}dy \tag{3.2}$$

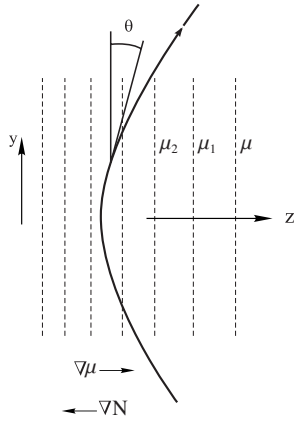

Figure 3.7: Light ray deviation in a density gradient.

This refraction phenomenon could be described with the eikonal equation in which the variable is represented by the ray vector position $\mathbf{r}$ as a function of the curvilinear abscissa s. This equation corresponds to three differential equations in the Cartesian components of this abscissa and could be numerically integrated by constructing the trajectory with vectorial elemental increments ($d\mathbf{r}$). The equations are:

$$\nabla N = \frac{d}{ds}\left[N\frac{\mathbf{r}}{ds}\right] = \frac{dN}{ds}\frac{d\mathbf{r}}{ds} + N\frac{d^2\mathbf{r}}{ds^2} \tag{3.4}$$

$$\frac{\partial N}{\partial x} = \frac{dx}{ds}\left[\sum_{\xi=x,y,z}\frac{\partial N}{\partial \xi}\frac{d\xi}{ds}\right] + N\frac{d^2x}{ds^2} \tag{3.5}$$

$$d\mathbf{r} = \sum_{\xi}\frac{d\xi}{ds}ds\mathbf{u}_{\xi} \tag{3.6}$$

After crossing the gas jet the probe beam is collected by a lens and finally imaged onto a CCD camera. Of course there is a certain number of rays which, strongly deviated from the denser regions, could not be collected, thus producing a shadow in the image.

Assuming that μ and $\frac{d\mu}{dz}$ are constant along y and by using the Eq. 3.7, we can write

$$\theta = \frac{l}{\mu}\frac{d\mu}{dz} = -\frac{l}{2n_c}\frac{dn}{dz} \tag{3.3}$$

The dispersion relation for an infinite electromagnetic wave travelling in a uniform plasma, could be written

$$\mu = \frac{c}{v_\varphi} = \frac{ck}{\omega} = \left(1 - \frac{\omega_p^2}{\omega^2}\right)^{\frac{1}{2}} = \left(1 - \frac{n_e}{n_c}\right)^{\frac{1}{2}} \tag{3.7}$$

where ω and k are angular and wave vector respectively. The quantity $v_\varphi = \omega/k$ is the wave phase velocity, μ is the plasma refraction index, n_e and n_c are the electron density and the critical density respectively, for a wave with a frequency ω.

Variation in the brightness of the shadowgraphy images depend on the variation of $d\mu/dz$, that is to say on $d^2\mu/dz^2$. In the regions of a plasma where $\omega_p > \omega$ the light could not propagate and as a consequence they are dark the shadowgraphy images. Fig. 3.8 shows how a $d^2\mu/dz^2 \neq 0$ could allow to the light rays focusing.

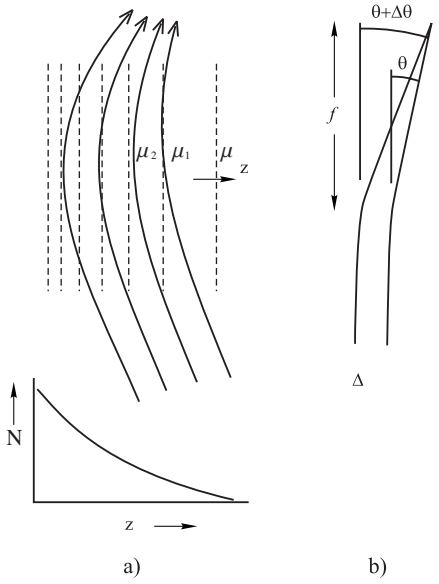

Figure 3.8: Focusing of the light rays in a plasma with a finite $d^2\mu/dz^2$.

From Fig. 3.8 and Eq. 3.3 we can see that:

$$\theta = \frac{l}{\mu_1}\frac{d\mu_1}{dz} \tag{3.8}$$

and

$$\theta + \Delta\theta = \frac{l}{\mu_2}\left(\frac{d\mu_1}{dz} + \frac{d^2\mu}{dz^2}\frac{1}{\Delta z}\right) \tag{3.9}$$

if we assume $\mu_1 \approx \mu_2 \approx \mu$, thus

$$\Delta\theta \approx \frac{l}{\mu}\frac{d^2\mu}{dz^2\Delta z} \tag{3.10}$$

this implies the focusing of the rays with a focal length, f, given by:

$$f = \frac{\Delta z}{\Delta\theta} = \frac{\mu}{l\frac{d^2\mu}{dz^2\Delta z}} \tag{3.11}$$

The focusing power of a plasma indeed depends on the second derivative of the refraction index.

3.2.2 "Classical" shadowgraphy: 2D snapshot images

The classical shadowgraphy set-up is shown in Fig. 3.9.

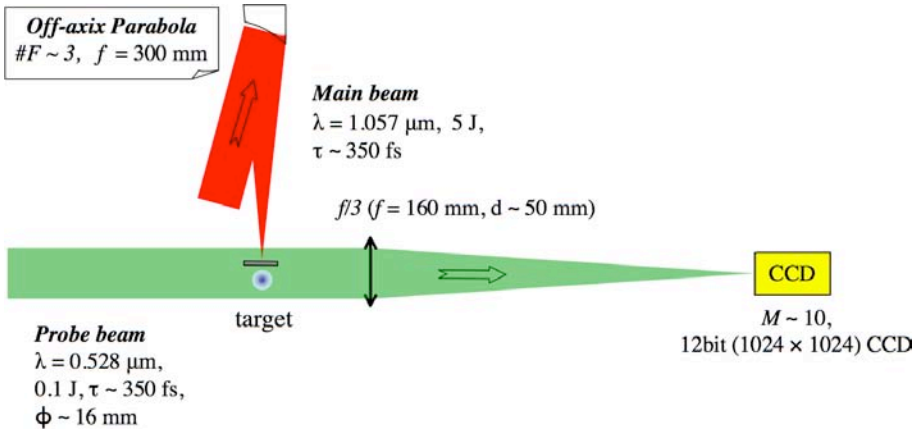

Figure 3.9: 2D Shadowgraphy setup. The transimitted probe beam is imaging on a CCD camera ("traditional" technique) with a magnification $G \sim 10$.

In the classical shadowgraphy experiment, the probe beam has been doubled in frequency by means of a doubling crystal and after crossing the gas medium, it is collected by a $\sim f/3$ lens ($f = 160$ mm, $d = 50$ mm), to be imaged on a 12bit (ARP, 1024×1024) CCD camera. The probe beam is a small fraction ($\sim$ 0.1 J, 16 mm diameter) of the main beam converted to 2ω. This allows 2D transverse imaging on

a 528 nm filtered CCD, with an optical magnification $\mathscr{M}_{opt} \sim 10$ and a resolution of ~ 5 μm and ~ 400 fs. The ionized region is opaque to the probe beam, producing an instantaneous 2D snapshot image. The time delay between main and probe beam was then changed from shot to shot (from 0 to +70 ps by successive displacements), allowing to follow the ionization dynamics within the gas in a sequence of *comparable* images, and to reconstruct the time evolution of fast electron propagation in the gas. Fast electrons were created by an high intensity laser on a thin foil (Ti) placed before a gas jet. Let us however notice that from shot to shot, several parameters could fluctuate (intensity, focusing, foil target surface quality), introducing additional sources of errors.

3.2.3 "Chirped" shadowgraphy: 1D temporal resolved images

In order to better investigate the fast electron cloud expansion at early times and decrease the influence of fluctuations we used the chirped shadowgraphy. The chirped shadowgraphy set-up is shown in Fig. 3.10.

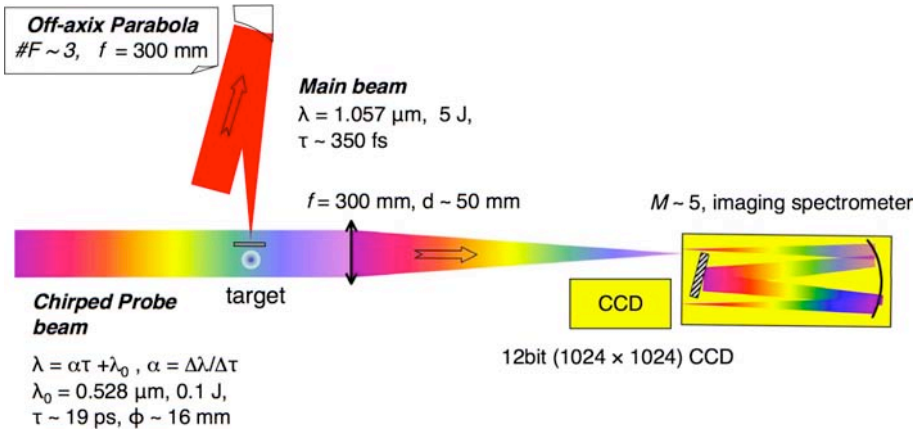

Figure 3.10: Chirped Shadowgraphy setup. The transimitted probe beam is imaging on the entry slit of an imaging spectrometer with a magnification $G \sim 5$ coupled to a CCD ("chirped" technique).

This technique, unlike the traditional shadowgraphy, can provide measurements in an extended temporal window (several tens of ps) in the *same* shot. Here, the gas medium is imaged on the entry slit of an imaging spectrometer. A 12bit CCD is placed in the exit plane of the spectrometer, in order to record the image. This was spectrally dispersed on one axis and spatially resolved on the other one. The duration of the probe beam was regulated to ~ 19 ps. This diagnostic, whose principle is explained below, makes it possible to treat the spectral axis of the image as a temporal axis:

each image shows the temporal evolution of the fast electron dynamics. The spatial resolution is preserved by the imaging spectrometer only in the direction parallel to the entry slit.

Chirped shadowgraphy principle

This technique, recently developed [131] uses the fundamental characteristic of a "chirped" pulse: there is a univocal relation between the frequency and time or - in other words - different spectral components are temporally shifted as shown in Fig. 3.11.

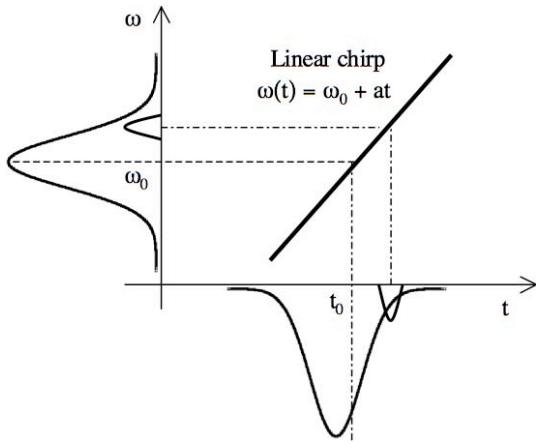

Figure 3.11: Diagram of the linear chirp of the probe beam where $a \sim \Delta\omega/\Delta t$ connect the spectral width to the chirped pulse duration.

In our case, the chirp is imposed by the stretcher of the laser chain and it is partially reduced by the compressor of the probe beam. For a linear chirp, one has:

$$\omega(t) = \omega_0 + at \tag{3.12}$$

One can rewrite Eq. 3.12 as a function of λ (by using the relation $c = \lambda\omega/2\pi$) and then develop to the first order. Then:

$$\lambda(t) = \lambda_0 + \alpha\, t \tag{3.13}$$

where $\alpha \sim\ a\lambda_0^2 \pi\, c \sim \Delta\lambda/\Delta\, t$

this means the spectrum contains a temporal information, in the sense that a phenomenon affecting the intensity of the pulse at a certain time t (for example a sudden fall of the transmission during the crossing of the gas medium) will only appear as

a disturbance around the spectral component corresponding to t, as shown schematically in Fig.3.11. If the pulse spectrum is dispersed, one can then recover the temporal information: it is then sufficient to known the chirp relation (Eq. 3.13) to deduce the time. The dispersion of the spectrometer doesn't determine the temporal resolution since there is an lower limit to the duration of the shortest measurable disturbance, according to the parameters of the chirped pulse [135]. This limit, which arises from the relation of uncertainty between time and angular frequency can be expressed in the following way, taking into account the chirp definition:

$$dt \geqslant k\sqrt{\frac{\Delta t}{\Delta\omega}} \sim k\sqrt{\frac{\Delta t\lambda^2}{2\pi c\Delta\lambda}} \tag{3.14}$$

where $k \simeq 1$ is a constant which depends on the pulse profile. We can see that, with the same spectral width, the limit grows with the pulse duration. That means that larger observation temporal windows corresponds to smaller precisions. Even with this limitation, the advantage of the chirped technique compared to the use of an ordinary streak camera is of being able to reach a much better temporal resolution, ($\simeq 1$ ps, compared to $\geqslant 10 - 15$ ps).

Experimental parameters

We reduced the distance between the compressor gratings of the probe beam of approximately 6 mm from the best compression position, obtaining a duration of 19 ps FWHM. Then we compensated the delay between the main and the probe beam. The synchronisation between main and chirped probe beam was done by using a streak camera. We used a spectrometer with 1000 mm focal length and a grating groove density of 1200 lines/mm. The spectrum width is about 4 nm, which makes it possible to obtain the chirped factor $\alpha = \Delta\lambda/\Delta t$. The dispersion of the imaging spectrometer finally gives a temporal dispersion of ~ 115 fs/px in the (1024×1024) recorded images with an optical magnification $\mathscr{M}_{opt} \sim 5.1$

3.3 Proton imaging diagnostic

3.3.1 Principles of proton probing techniques

The experimental arrangement for proton probing techniques is shown in Fig. 3.12 a short and intense CPA laser pulse is focused onto a metal foil (proton target) in order to accelerate a proton beam. The proton beam is employed as a charged particle probe for the electric and magnetic fields around a second target (interaction target)

irradiated by a second laser pulse. In proton imaging a projection of the probed region is obtained, which mainly reflects the field gradients distribution.

The techniques exploit the fact that, as a consequence of the high degree of laminarity of the beam, the proton source, while being physically extended, is practically equivalent to a nearly point-like virtual source. A point projection of the probed region is obtained with a geometrical magnification given by:

$$\mathscr{M} = \frac{l_s + l + L}{l_s + l} \simeq \frac{l + L}{l} \tag{3.15}$$

where l_s is the displacement of the virtual source with respect to the physical source, l is the distance between the proton target and the interaction target and L is the distance between the interaction target and the detector. l_s is usually in the range $10 - 10^2 \mu$m, and for a typical experimental arrangement l is $1 - 4$ mm and L is $3 - 4$ cm.

The technique also exploits the fact that the proton beam has a broad energy spectrum. The experimental set-up has in fact a time of flight arrangement, as protons with different energies will reach and probe the interaction target at different times. If a detector capable of separating the different spectral components of the beam is employed, the contributions from different probing times will also be distinguished. Thus the spectral multi-frame capability of the detector results in a temporal multi-frame capability of proton probing techniques within a single laser shot.

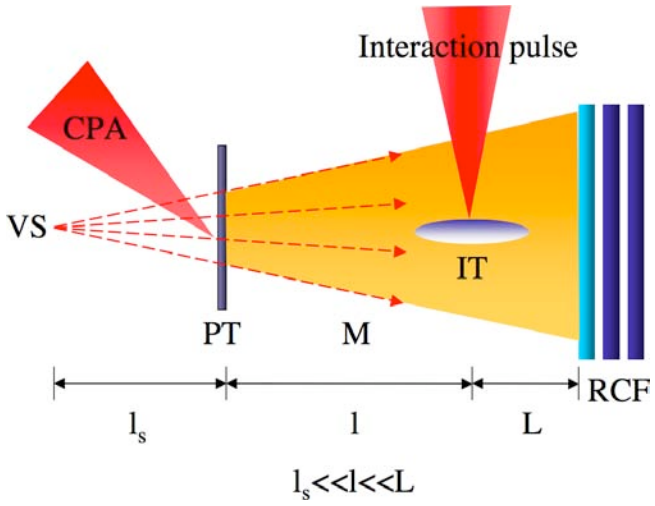

Figure 3.12: Proton probing typical experimental arrangements.

Finally it should be noted that PIC simulations generally indicate that laser accelerated proton beams are neutralized by a cloud of co-moving electrons. Therefore

it can be argued that electric fields at the interaction target could be shielded by the electrons co-moving with the proton beam, hence forbidding the field detection. However, fluid simulations of the expansion of a proton-electron plasma into a vacuum (see [136]), indicate that the cloud of electrons globally neutralizing the probe proton beam was unable to shield the detected fields at the back of the interaction target, as the local Debye length of the probe beam when reaching the target was much larger than the fields' spatial scale length practically in any case encountered.

The techniques are based upon the deflection undergone by the charged particles in a probe beam when crossing an electromagnetic field. A single test proton crossing an electric and magnetic field distribution localized in a region of finite linear extension b acquires a transverse velocity:

$$\delta\mathbf{v}_\perp = \frac{e}{m_p}\int_b \left(\mathbf{E} + \frac{\mathbf{v}_p \times \mathbf{B}}{c}\right)_\perp dt \simeq \frac{e}{m_p v_p}\int \left(\mathbf{E} + \frac{\mathbf{v}_p \times \mathbf{B}}{c}\right)_\perp dx \tag{3.16}$$

where it is assumed that the transverse motion of the proton is negligible compared to the longitudinal motion:

$$v_x = \frac{dx}{dt} \simeq v_p \tag{3.17}$$

that is we neglect the initial beam divergence and we assume that the proton acquires a small angular deflection due to the field. After the proton has travelled the distance L from the region where the field is localized to the detector, it has been transversally displaced of a quantity $\xi_\perp$ due to the fields:

$$\xi_\perp \simeq \delta\mathbf{v}_\perp \Delta t \simeq \frac{eL}{2\mathscr{E}_p}\int_b \left(\mathbf{E} + \frac{\mathbf{v}_p \times \mathbf{B}}{c}\right)_\perp dt = \left\langle \frac{eL}{2\mathscr{E}_p}\left(\mathbf{E} + \frac{\mathbf{v}_p \times \mathbf{B}}{c}\right)_\perp \right\rangle_b \tag{3.18}$$

where $\Delta t \simeq \frac{L}{v_p}$ is the time of flight of the proton from the field region to the detector and $\mathscr{E}_p = m_p v_p^2/2$ is the proton energy. We have defined the averaged field along the proton trajectory:

$$\left\langle \left(\mathbf{E} + \frac{\mathbf{v}_p \times \mathbf{B}}{c}\right)_\perp \right\rangle_b = \frac{1}{b}\int_b \left(\mathbf{E} + \frac{\mathbf{v}_p \times \mathbf{B}}{c}\right)_\perp dx \simeq \frac{2\mathscr{E}_p}{eLb}\xi_\perp \tag{3.19}$$

If field gradients are present, protons experiencing different electromagnetic fields will suffer a different deflection and modulations will be imprinted on the proton density across the beam transverse section (Fig. 3.13).

If proton trajectories do not cross each other, i.e. if the proton beam behaves like a fluid, the proton density n_p at the detector plane is related to the proton density in

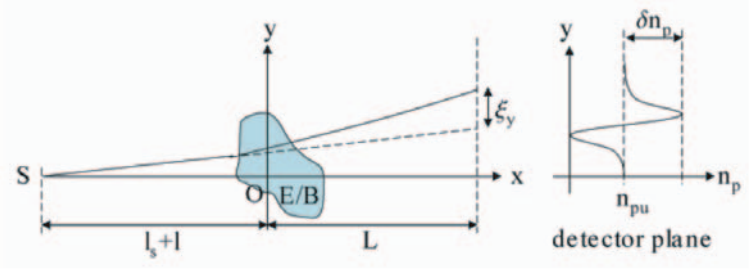

Figure 3.13: Scheme of proton probing techniques.

a plane located before the electric field region and finally (see [136] and [132]) to the unperturbed proton density at the detector plane n_{pu} (that is the proton density in absence of a field deflecting the protons). By defining $n_p = n_{pu} + \delta n_p$ we finally find:

$$\left\langle \nabla_{\perp 0} \cdot \left(\mathbf{E} + \frac{\mathbf{v}_p \times \mathbf{B}}{c} \right)_\perp \right\rangle_b = \frac{1}{b} \int_b \left(\mathbf{E} + \frac{\mathbf{v}_p \times \mathbf{B}}{c} \right)_\perp dx \simeq \frac{2\mathscr{E}_p M}{eLb} \frac{\delta n_p}{n_{pu}} \tag{3.20}$$

Here $\nabla_{\perp 0}\cdot$ is the divergence operator with respect to the transverse initial coordinates of the protons. In proton imaging the quantity $\frac{\delta n_p}{n_{pu}}$ is directly measured, thus providing information about the field gradients. We see in fact that the proton density map corresponds to a map of the field transverse gradients and that proton imaging data allows an estimation of the average field gradients (Eq. 3.20). It is possible to develop further the analysis (cf. [136, 132]) showing that the proton density map can also give a map of the charged density in the probed plasma, obtaining an estimation of the average charge and current densities:

$$\frac{1}{b} \int_b \left(\rho - \frac{\mathbf{v}_{p0} \cdot \mathbf{J}}{c^2} \right) dx \simeq -\frac{\mathscr{E}_p M}{e\pi Lb} \frac{\delta n_p}{n_{pu}} \tag{3.21}$$

If large field gradients are present, crossing of proton trajectories in the probe beam may occur. In this case the fluid approximation for the proton beam propagation breaks down, and these relations are no longer applicable. Experimentally this corresponds to the case of caustics formation.

3.3.2 Sensitivity and resolution

The Proton Imaging sensitivity is set by the minimum proton density modulation that can be detected. The minimum detectable electromagnetic field gradient reads from

3.20:

$$\nabla_{\perp 0} \cdot \left(\mathbf{E} + \frac{\mathbf{v}_p \times \mathbf{B}}{c} \right)_{\perp} \simeq \frac{2\mathscr{E}_p M}{eLb} \frac{\delta n_p}{n_{pu}} \tag{3.22}$$

corresponding to a minimum charge density and density current:

$$\rho - \frac{\mathbf{v}_{p0} \cdot \mathbf{J}}{c^2} \simeq -\frac{\mathscr{E}_p M}{2\pi eLb} \frac{\delta n_p}{n_{pu}} \tag{3.23}$$

The minimum detectable proton density modulation depends on the background noise level, set by the spatial uniformity of the proton beam. Referring to the experimental results presented in the following Chapter, the typical minimum detectable proton density modulation could be estimated to be $\frac{\delta n_p}{n_{pu}} \sim 0.05$, with a minimum detectable proton energy $\mathscr{E}_p \sim 1$ MeV. In the adopted arrangement we had $L = 3.8$ cm and $\mathscr{M} = 8$, and for the typical case of a field distribution extending over $b \sim 500$ μm along the direction of propagation of the probe proton beam, this leads to a minimum detectable electric field gradient $|\nabla_{\perp 0} \cdot \mathbf{E}| \sim 10^{10}$ V/m^{2}corresponding to a charge density $\rho \sim 10^{-7}$C/cm^3. The spatial resolution is set by the competition between the virtual proton source size and lateral spread of the protons due to multiple scattering inside the detector divided by the magnification. Typically the proton source size is < 10 μm. On the other hand the proton lateral spread in the detector is usually in the range $10 - 100$ μm, and the magnification for a typical experimental arrangement is $10 - 20$. In either case the spatial resolution is in the μm range. The temporal resolution is set by the competition between the proton burst duration, the proton time of flight through the observed structures and the time resolution of the detector. The proton burst duration has never been measured experimentally, but if it is usually supposed to be in the ps or sub ps-range depending on the proton energy. For a structure with a spatial scale length of few hundreds of μm the proton transit time can be above 10 ps. Finally the temporal resolution of the detector is in the few ps range, as we shall see in Sect. 3.3.4.

3.3.3 Proton density modulation and deflection extraction

Proton probing experimental data have been originally recorded on RadioChromic Films (RCFs) and then digitized employing an optical scanner. Proton imaging data were converted from scan value to optical density and then to deposited radiation dose (and to deposited energy density, by simply multiplying for the film density in g/cc) employing suitable calibration curves. The density of protons which are stopped in a given RCF was then obtained by simply dividing the deposited energy density by the average density deposited by a single proton which stops in the film. The latter was obtained from Monte Carlo simulations of the stopping of protons in the

detector, performed with the free-share code SRIM [137]. Line-outs of the proton density modulation across the structures observed in proton imaging data could then be easily extracted.

3.3.4 Radiochromic film detectors

Proton beams were detected employing multi-layer stacks of Radiochromic films (RCFs) [138]. RCFs are dosimetry media sensitive to ionizing radiation. A RCF consists of one or two layers of active component sandwiched between polyester foil substrates. Upon exposure the active component, transparent before irradiation, develops a dark blue color. No etching is required. The change in net optical density is related to the radiation energy dose absorbed by the film. A more detailed description of RCFs and of the proton detector characterization will be given in the following sections. The film packs were wrapped in 11 μm aluminum foils, giving a minimum detectable proton energy of about 1 MeV. The aluminum foil acted as a filter for soft X-rays and heavy ions and shielded the film pack from the target debris. However it was not possible to eliminate the electron signal. This did not constitute a serious issue, as the electron signal is easy to distinguish from the proton signal because it is much fainter and exhibits a far more gradual decrease with increasing the penetration depth into the detector.

Radiochromic films

The active component in the RCFs is a microcrystalline monomer, belonging to the diacetylene molecule class, dispersed in a gelatin matrix. Upon exposure to ionizing radiation, crystalline diacetylenes undergo a solid-state polymerization reaction producing a dye polymer referred to as polydiacetylene. Polydiacetylenes exhibit a characteristic spectral absorbance which depends on the specific molecular structure. The RCF active component shows a major absorbance peak at about 675 nm and a minor peak at about 615 nm, leading to the characteristic dark blue color of exposed films. The amount of polymer produced, and hence the optical density of the film, is related to the absorbed radiation dose. The polymerization process, initiated by the irradiation, does not stop immediately after exposure. The optical density stabilizes to its asymptotic value within 24 hours. As the active component is in the form of sub-micron sized crystals and the polymerization process does not spread between adjacent micro-crystals, RCFs have an intrinsical sub-micron spatial resolution.

In our applications we assumed that the film response is dose-rate independent even at the extreme rates achieved in the experiments, which are typically of the order of 10 Gy/ps. Tests performed by irradiating RCFs with γ-rays, electrons and

protons evidenced that the optical density after exposure only depends on the absorbed radiation dose, regardless of the nature of the radiation employed [139, 140].

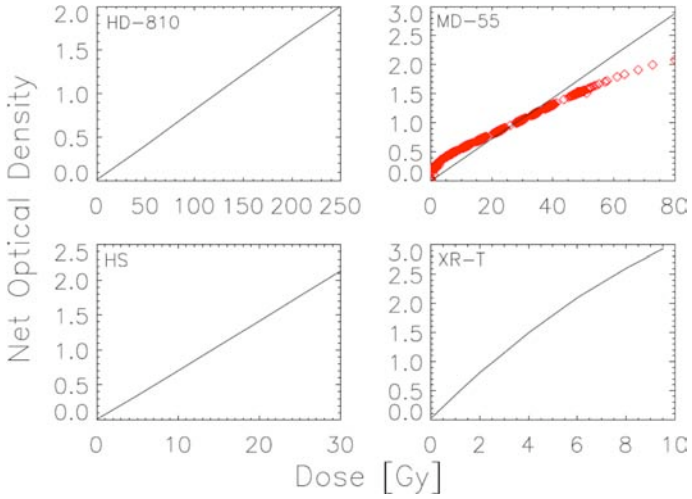

Figure 3.14: Calibration curves relating the net optical density after exposure to the absorbed radiation dose for different types of RCFs. The calibration obtained by irradiating a MD-55 wedge with controlled proton doses is also plotted (red dotted curve).

Dosimetry characterization

In the present work the experimental data recorded on RCFs were digitized with a scanner EPSON perfection 2450 PHOTO. The calibrations shown in Fig. 3.14 refer to optical density measurements performed with this scanner. In comparison with micro-densitometers the scanner provides the possibility of scanning large areas in a relatively short time, while still ensuring high spatial resolution and reliability of optical density measurements. The EPSON perfection 2450 scanner has a maximum optical resolution of 2400×4800 dpi, with a dynamic range nominally extending up to optical densities of 3.3. In the case of the data presented in this work the optical density of the exposed RCFs practically never exceeded 1.5 (unless the film was saturated). The scanner employs a broad band lamp (White cold cathode fluorescent lamp) as light source and a CCD Color MatrixCCD line sensor as detector. The scanner was absolutely calibrated in optical density and energy dose by means of a home-made step-wedge. The wedge was obtained by exposing a stripe of MD-55 to different and controlled proton doses, and was calibrated in optical density employing a He-Ne laser.

This provided an absolute calibration from scan value to optical density and dose for MD-55 RCFs and a calibration from scan value to optical density for all the other

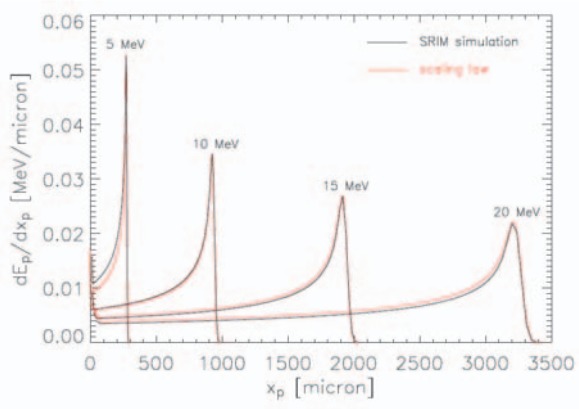

Figure 3.15: Proton stopping curves (black line) in the RCF pack for proton energies in the range 5-20 MeV. Results from SRIM simulations and from the scaling law are plotted on the same graph (red line) for comparison.

film models. Note in particular that for the MD-55 radiochromic films and for doses below 50 Gy, the ad hoc calibration is almost linear and does not differ from the calibration given in [138]. As independent calibrations were not available, the calibrations given in [138] are used for the other film types.

Spectral characterization

The multi-layer arrangement of the RCFs stack results in a spectral multi-frame capability of the detector. Protons with higher energies penetrate deeper in the stack and release their energy mainly in correspondence with the Bragg peak. Each film in the stack acts as a filter for the following ones and spectrally selects the protons whose Bragg peak is localized within the active layer. The proton energy loss and stopping inside the RCF stack were simulated employing the Monte Carlo code SRIM [137]. In the simulations the RCF stack is modelled as a 11 μm thick Al layer (representing the Al filter) followed by a polyester layer (representing the RCF stack) of thickness larger than the proton stopping range at the simulated proton energy.

Simulations were performed for proton energies in the range $1-30$ MeV at 1 MeV steps. As an example stopping curves from simulations in the range $5-20$ MeV are shown in Fig. 3.15. The curves exhibit the typical peaked structure, with the so-called Bragg peak located close to the end of the stopping range. For higher initial proton energies the penetration depth increases, the maximum energy loss decreases, while the Bragg peak broadens due to statistical spreading of proton trajectories. A calibration curve relating the position and value of the Bragg peak as a function of the proton

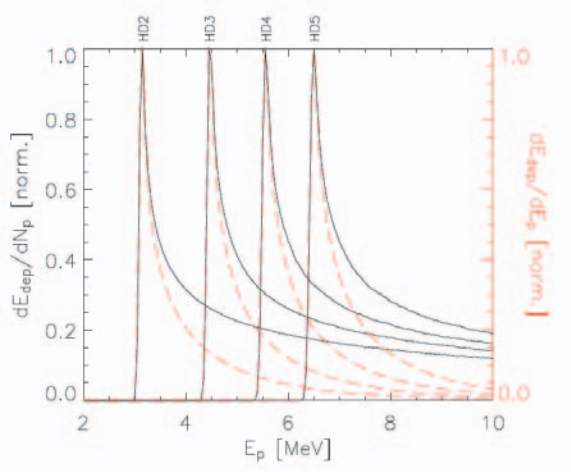

Figure 3.16: Normalized spectral response curves corresponding to different RCFs (HD) for a given RCF stack configuration (black solid line). Normalized response curves multiplied for a typical exponential proton spectrum with a characteristic temperature of 2 MeV (red dashed line).

energy was obtained by interpolation of the results from SRIM simulations. Given this calibration, stopping curves at any given proton energy could be reconstructed by means of scaling laws.

In Fig. 3.15 typical stopping curves obtained from SRIM simulations are plotted together with the curves corresponding to the same proton energies obtained from the scaling laws. It can be noticed that the scaling law reproduces reasonably well the simulations, especially in the most relevant region around the Bragg peak. The response curve of a given RCF for a given film pack configuration is represented by the energy per proton deposited in the film $d\mathscr{E}_{dep}/dN_p$ as a function of the proton energy $\mathscr{E}_p$:

$$R(\mathscr{E}_p) = \frac{d\mathscr{E}_{dep}}{dN_p} \tag{3.24}$$

The total energy deposited as a function of the proton energy is the product of the response curve and the proton spectrum $dN_p/d\mathscr{E}_p$:

$$\frac{d\mathscr{E}_{dep}}{d\mathscr{E}_p} = \frac{dN_p}{d\mathscr{E}_p} R(\mathscr{E}_p) \tag{3.25}$$

The integral of this product over all the proton spectrum gives the total energy

deposited in the film:

$$\mathscr{E}_{dep} = \int_0^\infty \frac{dN_p}{d\mathscr{E}_p} R(\mathscr{E}_p) d\mathscr{E}_p \tag{3.26}$$

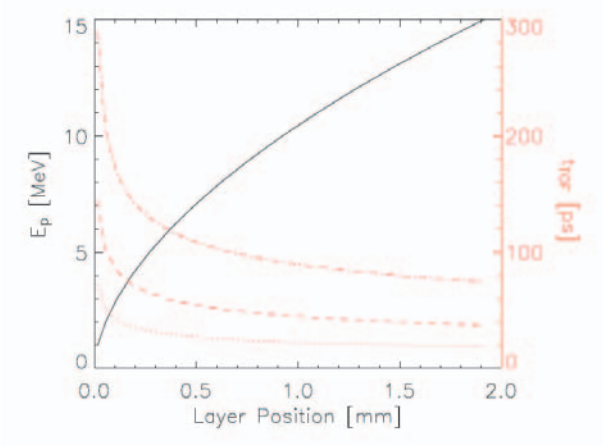

Figure 3.17: Conversion from the position of the RCF active layer in the stack to proton energy (black line) and proton time of flight (red lines). The different red lines correspond to different distances between the proton target and the interaction target (dots 1 mm, dash 2 mm, dash-dot 3 mm).

Once the stopping curve for any given proton energy was obtained, the film response curves could be calculated for any detector configuration by simply integrating the stopping curves over the RCF stack active layer thicknesses. As an example the response curves $R(\mathscr{E}_p)$ for four RCFs in a typical stack configuration are shown in Fig. 3.16. It can be noticed that each film exhibits a narrow spectral response, hence selecting the contribution from a narrow proton energy range. The product $R(\mathscr{E}_p)dN_p/d\mathscr{E}_p$ is also plotted for a typical Boltzmann-like proton spectrum with a temperature of 2 MeV. The spectral resolution can be estimated to be equal to the width of the $R(\mathscr{E}_p)dN_p/d\mathscr{E}_p$ curves, which is typically of the order of $1-2$ MeV. Thanks to the fact that a film response has a narrow peak at a certain proton energy, each film in the stack can be associated to the proton energy corresponding to the maximum of the total energy deposited in the film as a function of the proton energy, i.e. of the film response multiplied by the proton spectrum.

For the typical proton spectra encountered this calibration does not differ sensibly from the calibration obtained by simply considering the maxima of the film response curves or of the stopping curves. Also, as a consequence, the calibration does not depend on the detailed film pack configuration. A typical calibration curve from RCF film to proton energy is shown in Fig. 3.16.

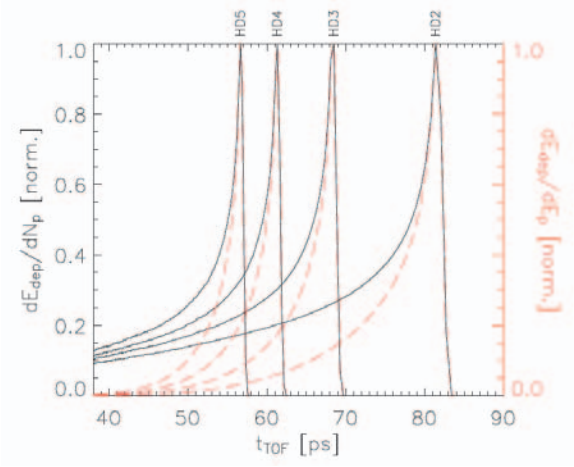

Figure 3.18: Normalized temporal response curves corresponding to different RCFs for a given RCF stack configuration (black line). The red lines correspond to taking into account the proton spectrum with a typical temperature of 2 MeV.

Temporal characterization

The time of flight arrangement of the experimental set-up combined with the spectral multi-frame capability of the RCF pack resulted in a temporal multi-frame capability within a single laser shot of proton probing techniques. In fact protons with different energies will have a different time of flight from the proton source to the probed target, as given by:

$$t_{tof} = l\sqrt{\frac{m_p}{2\mathscr{E}_p}} \tag{3.27}$$

Different films in the stack then will select the contribution from different proton energies, that is from different probing times. The RCF stack temporal response curves for given distance from the proton target to the interaction target and detector configuration are easily obtained from the spectral response curve through (Eq. 3.27). A typical example is shown in Fig. 3.18. It can be noticed that each film selects a narrow temporal range, and can then be associated with the time corresponding to the peak of the response curve. For a typical experimental arrangement, the temporal resolution set by the film response ranges from ~ 5 ps for the first film in the stack to 1 ps or less for the last films. A typical conversion curve from active layer position to proton time of flight is also shown in Fig. 3.18. The proton probing time is given by the sum of time of flight with the delay between the laser pulse employed to generate the probe proton beam and the laser pulse irradiating the interaction target.

3.3.5 Experimental arrangement

Two ultra-high-intensity laser beams were used, one CPA2 ($I_{MAX} \sim 2 \times 10^{18}$ W/cm^2) focused on onto 15 or 25 μm thick Al foils (*interaction target*) placed before the gas jet, acting as a fast electron source like in our previous experiment, the other one CPA1 (the most intense: $I_{MAX} \sim 3 \times 10^{19}$ W/cm^2) perpendicular to it, on an auxiliary target of 15 μm Al or W foils (*proton target* acting as a point-like source of protons with typical energies up to several MeV. Synchronization of the two pulses was finalized with the use of an optical spectrometer. The time delay between the two pulses could be changed and controlled with ps precision with an optical delay line placed in the CPA2 beam path. In the synchronization procedure the two pulses are extracted from the target chamber and are relayed along the same beam path either onto the streak camera or onto the spectrometer. In particular with the use of the spectrometer, pulse synchronization is obtained as follows. When two initially non-synchronized pulses are overlapped, beats are produced in the frequency domain. This leads to the formation of a periodic pattern in the frequency domain that can be resolved by the spectrometer. The period $\Delta\nu$ of the beats is proportional to the inverse of the time delay Δt between the two pulses. As the time delay Δt is reduced, $\Delta\nu$ increases. Eventually when the two pulses are made to overlap in time, $\Delta\nu$ becomes infinite and the beats disappear.

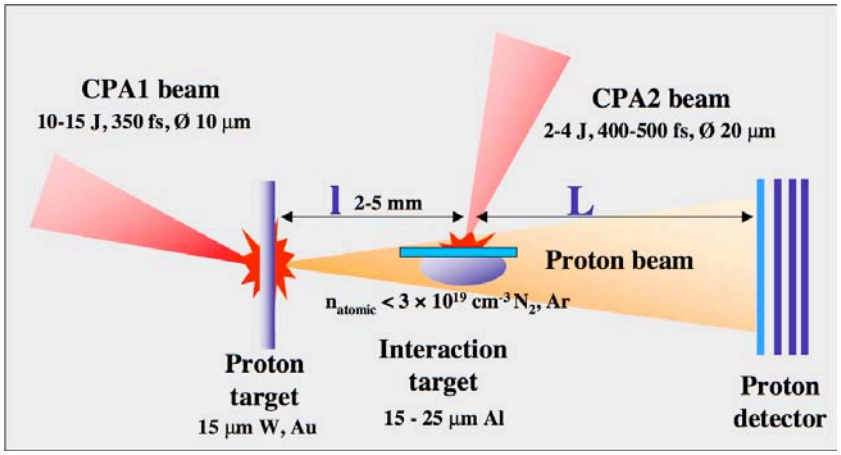

Figure 3.19: Experimental arrangement.

A proton beam was accelerated from the proton target and it was used as a transverse charged particle probe for the electric and magnetic fields at the back of the interaction targets. The distance l between the proton target and the interaction target was either 2 mm or 5 mm, while the distance L between the interaction target and the proton detector was $\sim$ 3.8 cm, leading to a magnification $\mathscr{M} \simeq (L + l)/l$ of either 20 or 8.6. The spatial resolution was typically of a few μm. The accelerated proton beams were detected employing stacks of several layers of RadioChromic Films

(RCFs). The probing time window accessible in a single laser shot was at most 200 ps wide, as determined by the distance $l = 2 - 5$ mm between the proton target and the interaction target and by the energy spectral cut-off of ~ 12 MeV of the probe proton beam.

The auxiliary beam produces a lower intensity on target than the main beam, and thus slower electrons. In order to characterize the source of electrons obtained with this less intense laser beam, we used a K_α spectroscopy diagnostic [129]. The high flux laser, delivering $\approx 2-4$ J on target, with a pulse duration of 350 fs is focused at normal incidence on the multilayered target. The fast electrons are produced and propagate in a first Al layer of variable thickness and finally reach a layer of fluorescent materials (10 μm Mo) where they induce K_α emission, depending on their number and residual energy. By varying the thickness of the propagation layer $(10, 25, 40, 75\,\mu\text{m})$ from shot to shot, we measured the typical penetration range of the electrons in the given material. K_α photons are detected by a CCD camera outside the interaction chamber, facing the target rear side, and used in single hit mode to allow spectroscopic analysis. The K_α yield of Mo is shown versus the propagation layer thickness in Fig. 3.20.

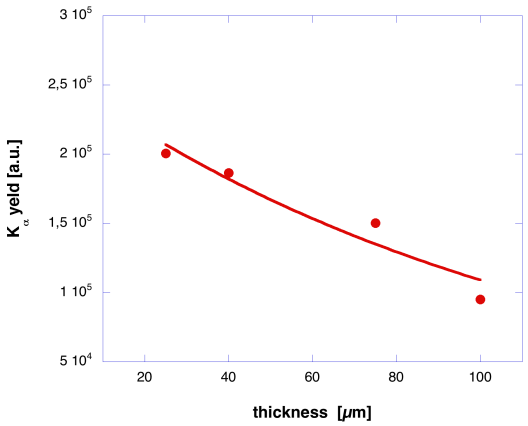

Figure 3.20: Experimental results K_α yield of Mo *vs* target thickness. The line is exponential interpolation of data, indicated by markers, and gives for Al a penetration depth of $\approx 110\,\mu$m.

Exponential fits to the results, i.e., $\exp(-R/R_0)$, give a typical value for the experimental penetration $R_0 \approx 110\,\mu$m. Experimental results are consistent with the scaling law by Bell et al. [110] which indicates that the typical penetration range of fast electrons due to electric fields alone is $\propto T_h(fI_{17})^{-1}$, T_h is the fast electron temperature in keV, I_{17} is the irradiance on target in units 10^{17} W/cm^2, and f is the fraction of laser energy converted in fast electrons. By assuming a laser conversion in fast electrons of the order of 30% we obtain an average electronic energy of 235 keV and thus a laser intensity of $I \sim 1.2 \times 10^{18}$ W/cm^2 (in good agreement with the

measured laser parameters).

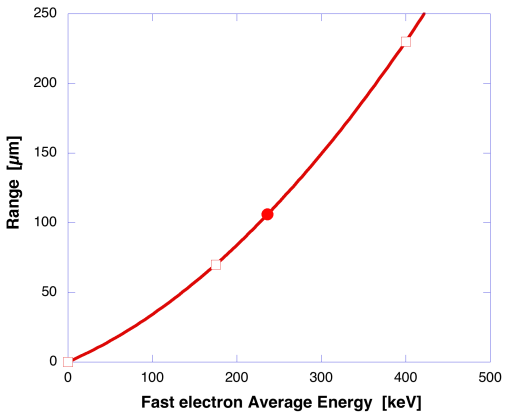

Figure 3.21: Fast electron average energy for our experimental arrangement (full marker), compared to experimental results obtained by Pisani *et al.* [129] (open symbols) in similar experimental conditions. All these results are consistent with the scaling law by Bell *et al.* [110].

In Fig. 3.21 we compare our experimental results with those obtained by Pisani *et al.* [129] in similar experimental conditions. All these results are in good accord with the Bell's law.

3.4 Experimental results

3.5 shadowgraphy

3.5.1 *Classical* shadowgraphy results

Fast electrons were created by a high-intensity laser on a thin foil (Ti) placed before a gas jet. Two gases (Ar and He) and different pressures were used. Fig. 3.22 is a typical shadowgraphy image, showing a large cloud and straight lines probably connected to electron jets. Such jets could be due to the first fast electrons, arriving to the rear of the first foil and propagating in the gas before a large field has developed. Hence, they are not too important in fast electron transport.

Fig. 3.24 shows shadowgrams obtained at different delays Δt between the Chirped Pulse Amplificated (CPA) beam and the probe (τ= 350 fs, $\lambda = 528$ nm, $E = 0.01 - 0.1$ J, $\phi < 16$ mm) beam. By changing Δt, it is possible to reconstruct the evolution of the

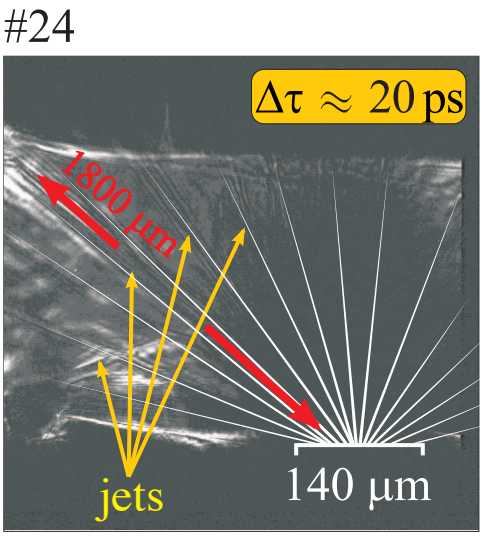

Figure 3.22: Shadowgraphy image: Ar 70 bar, $t \approx 30$ ps. Yellow lines show a few of the observed straight lines probably connected to electron jets.

ionized region in the gas (dark region in the shadowgraphy image in Fig. 3.23). Thus, cloud evolution can be followed and its velocity measured.

Another important experimental result was that the smallest cloudy region (at early times) is always at least > 150 μm in size, much larger than focal spot size as expected from previous experiments using other diagnostics [133, 141].

Fig. 3.24 shows the dimension of the cloud in direction perpendicular to the target, together with linear interpolations giving the average cloud velocity (the transversal expansion velocity is $\sim 2-3$ times smaller). The straight lines start from 0 at a time zero (roughly corresponding to the arrival of main beam on target) and correspond to linear interpolations of the data. The slope of the interpolation gives an average expansion velocity. The velocity shown in Fig. 3.24 is different for the 4 cases studied. Even if the velocity increase with the electron density in the background medium, it remains quite sub-relativistic ($c/30$ to $c/10$). In reality by carefully looking at the data, we do see a first fast expansion phase followed by a slowing down. This is especially clear from the series for He at 30 Bar, which extends to longer delays. Fig. 3.25 shows the same data of Fig. 3.24 interpolated with curves of the type $r(t) = r_0(1-\exp(-t/t_0))$ where r_0 is the typical penetration and t_0 the characteristic scale time. However, even if the results of *classical* shadowgraphy suggest such slowing down, it does not allow to easily reconstruct the first early phase which seems to be characterized by a faster expansion. Also since fast electron dynamics is inferred from several shots, the method

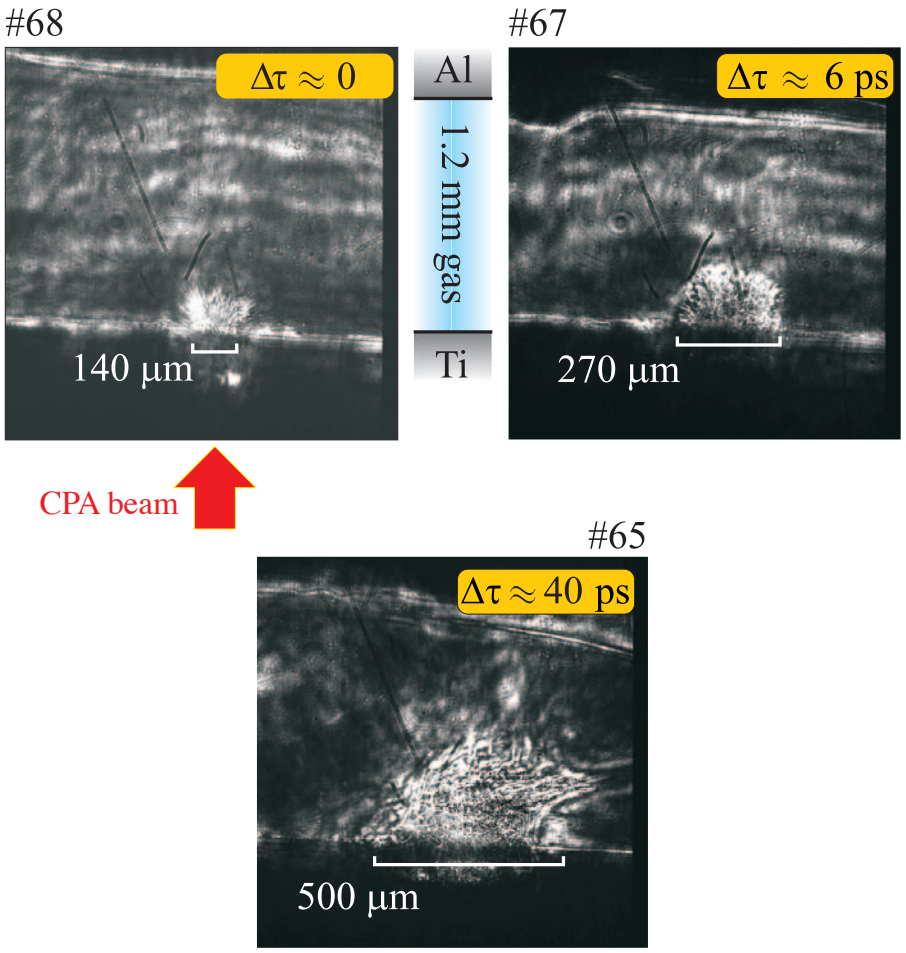

Figure 3.23: Evolution of the electron cloud (He, 30 bar). From left: $t \approx 10$ ps, ≈ 16 ps, ≈ 50 ps. Bars are 280, 540, and 1000 μm. The lower and upper dark part in all images, respectively, represent the Ti and Al foils.

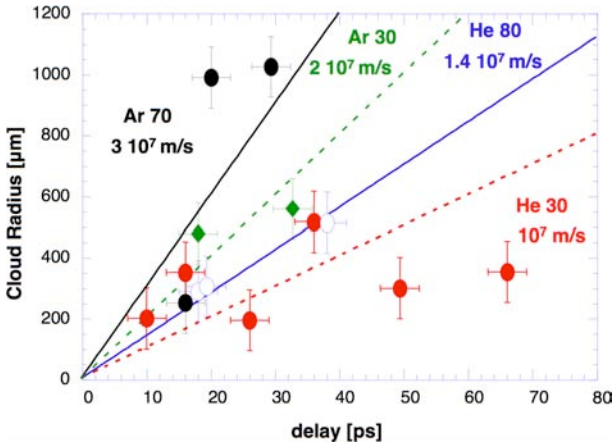

Figure 3.24: Cloud dimension in μm *vs* time delay between main and probe pulses. Atomic densities corresponding to pressures are 10^{19} cm^{-3} (He 30 bar, red circles), $3.2{\times}10^{19}$ cm^{-3} (He 80 bar, blue circles), 10^{19} cm^{-3} (Ar 30 bar, green circles), 2.8×10^{19} cm^{-3} (Ar 70 bar, black circles).

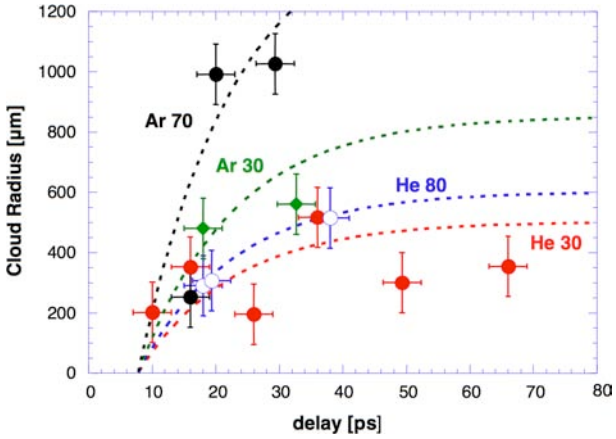

Figure 3.25: The same experimental data of Fig. 11.5 interpolated with curves of the type $r(t) = r_0(1{-}\exp(-t/t_0))$ where the rise time is 15 ps for all pressures and gases.

is strongly affected by shots-to-shots fluctuations, greatly increasing error bars.

3.5.2 *Chirped* shadowgraphy results

We will present here the shadowgraphy results obtained with the second technique, called *Chirped* shadowgraphy. Typical chirped shadowgraphy images are shown in Fig. 3.26 for shots on 15 μm Al followed by Ar gas at 20 and 100 bars. They allow to follow the electron cloud dynamics in a single laser shot. The image horizontal axis is the temporal axis which increases towards the right. For these two shots the probe beam was synchronized with the interaction beam. The synchronization was realized with a streak camera, the precision about the time zero is of the order of few ps. Even though this indetermination concerning the temporal origin, the chirped shadowgraphy has the great advantage, with respect to a snap shot sequence (obtained with different shots), of allowing a temporally resolved measurement in an extended temporal window in the *same* shot. The result is thus not affected by the laser shot to shot fluctuations. The vertical axis is the spatial axis and represents a *diameter*[3] in the gas jet. In Fig. 3.26 a perturbation (shadow band of $\lesssim$ 100 μm thickness) is clearly visible starting from the beginning of the image and extending until $\sim$ 12 ps after the interaction and over 400 μm at the image edge. This shadow structure is connected to the fast electron ionization front propagation in the gas jet.

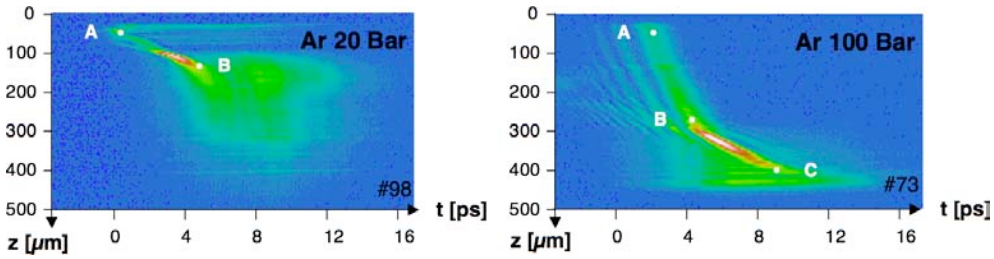

Figure 3.26: Chirped shadowgraphy images obtained with a 15 μm Al target and an Argon jet at 20 Bar (left panel) and 200 Bar (right panel). The laser intensity was 2×10^{19} W/cm^2.

The analysis of the ionization front propagation *vs* time allows to get the expansion cloud velocity. The velocity corresponding to the points in the figure are $v_{AB} \sim 0.12\,c$ for the first picture, and $v_{AB} \sim 0.67\,c$ and $v_{BC} \sim 0.16\,c$ for the second one. In agreement with the results of classical shadowgraphy, we see that: i) the velocity of propagation increases with gas pressure. The final size at the end of the image corresponds to the size observed in 2D shadowgraphy images (i.e. a fraction of 1 mm). ii) the propagation velocity decreases with time. For instance from Fig. 3.26 (on the right) (Ar at 100 Bar) we get $v \sim 0.67\,c$ at early times and $v \sim 0.16\,c$ at late times. Instead the propagation velocity in Fig. 3.26 (on the left) (Ar at 20 Bar) is always smaller ($v \sim 0.12\,c$) and the final penetration distance is much shorter ($\sim$ 300 μm).

[3]In this Chirped configuration we lost a spatial dimension of the taken image

As already noticed in Sect. 3.5.1, also the results of *classical* shadowgraphy suggest such slowing down.

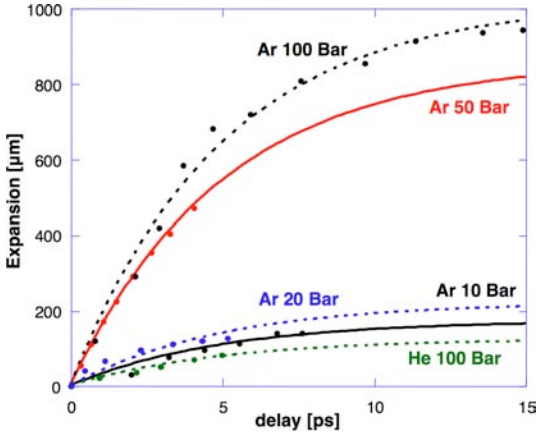

Figure 3.27: Reconstruction for typical shots of the spatial expansion of the electronic cloud *vs.* time for different gas pressures and gas type.

Fig. 3.27 shows the temporal evolution of the cloud size *vs* time for different gas pressures (10, 20, 50 and 100 Bars), obtained from typical chirped shadowgraphy images. Again we clearly see the fast slowing down of the velocity and the increased penetration at larger gas densities. These data are interpolated with curves of the type $r(t) = r_0(1-\exp(-t/t_0))$ where r_0 is the typical penetration and t_0 the characteristic scale time. From these curve we get a typical slowing down time to ~ 5 ps for all pressures. In reality, due to the short observation window, from these data it is not possible to conclude whether expansion completely stops or it continues with a small velocity. Therefore the absolute value of r_0 is not really meaningful; however it is significant that r_0 does increase with background density.

3.6 Proton imaging results

In the proton radiography experiment, one critical parameter was the distance between the gas jet and the proton target because the presence of a residual atomic density on the rear side of the proton target was a very important reason for the deterioration of the proton beam (maximum obtained energy). The maximum energy measured with the gas was of the order of $5-6$ MeV (or 4 radiochromic layers) against 12 MeV or more without the gas.

Fig. 3.28 shows typical proton radiography images. We clearly see a hemispherical shape, more pronounced at 100 Bars than at 15 or 30 Bars. This seems to show the

presence of a very strong electrostatic field, located at the ionization front (see for comparison the classical shadowgraphy images reported in Fig. 3.23), which deviates the protons. In this case the background gas pressure (N_2) has been changed, showing an increased penetration for the higher pressure, in agreement with the shadowgraphy results.

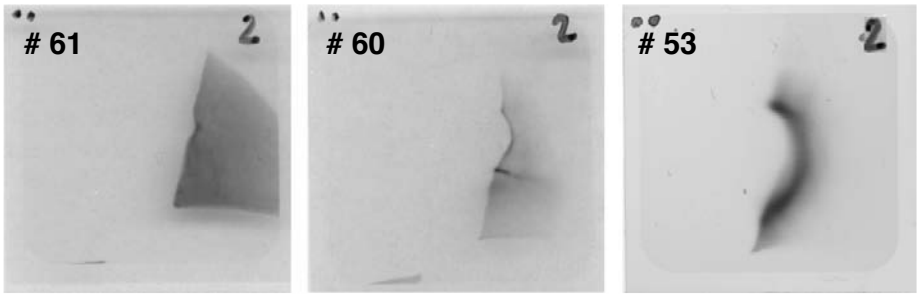

Figure 3.28: Proton images obtained with N_2 gas at 15, 30, and 100 Bars (shots 61, 60 and 53, respectively). In all cases, the size of the radiochromic films is 25 mm × 25 mm, the proton target 15 μm Au, the electron target 15 μm Al, the distance proton target - gas jet 5 mm, the distance gas jet − films 38 mm, the energy on the proton target ≈ 22 J and 1.1 J on the electron target. All images correspond to ≈ 20 ps after the arrival of the main laser beam on the electron target (i.e. they are formed by protons with ≈ 3 MeV energy).

Also, the size of the region is in qualitative agreement with shadowgraphy results. Fig. 3.29 shows the comparison between a proton image and a shadowgraphy image. The quantitative differences can be ascribed to the different gas and, above all, fast electron energy. The formation of proton images, due to proton deflection, gives a clear and direct evidence of the presence of very strong fields (quasi-static magnetic and electric fields) in the gas. Indeed the stopping power of the gas is clearly negligible for proton with these energies. However the time resolution was poor, due to the fact that we only registered some images on only 4 radiochromic layers. In particular, this didn't allow to temporally resolve the initial fast evolving phase. All of our images therefore practically correspond to the final quasi-stationary phase. This fact can also explain why in the proton radiography image we don't see the ionization filaments due to the faster high energy electrons, evidenced at early time in the shadowgraphy image.

In some other shots, however, we found some double-bubbles, i.e. spherical structures like those shown in Fig. 3.30, which have semi-macroscopical size (some hundreds μm) and seem to expand with time. Such results are still being analyzed and, for the

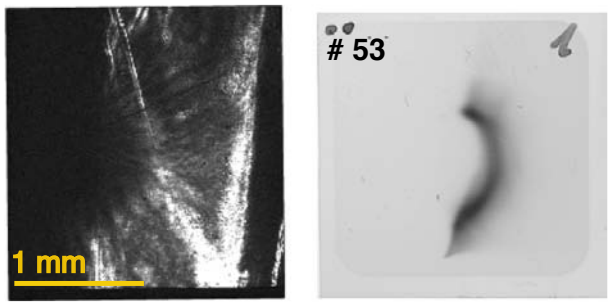

Figure 3.29: Comparison of shadowgraphy image (Ar 70 Bar, 5 ps after CPA firing, 1 MeV electrons) with proton radiography image (N_2 at 10 Bar, $\approx$ 200 ps, 200 keV electrons).

moment, the origin of such bubbles is not understood, nor the laser / target parameters which trigger their formation.

Figure 3.30: Double-Bubble structures observed in some shots. Here the proton image has been obtained with N_2 gas at 50 at $\approx$ 28.8 ps after the arrival of the main laser beam on the electron target (i.e. they are formed by protons with $\approx$ 3.1 MeV energy).

On the opposite, the expansion of the front, as shown in Fig. 3.29, seems to be well understood and in agreement, from the point of view of velocity and size, with the results obtained with the classical and chirped shadowgraphy.

Chapter 4

Fast electron propagation in gas jets: experimental results analysis

4.1 Fast electron propagation in conductors

In contrast to conventional particle accelerators, the high-power laser-plasma interaction is characterised by a high charge and current density of accelerated electrons. In this case [142, 110], the propagation of high electron currents requires charge and current neutralisation. This implies a striking difference between conductors and insulators (or neutral gases). In the case of a conducting target there is a large number of free electrons with typical density n_e up to 10^{23} cm^{-23}, which may compensate the beam electrons.

As seen in Chap. 2, the time of charge neutralization τ_c of the electron bunch depends on the relation between the plasma frequency of cold electrons, $\omega_{pe}(\lesssim 10^{16}$ s$^{-1})$, and the cold electron collision frequency, $\nu_{ep}(\gtrsim 10^{15}$ s$^{-1})$. In the strongly collisional limit ($\nu_{ep} > \omega_{pe}$) the time of charge neutralization is $\tau_c \sim 1/4\pi\sigma_c(sigma_c$is the electron conductivity $) = \nu_{ep}/\omega_{pe}^2$ while in the opposite case of weak collisions ($\nu_{ep} < \omega_{pe}$) the current relaxation time is $\tau_c \sim 1/\nu_{ep}$. A convenient interpolation formula reads $\tau_c \simeq \nu_{ep}/\omega_{pe}^2 + 1/\nu_{ep}$ and gives a very short time, typically less than 1 fs, because of the large number of free electrons in metals. So, if the effective velocity of charge neutralization, $min\{d, l\}/\tau_c$ with d and l the diameter and the length of the electron

bunch respectively, is larger than the electron parallel velocity, $v_b \lesssim c$, one can neglect the electrostatic effects in the beam propagation.

However, the current neutralization is gradually deteriorated for $t > \tau_c$ due to the skin effect and the magnetic field generation. The spatial separation of the electron beam and the return current occurs in the magnetic diffusion time scale $\tau_m = d^2/c\tau_c \simeq$ 10 ps. Thus for electron pulse duration, $t = l/v_b$, much shorter than τ_m, the magnitude of the electrostatic field can be evaluated from the condition of current neutralization ($j_c \simeq j_b$) as:

$$E_{rc} \sim e n_b v_b / \sigma_c \tag{4.1}$$

It is evident that current neutralization greatly reduces the electrostatic field: the electric field in the conductor is by a factor $d/c\tau_c$ smaller than in vacuum (estimated from the Poisson's equation as:

$$E_r \sim \pi e d n_b \tag{4.2}$$

Their ratio is of the order of 30 for typical metals. However Eq. 4.1 cannot be applied if the charge neutralization time is longer than the pulse duration as it happens in insulators or neutral gases. Here the response of the medium is determined by the secondary electrons generated by the ionization of the material. This ionization phenomenon is not important for metals, since the ionization cross section is small for relativistic electrons, indeed the so produced secondary electrons are much less than the free electrons in conductors.

4.2 Fast electron propagation in insulators and neutral gases: the *ionization*

In dielectrics and neutral gases there are no free electrons and they need to be created by ionization induced by the fast electrons. The processes of ionization are thus very important in the interaction of the electron beam with dielectric media. Three processes should be taken into account: *i.* the collisional ionization of atoms by the beam electrons, *ii.* the ionization of neutral atoms by the self-consistent electric field, and *iii.* the collisional ionization by the return current. The density of secondary electron–ion pairs is defined by the ionization equation

$$\partial_t n_i = (\nu_{ib} + \nu_{fZ})(n_a - n_e) + \nu_{ir} n_e \tag{4.3}$$

where $\nu_{ib} = n_b v_b \sigma_i(\mathscr{E}_b)$ is the frequency of collisional ionization by the beam electrons, ν_{fZ} is the frequency of the field ionization, and ν_{ir} is the rate of avalanche ionization by the return current electrons[1]. The cross sections of ionization by electron impact are well known [97, 143] and for high enough electron energies, $\mathscr{E}_e \gg J_Z$ they can be interpolated as follows[143]:

$$\sigma_i = 4\pi a_B^2 \frac{J_H^2}{J_Z \mathscr{E}_e} \left(a_Z \ln \frac{\mathscr{E}_e}{J_Z} + b_Z \right) \tag{4.4}$$

where $a_B = \hbar^2/m_e e^2$ is Bohr radius and a_Z and b_Z are the fitting coefficients of the order of unity. The typical cross section about 10^{-19} cm^2 for an electron with the energy $200-300$ keV. Correspondingly, the ionization frequency is proportional to the beam density and decreases with the electron energy from 20 ns^{-1} (for $\mathscr{E}_e$=10 keV) to 2 ns^{-1} for (for $\mathscr{E}_e$=1 MeV) for a beam density of 10^{-18} cm^{-3}. The ionization frequency of a few ns^{-1} can be sufficient for the charge neutralization, since it corresponds to the production of about 10^{18} cm^{-3} secondary electrons during the duration of a beam bunch ($\approx$ 10 fs) in a solid target. The probability of field ionization is defined by the Keldysh formula [144]:

$$\nu_{fZ} = 4\omega_a \left(\frac{J_H}{J_Z} \right)^{\frac{5}{2}} \frac{E_a}{E} \exp \left[-\frac{2}{3} \left(\frac{J_H}{J_Z} \right)^{\frac{3}{2}} \frac{E_a}{E} \right] \tag{4.5}$$

where $\omega_a = 2J_H/\hbar$ and $E_a = e/a_B^2$ are the atomic frequency and the atomic electric field, respectively. The rate of field ionization is a very steep function of the electric field and therefore of the density of the electron beam. Estimating the selfconsistent electric field from Eq. 4.2 for a beam diameter of 10 μm, we see that field ionization dominates the collisional one for the beam densities above $(3-4)\times 10^{17}$ cm^{-3}. For the densities above 10^{18} cm^{-3}, the rate for field ionization exceeds 1 fs $^{-1}$. However, the field ionization is limited to a relatively short time because of charge neutralization. The last term in Eq. 4.1 accounts for the collisional ionization by the secondary electrons, $\nu_{ir} = n_a v_e(\mathscr{E}_e)$. It can be important if the energy of secondary electrons in the selfconsistent electric field exceeds the ionization potential J_Z. However, under the conditions of interest, the lifetime of the large amplitude electric field is shorter than or comparable to the avalanche time $1/\nu_{ir}$. Therefore in the first approximation one can retain only the field ionization term in Eq. 4.3.

[1]We account here only for the interaction with one electron in atom which has the lowest binding energy $J_Z \sim J_H$, since it has the largest ionization cross section. Here, $J_H = e^2/2a_B$ is the ionization potential of the hydrogen atom.

4.2.1 Fast electron ionization in *dielectrics*

In order to analyze qualitatively the process of ionization of a dielectric one can consider a simple one-dimensional model which consists of the rate equations for ions and electrons,

$$\partial_t n_i = \nu_{fZ}(E)(n_a - n_i) \tag{4.6}$$

$$\partial_t n_e + \partial_x(n_e v_e) = \nu_{fZ}(E)(n_a - n_i) \tag{4.7}$$

and the Poisson equation for the electrostatic field

$$\partial_x E = -4\pi e(n_b + n_e - n_i) \tag{4.8}$$

completed by the mobility equation for the secondary electrons in the self-consistent field, $v_e = -eE/m_e\nu_{ep}$. Assuming that the profiles are stationary in the beam reference frame, $\xi = x - v_b t$, one finds the expression for the charge separation from Eqs. 4.6 and 4.7: $n_i - n_e = n_i eE/(m_e\nu_{ep}v_b - eE)$, and solves two coupled ordinary equations for the ion density and the electrostatic field. The ionization takes place in a narrow layer behind the beam front and it is sufficient to create much more free electrons than there are in the beam. One can make a simple estimate of the parameters behind the front. Assuming that $n_i \gg n_b$, from the Poisson equation one finds $n_b \simeq n_i eE/m_e\nu_{ep}v_b$ and the width of the ionization front $\Delta x \simeq E/4\pi e n_b$. Substituting these relations in the ionization equation one has:

$$E \sim \frac{E_a}{3\Lambda}\left(\frac{J_Z}{J_H}\right)^{\frac{3}{2}} \tag{4.9}$$

$$\Delta x \sim \frac{1}{6\pi\Lambda n_b a_B^2}\left(\frac{J_Z}{J_H}\right)^{\frac{3}{2}} \tag{4.10}$$

$$n_i \sim n_b\Lambda\frac{3\nu_{ep}a_B^2 v_b}{2r_c c^2}\left(\frac{J_Z}{J_H}\right)^{\frac{3}{2}} \tag{4.11}$$

where $\Lambda = \ln[2\omega_a r_c n_a c^2/3\pi\nu_{ep}n_b a_B^4 v_b^2)(J_Z/J_H)^4]$ is a large logarithmic term arising due to the exponential dependence of the ionization rate on the electric field amplitude. For the typical parameters of present laser-target interactions, $\Lambda \sim 20$. Correspondingly, the electrostatic field behind the front is about 30 times less than the atomic field, that is, $E \sim 100$ MV/cm, the ion density is about $50 - 100$ times larger than the beam density, that is, the charge separation is relatively small, $n_i - n_e \simeq n_b \ll n_i$, because of the large collision frequency ν_{ep}. The width of the ionization front is small:

less than a few microns. Note, that by comparing the width of the ionization front in Eq. 4.10 with the condition of the beam detachment (separation of the electron beam from the target), one can define the minimum electron energy which is needed for charge compensation in dielectrics: $\mathscr{E}_b > J_H d/3\pi\Lambda a_B$. It is about 20 keV for a beam diameter of 10 μm. One may also note that for the beam densities less than 10^{21} cm^{-3}, the ion density behind the ionization front is much less than the solid density n_a. That is, the ionization in a dielectric cannot be completed because of self-consistent screening of the beam electrostatic field. This estimation of the number of free electrons produced by the relativistic electron beam in the insulator demonstrates the important differences between the propagation of electron beams in metals and dielectrics. The smaller number of free electrons in dielectrics corresponds to a smaller electric conductivity. Therefore the electric field (cf. Eq. 4.2) and the Ohmic dissipation are stronger and beam electrons are losing their energy faster. Also the ionization itself represents an additional and important channel for beam energy dissipation.

4.2.2 Fast electron propagation in gases

The propagation of intense electron beam through the gases has been studied for quite a long time (see for example Refs. [145, 146, 147, 148, 149] and the references therein). One of the important processes, which accompanies beam propagation, is the neutralization of both beam charge and current due to the ionization of the gas and generation of a current of secondary electrons. In early experiments where beam density was not very high, the ionization of the gas was solely due to binary collisions of beam and secondary electrons with gas particles. However, with the increase of the beam energy density, the electric field generated by the beam increases to the magnitude $E \simeq 0.1 \times E_a$, where $E_a \approx 10^9$ V/cm is the atomic electric field. As we have seen in the previous section, at such high electric field the collisionless electric field ionization becomes the dominant mechanism [110, 96, 150]. Usually electric field ionization starts to be important at beam densities above $n_{crit} \sim 10^{18}$ cm^{-3} [96]. In our experiments we studied the propagation of electron beam, with the density higher than n_{crit}, through the gas with a neutral density corresponding to a pressure larger than one bar.

One of our experimental results, concerning an intense electron beam generated by a laser-foil interaction, was the rather slow expansion of the beam cloud into the gases. We have deduced speeds of 10^9 cm/s and $1.4 - 10^9$ cm/s for Helium densities of 10^{19} cm^{-3} and 3.2×10^{19} cm^{-3}, and speeds of 2×10^9 cm/s and 3×10^9 cm/s for Argon densities 10^{19} cm^{-3} and 2.8×10^{19} cm^{-3}. It is plausible that to describe properly these experimental results concerning the electron beam expansion,s one should take into account the electric field ionization.

4.3 Shadowgraphy discussion and analysis

Let us first discuss what happens at the foil / gas interface. The condition on neutralisation of fast electron and return current gives

$$J_{TOT} = en_b v_b – en_e v_e \simeq 0, \tag{4.12}$$

and since v_e cannot be $> c$, it follows that: *i.*) the maximum fast electron current which can propagate is $n_e c$, and *ii.*) background electrons are also accelerated to high velocities (hence speaking of fast and slow electrons is no longer correct).

While for dense matter ($n_e \gg n_b$) a small return velocity is sufficient for current neutralization, in our case the few background electrons are strongly accelerated and the fast electron beam is forced to move with the same velocity as the return current. The condition in Eq. 4.12 also explains why the cloud minimum size is large. When fast electrons reach the rear side (in a time $t \sim d/c$, shorter than pulse duration), their density is large and cannot penetrate the gas because their current cannot be compensated. Only a few escape, setting up an electrostatic field, which completely stop all other fast electrons (until ions are also set in motion). These electrons are effectively confined in the target and either reflux or move along the rear surface, effects which brings to a density reduction, until $n_b \sim n_e$ in the background gas. A final electron beam radius in agreement with observed size can then easily be calculated. When fast electrons start to propagate in the gas, their motion will be dominated by charge separation. Propagation is discussed in detail in the Sect. 4.2.1, were we explicitly derives charge separation (using for simplicity an ionization degree $Z^* = 1$) as

$$\Delta n = n_e - n_i = n_i E/(m_e \nu v_b/e + E), \tag{4.13}$$

where E is the electrostatic field due to charge separation, v_b is fast electron velocity, and ν the collision frequency. In the case of solids ($n_e \gg n_b$), which implies small charge separation Δn, relatively small fields, and weak inhibition (in particular, E can be neglected in the denominator of Eq. 4.13), the beam velocity v_b is not very different from c. In our case, on the contrary, fast electron density, as generated in the foil, is much larger than background gas density. The two terms in the denominator become comparable, implying

$$\Delta n \sim n_i/2 \tag{4.14}$$

i.e. charge separation is of the order of background density, as it could be heuristically estimated. Then taking into account that $n_b \sim n_e$ from Eq. 4.13, we have

$n_e \sim n_i \sim n_b$, and from Poisson equation we get:

$$\nabla E \sim E/\Delta x = +4\pi e \Delta n \sim -4\pi e n_b, \tag{4.15}$$

To find the width Δx, and electric field E, we consider that the maximum potential energy of fast electrons in the field must be of the order of their initial kinetic energy: $kT_{hot} \sim eE\Delta x$, where kT_{hot} is fast electron average energy (here ~ 1 MeV). Then

$$\Delta x \sim E/4\pi e n_b = (kT_{hot}/e\Delta x)/4\pi e n_b = \lambda_D \tag{4.16}$$

i.e. neutrality can only be violated over the Debye length (of fast electrons). Although this result sounds very usual, we stress the point that it can only be derived in the limiting case of low background densities (indeed in the solid case we used a different expression for Δx). At the same time, we get the usual ambipolar expression for the electrostatic field

$$E \sim kT_{hot}/e\lambda_D = (4\pi e n_b kT_{hot})^{1/2} \tag{4.17}$$

which, in our experimental conditions, can easily reach 10^{12} V/m. Such enormous electric field very rapidly produces a strong ionization of background gas, creating the free electrons, which are needed for the neutralizing return current. Then the distance $\Delta\, x$ also corresponds to the width of the ionization front in the gas. The ionization time can be calculated by using the Keldish's formula [144] as $t = 1/\nu(E)$ (Keldish's ionization frequency). Calculated ionization rates for Ar are shown as a function of background gas density in Fig. 4.1. Notice that Keldish's ionization frequency only depends on the strength of the electric field. However in our model E depends on density (since, again $n_b \sim n_e$), which explains the dependence shown in Fig. 4.1. Although the ionization phase is very rapid, nevertheless it is fundamental, not only to create free electrons, but also to fix the background density. The huge electrostatic fields arising in the gas only exist over a distance λ_D and for a time $t_E < \lambda_D/v_b$. Ionization must then take place in a shorter time. Hence in our conditions, reachable ionization stages are Ar^{6+} and He^{2+}.

Finally, free electrons, are set in motion and establish a return current which cancel the positive charge left behind by fast electrons. The drift velocity is found by solving the motion equation for an electron in an external electric field under the influence of collisions:

$$m_e \frac{dv_e}{dt} = -eE - me\nu v_e \tag{4.18}$$

Here we have another big difference with the solid case. Indeed, for the drift velocity v_e of return electrons, in dielectrics we used Drude model (or Ohm's law for

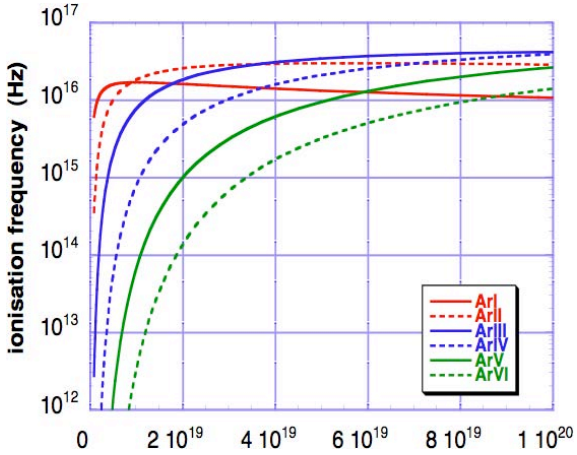

Figure 4.1: Ionization frequency *vs* Ar gas density (cm^{-3}), according to Keldish's formula (for comparison $t_E \sim \lambda_D/c/20 \sim 10^{-14}$ s). Electric field strength is calculated according to Eq. 4.17 for a $kT_{hot} \sim 1$ MeV

conductors). This means that the collision frequency ν is related to conductivity by the relation $\tau_c \sim 1/4\pi\sigma_c \simeq \nu_{ep}/\omega_{pe}^2 + 1/\nu_{ep}$. Since in this case the conductivity is not known, we can take heuristically $\nu = (\lambda_{ii}/v_T)^{-1}$, where λ_{ii} is the inter-ionic distance in the material and v_T the electron thermal velocity.

As it is well known, using such expression for ν, implies that the drift forces increase as the electron velocity v_e increases. Therefore electron acceleration slows down. A final stationary value of velocity is then reached when friction balances the electric force. This "drift velocity" is

$$v_e \sim \frac{eE}{m_e \nu} \tag{4.19}$$

Let's finally notice that if we assume the collision frequency given by Spitzer's formula from the beginning, we get no drift velocity. Indeed ν decreases as v_e increases and soon friction becomes negligible. Electrons are then accelerated as if they were free (runaway electrons).

The establishment of the return current and the cancellation of the positive charge left behind by fast electron takes a time of the order of $t \sim \lambda_D/v_e$, where v_e is the drift velocity, given in our model by Eq. 4.19. This process is slow because the free background electrons are (at least initially) slow and strongly collisional, and collisions inhibit the return current. Since however, no further propagation of fast electrons is possible before the charge separation has been cancelled, the fast electron current is finally forced to move with a velocity equal to the return velocity of background electrons, i.e. practically the expansion velocity is v_e. This gives a slow velocity and

a strongly inhibited motion. Let's also notice that then, considering the reachable ionization stages Ar^{6+} and He^{2+} from Fig. 4.1, the experimental expansion velocities in Figs. 11.8 and 11.9 simply scale with background density n_e (and are larger for bigger densities) irrespective of gas type. Also, the beam velocities from Eq. 4.19 are very close to experimental values. We should also wonder about energy loss in a gas medium which is non collisional (over our distances) for fast electrons. OTR and K_α results show that not many electrons reach the second foil, or at least they are no longer *energetic*. Indeed the energy spent in ionizing a gas region as large as ~ 1.2 mm may be comparable to that in fast electrons ($\leqslant 30\%$ of laser energy). By a simple calculation we can show how the ionization process may completely deplete the fast electron beam energy. Assuming the maximum possible ion density, corresponding to full gas ionization, for the case of the Ar at a backing pressure of 70 bar (cf. Fig. 11.4) we have $n_i \simeq 2.7 \times 10^{19}$ cm^{-3}, and thus in the volume of the electronic cloud region at late times we can extimate a number of ions given by:

$$N_i \simeq \frac{1}{2}\left(\frac{2}{3}\pi\, r_c^3\right) n_i \tag{4.20}$$

Where for a cloud radius r_c, as evidenced in Fig. 11.4, of the order of the gas jet diameter at late times, $r_c \approx 1.2$ mm, we finally get a number of ions $N_i \simeq 7.2 \times 10^{16}$.

Thus, for a reachable ionization stages Ar^{6+}, the energy spent by the fast electron in the ionization process could be equated as:

$$\mathscr{E}_{ioniz} \simeq N_i \sum_{j=1}^{6} \mathscr{E}_j \tag{4.21}$$

$\mathscr{E}_j$ for different processes in Argon are listed in Tab. 4.1.

Indeed, with $\sum_{j=1}^{6} \mathscr{E}_j = 4.34 \times 10^2$ eV, we finally get $\mathscr{E}_{ioniz} \simeq 2.4$ J, which corresponds to $\gtrsim 80\%$ of the total extimated fast electron energy. Moreover, also the electrostatic field itself could be an efficient loss mechanism, stopping all fast electrons involved in the charge separation process in a distance $\sim \lambda_D$. Finally, we can thus conclude that these effects provide effective mechanisms for cloud deceleration, as evidenced by our experimental results.

In order to better understand the slowing down of fast electrons during their propagation in gas jets evidenced in chirped shadowgraphy images, we have also performed some (preliminary) simulations using the 1D Vlasov-Poisson code ESTATIC developed by A. Antonicci. This code treats fast electrons using a Vlasov equation, while the electrostatic field is treated self consistently through Poisson equation by calculating the total charge density (fast + background electrons) at each time step. The background electrons are treated with a mobility equation with an ad-hoc resistivity ($\nu \sim v_T/\lambda_{ii}$).

Process	$\mathscr{E}_j$ [eV]
$Ar \rightarrow Ar^{+} + e^{-}$	15.76
$Ar^{+} \rightarrow Ar^{2+} + e^{-}$	43.39
$Ar^{2+} \rightarrow Ar^{3+} + e^{-}$	84.11
$Ar^{3+} \rightarrow Ar^{4+} + e^{-}$	143.69
$Ar^{4+} \rightarrow Ar^{5+} + e^{-}$	218.53
$Ar^{5+} \rightarrow Ar^{6+} + e^{-}$	309.67
$Ar^{6+} \rightarrow Ar^{7+} + e^{-}$	434.08

Table 4.1: Ionization potentials for atomic argon.

Finally the ionization phase is neglected (being so fast), so that practically the case of propagation of fast electrons in a low density plasma is considered.

Even if the results of these simulations are only preliminary, ESTATIC allows us to obtain some indications concerning dynamics of the fast electron population, by assuming a background population initially at rest and an injected hot population with a flat mono-kinetic distribution (with $E_f = 1$ MeV). Fig. 4.2 (a) represents the result of the progressive penetration of fast electrons in the plasma (and of the consequent acceleration of the background plasma electrons in the opposite direction). The front velocity of the fast electron beam can be evaluated from the penetration range R as: $v_f \sim R(\Delta t)/(\Delta t)$. This gives sub-relativistic velocities of the order of $c/30$, in agreement with the experimental measures.

In Fig. 4.2 (b) we show the temporal evolution of the fast electron front of Fig. 4.2 (a). Furthermore, looking at Fig. 4.2 (c) we can see that by varying the density of the background plasma we can observe that the penetration in gas and the propagation speed increase with background density. This result is in qualitative agreement with the experimental results. The fast electrons are able to propagate only when the injected fast electron density is inferior to the background density, when it becomes equal or greater, the propagation is strongly inhibited and the characteristic velocity becomes smaller than $c/100$. This dynamics is also more evident in the profiles of Fig. 4.2 (d) obtained maintaining the plasma density constant and varying however the fast electron beam density. As in the case analyzed before, the fast electrons can propagate only if its own density is smaller to the plasma density. Thus, if the density of the injected fast beam continuously increases, a strong accumulation of negative charge and a strong electric field will be generated in the first thickness of the target. Fast electrons and electric field will remain prisoners in a very thin layer and

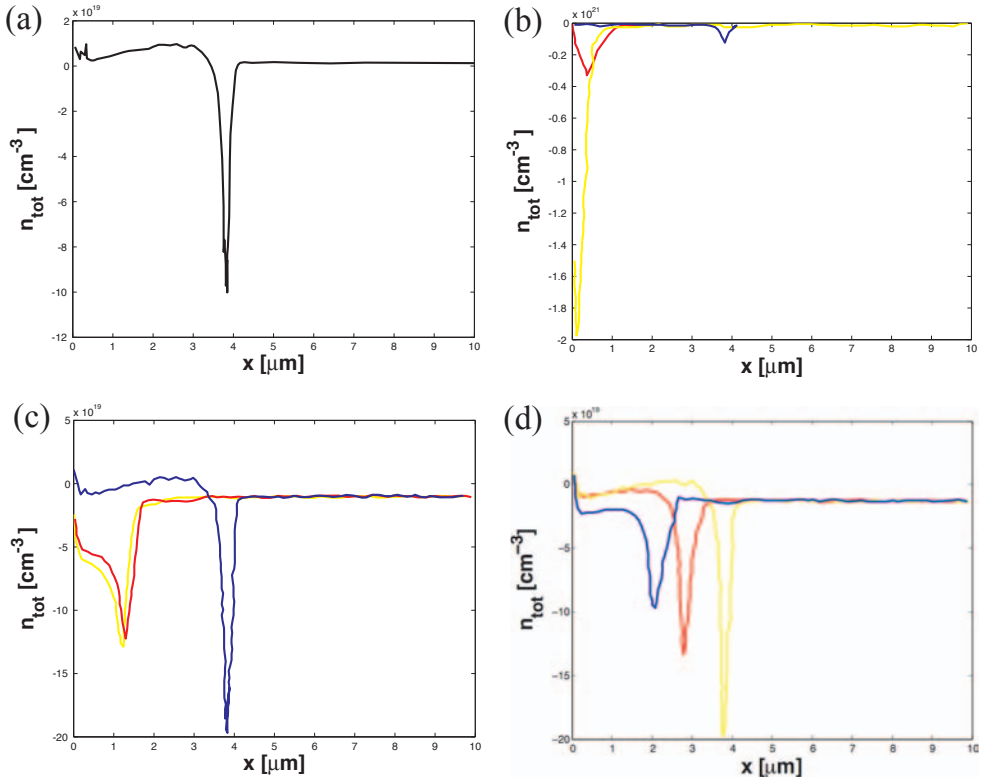

Figure 4.2: **(a)** The density profile of fast electrons is represented at the time $t = 416$ fs, corresponding to the end of the injection phase. The fast electron beam with density $n_f = 5 \times 10^{18}$ cm^{-3} is injected into a plasma initially characterized by the same ionic and electronic density $n_i = n_s = 5 \times 10^{19}$ cm^{-3}. **(b)** The characteristics of background and fast electrons are the same of Fig. 4.2. Blue curve correspond to a time $t = 100$ fs after the injection, red curve to $t = 200$ fs and yellow one to $t = 416$ fs. **(c)** The density profile of fast electrons is represented at the time $t = 416$ fs, corresponding to the end of the injection phase. The fast electron beam with density $n_f = 5 \times 10^{18}$ cm^{-3} is injected into a plasma initially characterized by different ionic and electronic densities $n_i = n_s = 5 \times 10^{19}$ cm^{-3} in blue, 5×10^{18} cm^{-3} in red, 5×10^{17} cm^{-3} in yellow. **(d)** The density profile of fast electrons is represented at the time $t = 416$ fs, corresponding to the end of the injection phase. The fast electron beam with different densities n_f is injected into a plasma initially characterized by the same ionic and electronic density $n_i = n_s = 5 \times 10^{19}$ cm^{-3}. The blue curve corresponds to a fast electron density n_f of 5×10^{18} cm^{-3}, the red curve to 5×10^{19} cm^{-3} and the yellow one to 5×10^{20} cm^{-3}.

the plasma will be submitted to a strong disturbance but limited to this region. We summarized in the graph of Fig. 4.3 the variation of the penetration of fast electrons when varying the density of the incident beam or the density of the plasma. When varying the latter one, an evident variation in the propagation range, and the speed of propagation of fast electrons, is observed.

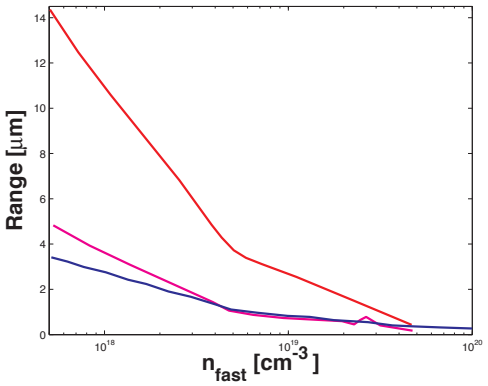

Figure 4.3: Propagation range R of the fast electron beam as a function of the hot beam density n_f, for different initial densities of the background plasma $n_i = n_s$: respectively equal to 5×10^{19} cm^{-3} in red, to 5×10^{18} cm^{-3} in violet and to 5×10^{17} cm^{-3} in blue.

Another typical result of ESTATIC simulations is shown in Fig. 4.4. We can see that, as already observed in the shadowgraphy images, the fast electron propagation velocity is predicted to decrease with time.

Let us also notice that even if the temporal and propagation ranges are different from those evidenced in our experimental conditions (cf. Sect. 3.5.2), the fast electron velocity at early times is nevertheless of the order of $\sim c/10$ for electron densities comparable to the case of the Ar at a backing pressure of 20 Bar, where $v \sim 0.12\,c$. Another important point evidenced by the simulations is that the fast electron velocity and slowing down effect seem to decrease with the fraction of the fast electrons in the ionization front, the last one vanishing for a fast electron density of the same order of the background plasma density, $n_b \sim n_e$.

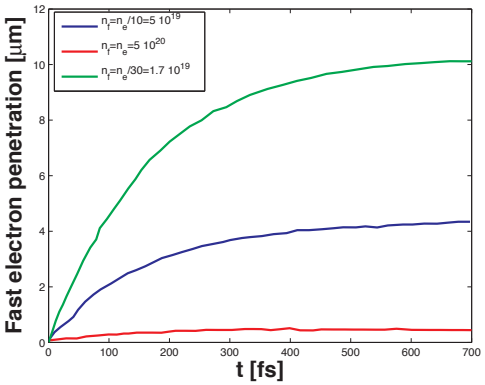

Figure 4.4: Results of simulations of the fast electron propagation in gas jets (made with the code ESTATIC). Atomic density is 5×10^{19} cm^{-3}. Propagation peak velocity at early times is $v \sim 0.15\,c$ is of the order of what observed experimentally and decreases with time.

4.4 Proton imaging discussion and analysis

4.4.1 Particle tracing

The field spatial distribution were inferred by comparison of Proton Imaging experimental data with particle tracing simulations [151]. In particle tracing simulations the proton deflections in a given time-dependent electromagnetic field configuration are calculated. The main advantage of numerical inversion of integrals 3.18 lies in the fact that no assumption needs to be made on the field distribution symmetry and that the time evolution of the fields and the broad spectral content of the probe beam can be easily taken into account. However in our case we have too strong fields which could produc a caustic formation and crossing proton trajectories. We thus need to make an assumption about the filed symmetry.

PTRACE, the particle tracer we used, was developed by A. Schiavi and its main features are described in Appendix B. The geometry of the experimental Proton Imaging arrangements is fully reproduced in the code. The proton trajectories are traced from the virtual point source, through the electromagnetic field region up to the proton detector. The relativistic equation of motion for the protons in an external electromagnetic field:

$$\frac{d\mathbf{p}}{dt} = \mathbf{F} = q(\mathbf{E} + \mathbf{v_p} \times \mathbf{B}), \tag{4.22}$$

is numerically integrated along the proton trajectories. The mutual interaction

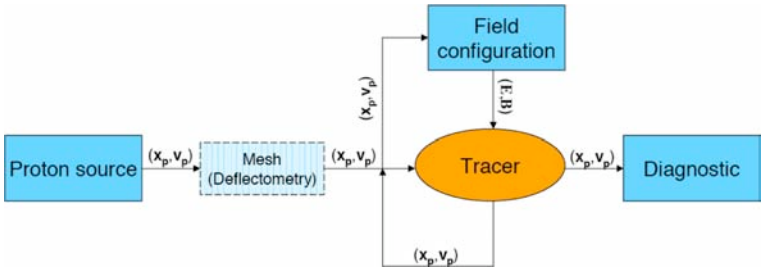

Figure 4.5: Flow chart of the particle tracing code.

between the protons in the probe beam is neglected and the co-moving electron cloud is not modelled. The diagnostics of the code include:

- a proton detector, which provides the particle density across the beam transverse section (analog to the proton detector in the real experiment and particularly suitable for Proton Imaging experimental data analysis)
- a routine which calculates the proton transverse deflection as a function of the proton transverse position and time
- a tracer which allows the proton trajectories to be followed for one particle at the time

4.4.2 Front fields analysis

In order to extract a more detailed information from the experimental data regarding the detected field spatial structure, time evolution and absolute field values, the experimental data from proton probing techniques were compared to particle tracing simulations. The detection from the expanding front was simulated in the Proton Imaging arrangements by using the PTRACE ray-tracing code. A sketch of the field configuration used in the simulation is shown in Fig. 4.6

The broad spectral content of the probe proton beam was taken into account. In agreement with chirped shadowgraphy results, we assumed an hemispherical front expanding with the law:

$$z_{front} = r(t) = r_0(1–exp(-t/t_0)) \tag{4.23}$$

The field lines were assumed straight and originating from a point located at a position $z_s < 0$ behind the target on the symmetry axis, as suggested by our experimental shadowgraphy results (cf. Fig. 11.4) and the laminarity of the proton

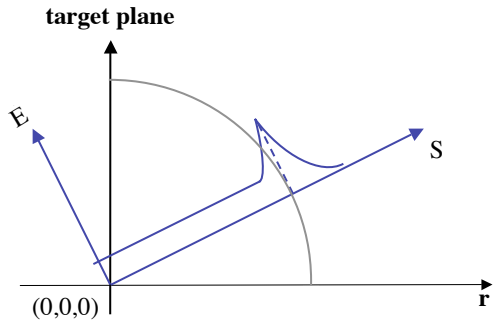

Figure 4.6: Sketch of the axes and field orientation in the particle tracing simulation of the expanding front field. The field dependence along a given field line s is also sketched. The circle represents the front position.

source evidenced in previous experiments performed on the same LULI laser installation (cf. [136]). Also, in agreement with the theoretical model discussed in Sect. 4.3, we assumed an electric field, concentrated at the hemi-sphere edges and which radially decays exponentially over a typical distance of the order of a few fast-electron Debye-lengths (i.e. a few microns). Inside the sphere the electrostatic field is constant and much lower, at least two orders of magnitude, outside it is zero.

Along each field line the field then was:

$$\begin{cases} E = (E_{peak} - E_{plateau})e^{-[(s_{front}-s)/l_{in}]} + E_{plateau}, & \text{if} \quad 0 < s < s_f \\ E = E_{peak}e^{-[(s-s_{front})/l_{out}]}, & \text{if} \quad s_f < s < \infty \end{cases}$$

where s is the coordinate along a given field line. s_{front} is the position of the ionization front (where the electric field is manly concentrated), while l_{in} and l_{out} are respectively the inner and outer rising and falling scale lengths of the field around the front. At the moment we do consider only a snapshot of the static field configuration without taking into account its temporal evolution. In the simulations the field value E_{peak} at peak and $E_{plateau}$ in the plateau region at the given probing time and the field spatial scale lengths l_{in} and l_{out} are chosen in order to match the experimental results. The best match was found for $E_{peak} \approx 10^{11}$ V/m and $E_{plateau}$ roughly 6 order of magnitude smaller, i.e. $E_{plateau} \approx 10^5$ V/m. The field gradient scale lengths were found to be $l_{in} \sim l_{out} \approx 10$ μm.

Fig. 11.13 (left panel) shows a typical simulation result of a proton image, corresponding to such a parameters: a maximum electrostatic field of $\approx 10^{11}$ V/m and a fall-off distance of ≈ 10 μm.

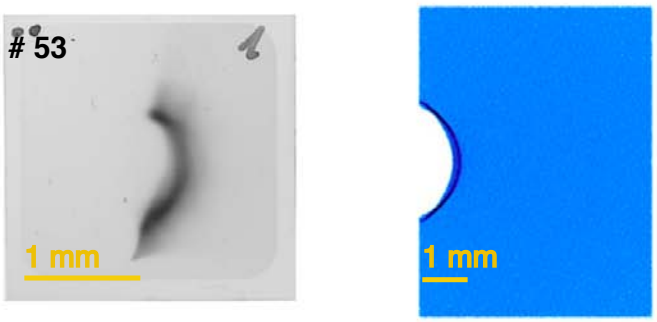

Figure 4.7: Comparison of proton radiography image (N_2 at 100 Bar, 20 ps) with a simulation obtained with a proton energy of 3.1 MeV and the parameters: $E_{max} = 10^{11}$ V/m, $E_{plateau} = 10^5$V/m, $r_0 = 100\,\mu$m, $L_{in} = 10\,\mu$m, $L_{out} = 10\ \mu$m (internal and external fall-off distances).

Such values are in fair agreement with the expectations from theory (cf. Sect. 4.3) and confirm that the characteristic peaked structure of the electric field which is expected, is indeed observed in the experiment. However let us notice that since the total deviation depends on the line integral $\int Edx$, other values of the maximum field and fall-off distance can also reproduce our images. However for too-low electric fields, it is not possible to expel all the protons from the region inside the front, as instead is the case of our experimental images shown in Fig. **??**.

Moreover, we also used the particle tracer PTRACE in order to reproduce the proton piling profile observed experimentally. In Fig. 4.8 we compare the experimental with the simulated proton profiles for two different shots (cf. Fig. **??**). Also in this case we can note a fair agreement between simulations and experiments, both the pilling shape and the spatial pattern are very similar, evidencing the presence of a quite large number of protons also after the peak region.

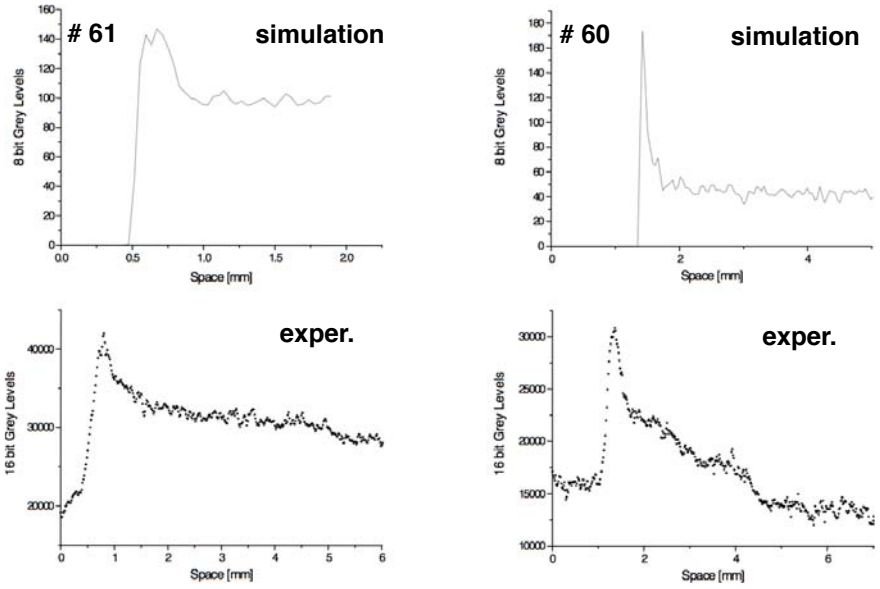

Figure 4.8: Comparison of proton piling up (as a function of the distance from the target plane) deduced by radiography images (N_2 at 15 and 30 Bars, 20 ps after the arrival of the main laser beam on the electron target, i.e. they are formed by protons with ≈ 3 MeV energy) (bottom panels) and by simulations (top panels) obtained with a proton energy of 3.1 MeV.

Chapter 5

Fast electron propagation in solid targets: target rear side emission

5.1 Previous experiments and motivation

As we seen in Sect. 1.3.1, it is crucial for the FI concept that the energy of the ignitor laser be efficiently converted into an intense electron beam that can propagate through the high density overcritical plasma and initiate the thermonuclear burn in the core [4]. On the other side in the TNSA scheme for ion acceleration [18], fast electrons need to escape from the back face of a solid target after having crossed all the target thickness. Thus, a precise characterization of the fast electron current is crucial for understanding the dynamics of its propagation in dense matter, with the goal of optimising applications such as the fast ignitor inertial fusion scheme [4] and laser-produced ion beam sources [19].

This is a challenging task and despite the wide spectrum of diagnostics which have been used (K_α [152, 141], Bremsstrahlung [95, 153] visible emission [133], neutron production [50, 154]), practically all previous experiments have only been able to determine global parameters like the electron distribution average energy (i.e. the temperature), the penetration range, the electron average angular divergence.

In the attempt to investigate the temporal modulation of the fast electron population, very recent experiments performed at LULI laboratory [134, 155] have shown

evidence that part of the fast electron population is micro-bunched in time. Moreover, other experiments [156], based on the detection of X-Thermal radiation emitted from a layer buried inside the irradiated target have shown a heating of few 100's eV, attributed to fast electrons, at depth of 10's μm for laser intensity of $10^{19} - 10^{20}$ W/cm^2 [156]. These results thus show that the fast electron propagation induces detectable effects on the solid rear target surface. In particular, we expect a ionization front breakout which can modify the rear side electrical and optical properties. If the energy deposition is large enough, the surface is ionized and heated to high temperature (10's eV) and it will release explosively in vacuum, under the effect of the thermal pressure. At the same time, because of the achieved temperature, the surface will emit detectable Planck radiation in a spectral region going from the visible to the XUV.

These considerations led us to perform a few experimental campaigns using the target rear side visible emission as diagnostic and studying the total emitted signal (CTR and Thermal emission) and its spectrum versus target thickness, in order to completely characterise the fast electron distribution and estimate the fast-electron induced-heating.

Another key point is that, in the FI concept, the transport of the electrons to the precompressed core involves currents of the order of $100 - 1000$ MA which largely exceeds the Alfvén limit. Their propagation is possible only if return currents formed by the background electrons of the material balance the incoming fast electron current and cancel the charge separation. However, under these conditions (two counterstreaming intense currents), kinetic instabilities such as two-stream or Weibel-like instabilities [113, 157] may develop and PIC simulations seem to predict that the transport of the relativistic electron beam leads to filamentation.

In this context, a number of experiments investigating the propagation and filamentation of laser produced relativistic electron beams have been performed using metal and plastic foils, foam targets, glass slabs and gas jets [158, 123, 122, 159, 160, 161, 162, 163]. However, at the moment there is no clear experimental evidence of filamentation instabilities because until now, no parametric study has been performed by systematically changing the target and/or laser parameters. Filamentary structures have been reported in [163] but their observation was indirect, far from the target where propagation and filamentation take place. The filaments and electron jets have been directly observed in [123, 122, 159, 163] but only in insulator targets. Moreover, from these data, it is not possible to conclude whether the filamentation is due to a volumic mechanism (like two-stream or Weibel instability) or whether it is connected to the ionization instability taking place at the electron beam front.

Indeed, as we previously discussed in Chap. 3, in insulators, the charge separation at the edge of the propagating intense electron beam produces a strong electrostatic field [96, 116], which very rapidly ionizes the material. Free electrons are then set in

motion and they establish a return current. Thus, the bulk of the fast electron beam propagates in a dense plasma, the conductivity of which is only marginally different from the conductivity of a metal. However, according to [114], the ionization front becomes unstable because its velocity increases with the electron beam local density. This could enhance small corrugations of the ionization front which grow in time. Let's notice that, if the Weibel instability is the dominant filamentation process, it should act in a similar way in insulators and conductors. On the contrary, a ionization instability takes place only at the fast beam edge (ionization front) during the electron beam propagation through an insulator.

Again, the target rear side optical radiation can be a powerful diagnostic tool to detect such instabilities. In the case of transparent dielectric targets, this is also determined by Čerenkov emission [162]. More in detail, as we will discuss in Chap. 3, Čerenkov light can be emitted by fast electrons in the ionization front only (because the ionized plasma is not transparent and it has a refraction index $n \lesssim 1$), and hence diagnostic based on Čerenkov emission is naturally adapted for detecting ionization instabilities in dielectrics.

5.2 Target rear side radiation emission

One of the main objective of this thesis is to characterize the population of accelerated electrons and its propagation in over-dense matter. As we discussed in Sect.5.1, our principal diagnostic is the measurement of the visible radiation, typically between $\lambda_{min} \approx 350\,\text{nm}$ and $\lambda_{max} \approx 700\,\text{nm}$, emitted by the irradiated target rear side[1]. In fact, the electrons propagating through the target and then passing through the target vacuum interface, emit detectable radiation which allows the characterisation of the fast electron population: its total energy and its energy distribution, the geometry of propagation in dense matter, its temporal and spatial evolution. Therefore, we need to analyse and quantify the different emission mechanisms. In this chapter we will consider *i.* the thermal radiation emitted by the relaxation of the hot plasma formed at the back target surface, *ii.* the Transition Radiation from the transition at the target-vacuum interface, *iii.* the Synchrotron and Bremsstrahlung radiation in the potential sheath and *iv.* the Bremsstrahlung and Čerenkov radiation associated with the electronic transport through the matter.

Indicating the radiated energy per unit solid angle and unit wavelength as $\frac{dW}{d\Omega d\lambda}$ and taking into account the detection system and its absolute calibration (cf. Chap. 6

[1]For target rear side we mean the surface opposite to the side irradiated by the laser main pulse.

and Appendix G), the integral:

$$W = \int_{\lambda_{min}}^{\lambda_{max}} \int_{\Omega} \Phi(\lambda) \, \frac{dW}{d\Omega d\lambda} d\Omega \, d\lambda \ , \tag{5.1}$$

can be compared to our experimental results, W_{exp}. The integration over the wavelength is made in the spectral band of the detection system, $\lambda_{min} < \lambda < \lambda_{max}$ and weighted by using the spectral response $\Phi(\lambda)$ (optical system transmission + detector response). The solid angle Ω is determined by the collection optics (see the experimental set-up description in Chap. 6).

In this chapter we will begin neglecting the experimental detection limitations, and consider only the physical aspects of the different radiative mechanisms. Thus, we will take $\Phi = 1$ and we will not restrict the spectral distribution to the range $[\lambda_{min}, \lambda_{max}]$. However, in order to make more predictive estimation and comparisons between the different emitting mechanisms, which can be very directional, we will often consider our real collection angle. Nevertheless, the real complete experimental conditions will be considered only in Chap. 6, where we will analyze the experimental results in the light of the models introduced here.

5.2.1 Black body Thermal radiation

Thermal black body radiation is naturally emitted by any body with a not-zero absolute temperature. If we supposed that the body is in equilibrium, it is produced by the atoms of the medium undergoing atomic transitions or vibrations, and by passing on lower and more stable energy levels. At the same time, the medium can gain energy from the external radiation. If the body is characterised by an absorption coefficient $A = 1$ at all wavelengths, then it's a black body and the spectral distribution of the emitted radiation depends on its temperature T and it is given by the Planck formula

[164][2]:

$$B_{\lambda,Planck}(T)\,[\mathrm{W\,m^{-2}\,sr^{-1}\,m^{-1}}] = \frac{2hc^2}{\lambda^5}\,\frac{1}{\exp\left(\frac{hc}{\lambda eT[\mathrm{eV}]}\right)-1} \tag{5.2}$$

Whenever A is not identically 1, the emitted spectrum is modulated by the absorption coefficient (Kirchoff's law) and we speak about *grey* body emission.

Eq. 5.2 shows that the higher the temperature, the lower are the wavelengths where the radiation is concentrated. The maximum of the Planck distribution corresponds to a photon energy

$$h\frac{c}{\lambda_{max}}[\mathrm{eV}] = 2.822\,T[\mathrm{eV}] \tag{5.3}$$

Table 5.1 summarizes the wavelength values λ_{max} for various orders of magnitude of the temperature. Our diagnostics, limited to the optical spectral band, will detect the maximum of the black body only for low temperatures, $\sim 1\,\mathrm{eV}$. Fig. 5.1 illustrates the evolution of brightness as a function of the temperature (Eq. 5.2) and for two different wavelengths, in the XUV range (solid curve) and in the visible range (dashed curve). We see that in XUV range the Planck brightness is definitely more sensitive to temperature.

Thermal emission by an instantaneously heated plasma

Here we are not interested to the exact heating mechanism by which the fast electrons can produce a plasma while propagating in the target. However, by assuming a thermalized heated medium, we can consider an emitting plasma as an *energy reservoir* with a radial dimension r_f related to the angular dispersion of the electrons $\theta/2$ and the traversed target thickness (L)(cf. 6.2.1). Thus, by using the Planck formula 5.2 in order to roughly estimate the black body emission, we can write:

$$\frac{d^2W}{\Delta V d\lambda}[\mathrm{Jm^{-4}}] = \frac{8hc^2}{\lambda^5}\,\frac{1}{\exp\left(\frac{hc}{\lambda eT[\mathrm{eV}]}\right)-1} \tag{5.4}$$

[2]In order to facilitate the analysis of the experimental results, we prefer the wavelength λ, instead of the frequency ν, as spectral variable:

$$\lambda = \frac{c}{\nu}\,, \qquad \begin{aligned} B_\lambda &= \left|\frac{d\nu}{d\lambda}\right| B_\nu \\ &= \frac{c}{\lambda^2} B_\nu \end{aligned}$$

T [eV]	λ_{max} [nm]
1	440
10	44
100	4
1000	0.4

Table 5.1: Wavelength of the maximum of the Planck distribution, for different temperature values.

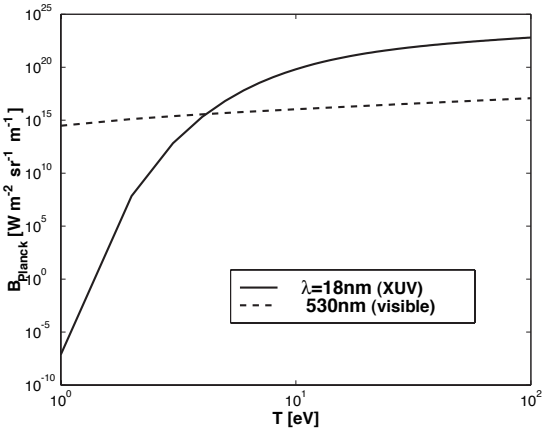

Figure 5.1: Planck brightness as a function of the black body temperature for two different wavelengths: 18 nm (XUV) and 530 nm (visible).

the quantity $\frac{d^2W}{\Delta V d\lambda}$ is the spectral energy density, i.e. the energy emitted per unit volume per unit spectral interval. This relation is valid for an ideal black body, i.e. a closed black cavity, inside which the radiation is in equilibrium with the cavity walls. However, in our case one must take into account also aluminium absorption and consider its grey body emission at the considered temperature. It is also necessary to relate the volume element to the solid angle corresponding to the optical aperture of our experimental diagnostics path.

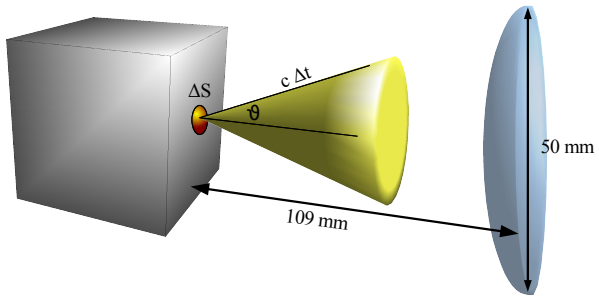

Figure 5.2: Volume ΔV corresponding to our experimental system.

The element of volume ΔV is calculated in the following way (see Fig. 5.2):

$$\Delta V = \int_{\Omega} dV = \int_{\theta} \int_{\varphi} c\Delta t \Delta S \cos(\theta) d\theta \, d\varphi \tag{5.5}$$

where ΔV is the infinitesimal element containing the photons emitted inside the cylinder of section $\Delta S \cos(\theta)$ and side $c\Delta t$. Δt is the black body emission duration. Thus, we have:

$$\Delta V = 2\pi \, c\Delta t \Delta S \sin(\theta) \tag{5.6}$$

where $\theta_{max} \approx 0.23\,[\text{rad}] = 13°$. Thus, finally:

$$\frac{dW}{d\lambda}[\text{Jm}^{-1}] \simeq \frac{5\pi^2 hc^2 \Delta t \Delta SA}{\lambda^5} \frac{1}{\exp\left(\frac{hc}{\lambda eT[\text{eV}]}\right) - 1} \tag{5.7}$$

The radius r_f of the emitting region is related to the initial spot radius r_0, $r_f \simeq r_0 L\sqrt{3}$ (corresponding to an angular dispersion of electrons, $\theta/2 \simeq 13°$, and the traversed target thickness L (cf. Chap. 6.2.1)) and the emitting surface is πr_f^2. The emission duration is a few tens of ps, with a temperature reached by the target of some eV for a 50 μm thickness target [54, 165]. Aluminium absorption for this temperature and in the spectral Visible-UV range is $A \simeq 0.5$.

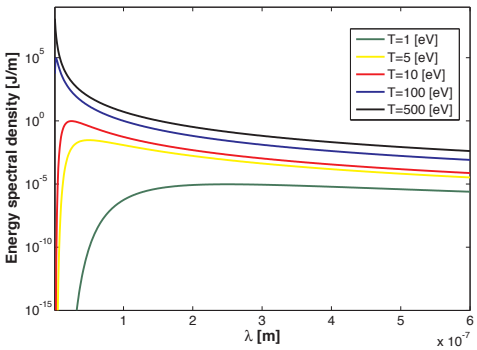

Figure 5.3: Black body emission for different temperature, an emitting surface of 450 μm^2 and an emission duration of 30 ps.

More in detail, from the curves plotted in Fig. 5.3, we can see how for temperatures $T = 5 - 100$ eV and an emitting surface $\pi\, r_f^2 \simeq 400 - 900$ μm^2, (corresponding to the case of $20-30$ μm thickness targets) the spectral density $\frac{dW}{d\lambda}$ collected by our diagnostic is, as we will see in Chap. 7, of the same order of our experimental results, obtained for the same target thicknesses.

However, this very simple model, based on the assumption of a thermalized emitting plasma, doesn't take into account its expansion as well as its temperature evolution in time. Since these aspects can not be neglected for a more detailed estimation of the thermal emission mechanism, we will better discuss them in Chap. 7.

In Fig. 5.3 we represent the black body emission (from Eq. 5.7) for several temperatures. The position of the maximum emission changes with the emitting temperature accordingly to the Wien's law: the temperature gives the slope of the various spectral curves, while the emission duration as well as the emitting surface give the absolute value of the signal.

5.2.2 Transition radiation at the target-vacuum interface

A charged particle crossing the interface separating two media with distinct dielectric properties emits a radiation known as Transition Radiation [166]. If the observation is made in the visible and near UV range, we speak of **Optical Transition Radiation** (OTR). This type of radiation is associated with the polarization and the depolarization of the crossed media, and a rearrangement of the fields in the proximity of the electromagnetic discontinuity created by the interface between the two media (more details are included in the Appendix C). Such a phenomenon usually occurs in the Ultra High Intensity laser/solid interaction: after propagating through the target, the

supra-thermal electrons, cross the target/vacuum interface and emit transition radiation. This radiation depends on the energy of each electron and on the orientation of its trajectory with respect to the interface (Fig. 5.4). Its angular distribution is characterised by a conical lobe, directed forward, in the direction of motion.

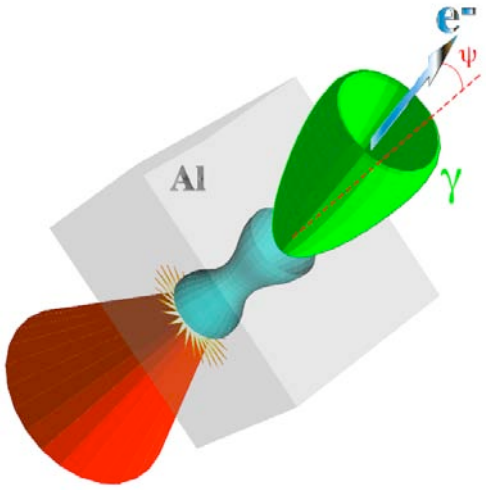

Figure 5.4: Optical Transition Radiation (OTR) emitted at the rear side of targets irradiated by laser pulses.

In TW laser-solid interaction, we deal with moderately relativistic electrons. This prevents us from considering the simpler asymptotic approximations (either $\gamma \simeq 1$, or $\gamma \gg 1$) and forces us to use the complete expressions for the spectral density energy, where all the terms (direct, reflected and refracted) are taken into account. Under these conditions[3] the radiation energy distribution from the transition medium $\rightarrow$ vacuum per unit solid angle Ω and per unit wavelength λ, is written according to Wartski [167] (cf. Appendix C):

$$\begin{aligned}\frac{d^2W_{OTR,\parallel}}{d\Omega d\lambda} &= \frac{e^2}{2\pi^2\epsilon_0\lambda^2}\frac{\beta_z^2\cos^2\theta_z|1-\epsilon|^2}{[(1-\beta_x\cos\theta_x)^2-\beta_z^2\cos^2\theta_z]^2\sin^2\theta_z} \\ &\times \left|\frac{(1-\beta_z\sqrt{\epsilon-\sin^2\theta_z}-\beta_z^2-\beta_x\cos\theta_x)\sin^2\theta_z}{(1-\beta_x\cos\theta_x-\beta_z\sqrt{\epsilon-\sin^2\theta_z})(\sqrt{\epsilon-\sin^2\theta_z}+\epsilon\cos\theta_z)}\right. \\ &\quad \left.\frac{-\beta_x\beta_z\cos\theta_x\sqrt{\epsilon-\sin^2\theta_z}}{}\right|^2\end{aligned}$$

[3]For a transition vacuum $\rightarrow$ medium, changing the sign of β_z would be enough.

$$\frac{d^2W_{OTR,\perp}}{d\Omega d\lambda} = \frac{e^2}{2\pi^2\epsilon_0\lambda^2}\frac{\beta_x^2\beta_z^4\cos^2\theta_y\cos^2\theta_z|1-\epsilon|^2}{[(1-\beta_x\cos\theta_x)^2-\beta_z^2\cos^2\theta_z]^2\sin^2\theta_z} \times \frac{1}{\left|(1-\beta_x\cos\theta_x-\beta_z\sqrt{\epsilon-\sin^2\theta_z})(\sqrt{\epsilon-\sin^2\theta_z}+\cos\theta_z)\right|^2}$$

$$\frac{d^2W_{OTR}}{d\Omega d\lambda}\,[\mathrm{J\,sr^{-1}\,m^{-1}}] = \frac{d^2W_{OTR,\parallel}}{d\Omega d\lambda} + \frac{d^2W_{OTR,\perp}}{d\Omega d\lambda} \tag{5.8}$$

indexes $\parallel$ and $\perp$ refer to parallel and perpendicular components to the observation planeand $\epsilon = \epsilon(\lambda)$ is the dielectric function of the medium. As sketched in the Fig. 5.5, ψ is the angle between the electron velocity and the normal to the interface, and φ is the angle between the incidence (defined by velocity and the normal to the interface) and the observation planes. The projections of the electron velocity on our reference system are $\beta_x = \beta\sin\psi$ and $\beta_z = \beta\cos\psi$. Those of the observation direction, defined by the vector $\mathbf{n}$, are $\cos\theta_x = \sin\theta_z\cos\varphi$ and $\cos\theta_y = \sin\theta_z\sin\varphi$. The normalized electron velocity $\beta = \frac{v}{c}$ is related to the relativistic factor γ and the kinetic energy E_{kin} by the usual equations:

$$\gamma = \frac{1}{\sqrt{1-\beta^2}}\ ,$$
$$E_{kin}[\mathrm{keV}] = 511(\gamma-1) \tag{5.9}$$

For a normal incidence on the separation surface ($\psi = 0$) or if the incoming and observation planes are coincident ($\varphi = 0$), the emitted radiation is reduced to its component parallel to the observation plane: $\frac{d^2W_{otr}}{d\omega d\lambda} = \frac{d^2W_{OTR,\parallel}}{d\Omega d\lambda}$. On the other hand, the radiation admits a radial polarization in the plane perpendicular to the particle trajectory. Other than the electron kinetic characteristics, Eq. 5.8 requires the knowledge of the dielectric properties of the crossed medium.

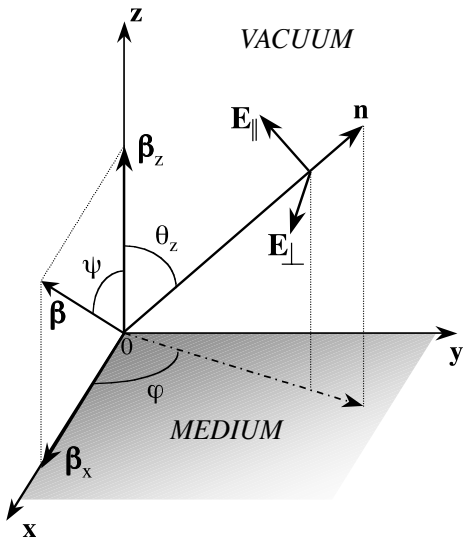

Figure 5.5: Incoming and observation planes and related angles. The incoming charge crosses the interface ($x-y$ plane) at the point 0, forming an angle ψ with the normal to the interface (z axis). The incoming plane is defined by the charge velocity β and the normal to the interface, and the observation plane by the observation direction **n** and the normal to the interface.

Dielectric properties of aluminium The back surface of our targets, was made of either aluminium or Polyethylene Terephthalate (PET). Fig. 5.6 represents the evolution of the refraction index $N(\lambda)$ and the absorption coefficient $K(\lambda)$ of this material (considered at the solid state) [168] as a function of the wavelength and related to the complex dielectric function as follows:

$$\sqrt{\epsilon(\lambda)} = N(\lambda) + iK(\lambda)$$

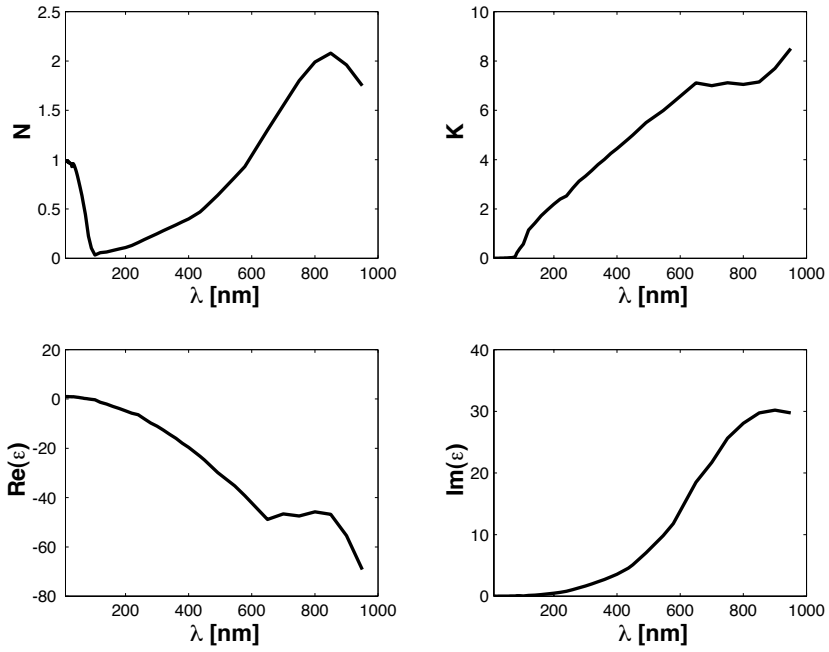

Figure 5.6: Aluminium dielectric properties: refraction index N, absorption coefficient K and the imaginary and real part of the dielectric function, with respect to the wavelength [168].

Transition Radiation produced by one electron

We initially consider the transition radiation emitted by only one electron crossing the steep target/vacuum interface.

Angular dependence of Transition Radiation Figs. 5.7, 5.8 and 5.9 show the angular distribution of the Transition Radiation spectral density (Eq. 5.8) emitted by an electron crossing the aluminium/vacuum interface, for three different values of the kinetic energy (500 keV, 2 MeV and 5 MeV). The three figures correspond to incoming angles ψ of 0°, 20° and 40° respectively.

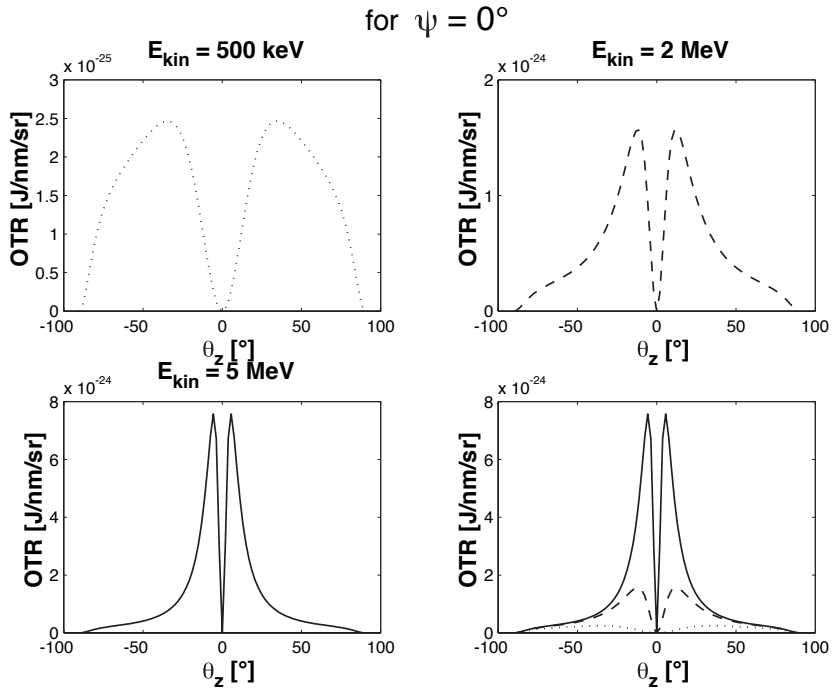

Figure 5.7: Angular distribution of the transition radiation spectral density from an electron (Eq. 5.8) for an incidence angle $\psi = 0$. Calculation was made for $\varphi = 0$, $\lambda = 530\,\mathrm{nm}$ and for three values of the kinetic energy: 500 keV, 2 MeV and 5 MeV. The fourth graph, below on the right, sums up the three others.

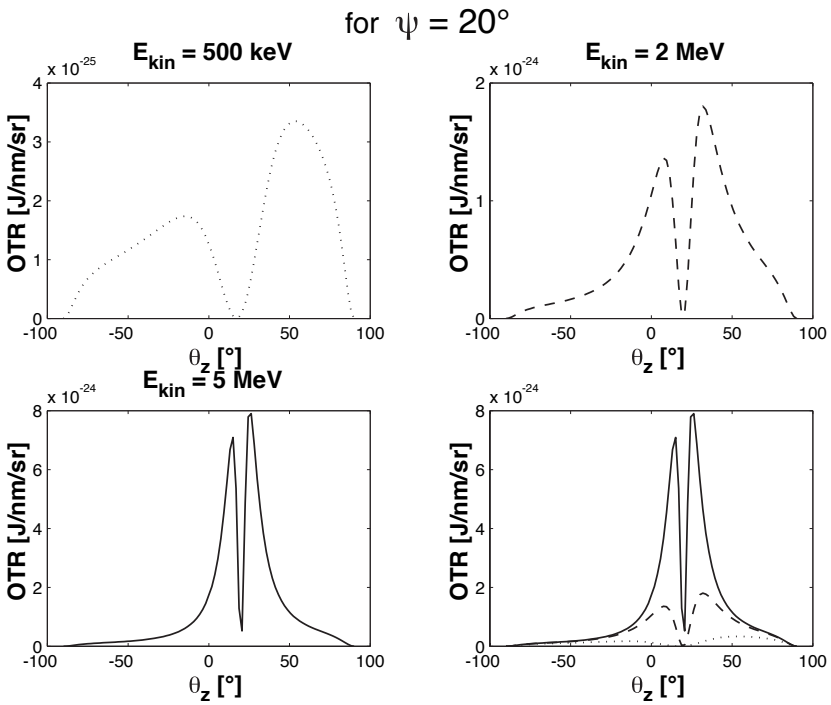

Figure 5.8: Idem Fig. 5.7, but for $\psi = 20°$.

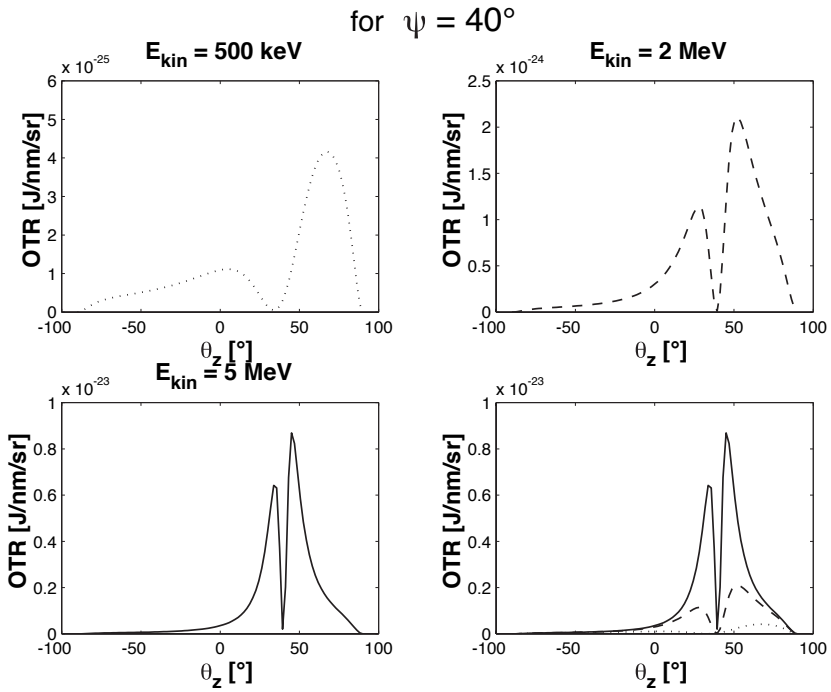

Figure 5.9: Idem Fig. 5.7, but for $\psi = 40°$.

We observe that the higher energy of the incident electron, the more the radiation is concentrated around the direction of its trajectory, but being always zero on this axis. The angular distribution of the radiation is symmetrical if compared to the trajectory for a normal incidence ($\psi = 0$) but becomes asymmetrical for an oblique incidence. Asymmetry grows with the obliqueness of the trajectory. The lower right corner of each of the three figures summarises the angular distributions for the various considered values of kinetic energy: we can note that the intensity maximum grows with the electron energy. This is particularly visible in Fig. 5.10, which corresponds to the case $\psi = 0$, but in logarithmic scale (only one lobe of the radiation is represented there). For a given energy, we find the emission maximum at an angle $\theta\,[\text{rad}] \simeq \gamma^{-1}$ with respect to the trajectory of the particle.

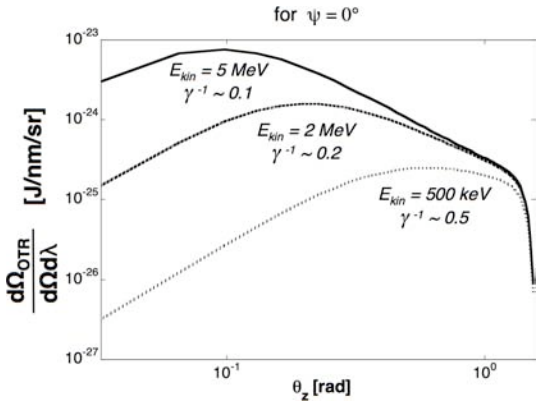

Figure 5.10: Angular distribution of the transition radiation spectral density from an electron (Eq. 5.8) for an incidence angle $\psi = 0$. Identical parameters to those of Fig. 5.7, but in logarithmic scale. Only one lobe of the radiation is represented and the angular scale is in radians.

Even if the transition radiation for very relativistic energies is very peaked, with the maximum at a very small angle, the tail of its angular distribution includes a considerable part of the radiated intensity [169]. As a result, the width (variance) of the angular distribution of the spectral intensity of the emitted radiation is considerably larger than γ^{-1}. Within the limit $\gamma\theta_{max} \gg 1$, where θ_{max} is the aperture of the detection system, it is given by [169]:

$$\begin{aligned} \sqrt{\langle\theta^2\rangle} &\equiv \left(\frac{\int \theta^2 \left(d^2W_{OTR}/d\Omega d\lambda\right) d\Omega}{\int \left(d^2W_{OTR}/d\Omega d\lambda\right) d\Omega} \right)^2 \\ &\approx \frac{\theta_{max}}{\sqrt{2\,\ln(\gamma\theta_{max})}} \end{aligned} \tag{5.10}$$

However, this effect is important only for energies in the range of GeV or higher. In

the range of energy accessible in our experiments, with a maximum value of about some 10 MeV, the effect is attenuated and we can consider that the majority of the radiation is emitted in a cone with an angle of some γ^{-1}[170].

The spatial resolution of OTR emission can be estimated by the Heinsenberg uncertainty principle, which imposes fundamental limitations in the simultaneous measurement of two conjugate Hamiltonian observable variables. For the simultaneous measurement of the radial position Δr and of the emission angle $\Delta\theta$, this principle, here associated to the radiation self-diffraction, becomes[4] :

$$\Delta r\, \Delta\theta \gtrsim \frac{\lambda}{2\pi} \tag{5.11}$$

Taking the maximum angle $\theta \simeq \gamma^{-1}$ for $\Delta\theta$, erroneous considerations established that the maximal spatial resolution of the emitting region is given by $\gamma\frac{\lambda}{\pi}$. For an energy of $\simeq 5$ MeV, the maximal resolution in the optical range would have been $\Delta r \simeq 0.5\,\mu$m. A theoretical study [171] shows that the geometric resolution of the transition radiation is much better, evaluating the radiation angular distribution variance). These considerations are confirmed by several experiments (Orsay, CEBAF, CERN) (see for example [171]).

Spectral dependence of Transition Radiation By integrating the equation 5.8 over the solid angle Ω_{exp} corresponding to our detection system ($f/2$ lens), we obtain the spectral distribution of total emitted energy:

$$\frac{dW_{OTR}}{d\lambda} = \int_{\Omega_{exp}} \frac{dW_{OTR}}{d\Omega d\lambda}\, d\Omega \tag{5.12}$$

Fig. 5.11 (on the left) shows the result of this calculation for the an electron kinetic energy of 5 MeV, in the case of a normal incidence to the interface ($\psi = 0$)[5]. The dependence on $1/\lambda^2$ in Eq. 5.8 is due to the variable change $\omega \to \lambda$ and hides the spectral distribution of the transition radiation as a function of the photon energy $E_{ph} = \hbar\omega = h\frac{c}{\lambda}$. In this case we thus prefer to analyze the curves $\frac{dW}{d\omega}$ as a function of λ (Fig. 5.11 on the right). The spectrum is independent on the wavelength for $\lambda \gtrsim 100$ nm (variation of the energy emitted per unit frequency $\frac{dW}{d\omega} < 1\%$). Below this value the influence of the dielectric permitivity begins to be important (cf. Fig. 5.6), in fact we leave the resonance region, and the refraction index becomes gradually close to 1. As a consequence, the different dielectric behaviour between the medium and the vacuum becomes less distinct and the radiation from the transition is cancelled. For

[4] $\Delta p = \frac{h}{2\pi}\Delta k = \frac{h}{\lambda}\Delta\theta$.

[5] total radiation emitted in the collection angle, slightly depends on ψ.

this reason its spectrum extends only up to frequencies of about $\lambda > \frac{2\pi\, c}{\gamma\omega_{pe}} \sim 80\gamma^{-1}$[nm], in the aluminium case.

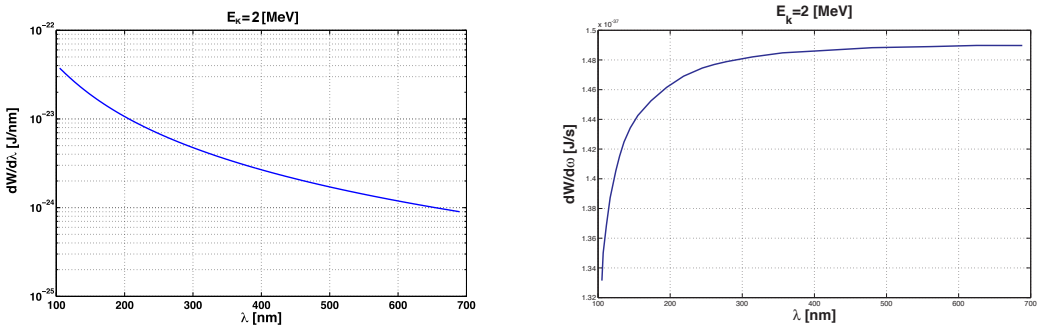

Figure 5.11: Spectral energy density of Transition radiation (in wavelength on the left and in frequencies on the right), produced by one electron (Eq. 5.12) for an incidence angle $\psi = 0$ and a kinetic energy of 2 MeV.

Emitted energy and efficiency of the optical transition radiation In order to make the study of the spectrum of the transition radiation more general, in Fig. 5.12 we estimate the energy radiated per unit wavelength interval as a function of the electron kinetic energy and wavelength, again in the case of a normal incidence ($\psi = 0$) and for the experimental solid angle $f/2$. According to Fig. 5.11 we can see that the emitted spectrum is almost constant in all the visible range we consider.

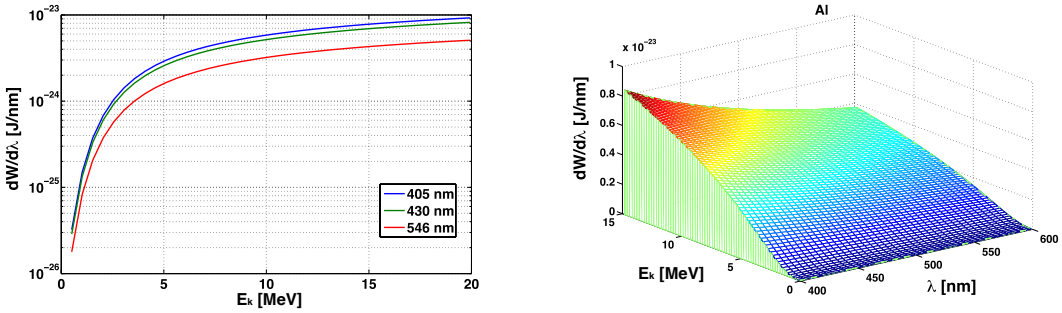

Figure 5.12: On the left: The OTR energy per wavelength unit increases with the electron energy. On the right: OTR energy per wavelength unit emitted in the experimental $f/2$ solid angle, as a function of the wavelength and the electron energy.

The radiated energy grows with the kinetic energy of the incident particle but the growth of the total radiated energy as a function of the incident energy is rather weak

and progressively decrease for $\beta \to 1$. This is related to the fact that we restrict the spectral range to the visible one. If we considered a spectral range extended up to the XUV, i.e., wavelengths of the order of $\sim$ nm, the displacement of the spectral cut can oppose this tendency, according to its $80\gamma^{-1}$[nm] dependence.

Transition radiation produced by an electronic population

In a physical system such as that one created by the interaction of an UHI laser pulse with a solid target, instead of only one electron or of a monokinetic electron beam at the target rear surface, we deal with a population of electrons with a certain energy distribution. We already saw, in Chap. 2, that the energy distribution of the fast electron population, accelerated at the front targets can be described by a Maxwellian distribution [3]. Let us suppose that such a distribution also applies to the rear target side (possibly with a different temperature as compared to the front side[6]:

$$f_\gamma(T_h) = \frac{e^{-\frac{m_0c^2}{T_h}}}{K_1\left(\frac{m_0c^2}{T_h}\right)} \exp\left(\frac{m_0c^2}{T_h}(\gamma-1)\right) \frac{\gamma}{\sqrt{\gamma^2-1}} \tag{5.13}$$

In this distribution, K_1 is the first term of the modified Bessel development [172]. f_γ is normalized as follows:

$$\int_1^\infty f_\gamma \, d\gamma = 1$$

Moreover, the electron beam is characterized by a certain angular divergence, typically with a half angle of about $20-30°$ according to experimental results of emission [54, 152, 173]. Thus, let us consider a Gaussian distribution in ψ:

$$f_\psi(\psi_0) = const_{\psi 0} \exp\left(-\frac{\psi^2}{\psi_0^2}\right) \cos\psi \ , \tag{5.14}$$

[6]Nothing indicates the presence at the rear side of such a distribution, because the electrons are disturbed by collisional and collective mechanisms during their transport in matter. A priori, the Maxwellian distribution at the target back side is valid only for electrons with sufficiently high energy, because they will be practically not sensitive to the deceleration and collisional deviations. In general, in our interaction regime, the total number of such collisional and low energy electrons is rather reduced so that, in first approximation, the collective effects triggered by the return current are also negligible.

where $const_{\psi 0}$ is a constant calculated by imposing $\int_{-\pi/2}^{\pi/2} f_\psi(\psi_0)\, d\psi = 1$. We took $\psi_0 = 20°$. The factor $\cos\psi$ in Eq. 5.14 imposes that the distribution becomes 0 for $\psi = \pi/2$ instead that for $\psi = \infty$. The transition radiation energy per unit solid angle per unit wavelength interval, produced by this electronic population will then be given by:

$$\frac{d^2W_{OTR,\,dist}}{d\Omega d\lambda} = \int_{-\pi/2}^{\pi/2} f_\psi(\psi_0)\, d\psi \int_1^\infty f_\gamma(T_h) \frac{d^2W_{OTR}(\gamma,\psi)}{d\Omega d\lambda}\, d\gamma \tag{5.15}$$

The angular distribution of this radiation is represented in Fig. 5.13 for various temperatures T_h of the electron population[7]. For comparison, the dashed curves in Fig. 5.7 show the result for only one electron with a kinetic energy $E_{kin} = T_h$ and $\psi = 0$.

Having an electronic population with an energy and angular distributions cancels the characteristic lobes of the transition radiation emitted by only one electron. Indeed, by increasing the electronic population temperature T_h, the two lobes gradually get closer. We have no longer a zero in the radiation angular distribution, but rather, for quite low temperatures ($T_h = 500$ keV), a minimum along the symmetry axis of the electronic beam. For hotter populations (case of $T_h = 2\,\mathrm{MeV}$ or $T_h = 5\,\mathrm{MeV}$), because of the radiation spectrum emitted by each electron along the direction of its trajectory, the minimum of the angular distribution is not resolved any more and becomes a maximum. Finally, if the temperature of the electronic population is known, its angular dispersion can be estimated:

- By comparing the value of the axial minimum to the lobes of the radiation angular distribution, in the case of a rather low temperature (so that $\gamma^{-1} \gtrsim \psi_0$ for the majority of the electrons in the distribution). In Fig. 5.14 on the left, we see that for $T_h = 500$ keV, the larger angular dispersion of the electronic beam, the less the minimum of the angular distribution is evident.
- By the width of the radiation angular distribution, if $\gamma^{-1} \lesssim \psi_0$. In Fig. 5.14 on the right, for $T_h = 5\,\mathrm{MeV}$, the width of the radiation angular distribution grows with the angular dispersion of the electrons.

In conclusion, from a deconvolution of the angular distribution of the OTR radiation, one can obtain the angular divergence of the electron beam.

[7]Let us note that this calculation is made for a normalized distribution with only one electron. A result corresponding to the radiation produced by all the population would be given, by supposing a random flux and thus an incoherent emission, by the multiplication of the total number of electrons.

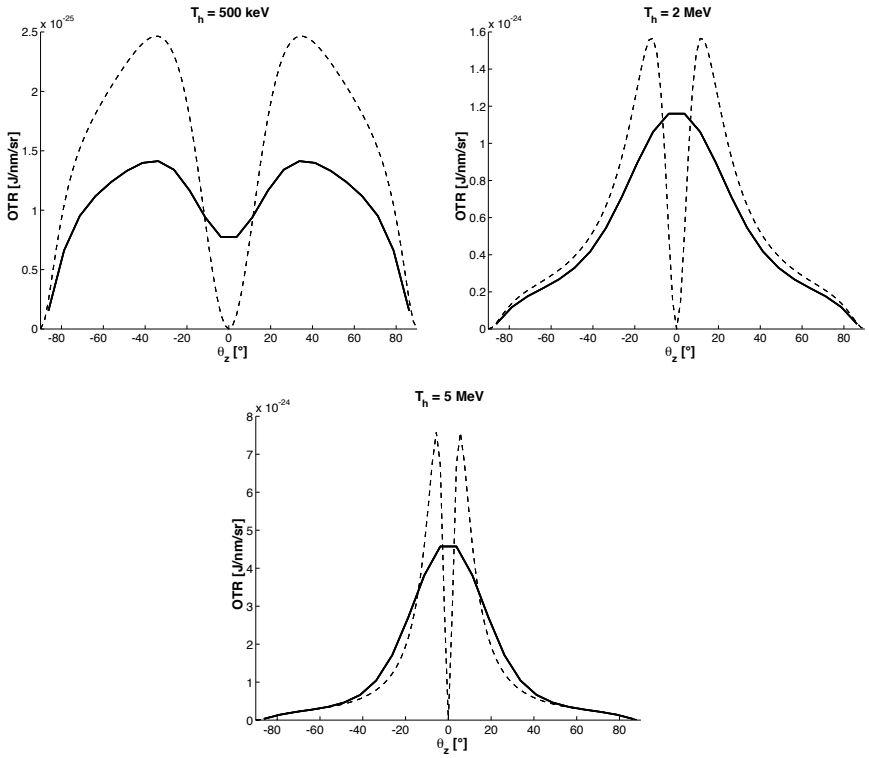

Figure 5.13: Angular distribution of the wavelength spectrum of the transition radiation produced by an electronic population with a Maxwellian energy distribution and a Gaussian distribution for the incidence angle. The figures are compared with the result for only one electron in normal incidence (dashed curves). Calculation has been made for $\varphi = 0$, $\psi_0 = 20°$, $\lambda = 530\,\text{nm}$ and for three different temperatures, 500 keV, 2 MeV and 5 MeV.

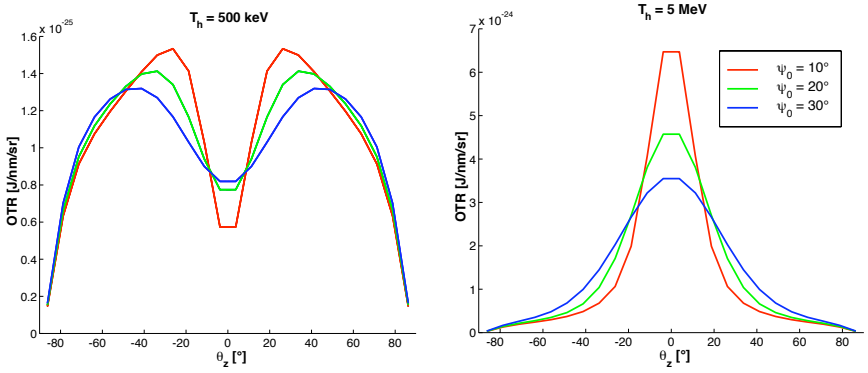

Figure 5.14: Idem Fig. 5.13. For a given temperature of the electronic population ($T_h = 500$ keV on the left, $T_h = 5$ MeV on the right), each curve represents the angular distribution of the transition radiation for three different angular dispersions: $\psi_0 = 10°$, $20°$ and $30°$.

5.2.3 Braking radiation in the potential sheath

The flux of fast electrons, with a density n_f and a temperature T_f, while crossing the target/vacuum interface at the target rear side, leaves behind itself a positive overcharge which creates a space charge field E extending over a distance of about the Debye length, $\lambda_D = \sqrt{\frac{\epsilon_0 T_f}{n_f e^2}}$ [174]. This length is characteristic of the electric shielding of charge density fluctuations in a plasma and is obtained by equating the equilibrium between the Coulomb forces and the thermal agitation [174]:

$$\lambda_D = \frac{T_f}{eE} \tag{5.16}$$

T_f is the temperature of the shielding population. We assimilate the electron beam to a non-neutral plasma with a temperature of the order of the beam average kinetic energy: $T_f \sim \langle E_{kin} \rangle \equiv m_e c^2 (\gamma_f - 1)$. The electrostatic field recalls the electrons towards the target (Fig. 5.15). They are slowed down and, if they are not enough energetic to escape, re-accelered towards the interior of the target. This disturbance in their trajectory could produce a significant radiation emission. We call this phenomenon **braking radiation**.

In order to quantify the energy which could be emitted by this phenomenon we need to estimate the electrostatic field and the trajectory of the electrons in the potential sheath. Concerning the field, we use the simple 1D model presented by Thikhonchuk [96]. Thus, let us consider a fast electron beam (or bunch) which is detached from the target. The field is created by the current surface density $\sigma = e n_f h$, where n_f is the

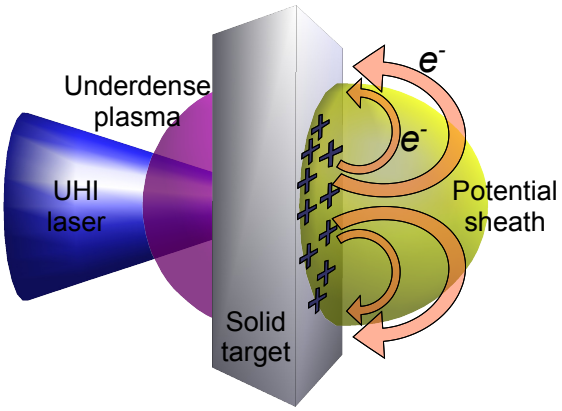

Figure 5.15: Sketch of the electron trajectories in the potential sheath created at the target rear surface. They emit *braking radiation* during their going away and going back towards the target.

beam fast particle density and h is the typical dimension of the electron cloud. We deduce from the *Poisson law*:

$$E \sim \frac{e n_f h}{\epsilon_0} \ ,$$

where h is obtained from the *energy conservation*:

$$\begin{aligned} m_e c^2(\gamma_f - 1) &= \frac{e\,\sigma\,\pi h^2}{4\pi\epsilon_0\, h} \\ T_f &= \frac{e^2 n_f h^2}{4\epsilon_0} \\ \Rightarrow \qquad h &= \sqrt{\frac{4\epsilon_0\, T_f}{n_f e^2}} \end{aligned}$$

the electrostatic field then becomes:

$$E = 2\sqrt{\frac{n_f T_f}{\epsilon_0}} \tag{5.17}$$

Then we take the energy radiated by an accelerated charge per unit solid angle per unit wavelength, given by the expression [97]:

$$\frac{d^2W}{d\Omega d\lambda} = \frac{e^2c^2}{2\epsilon_0\lambda^4}\left|\int_{-\infty}^{\infty} \mathbf{n}\times(\mathbf{n}\times\beta)\, e^{i\frac{2\pi c}{\lambda}\left(t-\frac{\mathbf{n}\cdot\mathbf{r}(t)}{c}\right)}\, dt\right|^2 , \tag{5.18}$$

where $\mathbf{r}$ is the particle position vector in the frame and

$$\mathbf{n} = (\sin\theta\cos\phi, \sin\theta\sin\phi, \cos\theta)$$

The unit vector along the observation direction. In the following, we will consider two approximations for the electron trajectory in the potential sheath formed at the target rear surface:

- The movement will be supposed to be initially mono-dimensional, subjected to a uniform field localised between the surface of the target ($z = 0$) and the position where the electron momentum becomes 0 and the electron changes the direction of motion ($z = z_{max}$). This maximum distance is a function of the electron energy and the electrostatic field intensity. We call the radiation thus calculated, *Bremsstrahlung type* radiation.

- As second approximation, knowing that the detector is placed at a distance from the target much larger than the trajectory dimensions, we will suppose that the electrons describe semicircular trajectories of ray $\rho \sim \lambda_D$ equivalent at the distance defined by their kinetic energy and the space charge field intensity. According to this approximation, we call the radiation thus calculated *Synchrotron type* radiation.

1st approximation: 1D trajectory of a relativistic electron in the presence of a uniform electrostatic field. The *Bremsstrahlung type* radiation

Therefore, let us consider a 1D round-trip movement, under the influence of a uniform electrostatic field, $E = E_z$, the space charge field created by the ejection of fast electrons at the back target surface. Let us also make the assumption that an electron leaves the target rear side ($z = 0$), with an initial velocity β_{0z}. The electron will be slowed down by the field until its velocity becomes 0 ($z = z_{max}$), and will be accelerated in the opposite direction until returning to the initial starting position ($z = 0$). The electron trajectory has been calculated in the Appendix E, thus here we shall restrict ourselves to the 1D case, where the electron trajectory, as a function of time, is defined by the vectors:

$$\mathbf{r}(t) = \big(0, 0, z(t)\big) \,, \tag{5.19}$$

$$\gamma\beta(t) = \frac{\mathbf{p}}{m_e c} = \big(0, 0, \gamma_z\beta_z(t)\big) \,, \tag{5.20}$$

where position $z(t)$ and momentum $\gamma_z\beta_z(t)$ are given by:

$$z(t) = \frac{m_e c^2}{eE}\left(\gamma_0 - \sqrt{1+\left(\frac{p_{0z}-eEt}{m_e c}\right)^2}\right) , \tag{5.21}$$

$$\gamma_z\beta_z(t) = \frac{1}{m_e c}\left(p_{0z} - eEt\right) \tag{5.22}$$

Initial energy and momentum are given, respectively, by: $W_0 = \gamma_0 m_e c^2$ and $p_{0z} = m_e c\sqrt{\gamma_0^2 - 1}$.

The position z_{max} is then:

$$z_{max} = \frac{m_e c^2}{eE}\left(\gamma_0 - 1\right) \tag{5.23}$$

Thus, taking into account the Coulomb character of the braking induced by the positive over charge on the target surface, we shall call the radiation produced according to this model: *Bremsstrahlung type* radiation.

Concretely, being given an electrostatic field E, generated by a fast electron beam with a density n_f and temperature T_f, the reflection distance z_{max} for each electron in the beam is calculated according to the model presented above (Eqs. 5.17 and 5.23) as a function of its kinetic energy. We suppose a beam with a density $n_f \simeq 10^{20}$ cm^{-3} and a temperature $T_f \simeq 1$ MeV (cf. Chp. 3, [96]), leaving the target normally ($\psi = 0$). The electrostatic field thus created is given by Eq. 5.17 and is $E \simeq 1\,\mathrm{MV}/\mu\mathrm{m}$[8]. Fig. 5.16 represents, the maximum braking distance reached by the electron (on the left) and motion duration (on the right), as functions of the electron kinetic energy. We can observe that for an electron with a kinetic energy of $\sim$ 1 MeV, the braking time is of the order of $\approx$ 5 fs, for a distance of about $\approx$ 1.5 μm.

Bremsstrahlung total radiated power Now, if we considered the power radiated per unit solid angle, instead of integrate 5.18 over all the wavelength, we can write [97]:

$$\frac{dP(t')}{d\Omega} = \frac{e^2}{4\pi\, c}\frac{\sin^2\theta}{(1-\beta\cos\theta)^5} \tag{5.24}$$

[8]This value is in agreement with the value deduced from our experimental results analysis (cf. Chap. 3).

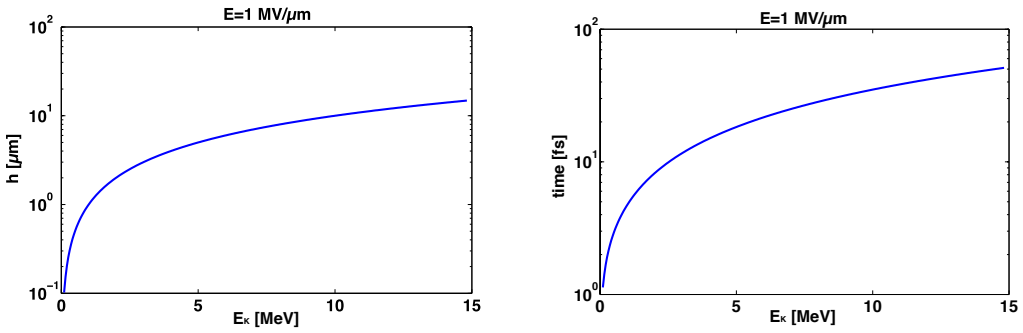

Figure 5.16: A fast electron beam of density $n_f \sim 10^{20}$ cm^{-3} and temperature $T_f \simeq 1\,\mathrm{MeV}$ leaves normally the target back surface. As a function to the electron kinetic energy: the maximum distance reached in the potential sheath (on the left), the braking duration (on the right).

This formula shows that in the relativistic case ($\beta \to 1$), the angular distribution is tipped forward more and more and increases in magnitude with the particle energy. The angle θ_{max} for which the intensity is a maximum is:

$$\theta_{max} = \arccos\left[\frac{1}{3\beta}(\sqrt{1+15\beta^2}-1)\right] \to \frac{1}{2\gamma} \tag{5.25}$$

where the last form is the limiting value for $\beta \to 1$. We can note that the angular distribution is confined to a very narrow cone in the direction of motion. Fig. 5.17 shows this angular distribution. Also, integrating 5.24 over all angles we can obtain the total power radiated:

$$P(t') = \frac{2}{3}\frac{e^2}{c^3}\dot{v}^2\gamma^6 \tag{5.27}$$

Even if this relation is integrated over all angles, for a detection system like ours, with an aperture larger than the emission cone, the power measured in our experimental condition is almost equal to the total real emitted power.

---

[9] Another way to write the power radiated consists in using the momentum variation. In the laboratory frame we have:

$$P = \frac{2}{3}\frac{e^2}{m^2c^3}\left(\frac{dP}{dt}\right)^2 . \tag{5.27}$$

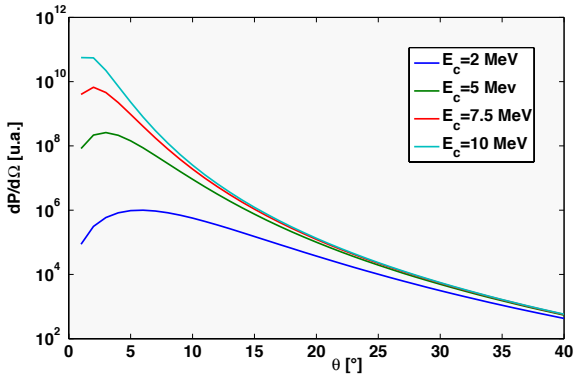

Figure 5.17: Angular distribution of the Bremsstrahlung emission for different electron energies.

Spectral dependence of the *Bremsstrahlung type* emission. The spectral distribution of the energy radiated in our experimental solid angle Ω_{exp} is represented in Fig. 5.18: as a function of the wavelength and initial kinetic energy of the electron (on the left), and as a function of the wavelength and for three different values of the kinetic energy (on the right).

Oscillations of the spectral energy density shown at small wavelengths are associated to the coherence, or rather the incoherence, of the emitted radiation. The coherence length, the distance covered by the electron on which all the emitted radiation remains in phase, is an increasing function of wavelength. Above this length, the radiation alternates constructive and destructive interferences. In our model, more energetic the electrons, more their path is long and more their coherent radiation is confined in long wavelength spectral regions (see Fig. 5.18 on the left). By looking only at the visible spectral band Fig. 5.18 on the right), we see that the energy of the emitted radiation is an increasing function of the electron energy in the coherence region. This law could be no more valid for short wavelengths.

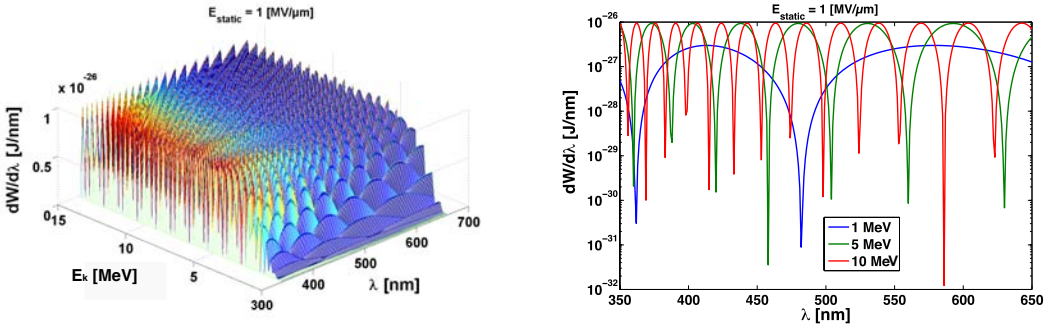

Figure 5.18: Spectral energy density of the *Bremsstrahlung type* radiation, emitted towards the vacuum by one electron (Eq. 5.18) as a function of its kinetic energy. On the right we show the same, restricted to the visible spectral range and for three different values of the kinetic energy, 1 MeV, 5 MeV and 10 MeV. Calculation is made by supposing a particle beam with density $n_f \simeq 10^{20}\,\mathrm{cm}^{-3}$ and a temperature $T_f \simeq 1\,\mathrm{MeV}$, giving an electrostatic field $E \simeq 1$ MV/μm. The signal has been integrated over our experimental $f/2$ solid angle.

2nd approximation: semicirculair trajectory. The *Synchrotron type* radiation

Let us now consider that the trajectory of the electron in the potential sheath at the target rear side is in a plane $x-z$ perpendicular to the target surface. To simplify, let us suppose a semicircular trajectory of curvature ray ρ, described at constant speed. The position and speed vectors of the electron are given respectively by

$$\mathbf{r}(t) = \big(\rho\sin(\omega_s t), 0, \rho\cos(\omega_s t)\big)\ , \tag{5.28}$$

$$\beta(t) = \big(\beta\cos(\omega_s t), 0, -\beta\sin(\omega_s t)\big)\ , \tag{5.29}$$

where $\omega_s = \frac{c\beta}{\rho}$ is the Synchrotron frequency. In this case, the terms intervening in the temporal integral of the expression 5.18 become:

$$\begin{aligned}\mathbf{n}\times(\mathbf{n}\times\beta) &= -\beta\cos(\omega_s t)\,\hat{x}\\ &= -\beta\cos\vartheta\,\hat{x}\ ,\end{aligned}$$

$$\begin{aligned}\phi(t) &\equiv \frac{2\pi c}{\lambda}\big(t-\frac{\mathbf{n}\cdot\mathbf{r}(t)}{c}\big)\\ &= \frac{2\pi}{\beta}\frac{\rho}{\lambda}(\vartheta-\beta\sin\vartheta)\end{aligned}$$

The temporal integral then becomes

$$\int_{-\tau}^{\tau} \mathbf{n} \times (\mathbf{n} \times \beta) e^{i\phi(t)} dt \qquad \rightarrow \qquad \frac{\beta}{\omega_s} \int_{-\pi/2}^{\pi/2} \cos\vartheta e^{iB(\vartheta - \beta \sin\vartheta)} d\vartheta \ ,$$

with $B = \frac{2\pi}{\beta}\frac{\rho}{\lambda}$. We prefer integrate over ϑ between 0 and π, and the spectral density of the energy radiated per unit of solid angle is then given, in this approximation, by:

$$\frac{dW_{sync}(\beta, \rho)}{d\Omega d\lambda} = \frac{e^2 c\rho}{2\epsilon_0 \lambda^4} \left| \int_0^{\pi} \sin\vartheta \, e^{iB(\vartheta - \beta \sin\vartheta)} d\vartheta \right|^2 \tag{5.30}$$

Considering the semicircular trajectory at constant speed taken in this second approximation, we allow ourselves to call the braking radiation thus calculated: *Synchrotron type radiation*. This spectral density of energy depends on the radius of the trajectory ρ, and on the normalized speed β of the particle (cf. Eq. 5.9).

Synchrotron total radiated power We can express the total radiated power per unit of solid angle as [97]:

$$\frac{dP(t')}{d\Omega} = \frac{e^2}{4\pi\, c^3} \frac{|\dot{\mathbf{v}}|^2}{(1 - \beta\cos\theta)^3} \left[1 - \frac{sin^2\theta\, cos^2\phi}{\gamma^2 (1 - \beta\cos\theta)^2} \right] \tag{5.31}$$

We can note that, although the detailed angular distribution is different from the linear acceleration case, a similar relativistic peaking at forward angle is present. More in detail, the lobes do not keep their symmetry around the instantaneous direction of propagation, they also depend on the angle ϕ. In the relativistic limit ($\gamma \gg 1$), the total power radiated can be found by integrating 5.31 over all angles:

$$P(t') = \frac{2}{3} \frac{e^2}{c^3} |\dot{\mathbf{v}}|^2 \gamma^4 \tag{5.32}$$

Furthermore, knowing that for a circular motion, the magnitude of the rate change of momentum (which is equal to the applied force) is:

$$\frac{d\mathbf{p}}{dt} = \gamma\, m \dot{\mathbf{v}} \tag{5.33}$$

Consequently, can be written as

$$P = \frac{2}{3} \frac{e^2}{m^2 c^3} \gamma^2 \left(\frac{d\mathbf{p}}{dt} \right)^2 \tag{5.34}$$

When this is compared to the corresponding result for rectilinear motion (Bremsstrahlung) (Eq. 5.27), we find a factor γ^2 of difference between the two types of acceleration. For a given magnitude of applied force the Synchrotron radiation is a factor of γ^2 larger than with a parallel acceleration. Generally we can consider that the radiation emitted by a relativistic electron moving randomly, is equivalent to the radiation emitted by an electron in circular motion, having the same instantaneous radius of curvature.

Qualitative discussions The Synchrotron radiation is very directional, emitting a great part of energy in the instantaneous direction of propagation of the electron. There are two lobes of emission whose aperture is smaller as the energy of the electron is large. There is also a cut-off frequency starting from which the emitted radiation is negligible. This frequency depends on the energy and on the curvature of the electron. However, this critical frequency largely exceeds the spectral range which interests us $(300 - 600$ nm). For this range the spectral dependence is generally $\sim \omega^{2/3}$. All these aspects are developed in detail in Appendix F.

Spectral dependence of the *Synchrotron type* emission The Synchrotron radiation is very directional, with emission lobes which are mainly directed in the propagation direction of the electron. If the electron leaves the target with a quasi-normal direction, the perpendicular component of the electrostatic field $E_\perp$ is very small (not a very important transverse acceleration), reducing considerably the intensity of the Synchrotron radiation. If the electron trajectory forms an angle $\varphi \neq 0$ with the normal to the target, $E_\perp$ could become sufficiently important to support a strong Synchrotron radiation. Qualitatively, one can say that the Synchrotron emission is as more important as the propagation angle of the electron is large. On the other hand, if the angle φ exceed the aperture of the experimental system, a great part of the energy contained in the emission lobes will be lost. As a consequence, the detection system would be mainly able to detect only the electrons leaving the target under angles smaller than the experimental aperture. In the general expression (see Appendix F) one observe that emitted energy depends on the instantaneous radius of curvature ρ as well as relativistic factor γ. To simplify the calculations one can reduce these two parameters to only one, by writing:

$$F_\perp = eE \sin\varphi \tag{5.35}$$

This is the centripetal force, that curves the trajectory, imposing an instantaneous radius of curvature given by:

$$eE \sin\varphi = \frac{\gamma\, m_e v^2}{\rho} \tag{5.36}$$

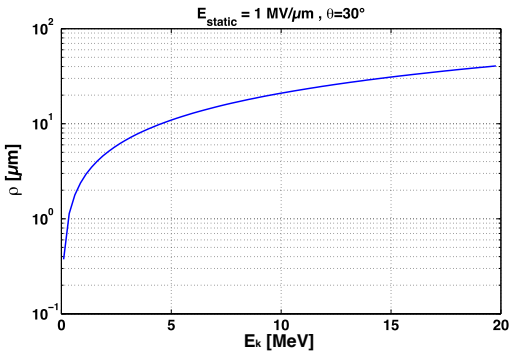

Figure 5.19: Instantaneous radius of curvature as a function of the initial electron energy

Where v is the electron speed. One observes that the radius of curvature increases with the electron energy, as shown in Fig. 5.19. Here, the calculations are made for an initial angle of 30° of the order of what we estimate experimentally (cf. Chap. 3) but larger than the aperture of our detection system ($\approx$ 30°). Normally, this radius of curvature increases with the electron angle (for a given energy), because the centripetal force decreases.

In Fig. 5.20, we represent the differential spectrum of the Synchrotron radiation emitted as a function of the electron kinetic energy, for several wavelengths, and an electrostatic field of 1 MV/μm. The radius of curvature of the trajectory is given by 5.35 and the total solid angle corresponds to our $f/2$ optical system.

Fig. 5.20 (top) shows this dependence for an electron quasi-normal ($\sim 0.5°$) to the target. Emitted energy increases with the electron energy, for all the wavelengths. In the ultra-relativistic energy regime (> 5 MeV), the emitted energy is quasi-constant and the difference between the different wavelengths is of the order of $5 - 20\%$. Below this limit, emission drops suddenly for all the wavelengths.

Fig. 5.20 (bottom) shows the spectral dependence of the Synchrotron radiation emitted for an electron which leaves the target under an angle of $\sim 30°$. We can observe that the emitted energy increases, if compared to the case of the normal trajectories, for relatively small energies, until 5 MeV. Beyond this value there is not a significant difference, when compared to the preceding case. Different spectral components could differ of $\sim 15\%$ in the range of $350 - 600$ nm.

By generalizing the preceding curves in the continuous Visible-UV range, we obtain the 3D representations of the energy emitted per unit wavelength (Fig. 5.21), as a function of the electron energy and wavelength. This energy is integrated over all the solid angle corresponding to the aperture of our $f/2$ experimental system. The direction of the electron can be normal (top) or under an angle of $\sim 30°$ (bottom). We can observe that, for each electron energy, the emitted spectrum can vary according

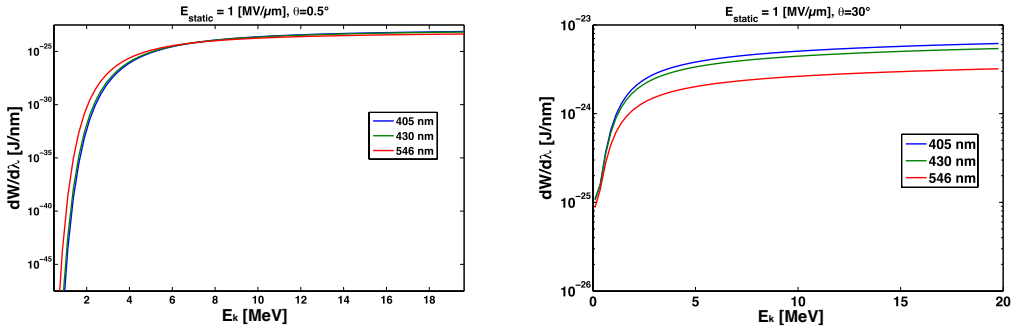

Figure 5.20: The spectral energy density of the Synchrotron radiation increases with kinetic energy of the the electron outcoming under a direction: (top) normal ($\sim 0.5°$); (bottom) of the order of the half-aperture of our detection system ($\sim 13°$).

to various conditions. In the case of Fig. 5.20, this spectrum increases with the wavelength (Fig. 5.20 (top)), for a normal direction of the electron, while for an angle of $\sim 30°$ it decrease with the wavelength (Fig. 5.20 (bottom)).

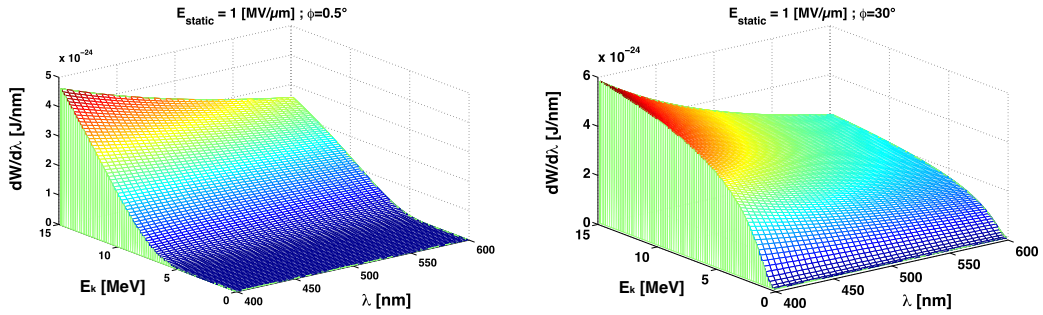

Figure 5.21: Energy emitted per unit wavelength as a function of the electron kinetic energy and wavelength, (top) for an outgoing angle of $\sim 0.5°$; (bottom) for an outgoing angle of $\sim 30°$. The electrostatic field is E_{stat}=1 [MV/ μm].

Even if these figures show the energy emitted by a relativistic charge in circular acceleration, they are still valid also in the case of an unspecified relativistic acceleration, with the instantaneous radius of curvature ρ, knowing that it is always the perpendicular component of the acceleration (Synchrotron) which dominates (by a factor $\sim \gamma^2$) on the longitudinal component (Bremsstrahlung).

5.2.4 Bremsstrahlung radiation due to the electron flux through the matter

The collisions with the atomic nuclei (primarily at the origin of angular deviations), without causing, in our moderately relativistic regime, important energy losses, are nevertheless responsible for the emission of a continuous radiation, the **Bremsstrahlung**.

Let us remember that our diagnostic is restricted to the visible spectral range. In the case of aluminium targets (not transparent to this radiation), we will be able to detect only the Bremsstrahlung produced over a path corresponding to the skin depth at the target back surface, $L_{skin} = \frac{2\pi c}{\omega_{pe}}$. However, in the case of plastic targets (transparent to this radiation), which we have also used, we could collect the Bremsstrahlung generated over all the target traversed thickness. An estimate of total emitted energy will show that this radiation type, in the spectral visible range, is in the aluminium case, negligible if compared to that produced by the above mentioned mechanisms of transition radiation and the Synchrotron radiation and it's of the same order of the collected Bremsstrahlung produced in the potential sheath, while in the plastic case, for enough thick target ($\approx 100\ \mu$m) it's comparable also to the OTR and Synchrotron emissions.

The cross section (energy $\times$ surface) per unit frequency interval of the Bremsstrahlung radiation, produced by the interaction of an incident electron of kinetic energy E_{kin} with a nucleus of charge Ze, is given by [97][10] :

$$\frac{d\chi_{bremss}}{d\omega} \simeq \frac{16}{3}\,\frac{Z^2e^6}{(4\pi\epsilon_0)^3 m_e^2 c^5}\,\frac{1}{\beta^2}\,\ln\left(\frac{(\sqrt{E_{kin}}+\sqrt{E_{kin}-\hbar\omega})^2}{\hbar\omega}\right) \tag{5.37}$$

In the energy range associated with our experiments (from few 100's keV to 10's MeV), we have in the visible range $\hbar\omega \ll E_{kin}$ and we can approximate the logarithm by $\ln\left(4\frac{E_{kin}}{\hbar\omega}\right)$. For an incident electron with a given energy, the Bremsstrahlung radiated energy per unit wavelength, due to its penetration in a medium of density n_i and over a length L_{skin}, is then given by:

$$\begin{aligned}\frac{dW_{bremss}}{d\lambda} &= n_i \Delta x\,\frac{d\chi_{bremss}}{d\lambda} \\ &= n_i \Delta x\,\frac{d\omega}{d\lambda}\,\frac{d\chi_{bremss}}{d\omega}\end{aligned} \tag{5.38}$$

In the aluminium case $\Delta x \simeq L_{skin} \simeq 80\,$nm, $Z = 13$ and electron density $n_i = 5.98 \times 10^{22}\,\mathrm{cm}^{-3}$. Fig. 5.22 represents this differential spectrum in the visible

[10] In order to avoid any confusion with variables related to the braking radiation according to the *Bremsstrahlung type* model, we use here the *bremss* index.

range, for three different values of the kinetic energy and for our collection angle. We see that emitted energy increases slightly with incidental electron energy, still remaining much lower (of a factor about 10^{-4}, than transition or Synchrotron models (cf. Figs. 5.20 and 5.21), but of the same order of the Bremsstrahlung sheath differential spectrum (cf. Fig. 5.18).

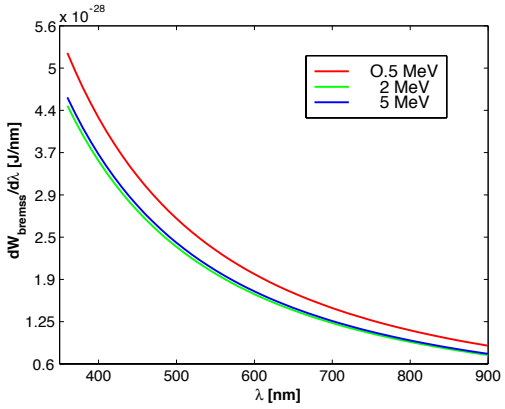

Figure 5.22: Differential spectrum of the Bremsstrahlung radiation emitted in the visible range by an electron propagating through an aluminium plasma over the skin depth $L_{skin} = 80\,\text{nm}$. The curves correspond to three different values of the electron kinetic energy, 500 keV, 2 MeV and 5 MeV.

In the plastic case Δx corresponds to the target thickness $\Delta x = L$, $Z \simeq 6$, $n_i = 8.9 \times 10^{21}$ cm^{-3}, thus giving a flat differential spectrum which for $\Delta x \sim 100\,\mu$m is very similar to the OTR and Synchrotron ones. However, as we will further discuss, in the case of plastic targets another radiation mechanism would be more efficient, also than the Bremsstrahlung: the Čerenkov emission.

We can thus conclude that, within the framework of our diagnostic of the visible emission from the target rear face, the Bremsstrahlung radiation resulting from the electron flux through not transparent solid targets can be neglected, if compared to the other radiation types, like the transition radiation or the Synchrotron radiation in the potential sheath.

5.2.5 Čerenkov radiation

The Čerenkov emission condition is: $\beta^2\epsilon(\omega) > 1$, which can be written in the more transparent form:

$$v > \frac{c}{\sqrt{\epsilon(\omega)}} \tag{5.39}$$

This shows that it is necessary for the speed of the particle to be larger than the phase velocity of the electromagnetic fields at frequency ω in the crossed medium. The energy radiated as Čerenkov radiation per unit distance along the path of the particle is [97]:

$$\left(\frac{dE}{dx}\right) = \frac{(Ze)^2}{c^2}\int_{\epsilon(\omega)>(1/\beta^2)} \omega\left(1 - \frac{1}{\beta^2\epsilon(\omega)}\right)d\omega \tag{5.40}$$

where Ze is the particle charge. For the electron obviously we have $Z = 1$. We can easily obtain the energy emitted per unit distance and wavelength:

$$\frac{d}{dx}\left(\frac{dE}{d\lambda}\right) = \frac{\pi\, e^2}{\epsilon_0}\frac{1}{\lambda^3}\left(1 - \frac{1}{\beta^2 n^2}\right) \tag{5.41}$$

The radiation is evidently not emitted uniformly in frequency. It tends to be emitted in bands somewhat below regions of anomalous dispersion, where $\epsilon(\omega) > \beta^{-2}$. If $\beta \to 1$ this region of anomalous dispersion could be quite extensive. However, in the spectral range of our interest, its spectrum constitutes a continuum in the visible region with a steady increase towards the UV.

Another characteristic feature of Čerenkov radiation is its angle of emission. The angle of emission θ_c of Čherenkov radiation relative to the velocity of the particle is given by

$$\cos\theta_c = \frac{1}{\beta\sqrt{\epsilon(\omega)}} \tag{5.42}$$

the criterion 5.39 can now be rephrased as the requirement $\cos\theta_c < 1$. The Čerenkov radiation is completely linearly polarized in the plane containing the direction of observation and the path of the particle. The emission angle θ_c can be interpreted qualitatively in terms of a *shock* wave front akin to the shock front accompanying supersonic flight. In Fig. 5.23 are sketched two sets of successive spherical wavelets moving out with speed $c/\sqrt{\epsilon}$ from successive instantaneous positions of a particle moving at constant velocity v. On the left v is assumed to be less than, and on the right greater than, $c/\sqrt{\epsilon}$. For $v > c/\sqrt{\epsilon}$ the wavelets interfere so as to produce a *shock* front or wake behind the particle, the angle of which is readily seen to be the complement of θ_c. An observer at rest sees a wave front moving in the direction of θ_c.

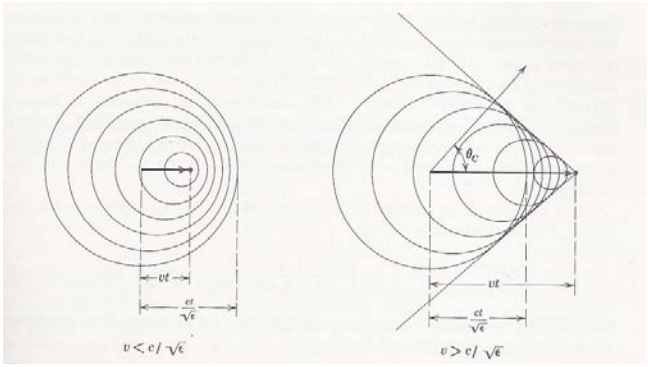

Figure 5.23: Čherenkov radiation. Spherical wavelets of fields of a particle travelling less than and greater than, the velocity of light in the medium. For $v > c/\sqrt{\epsilon}$, an electromagnetic *shock* wave appears, moving in the direction given by the Čherenkov angle θ_c.

In Fig. 5.24, we represent the differential spectrum of the Čherenkov emitted per a path length of 1 μm in our $f/2$ collection angle, in the case of the a plastic transparent medium with a refraction index $n \simeq 1.48$ and for four different values of the electron temperatures. Energy distribution is calculated, as in Sect. 5.2.2 (cf. Eqs. 5.13, 5.14), by using a relativistic 1D Maxwellian energy distribution $f_\beta(T_h)$ and a Gaussian angular distribution $g_\theta(\theta_0)$ normalized to only one electron.

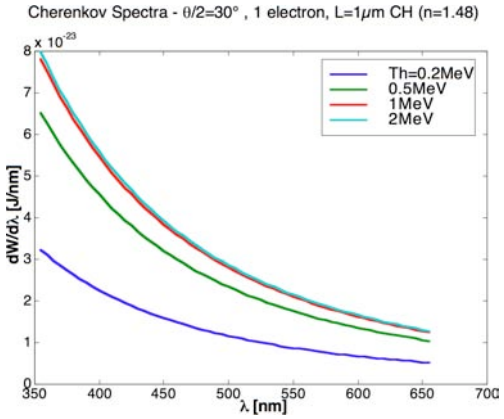

Figure 5.24: Differential spectrum of the Čherenkov radiation emitted in the visible range by an electron distribution normalized to one electron, propagating through an CH target over a 1 μm length. The curves correspond to for different values of the electron kinetic energy, 200 keV, 500 keV, 1 MeV and 2 MeV.

We can see, as expected, that the emitted energy is only slightly sensible to the electron incident energy and the emission wavelength. Let us note that in the case

of plastic targets (transparent to the visible wavelength) the emission per unit path length, being more than 2 order of magnitude larger than the OTR[11] and Synchrotron radiation and five order of magnitude larger than the Bremsstrahlung emission, is clearly the most important emission mechanism[12]. Moreover, let us also to note that Čherenkov radiation, like the Bremsstrahlung one, could be emitted all along the particle path through the target; thus for our thick targets ($\simeq 100\ \mu$m), Čherenkov in plastic could be more than 4 order of magnitude larger than OTR and Synchrotron emissions.

5.2.6 Competition between the different rear target emission mechanisms

In this Section, we considered various radiative phenomena able of explain the bright visible signal observed at the back surface of thin foil targets irradiated by UHI laser pulses, as described further in the Chap. 3. In order to better compare and resume

[11] We can consider that the OTR emission in the case of aluminium target in the visible range is not far from the plastic case. OTR emission is in fact not so sensible to the refraction index n of the different mediums during the transition medium $\rightarrow$ vacuum

[12] Another, more elegant way to compare the effectiveness of the Čherenkov and Bremsstrahlung mechanism in plastic is presented here.

We consider for simplicity sake a nonrelativistic particle and we then put its velocity v to c. In a collision of the electron with velocity v with a ion of a charge Ze, the deviation angle is $\theta = b/b_c$, where b is the impact parameter and $b_c = Ze^2/mv^2$ is the minimum impact parameter. Also, the collision time is $dt = b/v$ and thus, the acceleration is given by: $a = |v - v'|/dt = v\theta/dt$. Finally, the energy emitted in a collision is given by the Larmor formula: $dE_c = e^2a^2dt/c^3 = mv^2/Z(v\theta/c)^3$. Now, by integrating dE_c over all impact parameters we will find the average emitted energy in one collision: $eav = Zr_e^2mvc$, where $r_e = e^2/mc^2$ is the electron classical radius. It is also well known that the bremsstruhlung spectrum is flat and it spreads to the $\omega_{max} \sim 1/dt_{min} \sim v/b_c$. Therefore, the spectral energy is $S = eav/\hbar\omega_{max} = Z^2r_e^2(e^2/\hbar v)$, where $\hbar$ is the Planck constant. For our estimates, by taking $e^2/\hbar v = 0.01$ (that is $v \sim c$) we can see that the spectral energy losses can be estimated rather simple: for $Z \sim 10$ one has $S \sim r_e^2 \sim 10^{-25}$ cm^2. Then over the path length of $L = 100\,\mu$m each electron sees $n_iL = 10^{20}$ ions/cm^2 and the enery loss is $Sn_iL = 10^{-5}$ per electron.

Čherenkov emission intensity produced by a single electron is then: $E_{ch} = e^2k^2L$, where $k = 2\pi/\lambda$ is the photon wavenumber. Thus, for the wavelength of $\sim 1\,\mu$m the spectral energy loss is: $E_{ch}/\hbar k_c = (e^2/\hbar\, c)kL \sim 1$ for $L = 100\,\mu$m. It's thus clear that there is very large difference, of about 5 orders of magnitude between the Bremsstruhlung and the spontaneous Čherenkov emission.

the importance of these different emission mechanisms, we will proceed according to the different material of the target we used: aluminium and plastic.

Aluminium target emission possibilities

- The first possibility is represented by the *thermal radiation* due to the heating induced by the fast electron flux.

  This one was estimated in the range of 10 at 100 eV by a whole of previous experiments [175, 176, 177, 165]. According to a rough model of a static plasma produced at the rear surface, we have found a good agreement with experimental measurements by using a radial dimension for the emitting plasma of the same order of magnitude as the target thickness (ranging between 10 μm and 100 μm), which correspond to dimensions of the laser focal spot and the takes into account the angular dispersion of the electronic beam [133][13].

  We can thus conclude that this radiation mechanism, even if roughly modelled here, could not be neglected for the further analysis of the experimental results.

- The second emission possibility is represented by radiative phenomena connected to the trajectories of the electrons at the target/vacuum interface. The Bremsstrahlung radiation due to the collisions through the material proves to be negligible if compared to the transition radiation or the braking radiation due to the space charge field. Furthermore, concerning the braking radiation mechanisms we have seen how the most efficient one (of about five order of magnitude), for our electron beam parameters, is the *Synchrotron type* emission and we can thus neglect the *Bremsstrahlung type* mechanism.

  In Fig. 5.25, the transition radiation and the radiation of braking radiation (*Synchrotron type*) produced by an electron are compared, in terms of the differential spectrum of the energy radiated and under the same conditions (same electron energy, same optical system collection angle, same frequency). The curves relating to the Synchrotron type radiation are obtained by considering a particle distribution of density $n_f = 10^{20}\,\mathrm{cm}^{-3}$ and temperature $T_h = 1\,\mathrm{MeV}$.

  We can observed that OTR radiation is dominating for energies of the electron exceeding 5 MeV. Also, for energies < 5 MeV we can see that for an electron

[13]This point would be failing if the transport of the fast electrons shows filament structures [125], supporting a faster cooling. This phenomenon is not considered because such a transport was never showed experimentally in conductor targets. In addition, even in numerical simulations the filamentation is important only for *academic* electron beams, monokinetic and with an initial very small angular divergence [125]

in normal incidence, the Synchrotron type radiation becomes negligible if compared to the OTR. However for an out-coming electron with an angle of 30°, the Synchrotron emitted energy becomes larger of a factor $0-2$ than the OTR one. Among the different frequencies there is a maximal difference of $\sim 25\%$ (over the energy range where the Synchrotron radiation is larger than OTR). Furthermore, as we will further discuss in Sect. 7.2.1, in the case of a coherent emission, only the electrons with the energy larger than the temperature distribution (> a few MeV) could contribute effectively. In conclusion, in our experimental conditions the transition radiation mechanism is dominant over the braking emission.

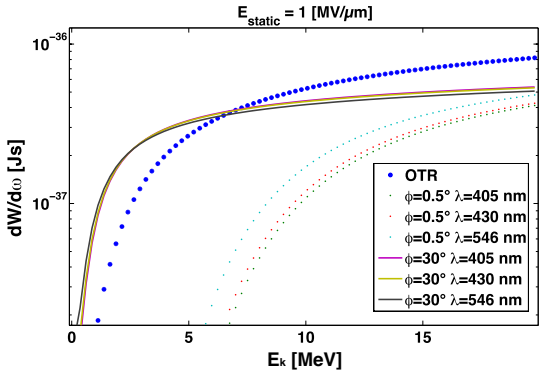

Figure 5.25: Comparison between the transition radiation (point curve) and the Synchrotron type radiation (solid curves) emitted by an electron, for different wavelength and for an electrostatic field of 1 MV/μm. The OTR is mainly dominating, except for the electrons of weak energy leaving under an important angle.

Plastic target emission possibilities

Concerning the discussion we have done in Sect. 5.2.6 concerning the importance of the thermal and emission mechanism is still valid also for the case of plastic targets. In fact, the OTR emission only slightly depends on the refraction index n of the medium and for the thermal emission the difference between an initial cold plastic or aluminium medium is completely negligible. However, in the plastic case the Bremsstrahlung emission due to the fast electron collisions in matter is much larger than in the aluminium case, becoming of the same order of magnitude for enough thickness target. Nevertheless, this striking and obvious difference concerning the Bremsstrahlung emission between aluminium and plastic is not so important for our experimental results, because the Bremsstrahlung radiation remains five order of magnitude smaller than the Čerenkov emission, which is clearly the most important emission phenomenon in

plastic irradiated targets in our detection range.

5.2.7 Radiation produced by an electronic population: possibilities of coherent radiation emission

Until now we have considered, according to certain physical mechanisms, the energy irradiated by only one electron per unit solid angle and unit wavelength:

$$\frac{d^2W}{d\Omega d\lambda}\Big|_{1\,e^-}$$

In the case of a great number of incident electrons[14], the total electromagnetic field measured by a detector is the sum of the individual fields associated to each electron, taking into account the relative phase between them. Whenever the electrons are joined together in the same compact beam, these fields interfere in a constructive way and are added in a coherent way for wavelengths much larger than the beam dimensions. The energy radiated in this spectral range is then proportional to the square of the electron number, N_{el}^2:

$$\frac{d^2W_{coh}}{d\Omega d\lambda} \simeq N_{el}^2 \frac{d^2W}{d\Omega d\lambda}\Big|_{1\,e^-} \tag{5.43}$$

In the laser/solid interaction, the electrons are accelerated during all the laser pulse, $\tau_0 \approx 40$ fs in the case of our experiments, forming a beam roughly of the same duration. On the assumption of a random spatial and temporal distribution, the coherence effect will occur only for wavelengths quite longer than $c\tau_0 \gtrsim 10\,\mu$m, so well beyond the spectral range of our experimental diagnostics. The total radiation thus emitted in the visible range seems to be incoherent: its intensity, given by the sum of the individual intensities, is therefore simply proportional to the electron number:

$$\frac{d^2W_{incoh}}{d\Omega d\lambda} \simeq N_{el} \frac{d^2W}{d\Omega d\lambda}\Big|_{1\,e^-} \tag{5.44}$$

This is true unless the electrons are set out in micro-bunches with a spatial length $c\tau$ close the measured wavelengths. The coherent radiation then emitted by the electrons joined together in such a bunch, will be given by the product of the energy radiated by only one electron with a factor which holds account of the quantity of charge which radiates in phase, in a constructive way:

$$\frac{d^2W_{coh}}{d\Omega d\lambda} = \big|f(\omega)\big|^2 \frac{d^2W}{d\Omega d\lambda}\Big|_{1\,e^-} \tag{5.45}$$

[14]Of the order of 10^{12} in our interaction experiments

The *coherence function* $f(\omega)$ is the Fourier transform of the longitudinal profile (i.e. temporal) of the bunch, $\rho_l(t)$, weighted by its electronic population [178, 179]:

$$\begin{aligned} f(\omega) &\approx P\int_{-\infty}^{+\infty}\rho_L(t)e^{i\omega t}\,dt \\ &\equiv P\tilde{\rho_L}(\omega)\ , \end{aligned} \tag{5.46}$$

where P is the number of electrons in the bunch[15]. We have then:

$$\frac{d^2W_{coh}}{d\Omega d\lambda} \simeq P^2\left|\tilde{\rho_L}(\omega)\right|^2\frac{d^2W}{d\Omega d\lambda}\Big|_{1\,e^-} \tag{5.47}$$

In general, if the divergence and radial dimensions $\rho_T(r)$ of the electron bunch are not negligible (which is clearly our case), the emitted coherent spectrum is thus given by [179]:

$$\frac{d^2W_{coh}}{d\Omega d\lambda} \simeq P^2\,F_L(\omega)\,F_T(\omega,\theta)\,\Psi(\theta)\,\frac{d^2W}{d\Omega d\lambda}\Big|_{1\,e^-}\ ,$$

$$\begin{aligned} \text{where} \qquad F_L(\omega) &\equiv \left|\tilde{\rho}_L(\omega)\right|^2\ , \\ F_T(\omega) &\equiv \left|\tilde{\rho}_L(k)\right|^2\ , \end{aligned}$$

and $\Psi(\theta)$ corresponds to the taking into account of the beam divergence.

A slightly different possibility of a coherent emission in the visible range ($\lambda_{obs} \simeq 1\ \mu$m), will occur if the responsible for the detected radiation is only the fraction ξ of the total electrons of the beam, which satisfies the condition: $\xi\Delta\,x \simeq \xi\,c\tau \simeq 1\ \mu$m.

---

[15]Total radiated filed is

$$E_{tot}(t) = \sum_{i=1}^{P} E(t-\tau_i) \sim P\int d\tau\rho(\tau)E(t-\tau)$$

Then, being radiation intensity at the frequency ω, $I_{tot}(t) = P^2|\rho \circ E|^2$, the signal intensity will be

$$I(\omega) = P^2|\rho(\omega)|^2|E(\omega)|^2 = P^2|\rho(\omega)|^2 I_{1\,e^-}(\omega)\,.$$

Effect of a temporal periodic modulation of the electronic population

Several accelerating mechanisms driven by laser in the relativistic regime, like $\mathbf{J} \times \mathbf{B}$ acceleration or vacuum heating (cf. Chap. 2), can periodically inject very short electron bunches in the targets with intervals of about a laser period. Let us consider δT the injection period of the electrons bunches. This modulation of the electronic distribution, if it is preserved after the crossing of the target, can generate an intense coherent radiation. If $E(t)$ is the field emitted by each package, a whole of N_p packages will produce a total field given by:

$$E_{total} = \sum_{n}^{N_p} E(t - n\delta T) \tag{5.48}$$

The coherent field at the frequency ω is then calculated by the Fourier transform:

$$\begin{aligned} E_{total}(\omega) &\equiv \mathcal{F}\big[E_{total}(t)\big] \\ &= \sum_{n}^{N_p} \mathcal{F}\big[E(t - n\delta T)\big] \end{aligned}$$

Knowing that:

$$\mathcal{F}\big[E(t - n\delta T)\big] = \mathcal{F}\big[E(t)\big] e^{i\omega n\delta T} \ ,$$

the total field transform becomes:

$$\begin{aligned} E_{total}(\omega) &= \sum_{n}^{N_p} \mathcal{F}\big[E(t)\big] e^{i\omega n\delta T} \\ &= E(\omega) \sum_{n}^{N_p} e^{i\omega n\delta T} \\ &= E(\omega) \frac{1 - e^{i\omega N_p \delta T}}{1 - e^{i\omega \delta T}} \\ &= E(\omega) \frac{\sin(N_p \omega \delta T\,/2)}{\sin(\omega \delta T\,/2)} \ , \end{aligned} \tag{5.49}$$

where $E(\omega)$ is the coherent field at the frequency ω due to an individual bunch. The energy radiated by a train of relativistic electron bunches can then be written as:

$$\frac{d^2 W_{coh}}{d\Omega d\lambda}\Big|_{N_p \text{ bunches}} \simeq \frac{d^2 W_{coh}}{d\Omega d\lambda}\Big|_{1 \text{ bunch}} \left(\frac{\sin(N_p \omega \delta T\,/2)}{\sin(\omega \delta T\,/2)}\right)^2 \ , \tag{5.50}$$

the first term is given by Eq. 5.47 and the second results from the coherent addition of the fields generated by each N_p bunch periodically separated by a temporal amount δT. This term reveals peaks with the frequencies:

$$\omega_n = n\frac{2\pi}{\delta T}\ , \quad n = 1, 2, 3, \ldots$$

The coherent energy is negligible for the other frequencies. This effect is illustrated in Fig. 5.26. At bunches with a period $\delta T = \frac{2\pi}{\omega_0}$ correspond peaks to $\omega_0, 2\omega_0, 3\omega_0, 4\omega_0, \ldots$.

In the same way, for $\delta T = \frac{2\pi}{2\omega_0}$ only the even harmonics of ω_0 appear. Calculation was made for $\frac{2\pi c}{\omega_0} = 815$ nm, the laser wavelength in our experiments.

These considerations related to the coherent radiation emission from the target rear surface will be included in Chap. 7, where we will analyze a spectral line of coherent radiation observed at the double frequency of the main interaction laser (see further Fig. 5.26).

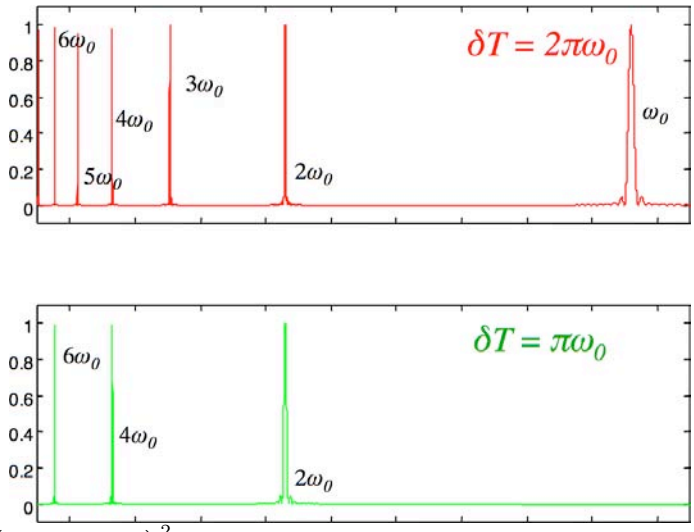

Figure 5.26: $\left(\frac{\sin(N_p\omega\delta T/2)}{\sin(\omega\delta T/2)}\right)^2$ as a function of the wavelength, $\lambda = \frac{2\pi c}{\omega}$, for $\delta T = \frac{2\pi}{\omega_0}$ (top) and $\delta T = \frac{2\pi}{2\omega_0}$ (bottom). Calculation was made for $N_p = 100$. The curves are normalized to the maximum, i.e.,, N_p^2.

Chapter 6

Fast electron propagation in solid targets: experimental results

6.1 Laser facility and experimental configuration

6.1.1 "Salle Jaune" laser system at LOA

The experiment was performed on the "Salle jaune" laser at Laboratoire d'Optique Appliquée, which is an infrared titanium-doped sapphire (Ti:Sa), *p*-polarized laser based on a classical CPA configuration [1]. It is capable of generating 60 TW laser pulses with a FWHM pulse duration of 40 fs [180]. An overall schematic of this laser chain is given in Fig. 6.1.

The laser chain starts from a Ti:Sa self-mode-locked oscillator, which produces a 88 MHz, 300 mW train of laser pulses of 15 fs duration. Each of these pulses is stretched up to 400 ps in an aberration-free stretcher and then injected into an acousto-optic dispersive filter (AOPDF). This permits to actively control the spectral shape and to adjust the spectral phase of the laser pulses. Subsequently, a pulse picker selects single pulses at a repetition rate of 10 Hz. Pockels cells act both as a back reflection isolator as well as a temporal gate which limits the ASE energy. These 1 nJ pulses are first amplified to 2 mJ in a 8-pass preamplifier and then injected into a 5-pass power amplifier to reach an energy of 200 mJ. After each amplification stage the beam is spatially filtered by Air Spatial Filters (ASF) and Vacuum Spatial Filters (VSF) to increase the spatial quality of the laser beam as well as to limit its flux below the damage threshold of the crystal of the third amplification stage. The high

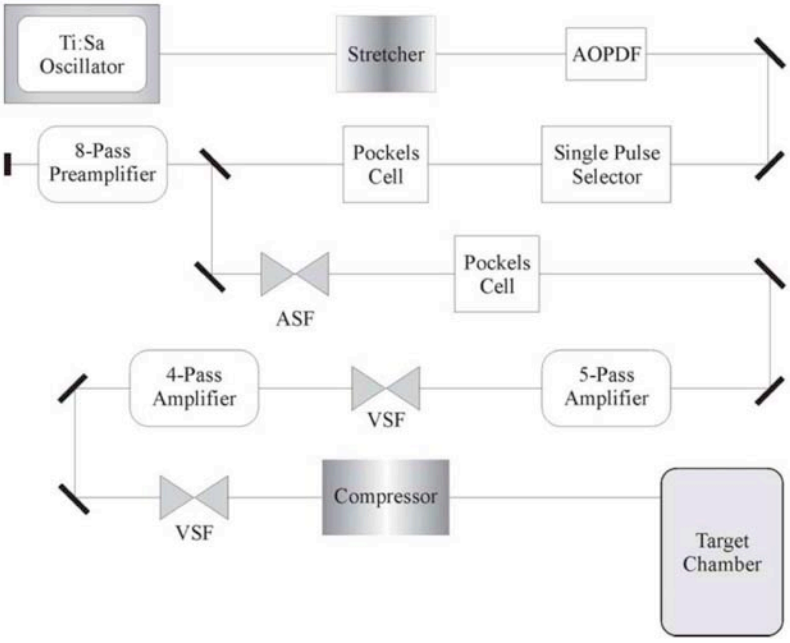

Figure 6.1: Schematic of the "Salle jaune" Ti:Sa laser chain. The single components are briefly described in the text.

power amplifier is cryogenically cooled to cancel the thermal dependence of the laser wavefront and to amplify the laser pulses after four passes up to a routine energy of 2.5 J. Finally, the laser pulses can be re-compressed with a 60% efficiency to 40 fs after four passes on two parallel gratings. For the described experiment, this laser beam was focused down to a focal waist, w_0, of 6 μm using a $f/5$ off-axis parabolic mirror. Table 6.1 gives the typical laser parameters during this experiment.

Laser Wavelength	λ_L	815 nm
Energy on Target	E_L	≤ 1 J
Pulse Length	τ_0	40 fs
Repetition Rate		10 Hz
Waist of Focal Spot	w_0	6 μm
Peak Laser Intensity	I_L	6×10^{19} W/cm^2
Contrast Ratio		$\geq 10^6$

Table 6.1: "Salle jaune" laser parameters for our experiment.

6.1.2 Target configurations

Several types of targets were used in our experiments. They are divided into 3 principal categories: a) thin foils of aluminium, b) polyethylene targets (CH), and c) CH foils with the front or the rear side covered by ultra-thin ($\approx$ 30 nm) aluminium layer, as shown in Fig. 6.2:

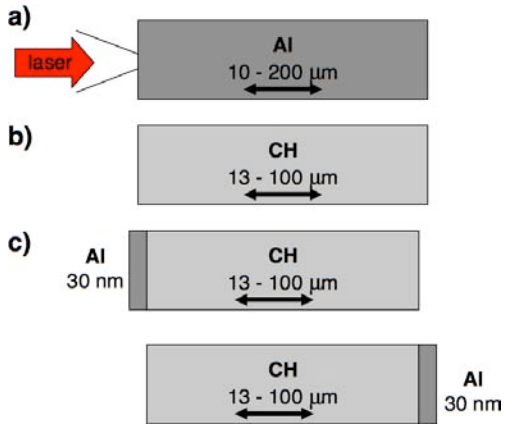

Figure 6.2: Different types of targets used in the experiments. The double arrow indicates a variable thickness.

- **a)** Thin foils of aluminium of variable thickness. This conducting material was selected because of the large number of available experimental data and theoretical models describing its thermodynamic and electric properties (Equation Of State (EOS) at high temperatures and pressures, electric and thermal conductivity).

- **b)** Thin foils of Polyethylene Terephthalate (PET)[1] of variable thickness. This material makes it possible to study the fast electron propagation in a medium which, at least the beginning of the interaction, is an insulator. CH target are also transparent to the emitted visible radiation and are thus suitable for directly following the ionization dynamics produced inside the target by the fast electrons.

  In CH fast electron propagation should be inhibited in comparison with the case of conductors because of the difficulty of establishing a neutralisation current, due to the conductivity of the medium (cf. Chap. 2). Previous experiments led at the LULI laboratory, based to the measure of total K_α output, had already confirmed this assumption [129].

- **c)** Thin foils of Polyethylene of variable thickness with the front or the rear side covered by ultra-thin (≈ 30 nm) aluminium layer. The ultra-thin Al deposition at the front side of the CH target allowed to change the laser interaction conditions on the front side. Furthermore, the possibility of shooting plastic target with the thin Al layer on the rear (thanks to the difference in the refraction index between Al and CH) could provide informations concerning the origin of the emitted signal.

The quantitative analysis of the experimental results of the visible emission from the back side of the targets, developed in Chap. 7, is centered on the images obtained with these three types of solid targets.

In addition, to ensure the integrity of the target rear surface before the passage of the fast electrons, we simulated, using a hydrodynamic code [181], the propagation of the heating front due to the laser ASE. We thus determined a minimal target thickness of $\simeq 30\,\mu$m as a threshold beyond which such effects are negligible (cf. Sect. 7.1).

6.1.3 Rear side optical emission diagnostic

Several details concerning the propagation of the fast electrons in the solid matter remained still badly understood. The purpose of our work was to investigate certain aspects of it, in particular the geometry, the dynamics and the energy distribution of the fast electron beam travelling in the target and the heating of matter induced by the passage of fast electrons. To reach these objectives, we concentrated on the visible radiation emitted by the rear side of solid flat targets (of Al or CH), irradiated by ultra-intense laser pulses.

The fast electron transport versus target thickness has thus been investigated by means of the optical self-emission of the foil rear side, with spatially and spectrally

[1] Its exact chemical formula is $C_2H_4O_4$ but we often refer to this kind of targets as to CH targets.

resolved and time integrated diagnostics. More in detail, the optical radiation of the rear side of the target was collected on axis into an optical spectrometer coupled with an intensified (1024×1024−16 bit) charge couple device (ICCD) camera (see Config. 1). The emitting region was imaged on another ICCD (see Config. 1) or on (256×1024−16 bit) CCD (see Config. 2) camera, selecting two different wavelengths, around 405 nm and 546 nm, with narrow-band interferometric filters ($\Delta\lambda \approx 10$ nm) or around 430 nm and 525 nm, with narrow-band filters ($\Delta\lambda \approx 75 - 90$ nm). These cameras were adequately filtered using BG38 and BG39 filters to suppress the undesirable 815 nm light from the laser beam. The sensitivity of the imaging system was obtained with an absolutely calibrated blackbody radiation lamp (see Appendix G).

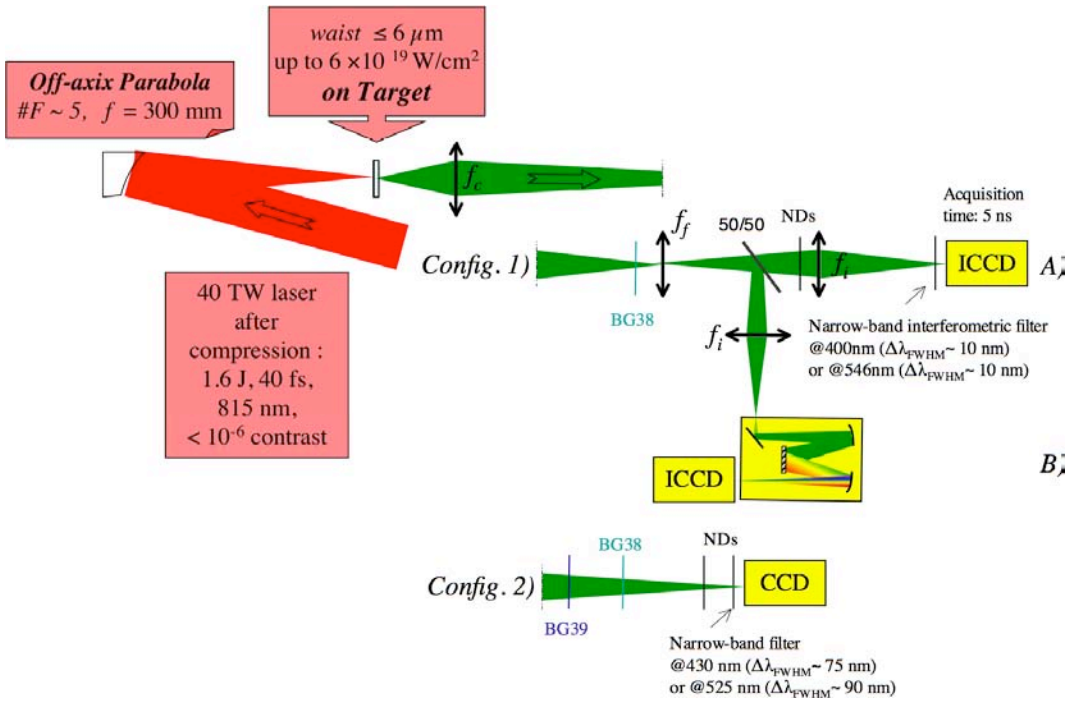

Figure 6.3: Setup of the rear-side emission diagnostic. The emitting region at the back of the targets is directly imaged on a CCD or an ICCD camera (Config. 2 and Config. 1 A), respectively), or on the entry slit of of an optical spectrometer (Config. 1 B)).

6.1.4 Imaging system

The target rear side imaging system need to be as bright as possible and able to produce an image of the emitting region with a rather large magnification ($\approx \times 10 - 15$).

Rear side imaging

One of the optical system adopted (see Config. 1), consisted of three achromatic lenses:

- the first lens, known as *collecting lens*, was placed inside the chamber, under-vacuum, at a distance D from the target, very close to its focal length f_c.
- the two other lenses were placed outside the interaction chamber: a *field lens* of focal distance f_f and an *imaging lens* of focal distance f_i.

Focal lengths and diameters of all the lenses used in the experiment are reported in Tab. 6.2 (all the values are in millimetres).

		f_c	Φ_c	f_f	Φ_f	f_i	Φ_i
Config. 1	ICCD	105-110	50	500	50	500	50
	ICCD + Spectrometer	105-110	50	500	50	100	50
Config. 2	CCD	40	50				

Table 6.2: Focal length and diameter of the achromatic lenses used for the imaging of target rear surface (all the values are in millimeters).

The field lens is needed to reduce the *vignetting* effect on the light beam, which results in a loss of brightness at the edges of an extended source. The field lens forms the image of the collecting lens on the imaging lens, thereby reducing the losses, which now, will be simply due to the limited aperture of the first collecting optics. Indeed, the field lens also acts as spatial filter: the intermediate image of the target produced by the collecting lens on the field lens corresponds, more or less, to the diameter of the last one, and the radiation transmitted to the detectors is thus filtered from that of any other source (from the background light, from parasitic reflections from the interaction chamber walls, ...).

However, in order to avoid a few chromatic effects (aberrations) of this 3 lenses imaging system, when we were more interested in the spatial distribution of the rear side target emission than in its signal intensity, we adopted an optical system (see Config. 2), consisted of only one achromatic lens.

The diagnostic alignment was done by imaging an object placed in the center of the interaction chamber (target position). The target placement before the shots was realized by using an additional CCD camera permanently looking the target chamber centre and analyzing the speckle patterns produced by the targets on the chamber walls

after being irradiated by an alignment He-Ne laser, collinear to the main interaction beam. In addition during few shots we also analyzed the focalisation of the interaction beam by observing the impacts due to low intensity pulses (10 Hz). In order to not have to set the detector alignment during each shot, we fixed the target rear side position along the interaction axis. The position along the interaction axis of the parabolic mirror was set according to thickness of the targets (we considered that this parabola displacement doesn't affect seriously neither the position nor the laser focal spot quality). The total alignment of the targets, interaction beam and diagnostics has been realized with an accuracy of the order of ≈ 30 μm, by supposing that the target rear side emitting region corresponds to the orthogonal projection of the laser interaction spot at the front face.

Solid angle

The collecting solid angle of the rear side emitted radiation is defined, for our experiments, by the opening of the collecting lens (the pupil of the imaging optical system), of diameter ϕ_c and placed at a distance $D \approx f_c$ from the target. The solid angle is then the integral of the spherical bowl defined by a cone whose top coincides with the emissive zone of the target[2] and of half angle at the top $\theta_{max} = \arctan(\phi_c/2D)$:

$$\begin{aligned} \Omega &= \int_0^{2\pi} d\varphi \int_0^{\theta_{max}} \sin\theta \, d\theta \\ &= 2\pi\big(1 - \cos\theta_{max}\big) \end{aligned} \tag{6.1}$$

	Ω [sr]
Config. 1	0.16
Config. 2	0.6632

Table 6.3: Acquisition solid angle of the visible rear side emission for our two different configurations: *Config. 1* and *Config. 2*.

[2]Rigorously, the emissive zone is not reduced to a point, but its dimensions ($\sim 10 - 100\,\mu$m) are much smaller than ϕ_c and D.

The value of the solid angle Ω collecting the visible rear side target emission for our experiment is $\approx 0.16\,[\mathrm{sr}]$ (Config. 1) or $0.66\,[\mathrm{sr}]$ (Config. 2).

Magnification and spatial resolution

The **optical magnification** $\mathscr{M}_{opt}$ on each detector is selected taking into account the desired image type and the available optical elements. Realistic values were established and presented in Tab. 6.4, defining the experimental setup, i.e., the relative distances between each optical elements. The effective magnification, i.e., the relationship between the size of the source and the size of the recorded images, takes into account not only the magnification of the optical imaging system, but also the intrinsic detector magnification. They were experimentally measured with the imaging system installed in two different ways:

- An object with a known dimension in the center of the interaction chamber (target position) was illuminated and imaged on each detector
- An object in the center of the interaction chamber was illuminated and imaged on each detector for two different positions separated of a distance corresponding to a known translation of a calibrated motor (UE31).

We thus deduced the correspondence between μm on the source and *pixels* on the images, this was called **experimental magnification**, $\mathscr{M}_{exp}$ (see Tab. 6.4).

The **spatial resolution** $\Delta\, r$ of our imaging system is limited either by the diffraction limit of the optical system, approximately related to its maximum aperture $\Delta R \sim \frac{\lambda}{2\theta_{max}}$, or, by the pixel size of $\approx 26\,\mu$m (Config. 1) and $20\,\mu$m (Config. 2)), compared to experimental magnification $\mathscr{M}_{exp}$.

The values obtained for the magnification and spatial resolution for each type of diagnostics are presented in table6.4. The size of the images, in *pixels*, is also indicated there (according to the characteristics of the CCD used). All images are recorded with 16bit cameras.

		$\mathscr{M}_{opt}$	$\mathscr{M}_{exp}$	images	res_{exp}
			[μm/px]	$n_{px} \times n_{px}$	[μm]
Config. 1	ICCD	$\times$16.25	1.6	1024×1024	~ 5
	Spectrometer HR2505	$\times$2	–	1024×1024	–
Config. 2	CCD	$\times$11.8	1.7	256×1024	~ 5

Table 6.4: Characteristics of the images recorded with the different detectors used: magnification and spatial resolution.

6.1.5 Optical transmissivity

Each imaging system is characterized by a certain transmissivity, which is the product of the transmissivity of each optical element (achromatic doublets, beam splitters), of the various spectral filters and optical densities used and of the spectral reponse of the various detectors. To protect the detectors against direct laser light, which could seriously damage them, we permanently used BG38 and/or BG39 filters before them.

Fig. 6.4 represents the transmission curves versus the radiation wavelength for one of our experimental configurations, *Config. 1*, corresponding to **a)**, BG38 filters of various thicknesses $\big(T_{BG}(\lambda)\big)$, **b)**, two interferometric filters centered at 405 nm or 546 nm ($T_{filter}(\lambda)$), **c)**, a broad band beam splitter (50/50) ($T_{BS}(\lambda)$) and **d)** neutral optical densities (ND) $\big(T_{ND}(\lambda)\big)$.

In Figs. 6.5 and 6.6 are also represented the transmission curves versus the radiation wavelength for the second of our experimental configurations, *Config. 2*. Fig. 6.5 shows the contribution of the optics and the chamber transparent window ($T_0(\lambda)$), **a)**, two narrowband filters ($T_{filter}(\lambda)$), **b)**, BG38 and BG39 filters $\big(T_{BG}(\lambda)\big)$, **c)** and neutral optical densities (ND) used to attenuate the rear target self emission, according to their thickness $\big(T_{ND}(\lambda)\big)$, **d)**. Fig. 6.6 also shows the total transmission of common optical element in the case of a 430 nm or a GG495 filter (cf. Sect. 6.2.2).

The total spectral response of the optical path represented in Fig. 6.6 is given by

$$T_{total}(\lambda) = T_0(\lambda)\, T_{filter}\, T_{BG}(\lambda)\, T_{ND}(\lambda) \tag{6.2}$$

where $T_{ND}(\lambda) = 1$ in absence of the neutral optical density during the acquisition. All these transmission functions have been measured with a spectrophotometer.

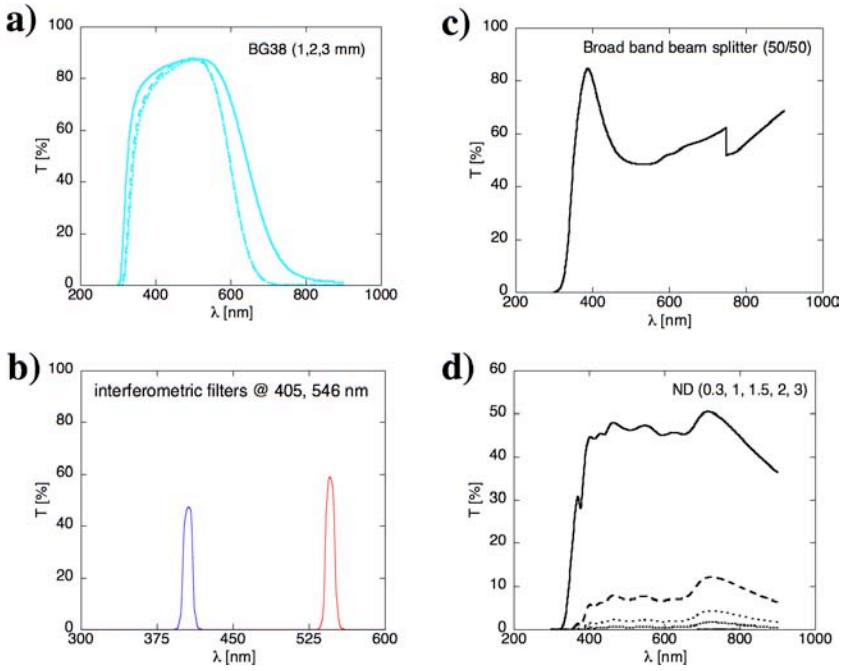

Figure 6.4: Transmission curves of optics and filters used in *Config. 1*: **a)** Transmission of BG38 filters of various thicknesses. Transmission of **b)**, two interferometric filters centered at 405 nm or 546 nm. **c)** Transmission of a broad band beam splitter (50/50). **d)** Transmission of the various Neutral Densities.

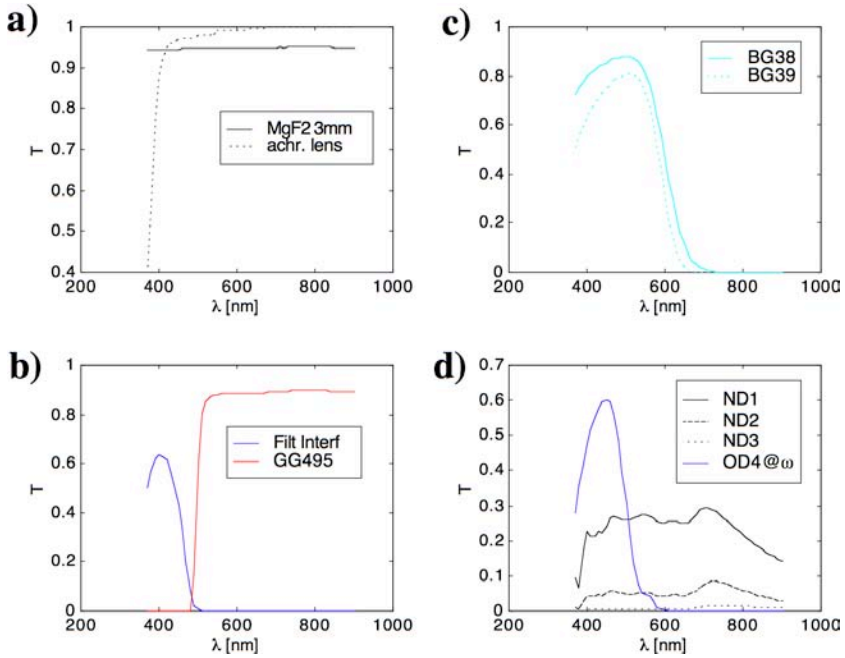

Figure 6.5: Transmission curves of optics and filters used in *Config. 2*: **a)** Transmission of common optical element (3 achromatic lenses+MgF_2). **b)** Transmission of a narrowband filter at 430 nm and of a GG495 filter. **c)** Transmission of BG38 and BG39.**d)** Transmission of the various Neutral Densities.

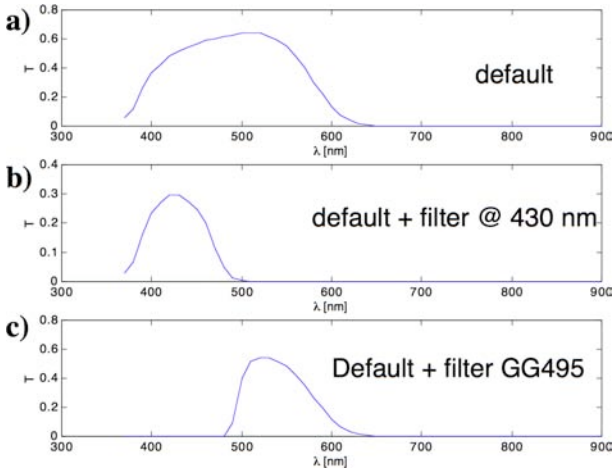

Figure 6.6: **a)** Transmission of common optical element. **b)** Transmission of common optical element using the 430 nm filter. **c)** Transmission of common optical element using the GG495 filter.

6.1.6 Absolute calibration in energy

In order to have an absolute measurement of the energy radiated by the rear surface of the thin foil targets, it is necessary on the one hand, to know the transmissivity of the imaging optical system (already presented in Sect. 6.1.5); and, on the other hand, to measure the relation between the energy collected by the detector and the number of *counts* on the obtained images.

To complete the calibration, it is thus necessary to find the correspondence between energy incident on the chip and the number of *counts* recorded on the CCD (or ICCD) images. The measured value, for the ICCD camera in the Config. 1 A) (without the spectrometer), is (see Appendix G.2.1):

$$\left(\frac{Counts}{Energy}\right)_{ICCD} = 10^{17}\,\text{cts/J}\ , \tag{6.3}$$

for an incoming radiation wavelength of 815 nm, while we have $\approx 5.6 \times 10^{16}$ (cts/J) and $\approx 2.25 \times 10^{17}$ (cts/J) for the signal recorded respectively at 405 and 546 nm (cf. Sect. 6.2).

6.1.7 The optical spectrometer: Spectral resolution

In order to get the spectrum of the visible emission, on several shots, we added an **optical spectrometer** just before the detector (see Fig. 6.3 Config. 1 B)). The emitting region was imaged with a magnification $\approx \times 16.25$ on the entry slit of the spectrometer, typically with an aperture of 100 μm. The spectrometer exit was coupled to an ICCD camera. This configuration made it possible to obtain spectrally resolved images of the target rear side emitting region.

Calibration of the diagnostic with spectral resolution

Here we summarize the obtained calibrations. The methods used are described more in detail in Appendix G. We used an HR2505 spectrometer with 250 mm focal length and a grating groove density of 150 lines/mm coupled to an intensified ($1024 \times 1024 - 16$ bit) (ICCD) camera. The spectrum at the spectrometer output was directly imaged on the chip of the ICCD just behind the spectrometer (see Fig. 6.3 Config. 1 B)). The obtained values are:

- **spectral dispersion**: $\Delta\lambda = 0.677\,\text{nm/px}$
- **spectral resolution**: $res \approx 5\,\text{nm}$

- **spectral response** $\eta(\lambda)$ of the optical system is represented in Fig. 6.7 (cf. Appendix G). In the green ($\approx 546\,\text{nm}$) its value is

$$\eta(\lambda = 546\,\text{nm}) \approx 1.6 \times 10^{17}\text{counts/J} \tag{6.4}$$

After removing the background noise from the images corresponding to the interaction shots (see for example Fig. G.1), we integrate the signal, thus obtaining the curve $C_{shot}(\lambda)$: number of *counts* per pixel of the wavelengths axis. For a given shot, the energy detected per unit wavelength is given by:

$$W_{exp}(\lambda)[\text{Jnm}^{-1}] = \frac{C_{shot}[\text{counts/px}]}{T_{shot}} \frac{1}{\Delta\lambda[\text{nm/px}]} \frac{1}{\eta(\lambda)[\text{counts/J}]} \tag{6.5}$$

where T_{shot} is related to transmission of the filters placed in the optical path during the shot.

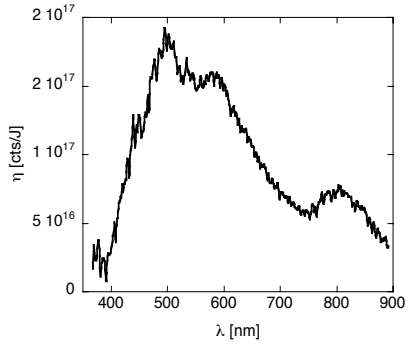

Figure 6.7: spectral response of the optical acquisition system.

6.2 Experimental results

All the experimental results in this section, concern the optical self-emission of the target rear side. These results are divided in relation to the target material: plastic or aluminium.

6.2.1 Experimental results in aluminium targets

These experimental results were obtained using the Ti:Saphire *Salle jaune* laser at Laboratoire d'Optique Appliquée (LOA).

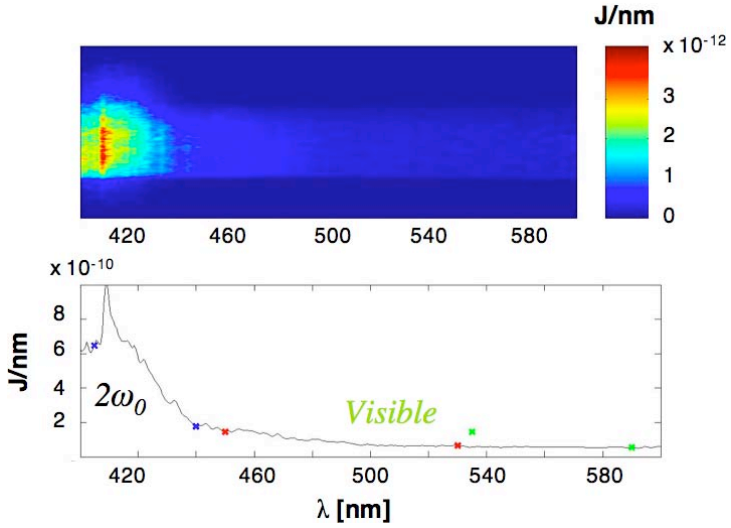

Figure 6.8: Time-gated (5 ns) spectrum at the rear of a 40 μm Al foil target. The spectral resolution of $\sim$ 5 nm is limited by the spectrometer entrance slit.

The optical self-emission of the foils rear side was collected on axis and sent to an optical spectrometer, coupled with an intensified charge coupled device ($1024 \times 1024 -$ 16 bit) (ICCD). It was also directly sent to another ICCD ($1024 \times 1024 - 16$ bit) camera, selecting two different wavelengths, 405 and 546 nm, with narrow-band interferometric filters ($\Delta\lambda \sim$10 nm), as shown in Sect. 6.1.4. These cameras were adequately filtered using a BG38 filter to suppress the undesired 815 nm light from the laser beam. The optical system had $\sim f - f/2$ openings, given by the diameter of the collecting lens. The experimental setup is shown in Sect. 6.1.4. Aluminium flat targets had thicknesses ranging from 10 to 200 μm. This setup allows us to obtain images which are spatially and spectrally resolved and time integrated. The global spectral sensitivity of both systems was measured with an absolutely calibrated blackbody radiation lamp. The acquisition time was limited to 5 ns.

In Fig. 6.8 we present a typical spectrum obtained for a 40 μm Al target and an on-target energy of 0.7 J in 40 fs (FWHM) with a focal spot waist of 6 μm, resulting in a maximal intensity of 6×10^{19} Wcm^{-2}. We can see a spike near 410 nm, the second harmonic of the laser light ($2\omega_0$), clearly distinguishable from the surrounding broad spectrum in the visible region. As already seen in previous experiments [134, 182, 183], and as we will discuss in Chap. 7, this $2\omega_0$ spike can be ascribed to the micro-bunching of relativistic electrons flowing through the targets.

Furthermore, in Fig. 6.9 (left panel) we present the measurements of the rear side emission signal versus Al target thickness for two spectral regions, the $2\omega_0$ region around 410 nm and a visible region between 450 and 550 nm (not related to any harmonic of the laser). These data show how both signals decrease with thickness

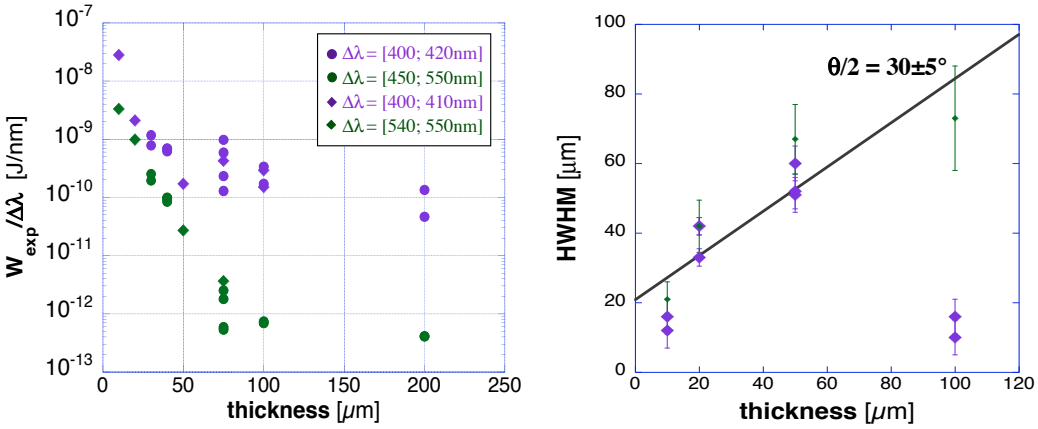

Figure 6.9: Integrated energy per unit of wavelength (left) and emitting region size (HWHM, right). Open purple symbols stand for the $2\omega_0$ signals and full green symbols for the visible signals, circles correspond to the spectral diagnostic and diamonds to the filtered imaging diagnostic (the considered spectral widths are indicated).

but the $2\omega_0$ signal is robust and still intense after a 200 μm thickness. The visible signal, instead, decreases faster. There is a striking difference between targets thinner than 50 μm where the $2\omega_0$ and visible signals have the same order of magnitude, and targets thicker than 50 μm for which the two signals differ by more than two orders of magnitude.

In Fig. 6.9 (right panel) we present the radial width (HWHM) of the emitted signal versus target thickness, still for the same spectral regions. Again, there is a significant difference between the two signals: where the radius of the visible signal grows monotonously, the $2\omega_0$ follows this growth but only until a thickness of 50 μm, and then, for the 100 μm targets, decreases back to the size observed for the thinnest targets. Together with the robustness of the $2\omega_0$ energy level, this is the signature of a relativistic and highly collimated component in the fast electron distribution [122]. With the exception of the $2\omega_0$ signals at 100 μm, the observed width increase quasi-linearly with target thickness (considering both spectral regions) implying an electron beam divergence of $30 \pm 5°$ (half-angle), starting from an initial radius of 15 ± 5 μm, in fair agreement with previous experimental results.

6.2.2 Experimental results in plastic targets

Data with plastic targets have been obtained on the Ti:Saphire *Salle jaune* laser at LOA, too.

The target rear side was imaged on-axis by means of a $\sim f$ optical system on a

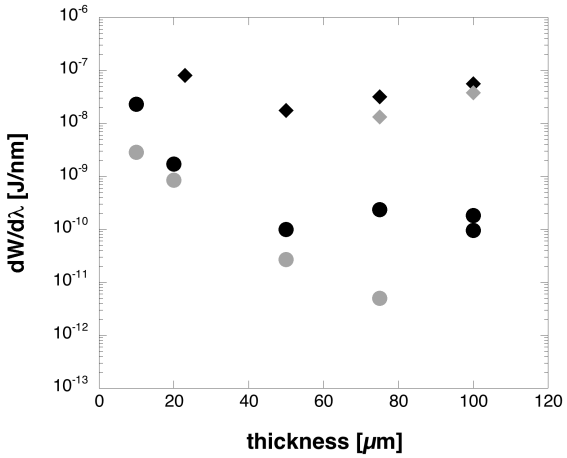

Figure 6.10: Data series for Al (circles) and CH (diamonds) targets for the laser intensity 6×10^{19} W/cm^2. Black symbols stand for the signals around 405 nm and the grey symbols for the signals around 546 nm.

($256 \times 1024 - 16$ bit) CCD or on an intensified ($1024 \times 1024 - 16$ bit) CCD (ICCD) camera as shown in Fig. 6.3 Config. A) and B) of Sect. 6.1.4. These cameras were adequately filtered using BG38 and BG39 filters to suppress the undesirable 815 nm light from the laser beam. In some shots, the spectral window of the camera was limited to a bandwidth of 10 or 90 nm around two wavelengths (405 ± 5 nm and 546 ± 5 nm for Config. A; 430 ± 37 nm and 525 ± 45 nm for Config. B) by using narrow-band filters. The sensitivity of the imaging system was obtained with an absolutely calibrated blackbody radiation lamp. The spatial resolution of the system was $\lesssim 5$ μm.

In Fig. 6.10 we present the measurements of the optical emission for aluminum and plastic targets *vs* the thickness L for two spectral bands: around 405 and 546 nm. These spatially resolved and time-integrated (over 5 ns) results were obtained with full energy shots (~ 0.7 J on target) and narrow-band interferometric filters ($\Delta\lambda \sim 10$ nm) coupled with an ICCD camera (see Fig. 6.3, Config. A)). The signals at both wavelengths are about 100 times more intense in CH than in Al. Also, apart from the range of the thin targets ($L < 50$ μm), for increasing thickness both signals decrease in Al (the 546 signal faster than the 405 nm signal) and increase in CH (with no remarkable difference between the 546 and the 405 nm signals).

In order to more deeply investigate the dynamics of the fast electron transport in dense matter, we also performed a detailed study of the spatial distribution of the rear side target emission. A series of typical optical images are shown in Fig. 6.11 for ~ 0.45 J laser energy on Al and CH targets with thicknesses varying from 10 to 100 μm. A spectral region around 525 nm was selected using a $\Delta\lambda \sim 90$ nm GG495

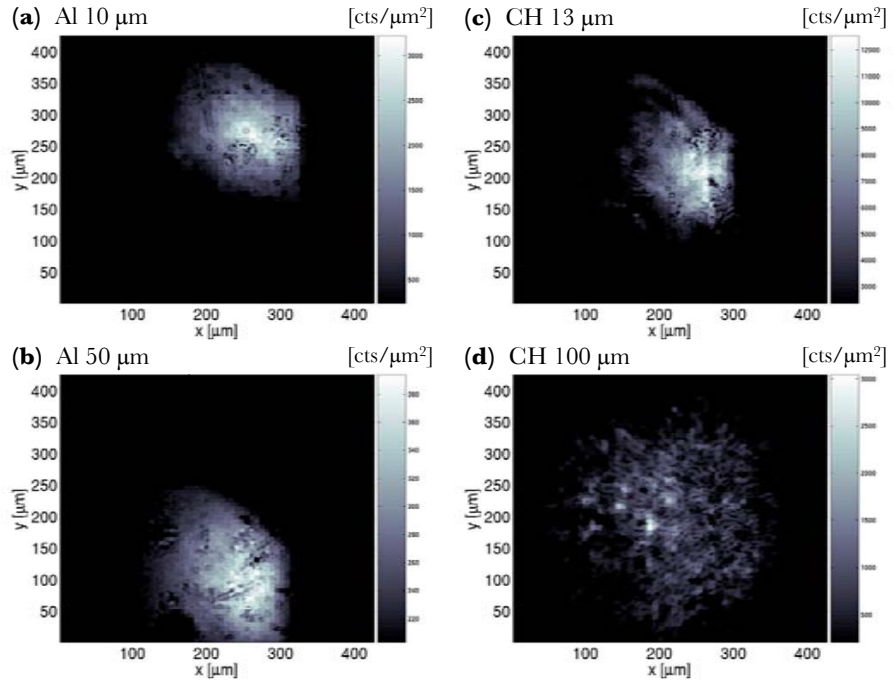

Figure 6.11: Optical emission (counts/μm^2) images obtained using 10 and 50 μm Al [(a), (b)] and 13, 100 μm CH targets [(c), (d)].

SCHOTT filter (see Fig. 6.3, Config. B)).

For thin targets, one observes a striking similarity between Fig. 6.11 (a) (Al) and 6.11(c) (CH). As we will discuss in Sect. 7.1, this is related to the fact that those targets are strongly perturbed by the ASE before the main pulse arrival. This perturbation creates creating similar conditions in both materials for the generation and transport of fast electrons.

However, a significant difference between conductors and insulators can be seen for targets thicker than 30 μm. In Al targets, the signal is spatially homogeneous, there is only a moderate increase in beam size and reduction in signal for larger thickness, as expected. On the contrary, in the CH targets, the electron beam is split into filaments (Fig. 6.11 (d)) with sizes of ~ 13 μm. In the next chapter we will see how, according to analytical predictions [114], this beam filamentation can be related to the instability of the ionization front.

Chapter 7

Fast electron propagation in solid targets: experimental results analysis

In order to explain the experimental results obtained with aluminium and plastic targets, we have to take into account and to model different emission mechanisms. As we have already discussed in Chap. 5 the most efficient phenomena are the Transition Radiation and the Thermal blackbody emission in the aluminium case and the Čerenkov radiation in plastic. However, for both target types we must include a brief description of the laser ASE influence on our experimental results, especially for those obtained with the thinner foil targets.

7.1 ASE influence

In our experiment, the main laser pulse is preceded by a low intensity pedestal, due to the Amplified Spontaneous Emission (ASE). This pedestal, measured with a fast photodiode, has an energy contrast of 10^{-2} (equivalent to an intensity contrast of $\sim 5 \times 10^{-7}$) and arrives ~ 3 ns before the short and much more intense part. Moreover, this pedestal, the intensity of which is of the order 10^{13} W/cm^2, induced a shock wave which propagate trough the target, changing the state of matter (in particular its conductivity) and therefore affecting the propagation of the fast electrons. We have estimated the effects of such a long and intense prepulse in hydrodynamic simulations

performed with the hydrodynamic code MULTI-1D [181, 184]. The propagation of the shock inside aluminium and CH targets of 10 μm is represented in Fig. 7.1. The shock density is represented as a function of the position and time in the target (Lagrangian reference system) for the images [(c), (d)] in Fig. 7.1 and in a Eulerian reference system for the images [(a), (b)].

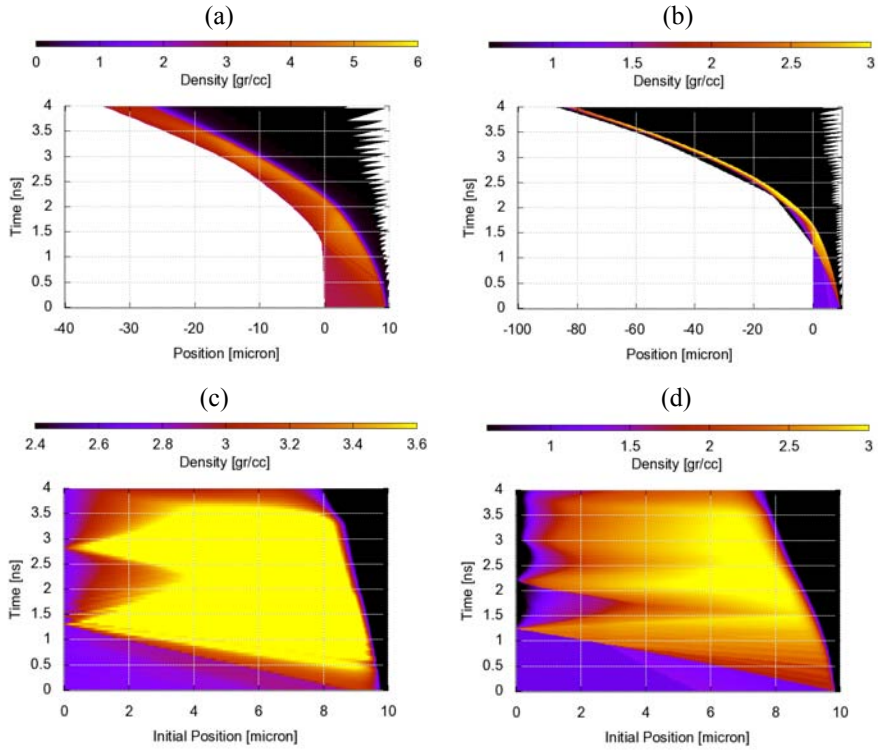

Figure 7.1: 1D Hydrodynamic simulations of the shock due to the pedestal ASE of the laser. The density profile of the shock is traced as a function of time and position for a laser irradiance of 10^{13}W/cm^2 and a total pedestal duration of $\sim$ 3 ns with a rising time of $\sim$ 2 ns. On the top [(a), (b)], the target is aluminium 10 μm and and on the bottom [(c), (d)], is CH of the same thickness.

We can note that after shock breakout, the target is accelerated and might displaced to a distance of a few tens of μm depending on its thickness (i.e. on its mass). In particular, the thinnest 13 μm CH foils move to about 40 μm (see Fig. 7.1 (c))(to be compared with the $\sim$ 100 μm focal depth of the laser beam) before the arrival of the main pulse. Such a motion might change the interaction conditions for thin targets but it should not affect the foils thicker than $\sim$ 30 μm where no shock breakout from rear side is possible before the main pulse arrival. We can also note in Fig. 7.1 [(b), (d)] that this ASE level is sufficient to evaporate $\sim$ 2 μm of material, producing an under-dense

preplasma with a rather long scale length ($> 100\,\mu$m). Moreover, the generated shock wave has a pressure of ~ 1.6 Mbar [185] (See Fig. 7.2) and a propagation velocity of $\sim 10\,\mu$m/ns.

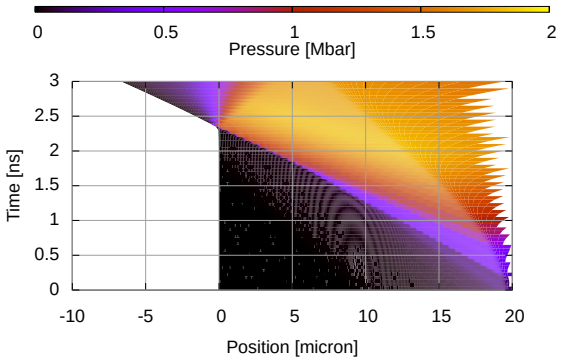

Figure 7.2: The pressure is traced as a function of time and position for an Al target of $20\,\mu$m. The laser parameters are the same of Fig. 7.1.

However, even if ASE influence is important for very thin targets ($\lesssim 30\ \mu$m), we need to consider that these dimensions are of the same order of the laser focal spot ($w_0 \sim\ 10\mu$m) and a consequence we need to take into account also 2D effects concerning the ASE induced shock propagation. We have thus performed some simulations using the 2D hydrodynamic code DUED [186, 187]. In Fig. 7.3 we show the shock density profile at the time $t = 1.2$ and 2.1 ns respectively, before the arrival the main pulse. We can note that the predicted radial spread out of the shock is of the same order of the longitudinal one $\sim 30 - 40\ \mu$m while the longitudinal shock evolution is quite similar to what predicted by the 1D simulations (cf. Fig. 7.1).

Furthermore, in Fig. 7.4 we directly compare the results of 1D and 2D simulations made for the same parameters. The red line corresponds to 1D analytical "local" model obtained by fitting the results of 10 different 1D-Multi runs for 10 different positions in the initial interaction region. The curves have been then overlapped just before the shock breakout at the rear surface of the target and in correspondence to the centre ($r = 0$) of the focal spot. Of course, even if the general shape of the shock is very similar for both case, as expected, the 2D simulation evidences a more evident concavity, due to the 2D effects. Moreover we can note that the shock evolution predicted by the 2D simulations is a little bit slower than the 1D predictions, again in good accord with the lateral spreading phenomenon. As a final consideration we can note that the 2D simulations seem to predict a large expansion of the target also far from $r = 0$, so far from the laser interaction axis. At $r = 40\,\mu$m the target thickness is predicted to be $8\,\mu$m against $6\,\mu$m (corresponding to the un-perturbated target thickness) of the 1D model (red line). Furthermore, 2D simulations seem to suggest a

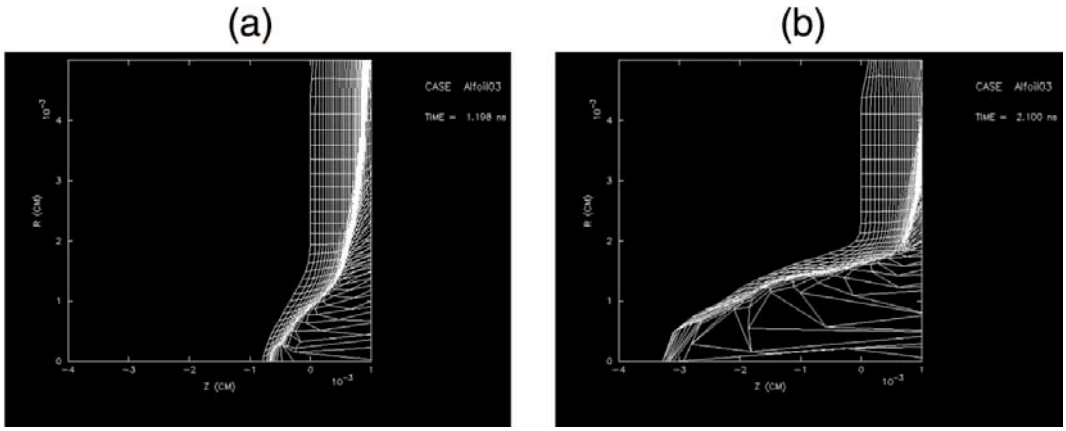

Figure 7.3: Simulations obtained by using the 2D hydrodynamic code DUED. The laser pulse has flat-top profile with an irradiance of 2×10^{13} W/cm^2 and the target is an aluminium thin foil target of 6 μm. The shock propagation is shown after the time $t = 1.2$ ns (on the left) and 2.1 ns (on the right)

.

not so important plasma coronal expansion, not larger than 35 μm. We thought that these 2D predictions could be explained by taking into account the approximations contained in the EOS used for low temperatures and density near to the solid one.

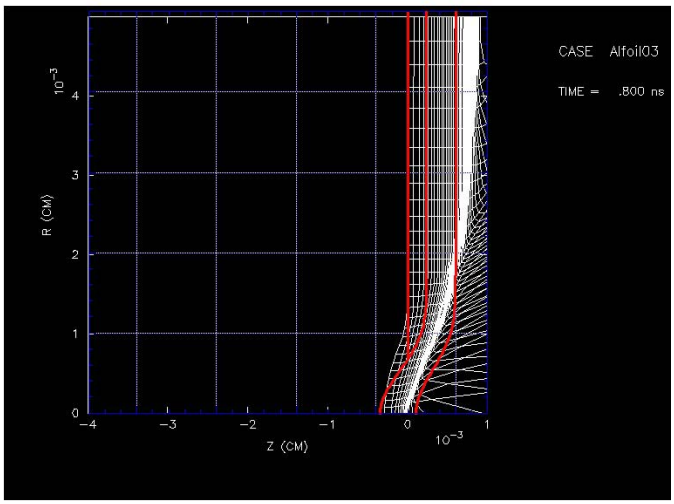

Figure 7.4: Comparison between 1D and 2D simulations made for the same parameters. The laser pulse has flat-top profile with an irradiance of 2×10^{13} W/cm^2 and the target is an aluminium thin foil target of 6 μm. The shock propagation is shown after the time $t = 0.8$ ns. The red line corresponds to 1D analytical "local" model obtained by fitting the results of 10 different 1D-Multi runs for 10 different positions in the initial interaction region.

7.2 Analysis of the experimental results in aluminium targets

7.2.1 Analysis of the experimental results for thick aluminium targets ($L > 30\,\mu$m): Coherent transition radiation (CTR) model

We have seen that our experimental results of the target rear side emission clearly show the presence of a spectral spike at the second harmonic of the laser light ($2\omega_0$), quite distinguishable from the surrounding broad spectrum in the visible region (see Fig. 6.8) and which is robust and still intense also after a 200 μm thickness (see Fig. 6.9). As already seen in previous experiments [134, 182, 155], we think that this $2\omega_0$ peak is ascribed to the micro-bunching of a relativistic electron flux through the targets while the surrounding broad spectrum observed in the visible region (see Fig. 6.8) can either correspond to an incoherent emission mechanism or to the foot of the $2\omega_0$ coherent spike.

In the Chap. 5 we discussed how, when reaching the rear side of the targets and suddenly passing from the solid material to vacuum, each fast electron emits transition radiation [166]. Thus, if the electron bunches are driven at the period δT and if the fast electron population remains periodically bunched after crossing a certain thickness, radiation will add up coherently for wavelengths close to $c\delta T$ and its harmonics (CTR). Furthermore, as we discussed in Chap. 2, this $2\omega_0$ modulation can be associated to different collective accelerating mechanisms: for normal laser incidence into a sharp density gradient the $\mathbf{J}\times\mathbf{B}$ ponderomotive heating [85] inject electrons at $2\omega_0$; for oblique incidence, the vacuum heating [83] or the resonant absorption [75] inject electrons at ω_0 instead. Nevertheless, if the laser power significantly exceeds the critical power for self-focusing, direct laser acceleration can produce fast electrons in betatron resonant bunches at $2\omega_0$ [31]. All these accelerating mechanisms probably operate simultaneously in our experimental conditions, even in the presence of a preplasma, as the target surface density gradient can be steepened by the laser ponderomotive push or by hole-boring, due to the extreme radiative pressure [87, 3] locally creating conditions for oblique incidence. Moreover, PIC Simulations [155, 20, 89] have shown that the average duration of these accelerated electron bunches is around $T_0/10$ with an energy distribution which is well described by a relativistic Maxwellian distribution with a temperature of few MeV.

From this information we can make some assumptions about the fast electrons, in order to analytically model the coherent emission. This model will be compared to our experimental results in order to quantify the various parameters intervening in our calculations.

Hypotheses We suppose that N_b identical electronic bunches are injected perpendicularly into the target front surface, spaced in time of an interval δT (period corresponding to the laser frequency). Each bunch is assumed to have both temporal $\propto e^{-(t/\tau)^2}$ and radial $\propto e^{-(2r/\Phi_0)^2}$ initial gaussian profiles with characteristic widths $\tau = T_0/10$ (according to PIC simulations results [155]) and $\Phi_0 = 30\,\mu$m, the electron source full width evidenced by the experimental data (cf. Fig. 6.9). A radial spreading of electrons during propagation can be considered, according to $\Phi = 2L\,\tan(\theta/2) + \Phi_0$, where L is the foil thickness and $\theta/2$ is the angular divergence half-angle. Each bunch has an initial relativistic Maxwellian energy distribution with temperature T_h, taken as a free parameter.

The spectral density of the detected coherent radiation is proportional to the square of the Fourier transform of the electron flux through the target rear side:

$$W_{coh}(\omega) \propto \left|\mathcal{F}\left[\tilde{j}(t)\right]\right|^2 \tag{7.1}$$

where $\tilde{j}(t)$ is the electron flux through the rear surface at time t. To clarify the effect of the electron bunches on the spectral density, let us begin with the case of only one bunch.

Signal produced by one electron bunch The electrons are supposed to propagate in a ballistic way over a distance corresponding to the target thickness[1]. The temporal spreading of the bunch during the propagation is due to its speed dispersion.

One can consider that, initially, each bunch is composed by an infinity of infinitesimal $\delta(t)$ bunches. These bunches $\delta(t)$ are obviously modulated by the temporal envelope of a bunch with a Gaussian profile. The electrons of each bunch $\delta(t)$ have a Maxwellian velocity distribution, therefore, after crossing a certain thickness z, they will be spread out temporally in the form of a current $\tilde{j}(t)$, according to the electronic temperature and the crossed thickness. The difference in speed at the front surface results in a difference in time of arrival at the rear surface:

$$f_v dv = \tilde{j}(t)dt \qquad \Rightarrow \qquad \tilde{j}(t) = \left|-\frac{z}{t^2}\right| f_v\left(\frac{z}{t}\right) \ , \tag{7.2}$$

where f_v is the velocity distribution[2] and $\tilde{j}(t)$ is the electron flux through the rear surface (i.e., at distance z) at time t, due to a bunch $\delta(t)$ (the velocity dispersion of the injected electron population is transformed into a modulation of the electron flux through the back face).

---

[1] It means that each electron preserves its initial speed (direction and absolute value) during its propagation. This assumption is probably justified for very fast electrons, above a range of MeVs

[2] $f_v = \frac{d\gamma}{dv} f_\gamma = \frac{v}{c^2}\left(1 - v^2/c^2\right)^{-3/2} f_\gamma$ and f_γ is given by Eq. 5.13.

This flux is represented in Fig. 7.5, where the temporal expansion of the electron bunch as a function of the traversed thickness is quite visible. The widening of the electron bunch, which is due, in our model, to the velocity distribution of the injected electrons, results in a dephasing of the fields radiated by each electron and in a reduction in the measured coherent signal, when the traversed thickness is increased.

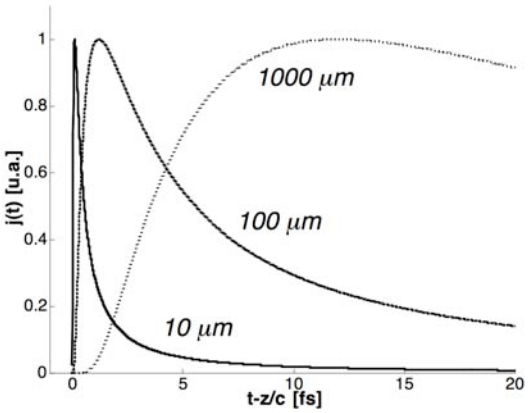

Figure 7.5: Evolution of the electron flux through the rear surface for three different target thicknesses, for an electronic temperature of 2 MeV. Each curve is normalized to its maximum. We can observe that the current is spread out very quickly, proportionally to the thickness. The fastest electrons arrive before, imposing a steep slope on the current. They are then followed by the slowest electrons, constituting the descending current slope.

By using the properties of the Fourier transform, we can study the effect of the electron flow on the produced coherent signal and identify the component of the electron flow, which is mainly responsible for the signal (cf. Eq. 7.1).

In order to find the current created at the back surface by the whole electron bunch, one must integrate the currents $\tilde{j}(t)$ of each $\delta(t)$ previously calculated, taking into account the temporal gaussian profile of the bunch and the differences in the time of arrival:

$$j(t) = \frac{1}{\sqrt{\pi}\tau} \int_{-\infty}^{+\infty} \tilde{j}(t-t') \exp\left(-\left(\frac{t'}{\tau}\right)^2\right) dt' \ . \tag{7.3}$$

The expression of the electric field radiated by an electron bunch at the moment t

is then given by:

$$E(t) = \frac{1}{\sqrt{\pi}\tau} \int_{-\infty}^{+\infty} \tilde{j}(t-t') \sqrt{\eta^*\big(\gamma(t-t')\big)} \, \exp\left(-\left(\frac{t'}{\tau}\right)^2\right) dt' \tag{7.4}$$

where η^* [J/nm] is the spectral energy density emitted by an electron arriving to the rear side at the time $t = z/v$, where z is the target thickness.

The coherent electric field at a given frequency ω is then obtained by the Fourier transform of Eq. D.1 (see Appendix D for the calculation details):

$$E(\omega) = \mathcal{F}\big[\tilde{j}(t)\sqrt{\eta^*(t)}\big](\omega) \, \exp\left(-\frac{\tau^2\omega^2}{4}\right) \tag{7.5}$$

Choice of the rear side emission mechanism: CTR radiation According to the Eq. D.1, the radiated signal depends on the considered radiative mechanism. We saw in Sect. 5.2.6 that, in fact, the visible radiation observed at the back of the targets can be explained either by a braking radiation of the electrons when they re-circulate toward the back of the targets under the action of very strong ambipolar fields, or by a transition radiation (OTR) when they cross the target/vacuum. However, as we will discuss later, the electrons intervening in coherent emission, are mainly those with the higher energy (larger than the temperature of the distribution). We can thus limit ourselves to the OTR mechanism, which as discussed in Sect. 5.2.6, for high energy electrons (> 5 MeV) is the most effective radiation mechanism in aluminium targets.

Furthermore, since high energy electrons are the first to leave the target, there has not yet been time to establish a strong electrostatic field on target rear side. The total number of electrons able to leave the target freely was estimated in experiments to be approximately 10^{11} [188]. According to the theory developed by Tikhonchuk [96], an electron beam with a given energy is detached completely from the matter in spite of the electrostatic attraction, if its total number of electrons is limited to:

$$N_f < (\gamma_f - 1)\frac{2r_0}{r_e} \ ,$$

where $r_e = \frac{e^2}{4\pi\epsilon_0 m_e c^2} \approx 2.8 \times 10^{-9}\,\mu$m is the classical electron radius and r_0 the radius of the beam. Calculations for $\gamma = 10$ (correspondent to a kinetic energy of $\simeq 5\,$MeV) and $r_0 = 15\,\mu\text{m}$[3], yield $N_f \approx 10^{11}$.

[3]Let us suppose that the radial dimension of the bunch is correlated to the dimension of the focal spot of the laser.

Under our the experimental conditions, the OTR spectral energy density is thus given by:

$$\left.\frac{dW_{OTR}}{d\lambda}\right|_{1\,e^-}(\gamma) = \int_0^{2\pi} d\varphi \int_0^{\theta_{max}} \left.\frac{dW_{OTR}}{d\Omega d\lambda}\right|_{1\,e^-}(\gamma)\,\sin\theta\,d\theta \tag{7.6}$$

with $\theta_{max} = \arctan\left(\frac{\phi}{2D}\right) \approx 13°$ and where $\left.\frac{dW_{OTR}}{d\Omega d\lambda}\right|_{1\,e^-}$ is given by the Eq. 5.8.

Thus, the observed spectral density of the coherent OTR is finally written as:

$$W_{coh}(\omega) \propto \left|\mathcal{F}\left[\tilde{j}(t)\sqrt{\eta^*(t)}\right]\right|^2 \exp\left(-\frac{\tau^2\omega^2}{2}\right)$$

where $\eta^* \equiv \left.\frac{dW_{OTR}}{d\lambda}\right|_{1\,e^-}$.

One then speaks of Coherent Transition Radiation (CTR)[4].

Signal produced by periodical electron bunches Here, we are not interested in the exact expression of the field emitted by each bunch (Eq. 7.5), but rather in the collective effect of a whole of bunches separated by δT. Fig. 7.6 corresponds to the case of two successive electron bunches (separated from half of the laser period $\delta T = T_0/2$) with an electronic temperature of 2 MeV. The electron flux (in arbitrary units) through the back surface is presented for three different target thicknesses as a function of the time of arrival to the rear surface $t - z/c$. In addition to bunch widening, a large thickness leads to the overlapping of the bunches and thus to a smaller temporal modulation of the electron flux, producing a decrease in the coherent signal: in Fig. 7.6 (left), the bunches are shown separately and the re-covering of two successive bunches is clearly visible for gradually larger thicknesses; on the right, where the flux resulting from the sum of the two bunches is represented, we can see that its temporal modulation becomes less and less pronounced as the crossed thickness increases. For large thicknesses, only the very high energy tail of each bunch can contribute to the formation of a coherent signal for wavelengths close to $c\delta T$.

Since the N_p bunches are supposed identical and at the origin of a field $E(t)$, the total field is written as:

$$E_{total} = \sum_n^{N_p} E(t - n\delta T) \tag{7.7}$$

[4]It is a phenomenon commonly used as control diagnostics for relativistic beams of particles in linear accelerators [179] or free electron lasers (FEL) [189, 190, 191, 192]

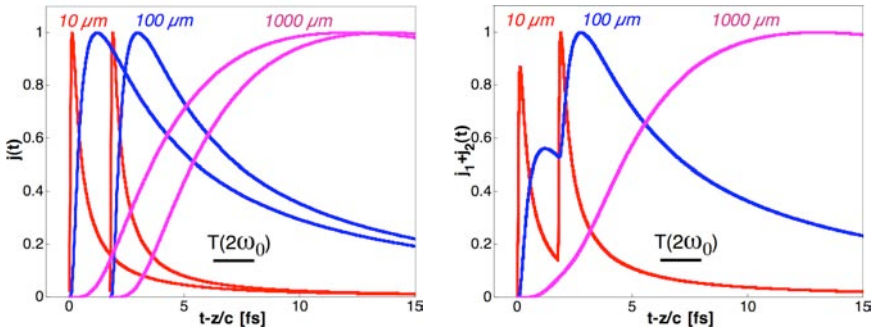

Figure 7.6: Evolution of the electron flux through the target rear surface for three different thicknesses. Results corresponding to two successive bunches separated of $T = \frac{2\pi}{2\omega_0}$ with an electronic temperature of 2 MeV. On right-hand side, the overlapping of the bunches at the rear side increases with the thickness. On left, the total flux for the three thicknesses is represented. Each curve is normalized to its maximum.

To obtain the spectrum emitted by N_p buches we Fourier transform the total electric field, which leads to the expression (cf. Chap. 5):

$$E_{total}(\omega) = E(\omega) t \frac{\sin(N_p \omega \delta T/2)}{\sin(\omega \delta T/2)} \ , \tag{7.8}$$

where $E(\omega) \equiv \mathcal{F}\big[E(t)\big]$ is the Fourier transform of the field due to one bunch only (Eq. 7.5).

Total coherent energy Summing up all the previous consideration, the general formula for the collected coherent energy per wavelength unit at the frequency ω is obtained starting from Eqs. D.1, 7.5 and 7.8:

$$\frac{dW_{coh}}{d\lambda} = P^2 |\mathcal{F}[\tilde{j}(t)\sqrt{\eta^*(t)}]|^2 \exp\left(-\frac{\tau^2\omega^2}{2}\right) \left(\frac{\sin(N_p \omega \delta T/2)}{\sin(\omega \delta T/2)}\right)^2 \tag{7.9}$$

where:

- In the first term, P is the number of electrons per bunch, injected into the target.
- The second term is the absolute squared value of the Fourier transform of the electron flux through the back side, due to a $\delta(t)$ source. The electron flow is weighted by the square root of the spectral density of the energy by an individual electron. As the coherent radiation is produced by the very energy tail of the electronic distribution before a space charge is established, we limit ourselves

to the Optical Transition Radiation, whose spectral density $\eta^* \equiv \frac{dW_{OTR}}{d\lambda}\Big|_{1\,e^-}$ is presented in Fig. 5.12 as a function of the electron energy.

- The convolution with the initial temporal profile ($\propto e^{-(t/\tau)^2}$) is taken into account in the third term.

- The convolution with the final radial profile ($\propto e^{-(2r/\Phi_f)^2}$) is taken into account in the fourth term.

- The last term corresponds to the coherent addition of the fields generated by each N_p bunch. Coherent energy is thus detectable only for harmonics of the injection frequency of the bunches (see Fig. 5.26):

$$\omega_{max} = n\frac{2\pi}{\delta T} \quad n = 1, 2, 3, \ldots$$

Because of the spreading of the bunches during propagation (Eq. 7.2), the intensity of the coherent radiation decreases with the thickness. This variation is due to the fast reduction in the Fourier transform of the electron flux (second term in Eq. 7.9) following the broadening of the peak current $\tilde{j}(t)$ (cf. Fig. 7.5).

Only the initial part of the flux is important with the exception of very thin targets, for which the duration of the signal produced by each bunch (in fact the duration of the bunch flux) is lower than the period of the observed radiation $\frac{T_0}{2} = \frac{2\pi}{2\omega_0} \approx 1.4\,\text{fs}$[5]. Thus, typically, only the electrons with a kinetic energy of the order or higher than the temperature of the electronic distribution can contribute to the signal.

Experimental results *vs* CTR model analysis

In Fig. 7.7 we compare the CTR model results with the experimental signals and we analyse their dependence on target thickness. To model these experimental results with our ballistic model, we assume a bunch injection at half the laser period $\delta T = T_0/2$, over the total laser pulse duration $\tau_0 \approx 40$ fs. This corresponds to the injection of $N_b = \tau_0/\delta T \sim 30$ bunches. However, an injection at $\delta T = T_0$ with $N_b \sim 15$ bunches gives the same result.

As previously discussed, we consider that each bunch has both temporal and radial initial gaussian profiles with characteristic widths $\tau = T_0/10$ and $\Phi_0 = 30\,\mu$m. We also take into account a radial spreading of electrons during propagation, according to $\Phi = 2L\tan(\theta/2) + \Phi_0$, where L is the crossed foil thickness and $\theta/2$ is the angular divergence half-angle. For a given thickness, the following parameters are taken as free parameters:

[5] We suppose $\omega\tau \ll 1$.

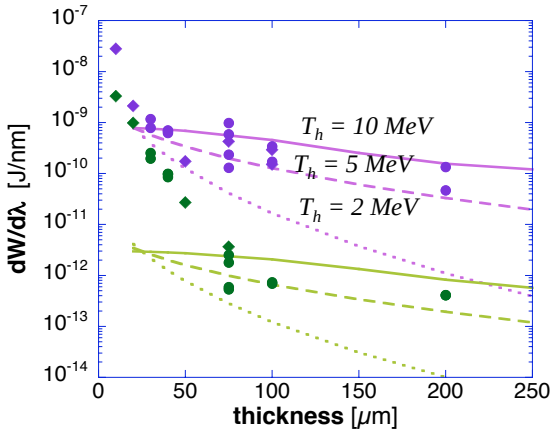

Figure 7.7: Experimental data *versus* the CTR model extimations for $\theta = 0°$ and different temperatures T_h (violet curves stand for $2\omega_0$ and green curves for the *visible* spectral region).

- The temperature T_h of the initial (relativistic Maxwellian) energy distribution of injected electrons. This parameter determines the variation of the signal with the thickness (i.e., the curve shape).
- The number of electrons per bunch P, which determines the amplitude of the signal.

To determine the total coherent energy emitted around $2\omega_0$, Eq. 7.9 (with $\eta^*\big|_{\lambda=405{,}546\,\mathrm{nm}}$, cf. Fig. 5.12) is calculated for various combinations of these parameters and is multiplied by the spectral width $\Delta\lambda_{FWHM} \approx 10\,\mathrm{nm}$. In Fig. 7.7, we compare the results of the CTR model for an highly collimated ($\theta = 0°$), micro-bunched electron population, with the experimental signal *vs.* the target thickness.

The experimental collection angle is taken into account and the divergence was chosen in order to reproduce the behaviour of the $2\omega_0$ HWHM, shown in Fig. 6.9. For $L > 30\,\mu\mathrm{m}$ we can fit the $2\omega_0$ data with an electron population with $T_h \gtrsim 5$ MeV (purple dashed curve). One interesting point is that the visible experimental signals for $L > 75\,\mu\mathrm{m}$ are also well fitted for the same parameters (green dashed curve), indicating that these signals ($\sim$ 100 times weaker) correspond to the foot of the coherent spectral line emitted at $2\omega_0$ rather than being due to an incoherent emission. We can note that the estimated population, involving $\simeq 2\times10^9$ electrons, corresponds to only 0.2% of the laser energy focused on target whereas, for our intensity, the laser energy conversion into fast electrons is about $\eta = 30 - 35\%$ [54, 193].

Concerning the CTR model, it's interesting to note that even for a collimated beam ($\theta = 0°$), taking into account the radial size of the CTR formation region decreases the emitted CTR energy in comparison with that given by a simple 1D propagation (cf. [155]) by at least a factor 2×10^{-2}. Also, as discussed in Sect. 7.2.1, the velocity dispersion progressively destroys the electron current modulation and consequently erases the coherent character of the emitted radiation. This means that to ensure the emission of radiation in a coherent way even after a large crossed thickness L (see $2\omega_0$ signals obtained for $L = 100\,\mu$m), the injected population must still conserve a certain modulation, that is, we need an electron population with a rather small velocity dispersion $\Delta\nu$. That is why we have established the following criterion for the coherent emission of radiation: $\Delta\nu\frac{L}{c} < \lambda_{obs}$, where λ_{obs} is the observed wavelength. $\Delta\nu$ is highly sensitive on the distribution temperature T_h. Thus, for a given initial temperature and divergence angle, this criterion artificially introduces a stopping mechanism for the less relativistic electrons on each bunch during propagation, in order to progressively assure the minimum required velocity dispersion.

Nevertheless our CTR model does not describe the experimental data for thinner targets ($L < 30\,\mu$m), there is a discrepancancy being flagrant in the *visible* region.

7.2.2 Analysis of the experimental results for thin aluminium targets ($L < 30\,\mu$m): resistive heating model

We suppose that such discrepant behaviour observed in thin aluminium targets is due to blackbody radiation from the target's rear side, heated by the intense fast electron jet flux. For our laser intensities ($\sim$ a few 10^{19} W/cm^2) and expected electron energies ($T_h \sim$ a few MeV), the main source is expected to be resistive heating associated with the return current [96]. In order to resolve this collective heating mechanism within the fast electron flux timescale duration ($\sim$ 100 fs) we developed and used a kinetic model.

Fast electron return current In order to characterize the fast electron flux through the target, let us begin with its duration, which we suppose given, for each traversed thickness, by : $t_f = t_{max} - t_{min} = \frac{L}{c}\left(\frac{1}{\beta_{min}} - 1\right)$, where L is the crossed aluminium thickness and β_{min} corresponds to the slower electrons ($E_{min} \sim 100$ eV) taken into account in our calculation. We consider a number of iterations of the order of $\sim 10^5$, sufficiently to acheive $\int f_\gamma, d\gamma = 1$ numerically (cf. Sect. 5.2.2). Thus for each target thickness L we have a radial dimension of the heated surface $r_f = \Phi_0 + L\tan\theta$ and

then a fast current density:

$$J_{hot}(t) = \frac{N_b e}{\sqrt{\pi} S \tau_{laser}} \int_{-\infty}^{+\infty} \tilde{j}(t-t') \exp - \left(\frac{t'}{t}\right)^2 dt' \text{[6]} \tag{7.10}$$

where $S = \pi\, r_f^2$ is the heated surface and $\tilde{j}(t-t') = \left| -\frac{L}{(t-t')^2} \right| f_v \frac{L}{(t-t')}$ (cf. 7.2.1)

Resistive heating The fast electron incident current produces a space charge field $\mathbf{E}$ which opposes the incident current $\mathbf{J}_{hot}$. This field produces a return current $\mathbf{J}_{cold} = \sigma\mathbf{E}$ (Ohm's Law). Thus, assuming a complete current neutralisation ($\mathbf{J}_{cold} = -\mathbf{J}_{hot}$) we can write the the following equation for the deposited energy per unit volume and time:

$$\rho\, C_V \frac{d}{dt}(T_e[\mathrm{K}]) = \mathbf{E} \cdot \mathbf{J} = \frac{J^2}{\sigma} \tag{7.11}$$

The time-scale of only a few ps associated to this heating process allows us to neglect the process of thermal diffusion and expansion. That is why we considered constant the heating capacity of the medium $C_V = \frac{3}{2} K_B (n_e/\rho)$[7], where K_B is the Boltzmann constant, $\rho = 2.7 \mathrm{gcm}^{-3}$ is the Aluminum density and $n_e = Z^*\, n_i$ is the the plasma electron density. According to More's formula [107] deduced from the Thomas-Fermi theory, in an aluminium plasma of ionic density $n_i \approx 6 \times 10^{22}$ cm^{-3}, the ionization degree Z^* is 3 for a temperature of 10 eV, 7 for 100 eV, 12 for 1000 eV. We thus assume a value of $Z^* = 3$ for the aluminium degree of ionisation and a conductivity $\sigma = 10^6\ \Omega^{-1}\mathrm{m}^{-1}$ (the right order of magnitude for electron temperatures in the range from a few eV to about 100 eV). Thus, finally the final temperature of the heated region with a radial dimension r_f, after the incident fast electron flux, is:

$$T_e[\mathrm{K}] = \int_{t_{min}}^{t_{max}} \frac{d}{dt}(Te[\mathrm{K}])dt \tag{7.12}$$

and

$$T_e[\mathrm{eV}] = \frac{K_B}{e}(T_e[\mathrm{K}]) \tag{7.13}$$

Since our acquisition time (5 ns) is much longer than the heating time, we have also to consider the cooling of this fast electron produced plasma.

[6] Numerically we integrate between $-10\tau_{laser}$ and $+10\tau_{laser}$, over 21 iterations.

[7] With the assumption the each free electron in our plasma has 3 freedom degrees

Self-similar releasing of an instantaneously heated plasma Under the reasonable assumption that the heating generated by their fast flux is much faster (~ 100 fs -1 ps) than the characteristic cooling time of the produced plasma ($\sim$ few ns) let us consider the emitting plasma as an *energy reservoir* with a radial dimension r_f related to the angular dispersion of the electrons ($\theta/2$) and the traversed target thickness (L)(cf. Sect. 6.2.1) and with a constant heating capacity given by $C_V = \frac{3}{2}K_B(n_e/\rho)$. We can thus write the following expression for our energy reservoir:

$$\xi[\mathrm{Jm}^{-1}] = Q[\mathrm{eVm}^2]e[\mathrm{JeV}^{-1}]\frac{3}{2}n_e[\mathrm{m}^{-3}] \tag{7.14}$$

Where (at $t = 0$ and for a radial dimension of the emitting surface $r_s(t = 0) = r_{f0}$) the heating source Q is given by: $Q[\mathrm{eVm}^2] = T_0[\mathrm{eV}]\pi\, r_{f0}^2$. Thus, assuming that the initial radial temperature distribution in the energy reservoir is homogeneous ($T = T_0 = const$, for $0 < r < r_f$), we can consider a self-similar expansion of the emitting surface.

More in detail, this energy source could generate, *i*. a *thermal conduction wave* and *ii*. a highly energetic *blast wave*. This implies that, under the reasonable assumption of a cylindrical symmetry, the evolution of the radial front of the emitting source is given by:

$$r_f(t > 0) = \max\{r_h(t), r_{sh}(t)\} \tag{7.15}$$

where

$$r_h(t)[\mathrm{m}] = 1.943 \times 10^{-5}\xi^{\frac{n}{n+2}}[\mathrm{Jm}^{-1}]t^{\frac{1}{n+2}}[\mathrm{s}] + r_{f0} \tag{7.16}$$

is the thermal wave front, and

$$r_{sh}(t)[\mathrm{m}] = 1.245 \times 10^{-1}\xi^{\frac{1}{4}}[\mathrm{Jm}^{-1}]t^{\frac{1}{2}}[\mathrm{s}] + r_{f0} \tag{7.17}$$

is the front of the blast wave.

The fast electron deposed energy region thus remains confined in a front with a radial size $r_f(t)$, during an expansion firstly ($t < 400$ ps) governed by an heat wave $r_h \sim t^{\frac{1}{7}}$ and afterwards ($t > 400$ ps) by a shock wave $r_{sh} \sim t^{\frac{1}{2}}$ which overtakes it.

The self-similar evolution implies that the temperature $T(r, t)$ inside the heated region ($r \in [0, r_f(t)]$), is:

$$T(r, t) = T(0, t)\left(1 - \left(\frac{r}{r_f(t)}\right)^2\right)^{\frac{1}{n}} \tag{7.18}$$

where, for an electron fluid inside a plasma, $n = \frac{5}{2}$ and $T(0,t)$ is:

$$T(0,t) = \frac{Q}{\int_0^{r_f(t)} \left(1 - \left(\frac{r}{r_f(t)}\right)^2\right)^{\frac{1}{n}} 2\pi\, r dr}{}^{8}. \tag{7.19}$$

The spectral distribution of the power radiated by this plane black body $\frac{d^2W}{d\lambda\, dt}$, is obtained by injecting the temperature (Eq. 7.18) in the Planck luminance (Eq. 5.2). This then is integrated over the emitting surface and over all the hemisphere $z > 0$[9]. As the blackbody radiation is isotropic, this last step corresponds to the multiplication by the factor 2π:

$$\frac{d^2W}{d\lambda\, dt}[\mathrm{Jm^{-1}s^{-1}}] = 2\pi \int_0^{r_f(t)} \frac{2hc^2}{\lambda^5} \frac{1}{\exp\left(\frac{hc}{\lambda e T[\mathrm{eV}]}\right) - 1} 2\pi\, r dr\ . \tag{7.20}$$

Experimental results *vs* resistive heating model

In order to estimate the blackbody radiation emitted during expansion, we further integrate the Planck luminance (Eq. 5.2) over the experimental solid angle $\Omega_{exp} \sim 0.17$ [sr], the emitting surface $\pi\, r_f^2$ and the acquisition time window (2-5 ns). As before, the temperature of the incident electron population T_h is taken as a free parameter. According to experimental data (see Fig. 6.9), we assume an initial diameter of the injection zone $\Phi_0 = 30\,\mu$m and a divergence half-angle $\theta/2 = 30°$.

The comparison with the experimental spectral scaling for the thinner targets (see Fig. 7.8) indicates an incident population with $T_h = 1 \pm 0.2$ MeV. The absolute signal level is well adjusted for an injected electron population corresponding to $30 \pm 5\%$ of the 0.7 J on-target laser energy ($\approx 2 \times 10^{12}$ electrons for a relativistic Maxwellian energy distribution).

The maximum background electron temperature of the rear side against target thickness predicted by our model is shown in Fig. 7.9. The value estimated for 10 μm targets, > 100 eV, is higher than results obtained at similar laser intensities but with longer laser pulses and measured by X-UV diagnostics [54]. Nevertheless, recent hybrid simulations reproduced such temperatures [194], and our predictions for thicker targets fairly agree with other measurements (optical emission and reflectometry [165], K_α [195]). We note that the heating of thin target rear side, either induced by the

[8] Let us to note that $\int_0^{r_f(t)} T(r,t) 2\pi\, r dr = Q = const$

[9] We use the point-like source approximation, as its dimensions are quite smaller than the distance from the source and the observation point.

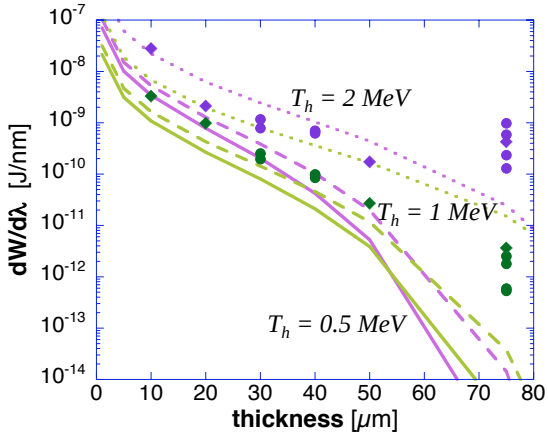

Figure 7.8: Experimental data *versus* the blackbody thermal emission model for $\theta/2 = 30°$, $\Phi_0 = 30$ μm, $\eta = 30\%$ and different temperatures T_h (violet curves stand for $2\omega_0$ and green curves for the *visible* spectral region).

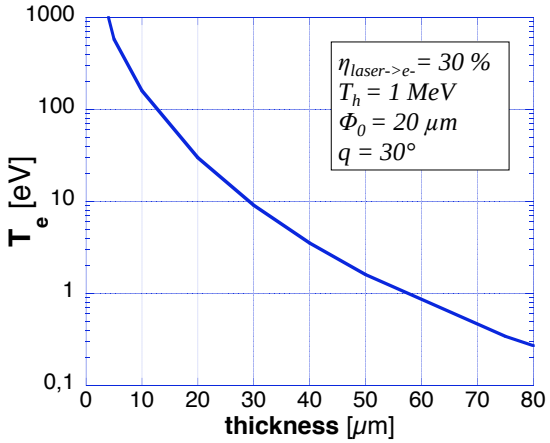

Figure 7.9: Rear side background electron temperature against target thickness corresponding to the resistive heating model.

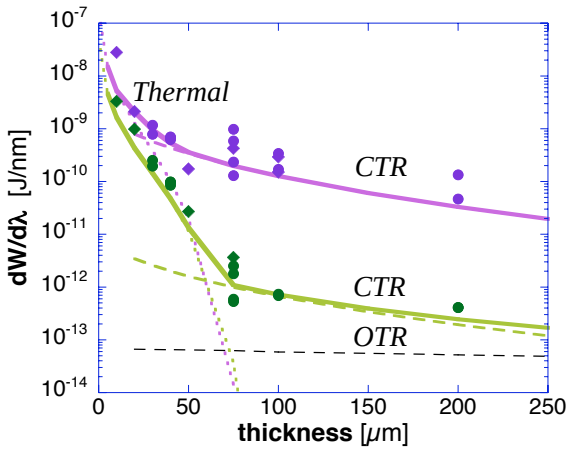

Figure 7.10: Experimental points are fitted (solid curves) summing the contributions of all the radiating models (Thermal: dotted curves; CTR: coloured dashed curves; OTR: violet dashed curve).

laser pre-pulse shock breakthrough (according to 1D hydrodynamic simulations [196]) or due to the absorption of the incident electrons energy by collisions and ionisation losses, is expected to be less than 10 eV. We can also conclude that the divergent propagation of the fast electron beam is probably the main reason for the less efficient heating of thicker targets.

Analysis of the experimental results in aluminium targets: conclusions

Summing the modeled CTR and thermal emission, we can correctly fit our experimental measurements of the rear side emission as a function of the target thickness for both the $2\omega_0$ and *visible* spectral ranges (see solid curve lines in Fig. 7.10). The thermal emission clearly dominates for the very thin targets (dotted curves). For intermediate thicknesses, the CTR emitted at $2\omega_0$ by a micro-bunched relativistic component becomes the dominant radiation (dashed curves). For enough thick targets (e.g. 200 μm), this coherent emission is degraded, but if we add the incoherent transition radiation (OTR) produced by the bulk population estimated before (black dashed curve, calculated as in reference [197]), we can still get a very good agreement with the measured signals.

In conclusion, the self-emission diagnostic is a powerful tool adequate for a detailed characterisation of the fast electrons population driven by an UHI laser-solid

interaction and the spatio-temporal dynamics of their transport through the targets. A spectrally broad incoherent blackbody emission is due to a resistive heating at the rear of thin targets ($T_e > 10$ eV for $L < 30\,\mu$m). This is associated to a return current set up to neutralise the incident flux of a bulk of moderately relativistic electrons (a few 10^{12} corresponding to a total kinetic energy of about $30 \pm 5\%$ of the 0.7 J on-target laser energy). They present a half-angle radial spreading of $30 \pm 5°$ (slightly larger than in other experiments [152, 141, 133] for similar laser intensities but longer pulses), starting from an initial source diameter of $30 \pm 10\mu$m, greater than the laser focal spot but yet smaller than the predicted by K_α fluorescence [141]. Besides, a coherent transition radiation at the second harmonic of the laser light is very sensitive to high electron energies and allowed to discriminate a small number (a few 10^9) of relativistic, micro-bunched and highly collimated electrons. The presented results, based on a simultaneous incoherent and coherent emission of radiation, therefore sensitive to both the moderately relativistic bulk electrons ($T_h \simeq 1$ MeV) and the high energy tail ($T_h \simeq 5$ MeV), are probably the first to fully resolve the fast electron population and to give a direct evidence of a two-temperature energy distribution [198]. For our few 10 TW, few 10^{19} Wcm^{-2} interaction regime, those temperatures are in good agreement with predictions for respectively a ponderomotive force acceleration [3] and a direct laser acceleration in a channel formed in the slightly under-dense pre-plasma [31].

7.3 Analysis of the experimental results in plastic targets

7.3.1 Optical emission *vs* target thickness: discussion and analysis

According to Sect. 5.2.6, three mechanisms have to be considered for optical emission from rear target surface: (i) the transition radiation, (ii) the thermal emission and (iii) the Čerenkov radiation.

As seen in Sect. 7.2, the first two mechanisms can correctly explain the signal from Al targets: *i.* for targets thicker than $30\,\mu$m, the emission is dominated by Coherent Transition Radiation (CTR) produced by a micro-bunched relativistic tail of the fast electron distribution and its intensity decreases with the target thickness; *ii.* the emission from the Al thinner targets ($\lesssim 30\ \mu$m) is mainly due to the second mechanism – the blackbody radiation emitted in consequence of the heating induced by the ASE-induced shock wave and the return electron current balancing the current of fast electrons. Thus, by summing the contribution of these two mechanisms, we have explained all Al data as seen in Fig. 7.10.

However, these processes cannot describe the CH data for which the optical signal increases with the target thickness. Such behavior can be explained only by the

Čerenkov emission, which gives a total emission proportional to the particle path length.

In some shots, the front side of the CH targets was covered by a thin ($\approx$ 30 nm) Al layer. However, this did not change the results, showing that the larger signal from the plastic target is not due to a change in the laser interaction conditions on the front side. Also, in order to check that the increased signal intensity is not due to OTR and to the difference in the refraction index between CH and Al, on some plastic targets a thin Al ($\approx$ 30 nm) layer was deposited on the rear side. The signals recorded with these targets only show a slight decrease (in agreement with the partial transmissivity of the Al layer) but were still higher than those from Al targets. This confirms that the signal comes from Čerenkov radiation in plastic.

Furthermore, Čerenkov light can be emitted by fast electrons from the ionization front only, because the ionized plasma is not transparent and it has a small refraction index $n \lesssim 1$. Thus, in order to correctly estimate the Čerenkov emission induced by the fast electron propagation in plastic targets, we need to go back to the analysis of the fast electron ionization in dielectrics (cf. Sect. 4.2.1) and to address to a few features concerning the ionization front, such as: *i.* the dependency of the ionization front velocity v_f *vs* the beam density n_b and *ii.* the dependency of the ionization front width Δ_f *vs* the beam density n_b. Those aspects, as we will see further, are fundamental for the understanding of both the Čerenkov emission and the observed beam filamentation behavior.

Structure of the 1D ionization front

Ionization front velocity In this part we will put in evidence the dependency of the ionization front velocity v_f on the beam density n_b. In the frame of the ionization front (moving at v_f), the fast electron beam moves at v_b. As we already shown in Chap. 4, one can assume a 1D model in which the ionization is exclusively due to the electric field. In this model, differently to Sect. 4.2.1, we don't suppose the front velocity v_f constant during propagation. Thus, if the fast electrons propagate along the x axis, in the frame of the ionization front we have the following rate equations describing the evolution of secondary electron, n_e, and ion, n_i, densities:

$$\partial_t n_e + \partial_x(n_e(v_e + v_f)) = \nu_{fZ}(E)(n_a) \tag{7.21}$$

$$\partial_t n_i + \partial_x(v_f n_i) = \nu_{fZ}(E)(n_a) \tag{7.22}$$

$$\partial_t n'_b + \partial_x(v'_b n'_b) = 0 \tag{7.23}$$

where n'_b is the beam density in the front frame. The Poisson equation for the electrostatic field remains the same that the Eq. 4.8, or in S. I. units:

$$\partial_x E = \frac{e}{\epsilon_0}(n_i - n'_b - n_e) \tag{7.24}$$

while the mobility equation for the secondary electrons in the self-consistent field became:

$$v_e = -\frac{eE}{\gamma_b m_e \nu_{ep}} \tag{7.25}$$

Writing $\delta n = n_i - n_e$, from 7.21 and 7.22 one has:

$$\partial_t \delta n + \partial_x(v_f \delta n - v_e n_e) = 0 \tag{7.26}$$

In the case of a stationary system ($\partial_t \delta n = \partial_t n_e = \partial_t n_i = \partial_t n'_b = 0$), we arrive in the frame of the front at the relation:

$$\delta n = \frac{v_e}{v_f} n_e \simeq \frac{v_e}{v_f} n_i \tag{7.27}$$

In order to close this equation system (and give an extimation of $v_f(n_b)$) we need an additional information about the fast electrons: i.e. its energy distribution.

The ideal case consists in taking a relativistic Maxwellian distribution (cf. Sect. 5.2.2). However, for the sake of simplicity, we will suppose a flat distribution in energy (up to a maximum given energy). In this case, in the laboratory frame we can define a function f_b as follows:

$$f_b = \frac{n_{b0}}{p_m} \tag{7.28}$$

where p_m is the fast electrons maximal momentum of fast electrons. Also, we can say that the fast electron maximal energy is equal to the potential energy:

$$m(\gamma'_b - 1)c^2 = e\varphi_m \tag{7.29}$$

where φ_m is the maximum of electrostatic potential φ in the ionization front. In fact, at the end of the fast electron beam, matter is not ionized and consequently there is no charge equilibrium: the electrostatic field φ appears and increases until when ionization re-establishes the charge equilibrium. At that moment the field will decrease. Thus, the field φ can vary from 0 (in $x = 0$) to its maximum $\varphi_m = \frac{W'_{bm}}{e}$, where W'_{bm} is the fast electron energy in the laboratory frame. However, only the

electrons with an energy larger than the potential φ will take part in the creation of the electric field:

$$n'_b(\varphi) = \int_0^{p'_{bm}-p'(\varphi)} \frac{n_{b0}}{p_{bm}} dp \tag{7.30}$$

where $p_{bm} - p(\varphi) = p_{bm} - mc\sqrt{\phi^2 + 2\phi}$, with $\phi = \frac{e\varphi}{mc^2}$ is the momentum of an electron affected by the potential φ. Thus, finally from Poisson's equation:

$$\frac{E_m^2}{2} = \frac{e}{\epsilon_0} \int_0^{\varphi_m} n'_b(\varphi) d\varphi \tag{7.31}$$

and Eq. 7.29, we find the asymptotic expression for v_f:

$$v_f(n_{b0}) = \frac{c}{\left(k_{nb0}^{-\frac{2}{3}} + 1\right)^2 + b^2} \left(ab - \sqrt{(b^2 - a^2)(k_{nb0}^{-\frac{2}{3}} + 1)^2 + (k_{nb0}^{-\frac{2}{3}} + 1)^4} \right) \tag{7.32}$$

where $K = \left(\frac{3p_{bm}\epsilon_0 E_m^2}{4\sqrt{2}m^2c^4}\right)^{\frac{2}{3}}$, $a = \frac{W_{bm}}{mc^2} + 1$ and $b = \frac{p_{bm}}{mc}$.

Let us note that integrating the Eq. 7.31 for $\varphi = \varphi_m$, we have the number of electrons in the ionization front.

More in detail, the fast electron population is assumed to have a relativistic Maxwellian energy distribution with temperature $T_h \simeq 1$ MeV, an angular divergence half-angle $\simeq 30°$ around the laser axis and a total number of particles $N_b = 2 \times 10^{12}$ injected in surface with a $r_0 \approx 15$ μm radius. The initial density of the electron beam is thus of the order of $n_b \simeq 2.4 \times 10^{20}$ cm^{-3} but it decreases by one order of magnitude at the rear side of a target with a thickness $L = 100$ μm as the beam radius increases to $r_f \sim 70$ μm.

In fact, the ionization front radius r_f grows linearly as $r_f = L\tan(\theta_0) + r_0$ and consequently, the number of electrons within the ionization front slightly changes between $N_f \approx 3.4 \times 10^{10}$ in the injection zone, and 5.3×10^{10} ($\sim 19\%$ of the total number of fast electrons) after crossing 100 μm of CH.

In Fig.7.11 (left panel) we show the normalized front velocity in the laboratory frame, against the CH target thickness.

Estimation of the width of the ionisation front We already roughly estimated the width of the ionization front from the Poisson equation ($\Delta_f \sim \epsilon_0 E/en_b$). Also, the estimation of the electric field at the ionization front shows that the threshold ionization field is of the order of $\sim 10\%$ of the atomic electric field E_a. Thus, taking

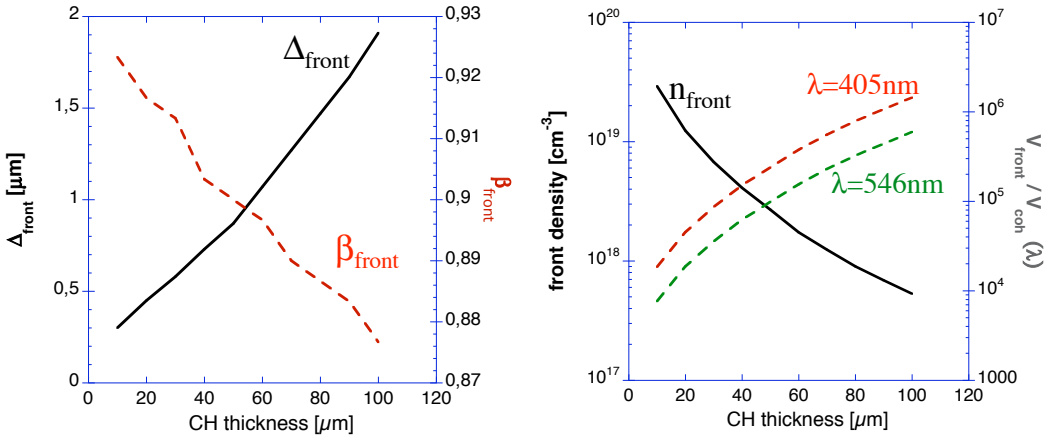

Figure 7.11: Ionization front width Δ_f and the normalized front velocity in the laboratory frame, against CH target thickness (left panel); number of the coherence volumes in the ionization front and front electron density n_f evolution with target thickness (right panel).

into that about $\sim 10\%$ of the fast electron participate in the ionization process, we can roughly estimate the width of the ionization as $\Delta_f \sim \epsilon_0 E_a / e n_b \sim 1-2\,\mu$m. This is about one tenths of the beam length, $l_b \sim c\tau \sim 10\,\mu$m, where τ is the laser pulse duration ($30-40$ fs), which is another way to estimate the relative number of electrons participating in the ionization process.

However, for a more detailed analytical calculation, we need to consider the variation of the ionization front length which occurs during the beam propagation in the medium, as a consequence of the interplay between the variation of v_f and n_b.

Again we will suppose an energy constant distribution. From the Eq. 7.30 and integrating the Poisson equation 7.31 over $e\varphi \ll mc^2$, we obtain:

$$E(\phi) = \frac{2}{3}\sqrt{3}2^{\frac{1}{4}} mc^2 \sqrt{\frac{n_{b0}}{\epsilon_0 p_{mb} c}}\phi^{\frac{1}{4}} \tag{7.33}$$

and after some algebra we finally obtain the following relation:

$$\Delta'_f = \frac{6}{\sqrt{3}2^{\frac{1}{4}}}\sqrt{\frac{\epsilon_0 p_{mb} c}{e^2 n_{b0}}}\phi_m^{\frac{1}{4}}. \tag{7.34}$$

In Fig. 7.11 (right panel), we show the ionization front length Δ_f in the laboratory frame, against CH target thickness.

Čherenkov emission: model and results

As we have seen in Sect. 5.2.5, the optical Čerenkov radiation is emitted by an electron propagating in a dielectric material with a velocity $v = \beta c$ larger than the phase velocity c/n of light [57]. This cannot be observed in nontransparent materials such as metals or dense plasmas because of strong absorption and a small refraction index $n < 1$. Furthermore, the radiation is emitted in a cone around the particle propagation axis with an angle given by $\cos\theta = 1/\beta n$. Our diagnostic is nevertheless limited by the $\sim f/2$ collecting optics, hence, accounting for the CH refraction index $n \simeq 1.48$ in a $400 - 550$ nm wavelength range, we can observe emission only in the narrow cone within $\theta_{max} \approx 8°$ around the target normal.

Another important limitation on the Čerenkov emission is imposed by the ionization process: the detected radiation is due to relatively high energy electrons ($\beta \sim 0.85 - 0.95$, see Fig. 7.11) propagating with the head of the ionization front at large angles $\gtrsim 30 - 40°$ (with respect to the target normal). This is because: (i) only electrons with velocities larger than the ionization front ($\beta > \beta_f$) can contribute to the measured signal, (ii) electrons moving along the laser axis emit radiation which is outside the collection angle.

According to previous analysis of the ionization front structure, developed in Sect. 7.3.1, in order to estimate the Čerenkov radiation due to the fast electron propagation in dielectrics we used an analytical ballistic model, which represents the ideal development of the model we used in Sect. 5.2.5. We assume:

- An injected electron population is assumed to have a relativistic 1D-Maxwellian energy distribution $f_\beta(T_h) \propto \exp\left(-\frac{E_c}{T_h}\right)$ with the temperature $T_h \simeq 1$ MeV
- A Gaussian angular distribution $g_\theta(\theta_0) \propto \exp\left(-\frac{\theta^2}{2\theta_0^2}\right)$ with an angular divergence half-angle $\theta_0 \sim 30°$
- A ionization front radius r_f supposed to grow linearly as $r_f = 2L\tan(\theta_0) + r_0$, where $r_0 \approx 15\mu$m
- Accordingly to previous assumption, the number of electrons within this ionization front slightly changes between $N_f \approx 3.4 \times 10^{10}$ in the injection zone, and 5.3×10^{10} after crossing $100\,\mu$m of CH

Only these N_f electrons in the ionization front can contribute to the Čerenkov emission. This emission should be largely coherent when formed within a volume of the order of $V_{coh} \sim \lambda^3$. The right panel of Fig. 7.11 shows how many of these coherence volumes exist in the ionization front $\frac{V_f}{V_{coh}} = \frac{\pi r_f^2 \Delta_f}{\lambda^3}$. The front electron density n_f evolution with target thickness is presented in the same graphic. The

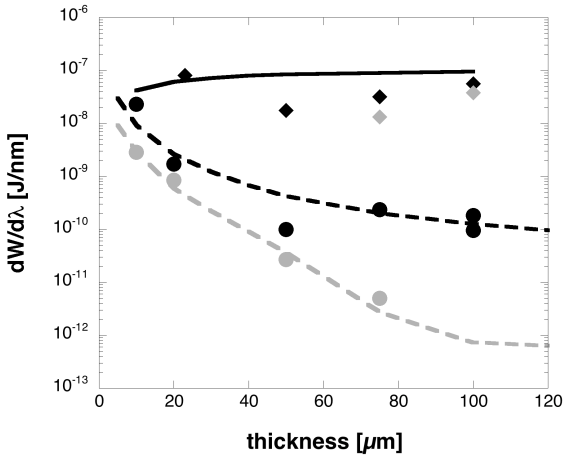

Figure 7.12: Data series for Al (circles) and CH (diamonds) targets for the laser intensity 6×10^{19} W/cm^2. Black symbols stand for the signals around 405 nm and the grey symbols for the signals around 546 nm. Aluminum data is completely fitted by the sum contribution of CTR and thermal emission (dashed curves). For the CH targets, one has to add the Čerenkov radiation and the total emission from all radiative contributions fits correctly the CH data (solid curves).

coherent Čerenkov radiation, emitted in the in our solid angle $\Delta\Omega$, is proportional to $\propto (n_f V_{coh})^2 \frac{V_f}{V_{coh}}$ and comes finally estimated by:

$$\begin{aligned} \frac{dW}{d\lambda} &\simeq \Delta\Omega\, n_f \frac{\pi e^2}{\epsilon_0} \int_{-\pi/2}^{\pi/2} \frac{L}{cos(\theta)} g_\theta(\theta_0) d\theta \\ &\times \int_{\beta_f}^{\beta_{max}(\theta)} f_\beta(T_h) \left(1 - \frac{1}{\beta^2 n^2}\right) d\beta \end{aligned} \tag{7.35}$$

where L is the CH target thickness, $\Delta\Omega \simeq \pi\theta_{max}^2$ is the acquisition solid angle and:

$$\int_0^1 f_\beta d\beta = \int_{-\pi/2}^{\pi/2} g_\theta(\theta) d\theta = 1 \tag{7.36}$$

As one can see in Fig. 7.12, the modelled Čerenkov emission is clearly the dominant radiation mechanism and well reproduces the CH experimental data.

7.3.2 Fast electron filamentation: role of the ionization instability

Concerning the detailed study of the spatial distribution of the rear side target emission, we thought that the different behavior shown in Fig.6.11 between Al and CH targets with thicknesses larger than 30 μm, is very probably related to the ionization front instability. In fact, all other ideal beam instabilities (Weibel, two stream) which could be the main responsible of the filamentation shown in insulator targets, should act in a similar way in insulators as well as in metal targets. Only resistive instabilities could develop in a very distinct way in plastic than in aluminium, thanks to an initial (cold material) extremely different conductivity. Anyway, very recent theoretical works [199], based on hybrid simulations, show how resistive instability in insulators, even if more significant than in metals, is still about 100 times less important than the ionization one. In order to compare the growth rate of this instability to our experimental data, we have done few simple estimations based on a recent analytical 2D model [114] of the ionization front.

Ionization front instability

In Sect. 7.3.1 and Sect. 7.3.1 we previously showed *i.* the dependency of the ionization front velocity v_f on the beam density n_b and *ii.* we estimated the width of the ionization front as $\Delta_f \sim 1-2\,\mu$m. Thus, because of our experimental results (see Fig. 6.11) show filaments with an approximate diameter of about $13\,\mu$m, we could consider the case in which the ionization front width Δ_f is smaller than the perturbation size λ_c. In other words, this is equivalent to consider the stability of the ionization front against long wavelength corrugation, $\Delta_f k_c < 1$, where $k_c = 2\pi/\lambda_c$ is the wave number of the perturbation. For a small corrugation amplitude, $h_c(\xi_c \equiv h_c k_c \ll 1)$, the corrugated ionization front, $X_f(y) = h_c cos(k_c y)$, shown in Fig. 7.13, does not change its internal structure much in comparison to the 1D case. Therefore local velocity of the ionization front will be determined by local beam parameters. However, due to the effect of the electric field of the front, which slows beam electron and turns them back the local beam density will be altered. The "valleys" in the corrugation front will work like focusing lenses and causing a local increase of the beam density, $\delta\, n_b/n_b \sim \xi_c$, while the "hills" will work the other way around see Fig. 7.13. In some sense this focusing works similar to the collimation of the electron beam by vacuum gap observed in the numerical modeling in Ref. [200]. As a result of local variation of beam density the local velocity of the front will be different and will cause the corrugation instability of the front for the case where v_f increases with increasing beam density see Fig. 7.13.

To make the quantitative estimate of the growth rate, Γ_c, of such corrugation instability we notice that the diversion of the beam along the y coordinate, $\delta\, Y_b$, caused by the electric field effects during beam propagation through the front can be estimated (from $\Delta_f \ll \lambda_c$) as follows: $\delta\, Y_b \approx \Delta_f \frac{dX_f(y)}{dy}$. Therefore the variation of

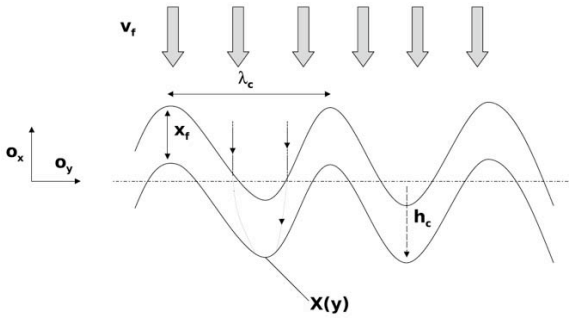

Figure 7.13: Schematic view of the corrugated ionization front.

the beam density due to such diversion is $\delta n_b/n_b \approx -\frac{d(\delta Y_b)}{dy}$ and the corresponding departure of the front velocity from the unperturbed value is:

$$\frac{\delta v_f}{v_f} = \frac{\delta n_b}{n_b}\frac{\partial \ln v_f}{\partial \ln n_b}. \tag{7.37}$$

As a result we find the equation for $X_f(y)$:

$$\frac{X_f(y)}{dt} = -\Delta_f v_f \frac{\partial \ln v_f}{\partial \ln n_b}\frac{d^2 X_f(y)}{dy^2} \tag{7.38}$$

and the following estimation (dispersion equation) for the growth rate:

$$\Gamma_c = \Delta_f v_f k_c^2 \frac{\partial \ln v_f}{\partial \ln n_b} \tag{7.39}$$

As we see the growth rate is positive for $\frac{\partial \ln v_f}{\partial \ln n_b} > 0$ and increases with increasing wave number of the perturbation. Also, the instability growth rate maximum corresponds to the wavelengths of the order of the front thickness, $\lambda_c \sim 2\pi\Delta_f$. Thus, in the case of a filament size of ~ 10 μm (see Fig. 12.6 (d)) and an electron beam density in the ionization front $n_f \simeq 5 \times 10^{-18}$ cm^{-3} for an electronic population with $T_h \simeq 1$ MeV (cf. Sect. 7.3.1), the predicted instability growth rate $\Gamma_c \sim 10^{13}$ s^{-1} ($\frac{2\pi}{\Gamma_c} \simeq 0.16$ ps correspond to a propagation over $\simeq 50$ μm) agrees to a beam filamentation distance of about ~ 100 μm, which is of the same order as that observed experimentally (Fig. 6.11 (d)).

Let us also note that filamentation maximum growth rate is predicted to be achieved for current densities ~ 100 A/μm^2, which agrees rather well with the estimate of 7 MA for the total current measured in our experiment. This is also in agreement with the current estimates in other experiments [133, 152]. On the contrary, producing filaments on the distance of 100 μm with the dissipative Weibel instability, would

require current densities above 1 kA/μm^2, which are not realistic in our conditions. Let us finally evidence that assuming a filament size of $\sim$ 13 μm (as measured in the experiment), one would get $\sim$ 40 kA of current per filament, which is quite close to the Alfvén limit.

Analysis of the experimental results in plastic targets: conclusions

The experimental results in plastic have shown how, even if the optical emission from the target rear side is ascribed to Coherent Transition Radiation and to thermal emission for Al targets, for CH targets Čerenkov emission is clearly the dominant mechanism. The Čerenkov diagnostic has also shown that the electron beam breaks up into filaments with a growth rate and a characteristic transversal scale in fair agreement with analytical predictions based on the ionization front instability. This large scale ($\sim$ 10 μm) and relatively slow ($\Gamma_c \sim 10^{13}$ s^{-1}) filamented behavior is completely absent in metals and therefore it cannot be explained with a volumic instability such as the Weibel or two-stream instabilities.

Part IV

General conclusions and perspectives

Chapter 8

Conclusions

This PhD thesis is related to the research on inertial confinement fusion, and more particularly it concerns the *fast ignition* approach, which is based on the use of ultra-intense laser pulses to ignite the thermo-nuclear fuel. Until now, the feasibility of this scheme has not been proven and depends on many fundamental aspects of the involved physics, which are not yet entirely understood and very far from being controlled. Furthermore, while important indications have already been obtained from our and other experimental results with different target types and configurations, it is presently not clear how these can be extrapolated to a realistic fast ignition scenario. Also computer simulations (either PIC or hybrid) working at realistic space and time scales and including all the relevant physics are not yet feasible. Therefore it is still essential to obtain new experimental data which allows to understand the physics at the base of fast ignition, even if at smaller laser energies and on shorter time and space scales.

This has indeed been the main goal of this thesis work which consisted in an experimental study of the processes of transport in over-dense (solid) and under-dense (gas jet) matter of a fast electron beam generated by laser pulses at the intensity of a few 10^{19} Wcm^{-2}.

The supra-thermal electron currents created in our experimental conditions correspond to about 10^7 A and current densities values of $10^{12}\,\mathrm{A\,cm}^{-2}$, probably the largest ever produced. In this regime, the physics of the electronic transport is very complex: collective mechanisms, associated to the huge fields, spontaneously induced by charge separation and current, involve the magnetic focusing of the electron beam, its electric deceleration, the resistive heating of crossed material and its fast ionization (in the case of insulators), and finally the possibility of beam degeneration as consequences of instabilities. These effects sum to the well-known collisional processes of deceleration and angular diffusion (cf. Chap. 2, [118, 201]).

In order to study the less-known aspects of such physics, several diagnostics were simultaneously installed in our experimental campaigns carried out on the 100 TW laser installation at the Laboratoire pour l'Utilisation des Lasers Intenses (LULI) (cf. Chap. 3) and on the 20 TW "Salle jaune" laser of the Laboratoire d'Optique Appliquée (LOA) (cf. Chap. 6). The goals of these experiments were: i) to investigate the dynamic of the fast electrons at low densities (gas jets), for which electric inhibition is maximized, and show the existence of huge electrostatic fields directly, and ii) to study certain aspects of the propagation of the fast electrons in the solid matter, in particular the geometry, the dynamics and the energy distribution of the fast electron beam travelling in the target, the heating of matter induced by the passage of fast electrons, and above all, the possibility of beam filamentation as a result of instabilities.

In order to reach these objectives, in the experiment on fast electron propagation in gases, we used complementary time and space resolved diagnostics: the *classical* and chirped shadowgraphy and *proton imaging*. Instead, concerning the electron transport in solid matter, we concentrated on the visible radiation emitted by the rear side of solid flat targets (of Al or CH).

The experiment in gases has shown several novel results:

- The density of the background material determines the characteristics of fast electron propagation. Smaller densities correspond to weaker return currents and more inhibited motion. In our experiments, we measured quite small propagation velocities, as a consequence of the low background density. Our results qualitatively agree with those in [122] obtained in solid fused silica, where a penetration velocity $\approx c/2$ was measured; however, quantitatively, those experiments, with $n_b \ll n_e$, did fall in a different regime. Indeed in our case the initial density of the fast electron current (as it is generated in the metallic foil) exceeds the background electron density in the gas. This situation is of interest for fast ignition because it may simulate the propagation of an intense fast electron beam in underdense coronal plasma.

- Propagation velocity and propagation distance increase with gas pressure and propagation velocity slows down with time. This feature too seems to confirm the role played by the density of the background medium in establishing a return current, and the essential role of charge separation and electrostatic fields. Moreover, our results give the first direct experimental evidence of the presence of the huge fields, which have long been predicted to be associated to fast electron propagation, but never directly observed before. They also show that the measured value of electrostatic fields can be of the order of theoretical predictions.

- The ionization phase is essential for producing the free electrons, which are essential for establishing a neutralizing return current. This sets a fundamental

difference between propagation in insulators and in conductors. Many effects (e.g. filamentation) which until now have been observed in insulators only, may therefore not be present in the case of hot plasmas, which are more similar to conductors (however the main limitation on return currents which we recalled before also apply to these cases). We have also shown that in our conditions, field ionization induced by the large electrostatic field is by far the dominant ionization effect.

- Electrostatic fields are fundamental in fast-electron propagation. They drive the free electrons to return with a velocity determined by field strength and by the number of collisions (i.e., by gas density). In our experimental conditions, such fields are so large that a linear description of the return current (Ohm's law-like) is no longer applicable. The electron motion is strongly saturated bringing to a square-root dependence (as predicted by Landau and Lifshitz in the case of very strong fields)

Concerning the study of the fast electron transport in solid targets, we observed how the self-emission diagnostic is a very powerful tool adequate for a detailed characterisation of the fast electron population generated in the interaction of an ultra-high-intensity laser with solids. It also allows characterizing the spatial-temporal dynamics of transport in the targets in a precise way.

More in detail, in Al target we have observed a spectrally broad incoherent black-body emission due to a resistive heating at the rear of thin targets ($T_e > 10$ eV for $L < 30\,\mu$m). We estimated that this is associated to a return current set up to neutralise the incident flux of a bulk of moderately relativistic electrons: a few 10^{12} electrons with an average energy of about 1 MeV, corresponding to a total kinetic energy of about $30 \pm 5\%$ of the on-target laser energy (about 0.7 J). They have a half-angle radial spreading of $30 \pm 5°$ (slightly larger than what obtained in other experiments [152, 141, 133] for similar laser intensities but longer pulses). The initial source diameter was $30 \pm 10\,\mu$m, larger than the laser focal spot but still smaller than what observed in other experiments using K_α fluorescence [141].

Besides, a coherent transition radiation at the second harmonic of the laser light has been observed [134, 133]. Since this coherent emission is very sensitive to high electron energies, it has allowed a detailed characterization of the *high-energy tail* of the fast electron distribution. This is made of a smaller number (a few 10^9) of relativistic electrons with typical energies of about 5 MeV or more, which are micro-bunched and highly collimated.

These results, based on the simultaneous use of incoherent and coherent emission of radiation, are sensitive to both the moderately relativistic bulk electrons and the high-energy tail. Therefore they are probably among the first to give a more complete characterization of the fast electron population and to give a direct evidence of a

two-temperature energy distribution [198]. For our few-10 TW, few-10^{19} Wcm^{-2} interaction regime, those temperatures are respectively in good agreement with predictions for ponderomotive force acceleration [3] and direct laser acceleration in a channel in the under-dense pre-plasma [31].

Our experimental results have shown that in the case of Al targets, the optical emission from the target rear side can be completely ascribed to Coherent Transition Radiation and to thermal emission. Instead in plastic we have shown that Čerenkov emission is clearly the dominant mechanism. The Čerenkov diagnostic also shows that the electron beam breaks up into filaments with a growth rate and a characteristic transversal scale in fair agreement with analytical predictions based on the *ionization front instability*. This large scale (~ 10 μm) and relatively slow ($\Gamma_c \sim 10^{13}$ s^{-1}) filamented behaviour is completely absent in metals and therefore it cannot be explained by instabilities such as the Weibel or two-stream instabilities which are *volumic* instabilities and should take place in a very similar way in insulators and in conductors. Our results are comparable to what already obtained by other groups [141, 163]. However by comparing results obtained in Al and CH in identical conditions, we clearly show that they take place in insulators only and, by analysing their behaviour as a function of target thickness we can give a more detailed characterization of the growth of the instability and allow to definitively conclude that Weibel-like mechanisms are not dominant, at least in the experimental conditions observed in experiments reported until now (both by ourselves and by other groups).

Furthermore, the ionization instability can take place only at the fast beam edge (ionization front) as long as the electron beam propagates in the insulator before this is ionized. Only a small fraction (about $\sim 10\,\%$) of the total electrons, with velocities larger than the ionization front ($\beta > \beta_f$), can therefore contribute to it. The remaining major part of the beam of electrons are thus not involved in this instability mechanism and therefore there should not be any substantial difference between propagation in plastic and in aluminium targets, except for a probable slowing down induced by the ionisation process in insulators (cf. Chap. 3 and 6).

This is an important point for the generation of low-emittance ion beams [202]. The foil irradiated material, in which the laser-driven fast electron pass before building up huge electric fields when emerging from the rear surface does not seem of crucial importance for the maximum energy of the ion beams. In fact, the accelerating space-charge fields (of the order of TV/m) are due to the moderately relativistic ($T_h \simeq 1$ MeV) bulk population (a few 10^{12}) of fast electrons and not to the few high-energy electrons ($T_h > 1$ MeV), responsible of the beam filamentation in the ionization front of CH targets. On the contrary the spatial disruption of the fast electrons propagating in CH targets, due to ionization [115] or ohmic resistive [199] instabilities can strongly effect the spatial uniformity of the accelerated ions [160, 22, 163].

Chapter 9

Perspectives

The results obtained during my PhD work, and contained in this thesis, address some of the main open problems related to the fast ignition approach to ICF: the final transport of the ignitor pulse energy to the compressed core by means of fast electrons. An important key problem, which we studied, was related to the fast electron distribution, which we have characterized in details, in particular allowing to distinguish the bulk of electrons and the high energy tail. However it is still very important to continue the characterization of the fast electron beam by using the smallest possible number of *external* assumptions concerning its directness, laser conversion efficiency and *temperature*.

In this direction, an important contribution could come from the use of novel diagnostics such as the use of polarization spectroscopy diagnostic in the X-ray domain [203, 204]. By using such diagnostics, and comparing the intensity of π and σ components of selected X-ray emission lines, it is possible to characterize the fast electron distribution in the phase space allowing to discriminate the longitudinal and transversal motion. In other words by modelling the fast electron distribution with a longitudinal ($T_\perp$) and a transversal temperature ($T_\parallel$), it is possible to characterize the ratio between the two temperatures. In particular indications related to limiting cases of *beam-like* or a *pancake-like* distribution functions could be obtained. This characterization will be much more detailed of what obtained until now, in terms of opening angle and a single temperature.

Moreover it would be essential also in assessing the possibility of development of Weibel-like instabilities. Indeed the developments of such instabilities, their growth rate, critically depend on the beam transversal temperature, a parameter that has never been directly measured until now. Let's notice how this puts considerable shading on all the models and the computers simulations observing a strong Weibel instabilities performed until now. Finally by using multi-layer targets with a first *propagation*

layer of variable thickness, it will be possible to reconstruct the behaviour of the two-temperature distribution function vs. thickness of the propagation layer. Preliminary experiments [204] have already been obtained at very low intensities ($\approx 10^{17}$ Wcm^{-2}) but it is now time to repeat them in a high-intensity regime of direct interest for fast ignition.

Another key point concerns the extrapolation of present results to a realistic fast ignition scenario. One may expect that the coronal plasma of ICF targets, and the dense plasma in their compressed core, react differently from solid foils and gas media. For instance, a petawatt pulse needed for fast ignition (10 kJ in 10 ps) carrying 10 MeV electrons over $\sim 10\,\mu$m implies fast-electron densities $n_b \sim 10^{23}$cm^{-3}. While at present it is not clear how these can be generated, still such densities are much larger than those in typical coronal plasmas ($n_e \sim 10^{21}$cm^{-3}). The propagation limit $n_b \geqslant n_e$, already met and studied in our gas experiment is therefore expected to play a major role even in a "true" ICF context.

Other key open questions concern the recent "cone-guided" approach to fast ignition [205]. Here the distance between the compressed core and the partially ablated tip of the cone is typically $50-100\,\mu$m. The gap is filled with residual plasma, which may have a density, which is substantially lower than the compressed foil and may also be lower than the density of the gold material in the cone tip. Thus the ignitor beam has still to be transported through this gap without significant beam divergence or losses, and charge separation and huge electrostatic fields may play a large role. Of course the presence of the cone will reduce the distance which the electrons needs to travel before reaching the compressed core but this alone does not eliminate all propagation problems. We can thus infer that, as in our gas jets experiments, also in this case the strength of the electrostatic fields could play an essential role in slowing down and stopping the electrons in addition to, or instead of, anomalous stopping mechanism due to stochastic scattering of plasma cold electrons by magnetic perturbation [206].

At the moment in simulation (hybrid) codes [111, 116, 118, 125], the electric effects in the fast electron propagation have been taking into account only inductively (from the Faraday's law), whereas the space-charge fields as well as the ionization phase have been neglected. (Let's notice that concerning analytical theoretical models, the situation is almost exactly the opposite. For instance Davies *et al.* [111] and Tikonchuk [96] consider electrostatic fields only). On the contrary in the case where $n_b > n_e$ we find that this approximation is not accurate and can lead to large errors.

We thus wish and strongly suggest that the next generation of computer codes should include space charge and the ionization aspects, which are crucial for a complete understanding of the fast electron transport in conditions near to those of the ignitor pulse for the Fast Ignition scheme. This could clarify the real dominant phenomena in electron stopping, among the many available candidates: space-charge effects, anomalous stopping, ...

Let me also notice that at the moment several effects related to laser-driven relativistic electron currents, as the Hole Boring [87], the Filament Coalescence [200] and Anomalous Stopping [206] are only predicted by 2D or 3D PIC simulations performed on very short time and space scale lengths, and assuming parameters (overdense plasma with only a few n/n_c) which are quite far from the real experimental conditions and from the parameters needed for Fast Ignition. Furthermore a clear experimental evidence of such effect has presently not yet been undoubtfully observed.

Moreover, although we can experimentally confirm that when the beam undergoes to a filamentation, the beam current in each filament does not seem to exceed the Alfvén current limit (cf. Sect. 7.3.2), at the moment any coalescence predicted by PIC simulations has not been experimentally observed yet. Also, it is not possible to conclude whether this is due to the extreme rapidity of the phenomenon (few laser cycles) and what should happen with longer laser pulses, of the duration, which is relevant for fast ignition.

Therefore experiments aimed at studying the fine details of the beam propagation geometry, including the possibility of beam filamentation and filament coalescence are still crucial in order to study the basic physics of beam transport and in order to assess the feasibility of fast ignition. This category of experiment could be similar to our experiment in solids (Al and CH targets) and should be performed using laser pulses of different duration (from 10's fs to ps) and higher energies in various material, metals and insulators again, but also foam and aerogels, allowing for a wider range of experimental parameters to be investigated. These experiments should probably use at the same time visible diagnostics related to thermal, OTR and Čerenkov emission (as we have already done) and X-ray diagnostics, in order to study what happens inside the material (especially when this is not transparent to visible light as it is the case of metals).

Finally, another key open question concerns the study of cone-guided targets. Cone targets have been recently proposed as a new alternative approach to fast ignition. Integrated experiments have shown an increase in neutron yield in compression of fusion targets in presence of the cone (the CPA beam being directed through the cone). Such results have recently been published in Nature [154]. Despite the clear interest of such results, still many points remain completely obscure. Such integrated experiments do not allow a real understanding of the underlying physics and hence do not allow the study of the scalability of such scheme. Therefore, simpler and "cleaner" experiments aimed at studying the basic physics of transport and generation in presence of the cone are essential. Also, it must be noticed how the presence of the cone was initially seen as a way to mitigate the problems of fast electron generation and propagation through the plasma corona to the compressed core. Indeed the cone would serve to avoid the interaction of the laser beam with the plasma corona (the inside of the cone remaining relatively "empty" of plasma), to allow a preferential interaction with denser regions in

the targets, and to reduce the propagation distance between the generation region and the compressed core. In reality, the presence of the cone can also act in order to change (and improve) the conditions of laser interaction and of fast electron generation, in several ways:

- The cone can effectively guide the laser beam to the interaction region. One well-known problem of short-pulse high-intensity CPA beams is the fact that the "nominal" focal spot only contains part of the total laser energy (between 30 and 50%) while the remaining energy is spread in a larger area. The presence of the cone may redirect such laser energy towards the cone tip, i.e. in the useful region.

- Many fast electrons are emitted towards the incoming laser beam, and do not penetrate the target directly. Only a few can escape due to space charge effects, while many of them are coming back in a "fountain" on larger regions around the focal spot. Again, the presence of the cone may recuperate such electrons and drive them to the interaction region. In this way the electron source size could be reduced and the number of "useful" fast electrons increased.

- Finally, the presence of the cone will change the geometry of the interaction region, affecting electric and magnetic fields both internally and externally to the targets. The geometry will be somewhat similar to the target deformation produced by ponderomotive action on initially flat targets [207].

In this context, I think that the various types of diagnostics that have been implemented and used in the works related to my PhD thesis work, can be successfully used to study the behaviour of cone-targets. In particular I'm referring to proton imaging (allowing to study the generation of electrostatic fields on the rear side of the flat target behind the cone), to visible emission from the rear side (allowing to study the beam geometry with and without the cone), to classical and chirped shadowgraphy.

Some preliminary experiments have already been performed recently at LULI and showed no significant "cone" effect [208]. However in that situation the cone filling from the preplasma produced by the prepulse seemed to be the dominant aspect. Clearly there is need for more experiments in this field. At the same time, we have already recalled how our gas jet experiment was also probably useful in order to simulate some aspects of the cone situation, i.e. the passage of fast electrons through the density gap formed by the gold cone one side and the interior plasma on the other side.

In conclusion, it seems that despite the considerable increase in our knowledge, over the past 10 years, the problem of the transport in matter of relativistic currents exceeding the Alfvén limit, is still far from being understood. This may not be a reason for being disappointed, but rather a motivation for performing other, new and more

refined experiments which will address not only key questions related to the feasibility of fast ignition, but also fundamental questions in physics, such as propagation of very large currents in astrophysical jets. I'm happy that the experiments contained in my PhD work have been useful to clarify at least some open questions in this very complex problem.

Part V

Résume en Français

Chapter 10

Contexte du travail de recherche

Le développement des systèmes laser à Ultra Haut Intensité (UHI), capable de produire nouveaux phénomènes physiques, a permis le développement d'une recherche originale dans un grand nombre de domaines. Cependant les résultats décrits dans cette thèse sont limités à l'interaction d'une impulsion laser intense et courte avec des cibles solides et à l'étude du transport dans la matière d'intenses courants d'électrons relativistes. Entre d'autres applications que j'évoquerai brièvement, cette recherche est plus profondément liée au concept de l'allumage rapide dans le contexte de la fusion inertielle (FCI) [4]. Dans l'approche de l'allumage rapide les phases de la compression et du chauffage de la capsule de Deuterium-Tritium sont découplées. Ce dernier est fait à l'aide des lasers UHI tandis que la compression est réalisée avec les lasers conventionnels pour la FCI. Dans sa formulation originale, le processus se compose de quatre étapes:

1. La compression doit être faite le plus adiabatiquement possible mais sans le but de créer un point chaud central. Le noyau de la cible passe d'une densité $\rho = 0.3\,\mathrm{gcm}^{-3}$ à $\rho = 300\,\mathrm{gcm}^{-3}$. Une couronne de plasma sous-dense d'un millimètre de longueur entoure le noyau de la cible.

2. Une première impulsion ultra-intense (intensité $\sim 10^{18}$ W/cm^2; durée ~ 100 ps) creuse un canal dans la curonne sous-critique, et pousse la surface critique vers le noyau dense de la capsule.

3. Le canal est utilisé comme guide pour une deuxième impulsion ultra-intense plus courte ($\gtrsim 10^{20}$ W/cm^2; $\tau \sim 1$ ps) qui doit approcher le noyau comprimé autant que possible ($n_e \sim 10^{26}\mathrm{cm}^{-3}$) pour produire un faisceau d'électrons suprathermiques capable de pénétrer dans le combustible dense.

4. Ces particules voyagent sur quelques centaines de microns avant d'atteindre le secteur périphérique du noyau où ils déposent leurs énergies. Ces particules, dont l'énergie est de $\sim 1\,\mathrm{MeV}$, ont un libre parcours moyen voisins de celui des particules α de 3.5 MeV et peuvent créer un point chaud "latéral" où les conditions d'allumage sont atteintes: une température $T \sim 5 - 10\,\mathrm{keV}$ et une densité de surface $\rho R \sim 0.3 - 0.5\,\mathrm{gcm}^{-2}$ [5].

L'intérêt pour ce concept vient, tout d'abord, du découplage de la compression et du chauffage du combustible, qui réduit au minimum les contraintes sur l'uniformité d'éclairage et de la symétrie d'implosion. Ceci devrait permettre une plus grande tolérance aux instabilités hydrodynamiques. En plus, le point chaud est créé de manière isochore, (c.-à-d. beaucoup plus rapidement que les échelles du temps hydrodynamiques typiques). Ceci produit théoriquement un gain plus élevé que le modèle isobare habituel [6].

Cependant d'autres incertitudes demeurent sur l'allumage, que j'ai essayé dans ma thèse d'éclaircir avec en particulier la caractérisation du transport électronique dans la matière dense. En fait dans le contexte de l'allumage rapide, les électrons de quelques MeV, accélérés à la surface d'un plasma sur-critique doivent se propager vers le noyau de la cible et y déposer leur énergie. Le transport de cette population électronique suprathermique est régie par deux genres de mécanismes:

- Les collisions avec les électrons et les ions du milieu croisé. Dans ce cas-ci, chaque électron interagit individuellement avec le milieu. Ces interactions causent la diffusion angulaire (collisions élastiques) et la décélération (collisions non élastiques) des électrons.
- La génération *spontanée* des champs électromagnétiques, issues des effets collectifs qui dépendent de la densité du courant électronique du faisceau. Les effets collectifs sont également associés au développement des instabilités.

10.1 Autres applications

10.1.1 Accélération de faisceaux d'ions

L'interaction et la propagation des électrons rapides au travers de cibles solides peut conduire à l'accélération d'ions dans deux régions distinctes. Sur la surface irradiée par le laser, des électrons sont poussés vers l'intérieur de la cible par la force pondéromotrice. Ceci produit un champ de charge d'espace capable d'accélérer aussi vers l'intérieur de la cible les ions proches de la surface [15, 16, 17]. Après avoir traversés toute l'épaisseur de la cible, les électrons rapides s'échappent par la face arrière. Comme en face

avant, un champ de charge d'espace très intense, associé à un potentiel électrostatique de l'ordre de l'énergie moyenne des électrons, accélère des ions de la surface arrière [18, 19, 20, 21, 22, 23]. Une expulsion ionique se produit aussi en face avant car certains électrons sont accélérés vers le vide, directement ou après avoir été réfléchis par le champ de charge d'espace [15]. Les ions accélérés sont le plus souvent des protons, provenant soit du matériau lui-même, soit de l'adsorption de quelques monocouches d'eau ou d'huile sur la surface. Leur énergie maximale mesurée jusqu'à présent est de quelques dizaines de MeV avec une "température" typique de l'ordre de quelques MeV [19, 15, 23]. Des ions plus lourds comme du Pb^{46+} ont aussi été observés jusqu'à 430 MeV [15]. Le transfert d'énergie global entre l'énergie laser et l'énergie cinétique ionique peut atteindre 10% avec un nombre de protons accélérés compris entre 10^{12} et quelques 10^{13} pour des puissances laser de 100 TW à 1 PW [19].

A cause de la géométrie du mécanisme d'accélération, préferentiellement normale à la surface de la cible, la divergence angulaire de ces faisceaux d'ions peut être très faible. Ils peuvent donc servir à sonder des plasma denses [24, 25, 26, 22], voire se substituer aux électrons dans les schémas d'allumage rapide [27].

10.1.2 Accélération d'électrons

Les lasers de forte intensité, en raison des champs électriques énormes qui leurs sont associés, peuvent être utilisés pour leur capacité à accélérer efficacement des particules. Les plasmas sont des milieux accélérateurs idéaux car, contrairement à la matière non ionisée, ils supportent de forts gradients de champ électrique. Ils requièrent cependant la conversion du champ électrique transverse du laser en un champ longitudinal capable de piéger et d'accélérer les particules.

L'accélération d'électrons à de hautes énergies peut faire intervenir:

- L'excitation d'ondes plasma intenses [28].
- La pression électromagnétique du laser, i.e., l'action de sa force pondéromotrice [3, 29, 30].
- L'intéraction directe avec le laser (*Direct Laser Acceleration*, DLA) [31, 32].

Dans la première méthode, une onde plasma de vitesse de phase très proche de c est excitée. Cette méthode donne lieu aux énergies les plus élevées, car l'énergie maximale des électrons accélérés dépend de la vitesse de phase de l'onde accélératrice. Une accélération optimale nécessite un volume de plasma sous-dense faiblement inhomogène. Cette condition est satisfaite dans l'interaction avec un jet de gaz, ou bien, dans le cas d'une cible solide, au moyen d'un pré-pulse créant un pré-plasma devant la surface de la cible avant l'arrivée de l'impulsion principale.

Différents mécanismes accélérateurs par génération d'ondes plasmas sont possibles, comme l'**accélération par battement d'ondes** [28, 33, 34], l'**accélération par le sillage de l'impulsion laser** [28, 35] et l'**accélération auto-modulée** [36, 37, 38].

Jusqu'à présent ont déjà été observés des électrons accélérés à des énergies jusqu'à $\sim$ 200 MeV [39]. Le développement de ces techniques suivent le développement de la technologie laser vers des éclairements toujours plus intenses et permet d'envisager d'autres applications que l'allumeur rapide, dans des domaines [40] tels que la physique des hautes énergies [41], la science des matériaux [43] et médicale [42].

10.1.3 Sources de rayonnement cohérent

Le rayonnement X cohérent produit dans l'interaction laser-plasma à très haut flux peut servir à sonder nombre de processus biologiques avec une résolution temporelle inégalée [44]. Pour résoudre clairement la matière organique, il doit être compris dans une gamme de fréquences particulière, qu'on appelle la fenêtre d'eau et qui s'étend de 23.3 Å à 43.6 Å. Le rayonnement doit être doté, de plus, d'une forte brillance, une bonne directivité et d'une certaine cohérence. Tirant profit de différentes propriétés des plasmas, deux voies sont étudiées pour produire un tel rayonnement:

- Le laser X utilise les propriétés atomiques des plasmas créés par l'interaction laser UHI - solide contenant des ions multichargés, et qui sont des sources naturelles d'emission X-UV [45].

- Les non-linéarités, en milieu gazeux ou dans un plasma, du mouvement d'un électron dans une onde laser ultra-intense entrainent le rayonnement d'harmoniques de l'onde laser initiale [46]. Ceci peut facilement être mis en oeuvre dans un plasma sous-critique, ou dans l'épaisseur de peau lors de l'interaction avec un solide, pour produire du rayonnement X cohérent. Dans le cas du solide, le couplage de l'onde incidente avec des modes de surface peut aussi produire des harmonique de l'onde laser [47, 48].

10.1.4 Sources de rayonnement incohérent

Un plasma dense et chaud, fruit de l'interaction d'un laser UHI avec une cible solide, est une excellente source de rayonnement X incohérent. Celui-ci résulte soit de recombinaisons radiatives (transition libre-lié) soit d'excitations ou de désexcitations atomiques (lié-lié). Lors du dépôt de l'énergie laser, le plasma émet des photons X dans une gamme d'énergie allant de quelques eV à quelques keV. Après l'interaction, le plasma se refroidit et n'émet plus de rayonnement.

De plus, un rayonnement X dans le domaine du MeV est engendré par les électrons suprathermiques créés lors de l'interaction à la surface du plasma. Leur propagation dans la matière dense s'accompagne d'un rayonnement qui est la juxtaposition d'un ensemble de raies dues à l'ionisation du milieu (transition lié-libre: arrachement d'électrons des couches atomiques K) et d'un fond continu de type bremsstrahlung consécutif aux collisions électron-ion (transition libre-libre). La distribution en énergie et en angle de ce rayonnement dépend de la distribution électronique, du type de matériau considéré et de l'épaisseur de la cible traversée. Si les électrons sont assez énergétiques, on peut s'attendre à du rayonnement γ avec l'émission de photons qui peuvent atteindre 20 MeV [49]. Ce rayonnement peut servir de faisceau sonde pour des expériences de radiographie éclair dans des milieux très denses à évolution rapide [18].

10.1.5 Source des neutrons

L'irradiation de matériaux deutérés par les lasers UHI peut produire des neutrons par les ions accélérés à la surface de la cible [50, 51, 52, 53], selon la réaction

$$\mathrm{D} + \mathrm{D} \longrightarrow {}^{3}\mathrm{He} + \mathrm{n}$$

Ces neutrons peuvent servir à diagnostiquer l'interaction laser-matière, notamment la distribution ionique.

Des photoneutrons sont également produits par l'interaction du rayonnement γ décrit plus haut avec les atomes de la cible [54].

10.1.6 Études d'astrophysique

L'interaction laser-matière à des éclairements supérieurs à 10^{20} Wcm^{-2} pourrait permettre de reproduire en laboratoire des conditions astrophysiques. On peut ainsi imaginer étudier les taux de réaction nucléaires dans la matière dense, la physique des métaux à ultra-hautes pressions (tranformation de phase, métallisation et cristallisation de l'hydrogène), ou les mécanismes physiques gouvernant les supernovæ, les étoiles et les nébuleuses [55, 56].

Chapter 11

Propagation d'électrons rapides dans des jets de gaz

Jusqu'ici, beaucoup d'expériences ont été effectuées en utilisant des diagnostics optiques afin d'étudier la propagation d'électrons rapides dans des cibles solides et plus pariculièrement le chauffage qu'elles induisent. Ces expériences ont été souvent basées sur le diagnostic d'ombroscopie [119, 120] ou de réflectométrie [121] visant à détecter la propagation du front d'ionisation à l'intérieur des cibles transparentes. L'effet de la densité de la cible sur la propagation des électrons a été mise en évidence dans des expériences utilisant la spectroscopie K_α et de cibles de mousse [124]. Ceci a été lié à la différence de conductivité pour différents chauffages induits par la propagation d'électrons rapides [124, 116]. La nécessité de neutraliser le courant aussi bien que la charge explique l'effet dramatique de la densité des électrons libres dans le milieu sur la propagation. Ceci explique qualitativement les différences observées entre les isolants et les conducteurs: dans les isolants, des électrons libres doivent être créés par ionisation d'effet du champ ou par ionisation d'impact, des processus qui exigent du temps et de l'énergie. Ceci a comme conséquence des champs plus forts et un mouvement plus empêché. Quant à la nature des champs produisant l'inhibition, Bell *et al.* considèrent un champ électrostatique [110]. Tikhonchuk [96] calcule explicitement la séparation de charge et les champs électrostatiques par l'équation de Poisson.

Cependant, la plupart des modèles numériques [111, 125, 126] négligent les champs électrostatiques; les champs inductifs jouant le rôle principal (hypothèse raisonnable dans des conducteurs mais probablement pas dans les isolants). En plus, la présence des forts champs électromagnétiques dans le matériel a été inférée grâce a l'observation de l'inhibition électrique de la propagation des électrons rapides dans les isolants [129] et les mousses [124], mais ils n'ont pas été directement démontrés. De ce point de vue,

la propagation des électrons rapides dans des cibles de gaz est la plus prometteuse: en effet en raison de la basse densité d'électrons du matériel, il est particulièrement difficile d'établir une courant de retour, contribuant à une grande séparation de charge et à des champs électrostatiques très forts.

Afin d'étudier la dynamique des électrons rapides à ces faibles densités où l'inhibition électrique est maximisée et afin de montrer directement l'existence de tels champs électrostatiques énormes, nous avons réalisé quelques expériences en utilisant deux diagnostics complémentaires, résolus temporellement et spatialement:

- *l'ombroscopie classique* et *chirpée*: puisque le gaz est transparent à la lumière sonde, nous avions utilisé l'ombroscopie (dans deux configurations différentes) pour suivre la dynamique des électrons rapides. Ceci dans sa configuration *chirpée* est un diagnostic nouveau, qui permet de suivre l'évolution lors d'un seul tir laser, à la différence de l'ombroscopie classique 2D. Le diagnostic de l'ombroscopie *chirpée* est tout à fait semblable à celui utilisé dans [131] à l'exception que là le faisceau sonde a été réfléchi sur une cible solide perturbée, alors qu'ici le faisceau sonde transversalement le gaz.

- *radiographie protonique*: les protons produits par laser peuvent être employés pour mesurer une différence de masse dans le matériel traversé [22]. Cependant, puisque les protons sont des particules chargées, ils sont sensibles aux champs électriques et magnétiques, permettant la mesure directe de tels champs [132]. Notons qu'une telle possibilité est limitée seulement aux champs quasi-statiques, qui est bien notre cas, puisque des champs d'oscillation rapides sont moyennés. En effet le milieu gazeux est pratiquement non-collisionel pour les protons sonde dû à sa faible densité. Par conséquent n'importe quelle déviation des protons peut seulement être due aux champs électriques et magnétiques.

Dans ce contexte, nous produisons d'abord des électrons rapides en éclairant une cible métallique mince (Ti) avec un laser UHI, avant de les propager dans un jet de gaz (Ar ou He) à différentes densités. Les avantages d'utiliser un gaz sont: (i) la densité peut être facilement changée en ajustant la pression; (ii) les gaz sont optiquement transparents de sorte que l'ombroscopie optique puisse être employée comme un outil diagnostique; (iii) un gaz, comme la mousse, la silice et le plastique, est un isolant, ce que implique la nécessité d'ionisation; (iv) des densités très faibles peuvent être employés, pour ainsi maximiser l'inhibition; ceci offre une possibilité unique d'étudier l'inhibition quand elle n'est pas marginale. En outre, le milieu gazeux est pratiquement non-collisionel pour les électrons rapides, par conséquent l'effet principal sur la propagation est dû aux champs auto-produits.

Il convient de noter que, dans l'allumage rapide, le dépôt de 10 kJ en $\sim$ 10 ps sur $\sim$ 10 μm [4] implique des densités d'électrons rapides $n_b \sim 10^{23}\text{cm}^{-3}$ beaucoup plus

grandes que celles des plasmas coronaux typiques ($n_e \sim 10^{21}\text{cm}^{-3}$). Cette inégalité en effet est aussi rencontrée dans notre expériences: pour laquelle les électrons ont une énergie typique de 1 MeV qui représente $15-25\%$ de l'énergie laser [129, 133, 134]. Puisque le faisceau d'électrons est produit à partir d'une région comparable à la tache focale pendant un temps de l'ordre de la durée de l'impulsion laser, nous obtenons $n_b \sim 5\times10^{20}\text{cm}^{-3}$, alors que les densités atomiques du gaz utilisées dans l'expérience sont $3\times10^{19}\text{cm}^{-3}$.

11.1 Configuration expérimentale

L'expérience a été réalisée avec le laser 100 TW du Laboratoire pour l'Utilisation des Lasers Intenses (LULI) (350 fs, 1.057 μm, impulsion laser avec une énergie jusqu'à 10 J) focalisé par une parabole hors-axe $f/3$ en incidence normale sur les cibles. Le diamètre de la tache focale était $\leqslant 15\,\mu$m donnant des intensités jusqu'a 5×10^{19} W/cm^2. La configuration expérimentale de l'ombroscopie est montrée dans la Fig. 11.1

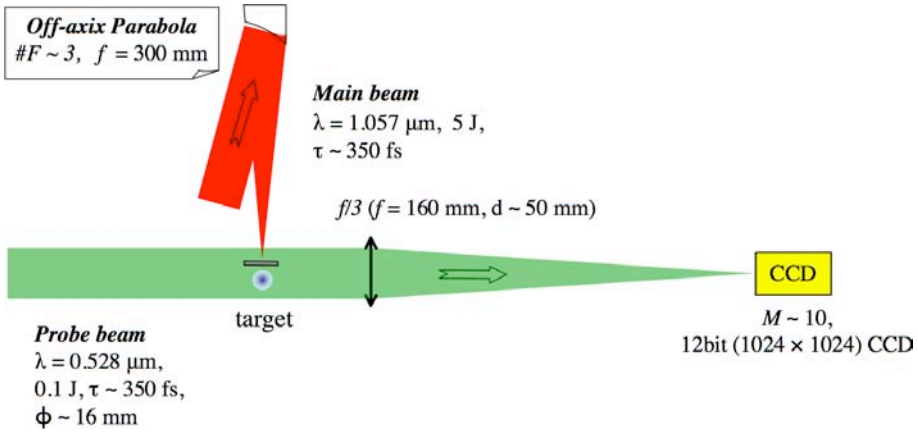

Figure 11.1: Configuration expérimentale pour le diagnostic d'ombroscopie. L'épaisseur du jet de gaz après la feuille est de 1.2 mm. L'épaisseur est de 20 μm (Ti) et 15 μm (Al).

Dans l'expérience d'ombroscopie *classique*, le faisceau sonde a été envoyé sur une caméra CCD par un systeme optique imageur. Le faisceau sonde est une petite fraction (0.1 J, diamètre de 16 mm) du faisceau principal converti à 2ω. Ceci permet la formation transversale d'images 2D sur une CCD avec un filtre centré à 528 nm et avec une résolution de $\approx 5\,\mu$m et de ≈ 400 fs. La région ionisée est opaque à la sonde et produit une image *instantanée* 2D. Le retard entre le faisceau principal d'interaction et le faisceau sonde a été alors changé de tir en tir nous permettant de suivre la dynamique d'ionisation dans le gaz et de reconstruire l'évolution temporelle de la propagation des électrons rapides dans le gaz.

Dans l'expérience d'ombroscopie *chirpée*, le faisceau sonde a eu une durée de $\approx$ 15 ps et a été temporellement chirpé. Après la traversée du gaz, le faisceau sonde a été envoyé dans un spectromètre imageur. La relation linéaire entre λ et t dans le faisceau chirpé permet d'obtenir des images 1D d'ombroscopie qui donne l'évolution temporelle en un seul tir laser. Les images obtenues sont par conséquent semblables à celles d'une caméra à balayage de fente mais avec une résolution temporelle qui peut être meilleure [131]. Dans notre cas, un tel diagnostic permet de mesurer avec précision la propagation du bord du nuage d'électrons dans le gaz (front d'ionisation) en fonction du temps.

Dans l'expérience de radiographie protonique, nous avons employé un deuxième faisceau, qui a été focalisé sur une feuille mince d'or ou de tungstène (15 μm) afin de produire un faisceau de protons [132]. Ceci a été alors employé pour obtenir des images radiographiques (imagerie en champ lointain) du gaz sur une pile de films radiochromics [132]. C'est un diagnostic unique permettant de détecter la présence des champs magnétostatiques et électrostatiques. L'arrangement expérimental est montré dans la Fig. 11.2

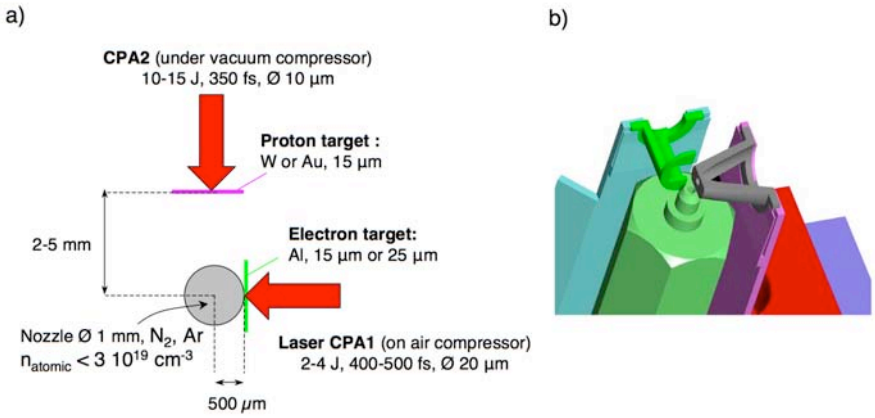

Figure 11.2: a) Configuration expérimentale pour la radiography protonique. b) Détail du système support de la cible/buse pour la l'expérience d'imagerie protonique.

Nous avons mesuré par spectroscopie K_α [129], une pénétration d'électrons rapides dans des cibles d'Al de 110 μm d'épaisseur, correspondant à une énergie moyenne de 235 keV et à une intensité laser de 1.2×10^{18} W/cm^2 (en employant la loi d'échelle bien connue pour l'énergie des électrons rapides rapportée dans [95]). Ceci doit être comparé aux énergies des électrons rapides ($\approx$ 1 MeV) créés par le faisceau principal [133].

Le jet de gaz a été caractérisé dans des conditions proches de celles de l'expérience. La densité atomique en position où le laser CPA a été focalisé (1.2 mm de la buse) a été mesurée par un diagnostic interférométrique (voir la Fig. A.11).

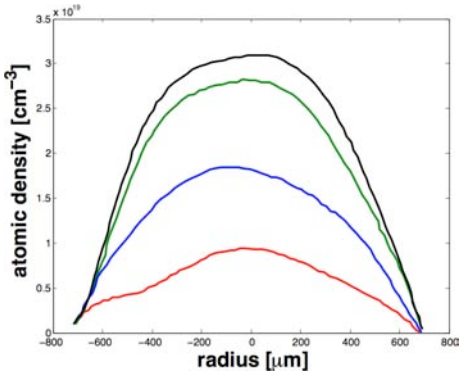

Figure 11.3: Profil de densité dans le jet de gaz: densité atomique (cm^{-3}) en fonction de la distance du centre du jet de gaz (μm).

11.2 Expériences d'ombroscopie classique

La Fig. 11.4 montre une image d'ombroscopie typique obtenue dans notre expérience (ici Δt est le retard entre le faisceau laser principal CPA et le faisceau sonde). En changeant Δt, il est possible de reconstruire l'évolution de la région ionisée dans le gaz (région foncée dans l'image d'ombroscopie dans la Fig. 11.4).

La Fig. 11.5 donne un sommaire de nos résultats pour différents gaz et différentes pressions. Les lignes droites correspondent à des interpolations linéaires des données. La pente de l'interpolation donne une vitesse moyenne d'expansion. En réalité en regardant attentivement les données, nous voyons une première phase d'expansion rapide suivie d'un ralentissement. C'est particulièrement clair dans la série avec He à 30 bar, qui se prolonge à des plus long retards.

Plusieurs caractéristiques émergent clairement:

- (i) la vitesse d'expansion du nuage d'électrons est tout à fait subrelativiste (de $c/10$ à $c/30$);
- (ii) la vitesse augmente avec la densité électronique dans le milieu;
- (iii) d'ailleurs, des images d'ombroscopie enregistrée pour des retards Δt courts montrent que la dimension initiale du nuage est de 100 μm, donc beaucoup

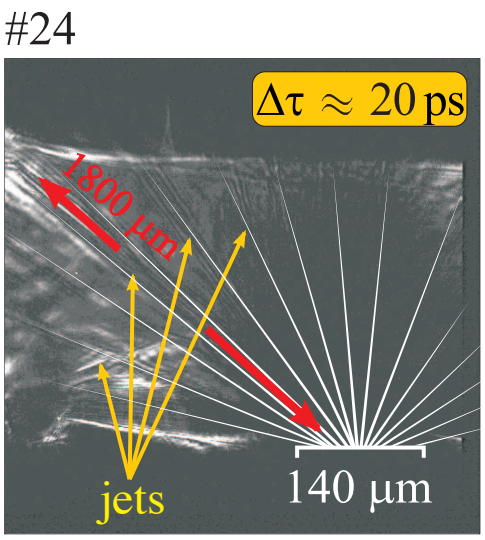

Figure 11.4: Image d'ombroscopie classique: Ar 70 bar, $\Delta t \approx 30$ ps. Les lignes jaunes montrent quelques unes des lignes droites observées reliées probablement à des jets d'électrons.

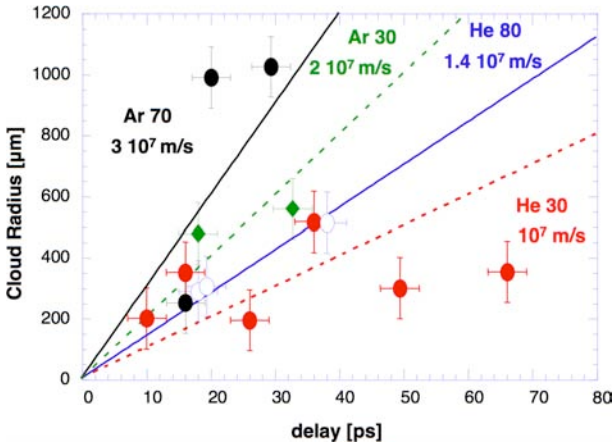

Figure 11.5: Reconstruction pour des tirs typiques de l'expansion spatiale du nuage électronique en fonction du temps et pour différentes pressions et types de gaz.

plus grande que la taille de la tache focale et de la taille prévue pour la source d'électrons rapides.

11.3 Modèle théorique

Nous pensons que, dans nos conditions expérimentales, la propagation des électrons rapides est principalement dominée par le besoin d'un courant de retour neutralisant et par la création des champs électrostatiques dus à la séparation de charge. D'abord nous discutons ce qui se produit à l'interface feuille/gaz.

La condition pour la neutralisation des électrons rapides et du courant de retour donne

$$J_{TOT} = en_b v_b – en_e v_e \simeq 0, \tag{11.1}$$

et puisque le v_e ne peut pas être $> c$, il suit que: $i.$) le courant maximal d'électrons rapides qui peut propager est $n_e c$, et $ii.$) les électrons du milieu sont également accélérés à des vitesses élevées (par conséquent parler d'électrons rapides et lents n'est plus correct).

Tandis que pour la matière dense ($n_e \gg n_b$) une petite vitesse de retour est suffisante pour la neutralisation en courant, dans notre cas les quelques électrons du milieu sont fortement accélérés et le faisceau d'électrons rapides est forcé de se déplacer avec la même vitesse que le courant de retour. La condition dans l'équation 11.1 explique également pourquoi la taille minimale de nuage est grande. Quand les électrons rapides arrivent sur la face arrière (dans un temps $t \sim d/c$, plus court que la durée d'impulsion), leur densité est grande et ils ne peuvent pas pénétrer le gaz parce que leur courant ne peut pas être compensé. Seulement quelques uns s'échappent, générant un champ électrostatique, qui arrête complètement tous les autres électrons rapides (jusqu'à ce que des ions soient également mis en mouvement). En effet tous les électrons rapides qui ne s'échappent pas, sont efficacement confinés dans la cible (avec un mouvement de reflux) où ils se déplacent le long de la surface arrière. Ces effets provoquent une réduction de densité, jusqu'à $n_b \sim n_e$ dans le gaz. Un rayon final du faisceau d'électrons en accord avec la taille observée peut alors facilement être calculé.

Quand les électrons rapides commencent à se propager dans le gaz, leur mouvement sera dominé par la séparation de charge. En employant pour simplicité un degré d'ionisation $Z^* = 1$, on dérive explicitement la séparation de charge:

$$\Delta n = n_e - n_i = n_i E/(m_e \nu v_b/e + E), \tag{11.2}$$

où E est le champ électrostatique dû à la séparation de charge, v_b la vitesse d'électrons rapides et ν est la fréquence de collision. Dans le cas des solides ($n_e \gg n_b$),

qui implique une petite séparation de charge Δn, des champs relativement petits et une inhibition faible (en particulier, E peut être négligé dans le dénominateur de l'équation 11.2) la vitesse du faisceau v_b n'est pas très différent de c. Dans notre cas, au contraire, la densité des électrons rapides produits dans la feuille est beaucoup plus grande que la densité du gaz de fond. Les deux termes dans le dénominateur deviennent comparables, impliquant

$$\Delta n \sim n_i/2 \tag{11.3}$$

c.-à-d. la séparation de charge est de l'ordre de la densité de fond, comme on peut l'estimer euristiquement. Compte tenu que $n_b \sim n_e$ à partir de l'équation 11.1, nous obtenons $n_e \sim n_i \sim n_b$, et grâce à l'équation de Poisson nous obtenons:

$$\nabla E \sim E/\Delta x = +4\pi e \Delta n \sim -4\pi e n_b, \tag{11.4}$$

Pour trouver la largeur Δx et le champ électrique E, nous considérons que l'énergie potentielle maximale des électrons rapides dans le champs doit être de l'ordre de leur énergie cinétique initiale : $kT_{hot} \sim eE\Delta x$, où kT_{hot} est l'énergie moyenne de l'électron rapide (ici ~ 1 MeV). Puis

$$\Delta x \sim E/4\pi e n_b = (kT_{hot}/e\Delta x)/4\pi e n_b = \lambda_D \tag{11.5}$$

c.-à-d. la neutralité peut seulement être violée au-dessus de la longueur de Debye (des électrons rapides). Bien que ce résultat semble très habituel, nous soulignons le point qu'il peut seulement être dérivé dans la limite des basses densités de fond (en effet pour le cas des solides on utilise une expression différente pour Δx). En même temps, nous obtenons l'expression ambipolar habituelle pour le champ électrostatique

$$E \sim kT_{hot}/e\lambda_D = (4\pi e n_b kT_{hot})^{1/2} \tag{11.6}$$

qui, dans nos conditions expérimentales, peut facilement atteindre 10^{12} V/m. Un si énorme champ électrique produit très rapidement une forte ionisation du gaz de fond, créant des électrons libres, qui sont nécessaires pour le courant de retour. Alors la distance Δx correspond également à la largeur du front d'ionisation dans le gaz. Le temps d'ionisation peut être calculé en employant la formule de Keldish [144] ou $t = 1/\nu(E)$ (fréquence de ionisation de Keldish). Des taux d'ionisation calculés pour l'Ar sont montrés en fonction de la densité du gaz de fond dans la figure 11.6. Notez que la fréquence d'ionisation de Keldish dépend seulement de l'amplitude du champ électrique. Cependant dans notre modèle E dépend de la densité (puisque, encore $n_b \sim n_e$), ce que explique la dépendance représentée dans la figure 11.6. Bien que la phase d'ionisation soit très rapide, elle est néanmoins fondamentale, pour créer

non seulement les électrons libres mais pour fixer également la densité de fond. Les champs électrostatiques énormes surgissant dans le gaz existent seulement au-dessus d'une distance λ_D et donc pour un temps $t_E < \lambda_D/v_b$. L'ionisation doit alors avoir lieu dans un temps plus court. Par conséquent dans nos conditions, les états d'ionisation accessibles sont Ar^{6+} et He^{2+}.

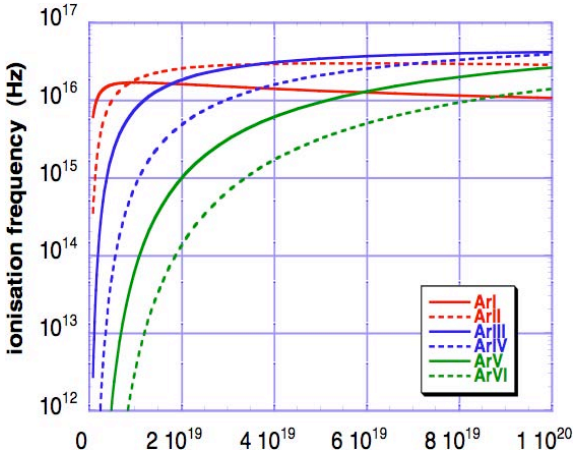

Figure 11.6: Fréquence d'ionisation en fonction de la densité de gaz d'Ar (cm^{-3}), selon la formule de Keldish (pour comparaison $t_E \sim \lambda_D/c/20 \sim 10^{-14}$ s). La force du champ électrique est calculée selon l'équation 11.6

En conclusion, des électrons libres sont mis en mouvement et établissent un courant de retour qui annule la charge positive laissée derrière par les électrons rapides. Ici nous avons une autre grande différence avec le cas des solides. Ceci est valide pour de faibles champs électriques parce que la vitesse atteinte par les électrons doit être à tout moment plus petite que la vitesse thermique ($v_e \ll v_T$). Par contre dans notre cas les champs sont très grands. En plus des électrons sont créés (par ionisation) avec une énergie très petite et mis en mouvement par le champ: par conséquence il n'y a aucune vraie vitesse thermique mais seulement la vitesse acquise dans le champ. Alors en identifiant euristiquement la vitesse de dérive et la vitesse *thermique* dans l'expression $v_e = eE/m_e v$ et $v = v_t/\lambda_{ii}$ (λ_{ii} est la distance inter-ionique dans le matériel) nous obtenons

$$v_e \sim \sqrt{\frac{eE\lambda_{ii}}{m_e \nu}} \tag{11.7}$$

L'hypothèse que ν soit déterminé par λ_{ii} peut être considéré comme l'analogue de la limite d'Ioffe-Regel pour les solides et est justifié parce que, bien que nous traitions un gaz ionisé, la *température* des électrons créés est au début si basse que l'approximation habituelle de plasma (menant à la formule de Spitzer pour la fréquence de collision) échoue, en raison du nombre très petit de particules dans la sphère de Debye.

Notons également qu'une dépendance quadratique de la vitesse de dérive en fonction du champ électrique est dérivée par Landau et Lifshitz [57] dans la limite des champs très forts.

L'établissement d'un courant de retour et l'annulation de la charge positive laissée derrière par les électrons rapides nécessite un temps de l'ordre de $t \approx \lambda_D/v_e$, où v_e est la vitesse de dérive, donnée dans notre modèle par l'équation 11.7. Ce processus est lent parce que les électrons libres sont (au moins au commencement) ralentis et fortement collisionels, et les collisions empêchent le courant de retour. Depuis, comme aucune autre propagation des électrons rapides n'est possible avant que la séparation de charge ait été annulée, le courant des électrons rapides est finalement forcée de se déplacer avec une vitesse égale à la vitesse de retour des électrons du fond, c.-à-d. pratiquement la vitesse d'expansion est v_e. Ceci donne une vitesse lente et un mouvement fortement empêché.

Notons également que, vu les états d'ionisation accessibles Ar^{6+} et He^{2+} (voir la Fig. 11.6), les vitesses expérimentales d'expansion dans la Fig. 11.5 dépendent simplement de la densité de fond n_e (et ils sont plus grandes pour de plus grandes densités) indépendamment du type du gaz. En plus, les vitesses du faisceau de l'équation 11.7 sont très près des valeurs expérimentales.

Nous devrions également nous interroger sur la perte d'énergie dans un milieu gazeux qui est non-collisionel (au-dessus de nos distances) pour les électrons rapides. Les résultats d'imagerie K_α et OTR prouvent que peu d'électrons atteignent le deuxième feuille ou au moins ne sont plus *énergiques*. En effet l'énergie dépensée en ionisant une région de gaz aussi grande que $\approx$ 1.2 mm peut être comparable à celle des électrons rapides (30% de l'énergie laser). En plus le champ électrostatique lui-même est un mécanisme dissipatif efficace, arrêtant tous les électrons rapides impliqués dans le processus de séparation de charge sur une distance $\approx \lambda_D$. Des calculs simples montrent comment ces effets peuvent complètement consommé l'énergie du faisceau d'électrons rapides. Ils fournissent également des mécanismes efficaces pour la décélération du nuage, comme précédemment noté.

11.4 Ombroscopie chirpée

Des images typiques d'ombroscopie chirpée sont montrées dans la Fig. 11.7 pour des tirs sur 15 μm d'Al suivi d'un gaz d'Ar à différentes pressions.

Elles nous permettent de suivre la dynamique du nuage d'électrons en un seul tir laser. En accord avec les résultats d'ombroscopie classique, nous observons:

- (i) la vitesse de propagation augmente avec la pression du gaz. La taille finale à la fin de l'image correspond à la taille observée dans les images d'ombroscopie

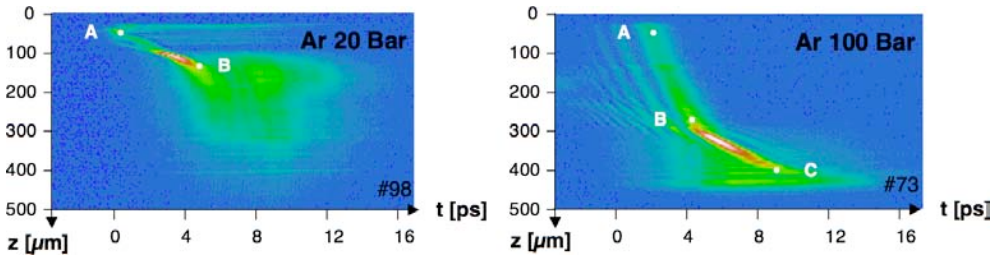

Figure 11.7: Images d'ombroscopie chirpée obtenues pour un gaz d'Ar et une cible d'Al de 15 μm à deux pressions différentes. Les vitesses sont $V_{AB} \approx 0.12\,c$ pour la premiere image et $V_{AB} \approx 0.67\,c$ et $V_{BC} \approx 0.16\,c$ pour la seconde.

2D (c.-à-d. une fraction de 1 mm);

- (ii) la vitesse de propagation diminue au cours du temps. Par exemple à partir de l'image dans la Fig. 11.7 à droite (Ar a 100 bar) nous obtenons $V \approx 0.67\,c$ pour le premiers instants et $V \approx 0.16\,c$ pour les retards plus grands. Par contre dans la Fig. 11.7 à gauche la vitesse est toujours plus petite ($V \approx 0.12\,c$) et la distance finale de pénétration est inférieure.

Comme déjà remarqué dans la section 11.2, les résultats de notre expérience précédente d'ombroscopie montrent en effet également un tel ralentissement.

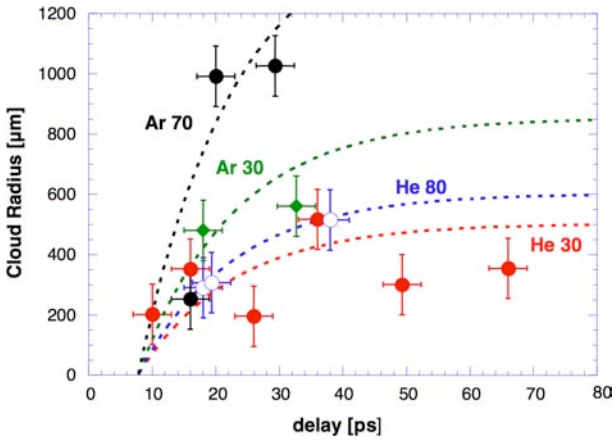

Figure 11.8: Les mêmes données expérimentales de la Fig. 11.5 interpolées avec des courbes du type $r(t) = r_{max}(1 - exp(-t/t_0))$ où le temps de montée est de 15 ps pour toutes les pressions et pour différents gaz. Symboles identiques à ceux de la Fig. 11.5

La Fig. 11.8 montre les mêmes données de la Fig. 11.5 interpolés avec des courbes

du type $r(t) = r_{max}(1 - exp(-t/t_0))$ où le r_{max} est la pénétration maximale et t_0 un temps d'échelle caractéristique.

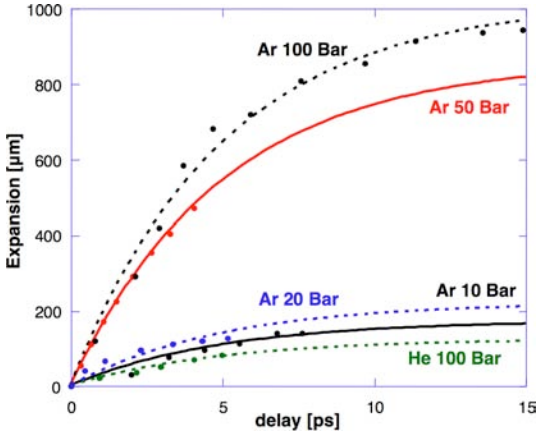

Figure 11.9: Reconstruction pour des tirs typiques de l'expansion spatiale du nuage électronique en fonction du temps pour différentes pressions et types du gaz.

La Fig. 11.9 montre l'évolution temporelle de la taille du nuage pour différentes pressions du gaz, obtenue à partir des images typiques d'ombroscopie chirpée. Toutes les courbes dans les Fig. 11.8 et 11.9 correspondent à un temps de montée de 15 et 5 ps, respectivement. En réalité, à partir de ces données il n'est pas possible de conclure si l'expansion s'arrête ou continue indéfiniment avec une petite vitesse. Par conséquence la valeur absolue du r_{max} n'est pas vraiment signicative; cependant, elle montre que le r_{max} augmente avec la densité du gaz.

11.5 Radiographie protonique

Dans l'expérience de radiographie protonique, un paramètre critique était la distance entre le jet de gaz et la cible de protons parce que la présence d'une densité atomique résiduelle à la face arrière de la cible de protons était une cause très importante de détérioration du faisceau de protons (énergie maximale obtenue). L'énergie maximale mesurée avec le gaz était de l'ordre de $5 - 6$ MeV (ou de 4 films radiochromic) contre 12 MeV ou plus sans le gaz.

La Fig. 11.10 montre des images typiques de radiographie protonique. Nous voyons clairement une forme hémisphérique, qui semble montrer la présence d'un champ électrostatique très fort, située dans le front d'ionisation (voyez pour comparaison une image d'ombroscopie classique rapportée dans la Fig. 11.4), qui dévie les protons. Dans ce cas-ci la pression du gaz (N_2) a été changée, montrant une pénétration accrue

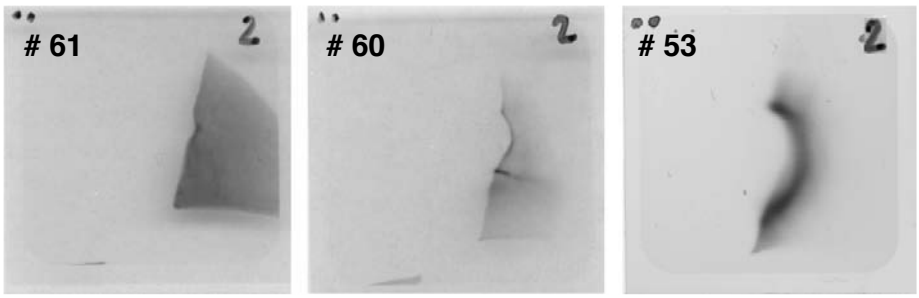

Figure 11.10: Images protoniques obtenues avec un gaz de N_2 à 15, 30, et 100 bar. Dans tous les cas, la taille des films radiochromic est de 25 mm × 25 mm, la cible pour les protons est de 15 μm d'or et la cible pour les électrons est de 15 μm d'Al. La distance entre la cible pour les protons et le jet de gaz est de 5 mm et la distance entre le jet de gaz et les films radiocromics est de 38 mm. L'énergie sur la cible de protons est de $\approx$ 22 J et de 1.1 J sur la cible d'électrons. Toutes les images correspondent à $\approx$20 ps après l'arrivée du faisceau laser principal sur la cible d'électrons (c.-à-d. elles sont produites par des protons avec une énergie de $\approx$ 3 MeV).

pour des pressions plus élevées, en accord avec les résultats d'ombroscopie.

De plus, la taille de la région est en accord qualitatif avec les résultats d'ombroscopie (notons que dans une expérience d'imagerie en champs lointain, le grandissement géométrique serait de $\approx$ 10. Cependant puisqu'ici nous employons plutôt une approche de déflectométrie, le grandissement géométrique n'est pas strictement respecté).

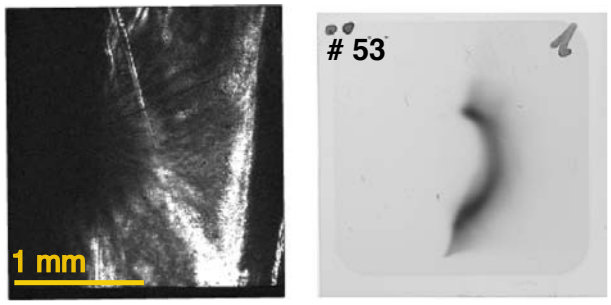

Figure 11.11: Comparaison d'une image d'ombroscopie (Ar a 70 bar, 5 ps après le tir CPA, électrons de 1 MeV) avec une image de radiographie protonique (N_2 a 100 bar, 20 ps après le tir CPA, électrons de 200 keV)

La Fig. 11.11 montre la comparaison entre une image de protons et une image d'ombroscopie. Des différences quantitatives peuvent être attribuées au différents gaz et, surtout, au différentes énergies des électrons rapides.

La formation des images protoniques, due à la déflexion de protons, donne une claire et directe évidence de la présence des champs très forts (champs magnétiques et électriques quasi-statiques) dans le gaz. En effet le pouvoir d'arrêt du gaz est clairement négligeable pour des protons à ces énergies. Toutefois la résolution temporelle était faible, étant donné que nous avons seulement enregistré ces images sur seulement 4 films radiochromic. En particulier, ceci n'a pas permis de résoudre temporellement la phase initiale d'évolution rapide. Toutes nos images correspondent donc pratiquement à la phase quasi stationnaire finale.

Cependant, dans quelques autres tirs, nous avons trouvé quelques double-bulles, c.-à-d. des structures sphériques comme celles montrées dans Fig. 11.12, qui ont une taille semi-macroscopique (de quelques centaines de μm).

De tels résultats sont toujours en cours d'analyse et, pour le moment, l'origine de telles bulles n'est pas comprises.

Au contraire, la présence d'un front, comme montrée dans la Fig. 11.10, semble être bien comprise et en bon accord, avec les résultats d'autres diagnostics (ombroscopie classique et chirpée).

Figure 11.12: Double-Bulle observée lors de quelques tirs laser. Ici l'image protonique a été obtenue avec un gaz de N_2 à $50 \approx 28.8$ ps après l'arrivée du faisceau laser principal sur la cible d'électrons (c.-à-d. ils sont produites par des protons avec une énergie de ≈ 3.1 MeV).

Ces images de protons ont été reconstruites en employant un code de tracé de rayons [25], qui simule la configuration expérimentale et tient en compte des distances. En accord avec les résultats d'ombroscopie chirpée, nous avons supposé un hémisphère en expansion selon la loi $r(t) = r_0(1 - exp(-t/t_0))$. En plus, à partir de notre modèle théorique décrit dans la section précédente, nous avons supposé un champ électrique qui est concentré aux bords de l'hémisphère et qui décroît radialement selon une loi exponentielle, sur une distance typique de l'ordre de quelques longueurs de Debye des électrons rapides (c.-à-d. quelques μm). À l'intérieur de la sphère le champ électrostatique est constant et décroît beaucoup (au moins deux ordres de grandeur) en dehors de cette zone. La Fig. 11.13 montre un résultat typique issu d'une simulation d'une image protonique, correspondant à un champ électrostatique maximale de $\approx 10^{11}$ V/m et qui tombe à zéro sur une distance de $\approx 10\,\mu$m.

De telles valeurs sont en bon accord avec les prévisions théoriques. Naturellement puisque toute la déviation dépend de l'intégrale linéaire $\int Edx$, d'autres valeurs du champ maximal et des distances de décroissance peuvent également reproduire nos images. Toutefois pour des champs électriques trop bas, il n'est pas possible d'expulser tous les protons de la région à l'intérieur du front, ce qui serait contraire aux images montrées dans la Fig. 11.10.

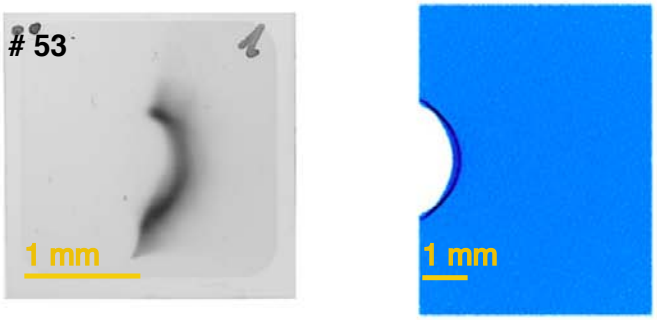

Figure 11.13: Simulation d'une image de radiographie de protons obtenue avec des protons de 3.1 MeV d'énergie et les paramètres suivants: $E_{max} = 10^{11}$V/m, $E_{plateau} = 10^{5}$V/m, $r_0 = 100\,\mu$m, $L_{in} = 10\,\mu$m, $L_{out} = 10\,\mu$m (distances de décroissance interne et externe).

11.6 Conclusions

Dans nos expériences sur la propagation dans un gaz, nous avons mis en place un diagnostic nouveau, qui nous a permis d'observer une inhibition très forte de la propagation des électrons rapides.

En particulier dans les expériences d'ombroscopie nous avons montré comment: (i) la densité du gaz détermine la propagation des électrons rapides. Aux petites densités correspondent des courants de retour plus faibles et un mouvement plus empêché. La vitesse de propagation comme la distance de pénétration augmentent avec la pression du gaz. (ii) La vitesse d'expansion diminue au cours du temps. (iii) La phase d'ionisation est essentielle pour produire les électrons libres pour le courant de retour. Dans nos conditions, l'ionisation de champ est dominante. (iv) Les champs électrostatiques sont fondamentaux dans la propagation des électrons rapides. Ils obligent les électrons libres à retourner avec une vitesse déterminée par la force du champ et par le nombre de collisions (c.-à-d., par la densité du gaz).

En plus, le diagnostic de radiographie protonique nous a permis de montrer la présence des champs électrostatiques très forts au bord du nuage dont les dimensions sont en accord avec le diagnostic d'ombroscopie. Ces résultats donnent la première évidence expérimentale directe de la présence de champs énormes qui ont été longtemps prévus associés à supposés être la propagation d'électrons rapides. Ils prouvent en effet que la valeur du champ électrostatique peut être de l'ordre des prévisions théoriques. En plus nous avons observé quelques structures de bulles dont l'origine n'est pas encore comprise.

Chapter 12

Propagation des électrons rapides dans des cibles solides

Comme nous avons déjà vu rapidement dans la partie 10 le transport d'électrons dans la matière est une question clé pour évaluer la faisabilité de l'allumage rapide (AR) pour la fusion inertielle. En effet, dans le concept de l'AR, l'allumage de la bille pre-comprimée contenant le combustible de fusion est réalisé par des électrons produits par laser avec des énergies de l'ordre du MeV [4, 5]. Il est donc crucial pour cet approche que l'énergie du laser d'ignition soit efficacement convertie dans un intense faisceau d'électrons qui peut se propager à travers le plasma sur-critique à haute densité et amorcer la combustion thermonucléaire dans le noyau [4, 5]. Le transport des électrons au noyau pre-comprimé implique des courants de l'ordre de $100 - 1000$ MA. Cependant plusieurs points importants liés au transport d'électrons rapides ne sont pas encore clairs.

D'abord, jusqu'ici la distribution en énergie et la divergence angulaire des électrons rapides n'ont pas été caractérisées avec précision. Naturellement, ces aspects sont cruciaux pour comprendre la dynamique de leur propagation dans la matière, ceci est important pour l'allumage rapide [4, 5] et pour l'accélération de protons [22]. Cependant cet objectif est tout à fait difficile à atteindre. En effet, malgré la gamme étendue de diagnostics employés (K_α [152, 141], bremsstrahlung [95, 153], émission visible [133], production de neutrons [50, 154]), pratiquement toutes les expériences précédentes ont seulement pu déterminer des paramètres globaux comme l'énergie moyenne de la distribution (c.-à-d. la *température*), la pénétration et la divergence angulaire moyenne. Une autre question principale est liée au fait que les courants de l'ordre de $100 - 1000$ MA dépassent largement la limite d'Alfvén. Leur propagation est par conséquent possible seulement si les courants de retour formés par les électrons du

milieu équilibrent le courant entrant des électrons rapides et annulent la séparation de charge. Cependant, dans ces conditions (deux jets parallèles de courants intenses), des instabilités cinétiques telles que des instabilités à deux faisceaux ou du type Weibel [113, 157], peuvent se développer et des simulations PIC (Particle-In-Cell) prévoient que le transport des faisceaux d'électrons relativistes mène à une filamentation.

Dans ce contexte, un certain nombre d'expériences étudiant la propagation et la filamentation des faisceaux d'électrons relativistes produits par laser ont été effectués en utilisant des feuilles de métal et de plastique, des cibles de mousse et des galettes de verre [123, 122, 159, 163, 130]. Des structures filamenteuses ont été observées dans [163] dans des images enregistrées sur des films radiochromic (RCF) à partir des faisceaux d'électrons produits dans l'interaction d'un laser de 10^{19} Wcm^{-2} avec des feuilles d'or de 20 μm d'épaisseur. Toutefois l'observation était très indirecte, loin de la cible, où la propagation et la filamentation ont lieu. Une filamentation et un hosing ont ete observés par ombroscopie dans un gaz à l'arrière d'une cible solide (isolante) par Tatarakis *et al.* [159]. Des filaments et des jets d'électrons ont été directement observés dans [123, 122, 159, 163, 130] mais seulement dans des cibles isolantes.

A partir de ces données, il n'est pas possible de conclure si le filamentation est dû à un mécanisme volumique (comme l'instabilité à deux jets ou de Weibel) ou si elle est reliée à une instabilité d'ionisation, ayant lieu dans le front du faisceau d'électrons. Dans les isolants, la partie principale du faisceau d'électrons rapides, se propage après le front d'ionisation, dans un milieu ionisé. Par conséquenct les différences entre les isolants et les métaux devraient être seulement marginales. Si l'instabilité de Weibel est le processus dominant de filamentation, elle devrait agir d'une manière semblable dans les isolants et les conducteurs. Cependant, selon [114], le front d'ionisation peut devenir instable parce que sa vitesse augmente avec la densité locale du faisceau d'électrons. Ceci augmente les petits plissements du front d'ionisation, qui se développent au cours du temps. Naturellement, une telle instabilité d'ionisation a lieu seulement au bord du faisceau rapide (front d'ionisation) pendant la propagation du faisceau d'électrons dans un isolant, et ne peut pas être présente dans des cibles en métal.

Remarquons qu' aucune étude paramétrique n'a été effectuée en changeant de façon systématique la cible et/ou les paramètres du laser. Par conséquent, afin d'essayer de clarifier certains de ces points, nous avons réalisé une double série d'expériences avec un laser ultra-intense (jusqu'à 6×10^{19} Wcm^{-2}) en étudiant le transport dans des feuilles métalliques (Al) et isolantes (CH). La dynamique de la propagation des électrons rapides en fonction de l'épaisseur de la cible a été étudiée en utilisant l'auto-émission optique issue de la face arrière des cibles.

12.1 Installation expérimentale

L'expérience a été effectuée sur le laser Ti:Sapphire de la "salle jaune" au Laboratoire d'Optique Appliquée (LOA), qui fonctionne en mode d'amplification a dérive de fréquence (technique CPA) à la longueur d'onde de 815 nm [180]. Le laser fournit des impulsions de 40 fs (FWHM) avec des énergies sur-cible inférieures à 0.7 J. Le faisceau laser a été focalisé avec un miroir parabolique hors-axe $f/5$ en incidence normale sur des feuilles minces d'aluminium (Al) ou du plastique (CH) avec des épaisseurs s'étendant de 10 au 100 μm. La taille de la tache focale était le 6 μm, ayant pour résultat des intensités focalisées (sous-vide) de l'ordre de 6×10^{19} Wcm^{-2}, et avec un contraste mieux de 10^6. La face arrière de la cible était imagée sur l'axe à l'aide d'un système optique $f/2$ sur une caméra CCD (256 $\times$ 1024 pixels, 16 bit) ou sur un détecteur CCD intensifié (ICCD, 1024 $\times$ 1024 pixels, 16 bit) comme montré dans la Fig. 12.1.

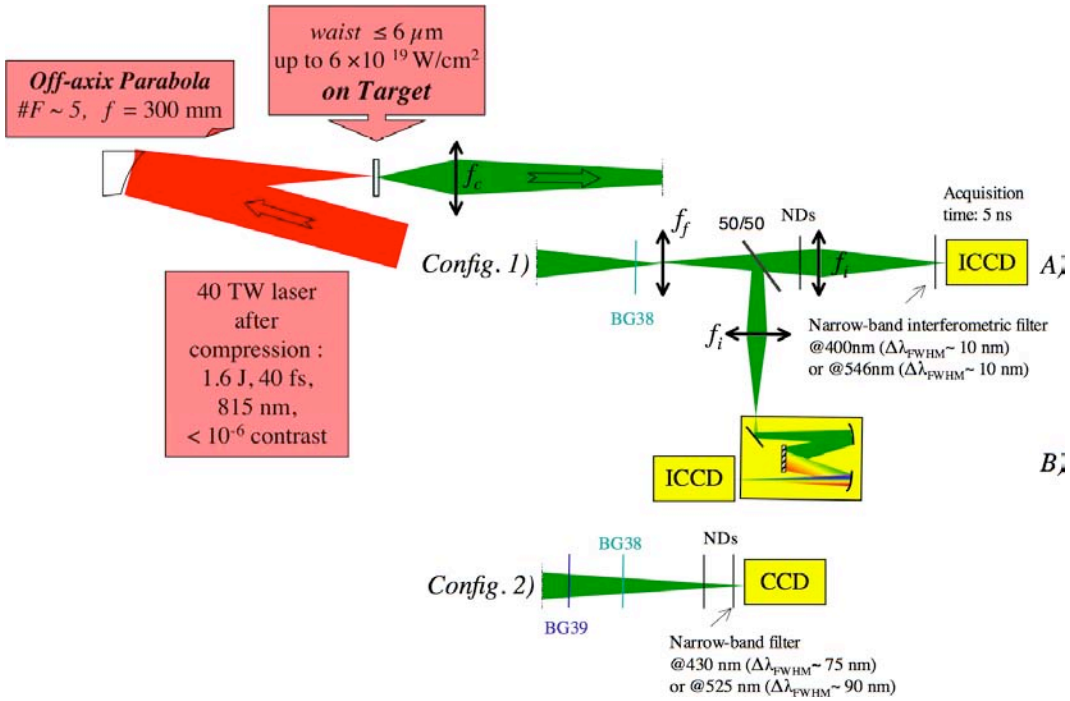

Figure 12.1: Installation expérimentale.

La lumiére arrivant sur les détecteurs CCD a été filtrée à l'aide des filtres BG38 et BG39 pour supprimer la lumière laser à 815 nm. Dans quelques tirs, la fenêtre spectrale des CCD a été limitée à une bande passante avec une largeur de 10 ou 90 nm autour des deux différentes longueurs d'onde (405.5 nm et 546.5 nm pour la configuration CCD; et 430.37 nm et 525.45 nm pour la configuration ICCD) en utilisant des filtres à bande étroite. La sensibilité du système d'imagerie a été obtenue avec une lampe à

rayonnement de corps noir calibrée de façon absolue. La résolution spatiale du système était le 5 μm. Le temps d'acquisition a été limité à 5 ns.

12.2 Propagation des électrons rapides dans des cibles d'aluminium

La Fig. 12.2 présente un spectre typique obtenu pour une cible d'Al de 40 μm: nous voyons un pic spectral près de 410 nm, la deuxième harmonique de la lumière laser ($2\omega_0$).

Comme déjà vu dans les expériences précédentes [134, 182, 155], ce comportement cohérent est attribué à des micro-paquets d'électrons relativistes, associées aux mécanismes d'accélération d'électrons collectifs cohérents: le chauffage pondéromotrice $\mathbf{J} \times \mathbf{B}$ [209] injectant des électrons à $2\omega_0$; et/ou le chauffage d'écrantage [83] injectant des électrons à ω_0. Quand en atteignant le face arrière des cibles et en passant soudainement du matériel solide dans le vide, chaque électron émet un rayonnement de transition avec un large spectre [166]. Si la population d'électrons rapides reste périodiquement rassemblée après avoir traversée une certaine épaisseur, ce rayonnement s'ajoute avec cohérence pour des longueurs d'onde près de cT et de ses harmoniques (CTR), où T est la période avec laquelle les paquets d'électrons sont injectés dans le matériel. Le large spectre environnant observé dans la région visible pourrait correspondre à une émission incohérente (OTR incohérent, rayonnement de corps noir) ou au pied de la raie du $2\omega_0$ CTR.

Nous avons étudié l'émission issue de la face arrière en fonction de l'épaisseur des cibles d'Al pour deux régions spectrales, la région à $2\omega_0$ autour de 410 nm et une région *visible* entre 450 et 550 nm (non liée à aucune harmonique du laser), et nous avons observé que les deux signaux diminuent avec l'épaisseur. Néanmois le signal à $2\omega_0$ est robuste et encore intense après 200 μm quand le signal visible diminue plus rapidement. Il y a une différence frappante entre le cibles $\leqslant 50$ μm, pour lequelles les signaux à $2\omega_0$ et visible ont le même ordre de grandeur, et les cibles $> 50\,\mu$m pour lesquelles les deux signaux diffèrent de plus de deux ordres de grandeur.

Sur la Fig. 12.3 (droite), nous montrons, pour les mêmes deux régions spectrales, la largeur radiale (HWHM) des sources des signaux émis en fonction de l'épaisseur de la cible.

Il y a une différence significative entre les deux signaux: le rayon de la source *visible* augmente linéairement, alors que la source à $2\omega_0$ suit au début cette croissance, il diminue pour des cibles de 100 μm à la taille initiale. Avec la robustesse du niveau du signal à $2\omega_0$, c'est la signature d'un composant relativiste et fortement collimaté de la distribution d'électrons rapides [123, 122, 155]. Par contre, l'augmentation

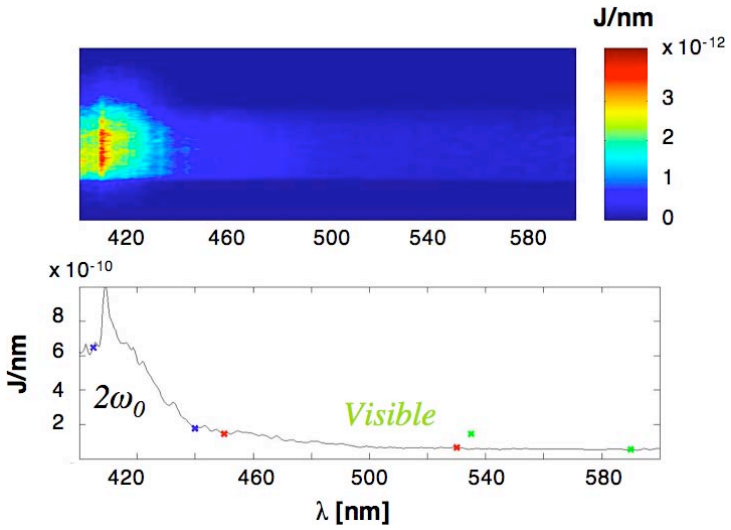

Figure 12.2: Spectre integrée temporellement (5 ns) à l'arrière d'une cible de feuille d'aluminium de 40 μm. La résolution spectrale de 5 nm est limitée par la fente d'entrée du spectromètre.

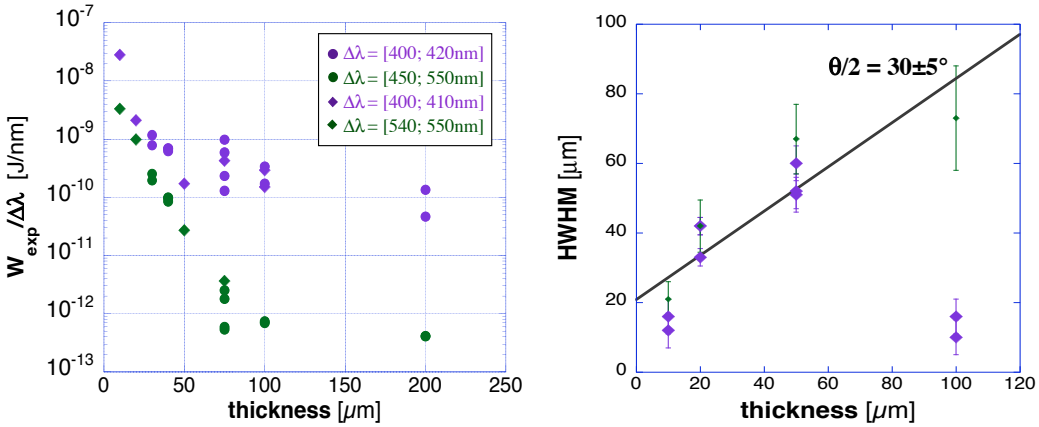

Figure 12.3: Energie spectrale per unité de longueur d'onde (gauche) et largeur radiale (HWHM) des signaux émis en fonction de l'épaisseur de la cible (droite). Les symboles violets vides correspondent aux signaux a $2\omega_0$, les symboles verts et pleins aux signaux visibles. Les cercles correspondent au diagnostic spectral et les diamants à la reprise d'image filtrée (les largeurs spectrales considérées sont indiquées).

quasi-linéaire observée pour la source *visible* avec l'épaisseur de la cible démontre une divergence globale du faisceau d'électrons avec un demi-angle de $30 \pm 5°$, à partir d'un rayon initial de $19 \pm 5\,\mu$m.

Pour expliquer nos données expérimentales, nous avons considéré différents mécanismes radiatifs [197]. Pour les cibles minces, l'émission est dominée par un rayonnement thermique du type corps noir dû à un courant de retour qui chauffe de façon résistive le matériel traversé. Pour les cibles épaisses, le mécanisme dominant devient le CTR produit par un flux d'électrons relativistes périodiquement modulé.

Pour modéliser cette émission cohérente, nous avons supposé une propagation ballistique des pacquets d'électron injectés à l'avant de la cible [134, 155] avec une période T_0 ou $T_0/2$ (T_0 étant la durée d'impulsion laser) durant un tier de toute la durée de l'impulsion laser de 40 fs. On suppose que chaque groupe a des profils gaussiens initiaux (temporels et radiaux) avec des largeurs caractéristiques de $T_0/10$ (selon des résultats de simulations PIC [155, 196]) et 16 μm, la taille initiale de la source d'électrons obtenue à partir des données expérimentales à $2\,\omega_0$. Chaque groupe a iniatellement une distribution d'énergie Maxwellian relativiste avec une température T_{hot}. La densité spectrale totale d'énergie produite par les pacquets d'électrons est alors indiquée par le produit du rayonnement émis par un électron par un facteur, qui tient compte de la quantité de charge rayonnant en phase.

La diminution du signal à $2\,\omega_0$ avec l'épaisseur de la cible, prévue par ce modèle, est provoquée par la taille radiale croissante de la région de formation du CTR, due à la divergence du faisceau d'électrons, et (plus important) par l'élargissement longitudinal de chaque groupe d'électrons dû à la dispersion en vitesse: quand l'épaisseur augmente, les pacquets successifs commencent à fusionner et la modulation en courant est progressivement détruite. Par conséquent, le caractère cohérent du rayonnement émis est perdu. Ceci signifie que pour assurer une émission cohérente du rayonnement pour des échantillons épais (des signaux intenses à $2\,\omega_0$ étaient encore obtenus pour $L = 200\,\mu$m), la population injectée doit conserver une certaine modulation, c.-à-d. correspondante à de copieux électrons relativistes avec une dispersion en vitesse plutôt petite.

Les calculs prouvent que nos données expérimentales sont bien reproduites en employant une température pour les électrons rapides $T_{hot} \approx 5$ MeV et une population estimée de 2×10^9 électrons, c.-à-d. seulement le 0.2% de l'énergie laser sur la cible [197]. Le rayonnement de corps noir, qui est dominant pour les cibles les plus minces, a été calculé en considérant que le chauffage de la cible, pour nos intensités laser et nos énergies électroniques prévues, est principalement dû au chauffage résistif lié au courant de retour et à la propagation d'un choc dû à la pré-impulsion laser [110]. Dans notre expérience en effet, l'impulsion laser d'interaction a été précédée par un piédestal spontané de 3 ns (ASE) avec un contraste en intensité supérieur à 10^6. Les effets d'une si longue et intense pre-impulsion ont été estimés par des simulations hydrodynamiques

effectuées avec le code hydrodynamique MULTI-1D [210, 184]. Nous avons constaté que ce niveau d'ASE est suffisant pour évaporer 2 μm de matériel et pour produire d'une onde de choc avec une pression de 1.6 Mbar [185]. Après le debouché du choc, la cible pourrait être accélérée et déplacée à une distance de quelques dizaines de μm selon son épaisseur. En particulier, les cibles plus minces de 13 μm peuvent se déplacer d'environ 40 μm. Compte tenu que la profondeur du champ du faiseau laser est de 100 μm, un tel mouvement ne devrait pas changer les conditions d'interaction non plus pour des cibles minces. En plus il ne devrait pas affecter le cibles plus épaisses de 30 μm où aucun débouché de choc de la face arrière n'est possible avant l'arrivée de l'impulsion principale.

Pour calculer le chauffage induit par le courant de retour, nous avons développé un modèle cinétique [197]. Deux différentes échelles temporelles sont impliqueés dans le processus. Initialement les électrons rapides et le courant de retour se propagent dans le matériel et le chauffent en seulement quelques ps. Une telle rapidité nous permet de négliger le processus de diffusion thermique et l'expansion. Cependant, puisque notre temps d'acquisition (5 ns) est beaucoup plus long que le temps de chauffage, nous devons considérer une expansion auto-similar avec une symétrie cylindrique du réservoir d'énergie déposée. Afin d'estimer le rayonnement de corps noir émis pendant une telle expansion plus lente, nous avons intégré la luminance de Planck sur l'angle solide expérimental et la fenêtre du temps d'acquisition. Nous pouvons estimer une température $T_{hot} \approx 0.3$ MeV avec une divergence de 30 ± 5 de demi-angle, et une conversion d'énergie de l'ordre du 40 % [197]. Le modèle permet également d'estimer le chauffage de la cible. Des températures de l'ordre de 100 eV ont été trouvées pour des cibles de $\leqslant 10\,\mu$m (et beaucoup plus petites pour des cibles plus épaisses). La propagation divergente du faisceau d'électrons rapides est la raison principale pour un chauffage moins efficace des cibles épaisses.

Additionnant le modelé CTR et l'émission thermique, nous pouvons correctement reproduire toutes nos mesures expérimentales d'émission de la face arrière des cibles en fonction de leurs épaisseurs dans les gammes spectrales à $2\omega_0$ et *visible*. L'émission thermique domine clairement pour les cibles très minces (courbes pointillées) et le CTR pour les cibles épaisses (courbes à tiret). Pour des cibles encore plus épaisses, cette émission cohérente est dégradée par une perte de cohérence, et nous pouvons s'attendre que l'OTR devient le mécanisme radiatif dominant.

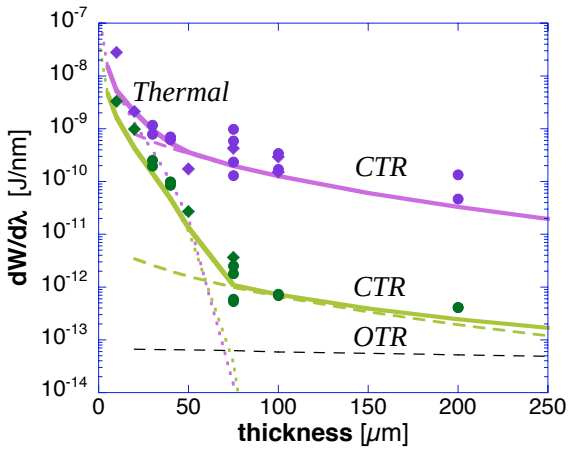

Figure 12.4: Les points expérimentaux sont reproduits (les courbes pleines) additionnant les contributions de l'émission thermique (courbes pointillées); CTR (courbes en tirets colorées); OTR (courbe en tirets noirs).

12.3 Propagation des électrons rapides dans les cibles en plastique

Le CTR et le rayonnement de corps noir ne peuvent pas décrire le comportement des données du CH, pour lesquelles le signal optique est stable et montre même une légère augmentation avec l'épaisseur de la cible (voir la Fig. 12.5).

Un tel comportement peut être expliqué par l'introduction d'un autre mécanisme d'émission, c.-à-d. le rayonnement Čherenkov, qui est proportionnel à la longueur de chemin de particules et donc à l'épaisseur de la cible.

Le rayonnement optique Čherenkov est émis par un électron se propageant dans un matériel diélectrique avec une vitesse $v = c\beta$ plus grande que la vitesse de phase de la lumière dans le matériel, qui est donné par c/n [57]. Cependant, nous ne pouvons pas l'observer dans des matériaux non-transparents tels que des métaux ou des plasmas denses en raison de la forte absorption et d'un index de réfraction $n < 1$. Le rayonnement est émis dans un cône autour de l'axe de propagation des particules avec un angle donné par $\cos\theta = 1/\beta n$. Etant donné le systeme optique de collection $f/2$ et l'indice de réfraction de la CH dans la gamme de longueurs d'onde entre $400 - 550$ nm ($n = 1.48$), nous pouvons observer l'émission seulement dans un cône étroit de 8° maximum autour de la normale à la cible. Le processus d'ionisation impose une autre

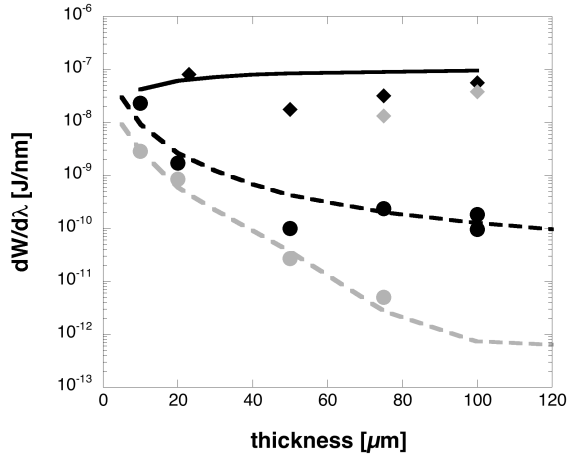

Figure 12.5: Série de données pour l'Al (cercles) et des cibles de CH (diamants) pour une intensité laser de 6×10^{19} Wcm^{-2}. Les symboles noirs représentent les signaux autour de 405 nm et le symboles gris les signaux autour de 546 nm. Les données de l'aluminium sont reproduits par la contribution totale de la CTR et de l'émission thermique (courbes à tiret). Pour les cibles de CH, on doit ajouter le rayonnement Čerenkov pour toute l'émission de toutes les contributions radiatives pour reproduire correctement les données expérimentales (courbe pleine).

limitation importante à l'émission Čherenkov: le rayonnement détecté est dû aux électrons d'énergie relativement élevée ($\beta = 0.85 - 0.95$) se propageant dans le front d'ionisation. En effet, l'ionisation des cibles de CH est déclenchée par les électrons les plus rapides, qui voyagent aux vitesses plus grandes que la vitesse du front d'ionisation et créent un champ électrique de séparation de charge, qui ionise les atomes neutres. Des estimations [114, 96] montrent que le champ électrique dans le front d'ionisation est de l'ordre du 10 % du champ électrique atomique E_a et qu'environ 10 % d'électrons rapides participent au processus d'ionisation. On peut estimer la largeur Δ_f du front d'ionisation par l'équation de Poisson ($E_a \Delta_f = 4\pi\, e n_b$, ou n_b est la densité d'electrons rapides du faiseau) qui vaut $1 - 2$ μm. Cette longueur est environ un dixième de la longueur de faisceau, ct, où t est la durée de l'impulsion laser, permet d'estimer le nombre relatif d'électrons participant au processus d'ionisation.

Sur quelques tirs, la partie antérieure des cibles de CH a été couverte par une couche mince (30 nm) d'Al. Cependant, ceci n'a pas changé les résultats, prouvant que le signal le plus grand issu des cibles en plastique n'est pas dû à un changement des conditions d'interaction laser sur la face avant des cibles. En plus, afin de vérifier que cette intensité accrue de signal n'est pas due à la différence de l'indice de réfraction entre le CH et l'Al, quelques cibles en plastique ont été tirées avec une couche mince d'Al (30 nm) sur la face arrière. Les signaux enregistrés avec ces cibles montrent une diminution (due à la petite absorption dans la couche d'Al) mais étaient encore plus hauts que les signaux OTR dans les cibles d'Al. De plus, les résultats n'ont pas été affectés, en confirmant que le signal dans la plastique vient du rayonnement Čerenkov.

Une information très importante a été obtenue en regardant les images des sources d'émission de la face arrière des cibles (voir la Fig. 12.6). Pour les cibles minces, on observe une similitude très forte entre Al et CH. Ceci est lié au fait que ces cibles ont été fortement perturbées par l'ASE avant l'arrivée de l'impulsion principale, en créant des conditions semblables dans les deux matériaux pour la génération et le transport des électrons rapides.

Une différence significative entre les conducteurs et les isolants peut être vue pour les cibles épaisses. Dans les cibles d'Al, le signal est spatialement homogène avec seulement une augmentation modérée de la taille et une réduction du signal. Au contraire, dans les cibles de CH, le faisceau d'électrons est coupé en filaments avec des tailles de 13 μm environ. Pour des cibles de ≈ 20 μm d'épaisseur la situation est quelque peu intermédiaire pour des cibles de CH et encore la même pour les cibles d'Al.

Notons que des résultats semblables (c.-à-d. une propagation filamentée dans des cibles de CH contre un faisceau homogène dans les métaux) ont été déjà observé dans des expériences réalisées au Ruttherford Appleton Laboratory [141]. Dans ce cas la prise d'images K_α a été employée comme diagnostic, en collectant des photons X des couches de Cu fluoré incluses dans l'Al ou le CH. Cependant dans cette expérience, à

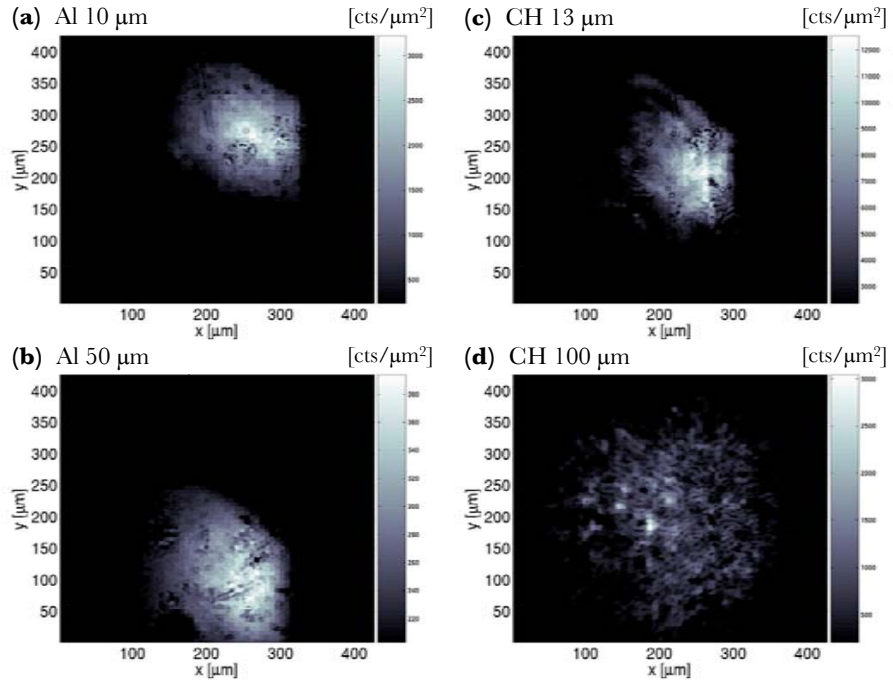

Figure 12.6: Images de l'auto-émisison (coups/μm^2) par la face arrière de la cible, pour de matériaux et épaisseurs différents.

la différence de la nôtre, il n'y avait pas d'étude systématique avec l'épaisseur de la cible.

La filamentation observée peut être liée à l'instabilité de plissement du front d'ionisation [114]. Le front d'ionisation est instable et il se coupe en filaments parce que la vitesse du front d'ionisation augmente avec la densité du faisceau d'électrons. En effet, une petite augmentation de la densité du faisceau d'électrons accélère l'ionisation et pousse plus loin le front d'ionisation. Ce phenomène accroît ultérieurement la concentration d'électrons et induit la filamentation. Le mécanisme est qualitativement illustré dans la Fig. 12.7 et donne un filamentation avec une longueur d'onde plutôt longue ($\Delta_f k_c \leqslant 1$), qui se développe avec un taux de croissance $\Gamma_c = \Delta_f V_f\, k_c^2 (\partial \ln V_f / \partial \ln n_b)$. Ici $k_c = 2\pi/\lambda_c$ est le nombre de l'onde de perturbation et V_f la vitesse du front d'ionisation ($\approx c$).

Le maximum du taux de croissance d'instabilité correspond aux longueurs d'onde de l'ordre de l'épaisseur du front d'ionisation $\lambda_c \sim 2\pi\Delta_f$. Cette évaluation correspond assez bien à la taille des filaments observée expérimentalement. Le taux de croissance prévu pour l'instabilité peut être estimé en supposant $\partial \ln V_f / \partial \ln n_b \approx 1$, pour lesquels on obtient $\Gamma_c \sim 10^{13}$ s^{-1} ($\frac{2\pi}{\Gamma_c} \simeq 0.16$ ps). Ceci correspond à une distance

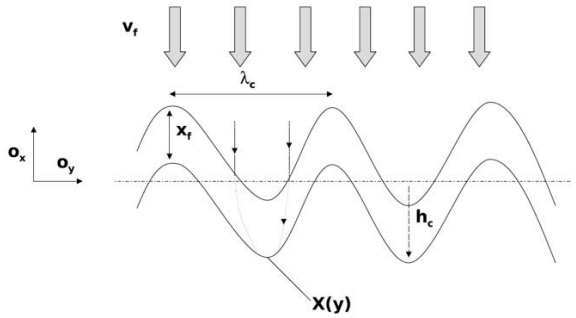

Figure 12.7: Mécanismes de l'instabilité de plissement. λ_c est la longueur d'onde de perturbation, Δ_f est la largeur du front d'ionisation et V_f sa vitesse.

de filamentation du faisceau de environ 100 μm, qui est du même ordre qu'observée expérimentalement [115]. Ce taux de croissance maximal a été obtenu pour une densité de courant de ~ 100 A/μm^2, qui est plutôt bien en accord avec l'évaluation de 7 MA pour le courant total dans notre expérience (c'est en accord avec les courants évalués dans d'autres expériences [152, 95, 130]). La production de filaments sur une distance de 100 μm avec l'instabilité dispersive de Weibel exigerait des densités de courant au-dessus de 1 kA/μm^2, qui ne sont pas réalistes dans nos conditions. Notons également qu'en supposant une taille de filament de 13 μm (comme mesurée dans l'expérience), on obtiendrait 40 kA de courant par filament, i.e. de l'ordre de la limite d'Alfvén.

12.4 Conclusions

En conclusion, nos expériences ont montré plusieurs aspects intéressants, qui sont importants pour l'étude de l'allumage rapide. D'abord, le diagnostic de l'auto-émission est un outil puissant qui permet une caractérisation détaillée de la population rapide d'électrons générée par lasers UHI et de la dynamique spatio-temporelle de leur transport. On a mis en évidence une émission de corps noir incohérente et spectralement large, due à un chauffage résistif à l'arrière des cibles minces ($T_e > 10$ eV pour des épaisseurs $< 30\,\mu$m). Ceci est associé à un courant de retour qui se forme pour neutraliser le flux incident de la majorité d'électrons modérément relativistes (quelques 10^{12}, correspondant à une énergie cinétique totale d'environ $40 \pm 5\%$ de 0.7 J d'énergie laser sur cible). Ils présentent un demi-angle d'ouverture radiale de $30 \pm 5°$ (légèrement plus grand que dans d'autres expériences [152, 141, 133], pour des intensités laser semblables mais des plus impulsions longues). En plus, le rayonnement de transition cohérent (CTR) correspondant à la deuxième harmonique de la lumière laser est très sensible aux énergies élevées des électrons et permet de distinguer un petit nom-

bre ($\leqslant 10^9$) d'électrons relativistes, en micro-pacquets et fortement collimatés. Nos résultats basés sur la détection simultanée de l'émission incohérente et cohérente sont aussi également sensibles à la majeure partie des électrons modérément relativistes ($T_{hot} \approx 0.3$ MeV) et à la queue d'énergie élevée ($T_{hot} \approx 7$ MeV). Ils démontrent la présence d'une distribution d'énergie à deux températures.

La comparaison entre les conducteurs et les isolants a montré la filamentation du faisceau dans la plastique. L'émission optique de la face arrière de la cible est attribuée au rayonnement de transition optique et à l'émission thermique pour les cibles d'Al [197], alors que pour des cibles de CH l'émission Čerenkov est le mécanisme dominant [115]. Le diagnostic de Čerenkov prouve clairement que le faisceau d'électrons se casse en filaments avec un taux de croissance et une taille transversale caractéristique en très bon accord avec des prévisions analytiques basées sur l'instabilité du front d'ionisation. Ce comportement filamenté à grande échelle transversale ($\approx 10\,\mu$m) et relativement lent est complètement absent dans les métaux, et il ne peut donc pas être expliqué avec une instabilité volumique telle que les instabilités de Weibel ou à deux-jets en contre-propagation.

Chapter 13

Conclusions générales

Cette thèse est liée à la recherche sur la fusion inertielle, et elle concerne en particulier l'approche de l'*allumage rapide*, qui est basée sur l'utilisation des impulsions laser ultra-intenses pour allumer le combustible thermonucléaire. Jusqu'ici, la praticabilité de ce schéma n'a pas été prouvée et dépend de beaucoup d'aspects fondamentaux de la physique impliquée, qui ne sont pas encore entièrement compris et qui sont aussi très loin d'être contrôlés.

Le but principal de ce travail de thèse est l'étude expérimentale des processus du transport dans la matière sur-dense (solide) et sous-dense (jet de gaz) d'un faisceau d'électrons rapides produit par des impulsions laser à une intensité de quelques 10^{19} Wcm^{-2}.

Les courants d'électrons supra-thermiques créés correspondent à environ 10^7 A et à des valeurs de densités de courant de $10^{12}\,\mathrm{A\,cm}^{-2}$, probablement les plus grandes jamais produites. Dans ce régime, la physique du transport électronique est très complexe: les mécanismes collectifs, associés aux champs énormes, spontanément induit par la séparation de charge et de courant, comportent la focalisation magnétique du faisceau d'électrons, son décélération électrique, le chauffage résistif du matériel traversé, une ionisation rapide (dans le cas des isolants) et finalement la possibilité de la dégénération du faisceau comme conséquences des instabilités. Tous ces effets s'ajoutent aux processus bien connus de collision, de décélération et de diffusion angulaire ([118, 201]).

Afin d'étudier les aspects moins-connus d'une telle physique, plusieurs diagnostics ont été simultanément installés dans nos campagnes expérimentales, effectuées sur l'installation laser 100 TW du Laboratoire pour l'Utilisation des Lasers Intenses (LULI) et sur le laser 20 TW de la "salle jaune" du Laboratoire d'Optique Appliquée (LOA). Les buts de ces expériences étaient : i) étudier le dynamique des électrons

rapides à de faibles densités (jet de gaz), pour lesquelles l'inhibition électrique est maximisée, et montrer directement l'existence des énormes champs électrostatiques; ii) étudier certains aspects de la propagation des électrons rapides dans la matière solide, en particulier la géométrie, la dynamique et la distribution en énergie du faisceau d'électrons rapides se propageant dans la cible, le chauffage de la matière induit par le passage des électrons rapides, et surtout, la possibilité de filamentation du faisceau en raison des instabilités.

Afin d'atteindre ces objectifs, dans l'expérience sur la propagation d'électrons rapides dans un gaz, nous avons utilisé des diagnostics complémentaires résolues temporellement et spatialement: *l'ombroscopie classique* et *chirpée* et la *radiographie protonique*. Pour l'étude du transport électronique dans les solides, nous nous sommes concentrés sur le rayonnement visible émis par la face arrière des cibles plates (d'Al ou de CH).

L'expérience dans le gaz a montré plusieurs résultats nouveaux:

- la densité du gaz aux affecte la propagation des électrons rapides. Aux plus petites densités correspondent des courants de retour plus faibles et un mouvement plus empêché. Dans nos expériences, nous avons mesuré des vitesses de propagation faibles. Nos résultats sont qualitativement en accord à ceux mesurés dans [122] la silice, où une vitesse de pénétration de $\approx c/2$ a été mesurée, avec $n_b \ll n_e$. Dans notre cas la densité initiale de courant électronique rapide excède la densité électronique du milieu (gaz). Cette situation est de grande intérêt pour l'allumage rapide parce qu'elle peut simuler la propagation d'un faisceau intense d'électrons rapides dans le plasma sous dense de la couronne.

- La vitesse de propagation et la distance de propagation augmentent avec la pression du gaz et la vitesse de propagation ralentit avec le temps. Cet aspect semble aussi confirmer le rôle joué par la densité du milieu en établissant un courant de retour, et le rôle essentiel de la séparation de charge et des champs électrostatiques. D'ailleurs, nos résultats donnent la première évidence expérimentale directe de la présence des champs énormes, qui ont été longtemps associés à la propagation des électrons rapides, mais jamais directement observé. Ils prouvent également que la valeur mesurée des champs électrostatiques peut être de l'ordre des prévisions théoriques.

- La phase d'ionisation est essentielle pour produire les électrons libres, qui sont nécessaires pour établir un courant de retour. Ceci etablit une différence fondamentale entre la propagation dans les isolants et dans les conducteurs. Beaucoup d'effets (par exemple la filamentation) qui jusqu'ici ont été observés seulement dans les isolants, peuvent ne pas être présents dans le cas des plasmas chauds, qui sont plus semblables aux conducteurs. Nous avons également prouvé que,

l'ionisation de champ induite par le grand champ électrostatique est de loin l'effet dominant d'ionisation.

- Les champs électrostatiques sont fondamentaux dans la propagation d'électrons rapides. Ils conduisent les électrons libres à retourner avec une vitesse déterminée par la force du champ et par le nombre de collisions (c.-à-d., par la densité du gaz). De tels champs sont si grands qu'une description linéaire du courant de retour (type loi d'Ohm) n'est plus applicable. Le mouvement des électrons est fortement saturé comme prévu par Landau et Lifshitz dans le cas des champs très forts.

Nous avons montré que le diagnostic d'auto émission est un outil très puissant pour la caractérisation détaillée de la population d'électrons rapides produite dans l'interaction d'un laser d'ultra-haut-intensité avec des solides. Il permet également de caractériser de manière précise la dynamique spatio-temporelle du transport dans les cibles.

Chapter 14

Perspectives

Les résultats obtenus pendant mon travail de thèse, montrent que certains problèmes majeurs ne sont toutjours pas résolus: le transport de l'énergie pour l'ignition du noyau comprimé au moyen des électrons rapides. Un problème important, que nous avons étudié, concerne à la distribution énergétique des électrons rapides: nous l'avons caractérisée en détail. Cependant il est toujours très important de continuer la caractérisation du faisceau d'électrons rapides en minimisant le nombre possible, hypothèses *externes* (ouverture angulaire, efficacité de conversion laser et *température*).

Dans cette direction, une contribution importante pourrait venir de l'utilisation d'un diagnostic nouveau tel que la spectroscopie polarisée dans le domaine du rayonnemment X [203, 204]. En employant un tel diagnostic, et en comparant l'intensité les composantes π et σ des lignes d'émission choisies du rayonnement X, il est possible de caractériser la distribution d'électrons rapides dans l'espace de phase permettant de distinguer le mouvement longitudinal et transversal. Autrement dit, en modélisant la distribution d'électrons rapides avec une température transversale ($T_\perp$) et une longitudinale ($T_\parallel$), il est possible de caractériser le rapport entre les deux températures. En particulier des indications liées aux cas limites de fonctions de distribution du type *"beam"* ou *"pancake"* peuvent être obtenues. Cette caractérisation sera beaucoup plus détaillée que ce qui a été obtenue jusqu'ici, en termes d'angle d'ouverture et de température.

D'ailleurs il serait également essentiel d'évaluer le rôle des instabilités de type Weibel. En effet le développement de telles instabilités et leur taux de croissance dépendent énormément de la température transverse du faisceau, un paramètre qui jusqu'ici n'a été jamais directement mesuré. Enfin en employant des cibles multicouches avec une première couche de propagation d'épaisseur variable, il sera possible de reconstruire le comportement de la fonction de distribution à deux températures en fonction de l'épaisseur de la couche de propagation. Des expériences préliminaires

[204] ont été déjà obtenues à des intensités très basses ($\approx 10^{17}$ Wcm^{-2}) mais c'est maintenant le moment de les répéter dans un régime à haute intensité, d'intérêt direct pour l'allumage rapide.

Un autre point clé concerne l'extrapolation des résultats actuels à un scénario réaliste d'allumage rapide. Le plasma coronal des cibles pour la FCI, et le plasma dense du noyau comprimé, réagissant différemment des feuilles solides et des milieux gazeux. Par exemple, une impulsion PW requise pour l'allumage rapide (10 kJ en 10 ps) produit des électrons à 10 MeV sur $\sim 10\,\mu$m auxquels correspond des densités d'électrons rapides $n_b \sim 10^{23}$cm^{-3}. De telles densités sont toujours beaucoup plus grandes que ceux dans des plasmas coronaux typiques ($n_e \sim 10^{21}$cm^{-3}). On s'attend donc que la limite de propagation $n_b \geqslant n_e$, déjà rencontré et étudié dans notre expérience avec les jets de gaz joue un rôle important même dans un contexte "vrai" de FCI.

D'autres questions principales en suspend concernent l'approche récente du *guidage conique* à l'allumage rapide [205]. Ici la distance entre le noyau comprimé et le bout partiellement ablaté du cône est en général $50-100\,\mu$m. L'espace est rempli de plasma résiduel, qui peut avoir une densité, qui est sensiblement inférieure à la feuille comprimée et peut également être inférieure à la densité du matériel d'or dans le bout de cône. Ainsi le faisceau d'ignition doit toujours être transporté à travers ce gap sans divergence ou pertes significatives, et donc la séparation de charge et les énormes champs électrostatiques peuvent jouer un rôle majeur. Naturellement la présence du cône réduira la distance que les électrons doivent traverser avant d'atteindre le noyau comprimé mais n'élimine pas tous les problèmes de propagation. Nous pouvons penser ainsi que, dans nos expériences avec un jet de gaz, les champs électrostatiques peuvent jouer un rôle essentiel en ralentissant et en arrêtant les électrons en plus ou à la place du mécanisme d'arrêt anomal dû à la dispersion stochastique des électrons froids du plasma par la perturbation magnétique [206].

À l'heure actuelle dans les codes de simulation (hybride) [111, 116, 118, 125], les effets électriques pour la propagation des électrons rapides ont été pris en compte seulement inductivement (à partir de la loi de Faraday), tandis les champs de charge d'espace et la phase d'ionisation sont négligés. (Notons que concernant les modèles théoriques analytiques, la situation est presque exactement l'opposée. Par exemple Davies *et al.* [111] et Tikhonchuk [96] considèrent seulement les champs électrostatiques). Au contraire dans le cas où $n_b > n_e$ nous constatons que cette approximation n'est pas précise et peut mener à de grandes erreurs.

Nous souhaitons ainsi et proposons fortement que la prochaine génération des codes numériques devrait inclure la charge d'espace et les aspects d'ionisation, qui sont cruciaux pour une compréhension complète du transport des électrons rapides dans des conditions proche de l'allumage rapide. Ceci pourrait clarifier les vrais phénomènes dominants dans le freinage des électrons: effets de charge d'espace, arrêt anomal, ...

Laissez-moi également noter que plusieurs effets reliés aux courants relativistes

d'électrons produits par laser, comme le creusement [87], la coalescence de filaments [200] et l'arrêt anomal [206] sont seulement prévus par des simulations PIC 2D ou 3D, effectués sur des échelles temporelles et spatiales très courtes, et avec des paramètres (plasma légèrement sur-dense) qui sont tout à fait loin des vraies conditions expérimentales et des paramètres requis pour l'allumage rapide. En plus, une évidence claire (expérimentale) d'un tel effet n'a pas encore été observé.

Bien que nous puissions expérimentalement confirmer que quand le faisceau subit une filamentation, le courant du faisceau dans chaque filament ne semble pas dépasser la limite d'Alfvén et aucune coalescence prévue par des simulations PIC n'a été observé expérimentalement.

Par conséquent des expériences destinées à l'étude des détails fins de la géométrie de propagation du faisceau sont encore cruciales afin d'étudier la physique du transport du faisceau et afin d'évaluer la faisabilité de l'allumage rapide. Cette catégorie d'expériences pourrait être semblable à nos expériences dans les solides (des cibles d'Al et de CH) et devrait être effectuée en utilisant des impulsions laser de durées différentes (à partir d'une dizaine de fs jusqu'aux ps) et des énergies plus élevées dans des matériaux différents, métaux et isolants, mais également dans des aérogels, en permettant ainsi d'étudier une vaste gamme de paramètres expérimentaux. Ces expériences devraient probablement employer en même temps des diagnostics visibles liés à l' émission OTR et Čerenkov (comme nous l'avons déjà fait) et des diagnostics de rayonnement X, afin d'étudier ce qui se produit à l'intérieur du matériel (particulièrement quand celui-ci n'est pas transparent à la lumière visible comme c'est le cas dans les métaux).

En conclusion, une autre question principale en suspend concerne l'étude des cibles à guidage conique. Des cibles coniques ont été récemment proposées comme une nouvelle approche alternative à l'allumage rapide. Des expériences intégrées ont montré en présence du cône une augmentation du nombre de neutrons dans la compression des cibles de fusion (le faisceau CPA étant dirigé par le cône). Ces résultats ont été récemment publiés dans Nature [154]. Cependant malgré l'intérêt pour de tels résultats, beaucoup de points demeurent toujours complètement obscurs. Ces expériences intégrées ne permettent pas une véritable compréhension de la physique fondamentale et par conséquent ne permettent pas l'étude de la paramétrisation d'un tel schéma. Par conséquent, des expériences plus simples et "plus propres" visant à l'étude de la physique du transport et de la génération en présence du cône sont essentielles.

Dans ce contexte, je pense que les divers types de diagnostic qui ont été mis en place et employés dans les travaux reliés à mon travail de thèse, peuvent être employés avec succès pour étudier le comportement des cibles coniques. En particulier je me réfère à l'imagerie protonique (qui permet d'étudier la génération des champs électrostatiques à l'arrière de la cible plate derrière le cône), à l'émission visible de la face arrière (en

permettant d'étudier la géométrie du faisceau avec et sans le cône), à l'ombroscopie classique et chirpée.

Quelques expériences préliminaires ont été déjà récemment réalisés au LULI et n'ont montré aucun effet significatif du "cône" [208]. Cependant dans cette situation le remplissage du cône à partir du prèplasma produit par le prepulse a semblé être l'aspect dominant. Clairement il y a besoin de plus d'expériences dans ce domaine. En même temps, nous avons déjà rappelé comment notre expérience avec un jet de gaz était probablement utile afin de simuler quelques aspects dus à la présence du cône, c.-à-d. le passage des électrons rapides par le gap de densité constitué par le cône d'or d'un côté et le plasma interne de l'autre côté.

En conclusion, il semble que malgré l'augmentation considérable de notre connaissance, au cours des dix dernières années, le problème du transport dans la matière des courants relativistes dépassant la limite d'Alfvén est toujours loin d'être compris. Ceci ne doit constituer une raison d'être déçu, mais plutôt une motivation pour réaliser d'autres nouvelles expériences, encore plus astucieuses et qui adresseront non seulement des questions importantes liées à la faisabilité de l'allumage rapide, mais également des questions fondamentales pour la physique, telle que par exemple, la propagation de courants très grands dans des jets astrophysiques. Je suis heureux que les expériences contenues dans mon travail de thèse aient été utiles pour clarifier au moins quelques questions en suspend dans ce problème très complexe.

Part VI

Appendix

Appendix A

Gas jet interferometry analysis

A.1 Gas jet interferometry

A.1.1 Experimental setup

The interferometry was performed in the gas jet facility experimental room [211]. The experimental configuration is shown in Fig. A.1.

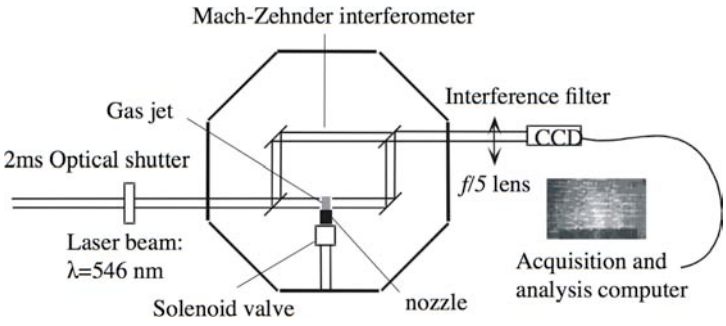

Figure A.1: Experimental Setup.

A green He-Ne laser beam working at 546 nm is expanded and collimated to a 1 cm diam beam which propagates in the vacuum chamber. The Mach–Zehnder interferometer is located in the vacuum chamber. The beamsplitters and mirrors of the interferometer have a surface quality of $\lambda/20$. The gas jet is positioned in one arm of the Mach-Zehnder interferometer (see Fig. A.1). Outside the vacuum chamber an $f/5$ spherical lens images the gas jet onto a linear CCD detector. The image is demagnified

(1:2) in order to have all of the gas jet in the recorded image. The spatial resolution is limited by the pixel size and is, with the current magnification, about 15 μm. The backing pressure in the gas reservoir is measured with a pressure transducer. The vacuum pressure (less than 10^{-2} mbar) in the chamber is measured with a baratron. A commercial solenoid valve (made by Parker- Lucifer) that is normally closed can be opened, giving the gas jet a constant flow for 80 ms. A *snapshot* of the gas flow is obtained using a 2 ms optical shutter. A narrow 10 nm bandwidth interference filter centered at 543 nm was used to reduce the noise level. The CCD is connected to a computer in order to record the 8-bit images. Mathematical extractions of the phase shift variation and the Abel inversion are made directly during the experiment. Very good shot to shot reproducibility of the gas flow was observed.

A.1.2 Abel inversion

A large number of optical diagnostics are based on phase shift measurement. This phase is always proportional to the product of the index of refraction with the optical path length. More precisely, it is proportional to the integral of index of refraction along the path length. It is thus necessary to know the index of refraction everywhere in the medium. If the medium is cylindrically symmetrical, the situation is greatly simplified, and from the phase shift measurement along one direction we can deduce the radial distribution of the index of refraction. The transformation which permits an axial distribution to reach the radial one is called *Abel inversion*.

In Fig. A.2 we present a schematic of the phase shift along the y axis and its connection with the radial one.

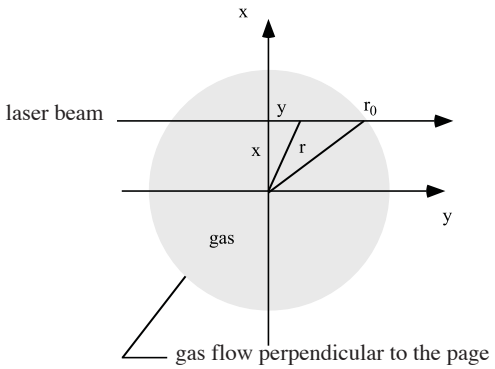

Figure A.2: Schematic of the Abel transformation. The gas flow is perpendicular to the page.

The phase shift variation, integrated along the y axis, due to the optical path

introduced by the gas jet is done by

$$\delta\varphi(x) = \frac{4\pi}{\lambda_0}\int_0^{y_0}[n(r)-1]dy \tag{A.1}$$

Changing the Cartesian coordinates by the cylindrical one, we obtain:

$$\delta\varphi(x) = \frac{4\pi}{\lambda_0}\int_0^{y_0}\frac{[n(r)-1]r}{r^2-x^2}^{1/2}dr \tag{A.2}$$

By using Abel's inversion this equation can be written as:

$$\frac{4\pi[n(r)-1]}{\lambda_0} = -\frac{1}{\pi}\int_r^{r_0}\frac{\varphi(x)}{x^2-r^2}^{1/2}dx \tag{A.3}$$

From the phase φ_k along the x-axis for n equidistant values $x_k = kr_0/n$ ($k = 0,1,2,...,n-1$), we obtain the value of the index of refraction corresponding to $r_j = jr_0/n$ ($j = 0,1,...,$
$n-1$) from the simple relation:

$$n_j - 1 = \frac{\lambda_0}{2\pi r_0}\sum_k a_{jk}\varphi_k, \tag{A.4}$$

where a_{jk} is the coefficient tabulated in [212].

Finally the neutral gas density is then obtained by:

$$N_k = \frac{(n_k-1)N_0}{(n_{gas}-1)}, \tag{A.5}$$

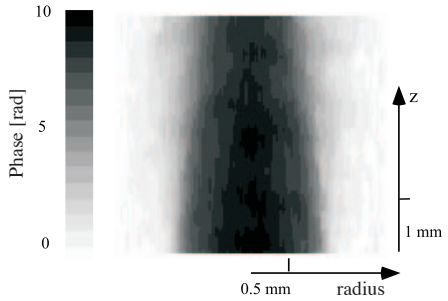

Figure A.3: small Typical phase shift measurement obtained from our interferograms.

where n_{gas} is the refraction index of the gas (for argon n is equal to 1.000281) at 532.5 nm and N_0 the density of atoms at the standard temperature and pressure ($N_0 = 2.68 \times 10^{19}$ cm^{-3}).

A.1.3 Phase shift method measurement method

We now present the mathematical treatment [135, 213] used in order to get the phase shift from the interferogram images, one obtained with gas and the other one (the reference) obtained without gas. We first consider the intensity profile $I(z)$ along the z axis in the fringe pattern. If the $\varphi(z)$ phase shift is induced by the gas, and there is d distance between two fringes, we have the following relation:

$$I(z) = 2I_0 \left[1 + \cos\left(\frac{2\pi z}{d} + \varphi(z)\right)\right] \tag{A.6}$$

If $\varphi(z)$ changes slowly over one fringe, the cosine factor corresponds to the fringe shift. The k spectrum presented in Fig. 4 is obtained by a Fourier transform of these plots. We see two components, one sharp at $k = 0$ and a second one broader at $k = 2\pi/d$. Phase information is deduced from the difference between the reference and the gas case at $k = 2\pi/d$ as follows. We take the inverse Fourier transform of these component in the gas case,

$$I_g(z) = I_0 \exp[2\pi\imath z/d + \imath\varphi(z)], \tag{A.7}$$

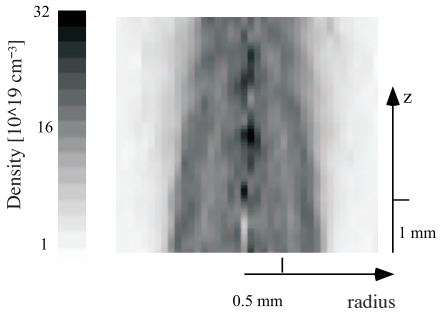

Figure A.4: Neutral density measurement obtained from our interferograms.

and the inverse Fourier transform of these components in the reference case,

$$I_r(z) = I_0 \exp(2\imath\pi z/d), \tag{A.8}$$

then we deduce the phase from the logarithm of the ratio $I_g(z)/I_r(z)$. Comparing two reference images we deduce that this method allows us to measure a phase shift variation of the order of 0.05 rad.

A.1.4 Experimental results

Typical interferograms

We present in Figs. A.1.4, A.6, A.7, A.8, at the output is 1.2 mm. These images correspond to argon at 30, 50, 70 and 80 bars, respectively.

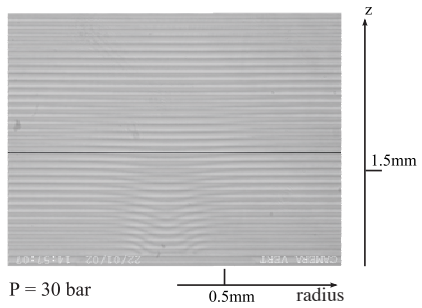

Figure A.5: Interferogram obtained at 30 bar.

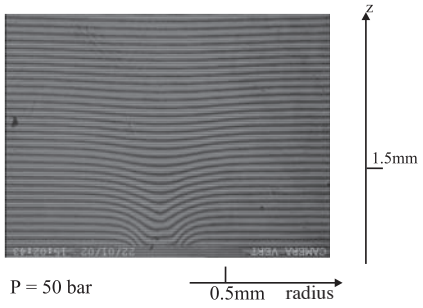

Figure A.6: Interferogram obtained at 50 bar.

These gas pressure are the backing pressure, i.e., the pressure in the reservoir thus, as we can see from the atomic densities measured, the gas pressure at the nozzle output is about 100 times lower. The value of the density is a linear function of the backing pressure. This result is shown in Fig. A.9.

The gas flow, ejected from the bottom to the top, is visible by the shift of the fringes. In Fig. A.10 we present the corresponding reference (without gas) interferogram. We can see the nozzle on the bottom. These data are recorded on a 378×286 pixel CCD.

We observe (cf. Fig. A.4) that the gas density along the flow axis z shows a

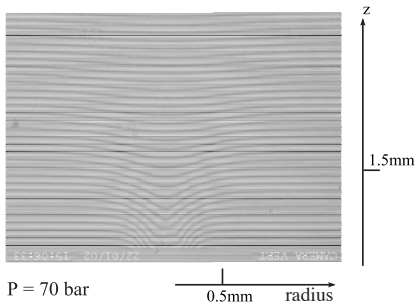

Figure A.7: Interferogram obtained at 70 bar.

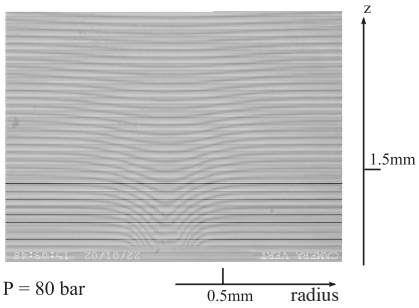

Figure A.8: Interferogram obtained at 80 bar.

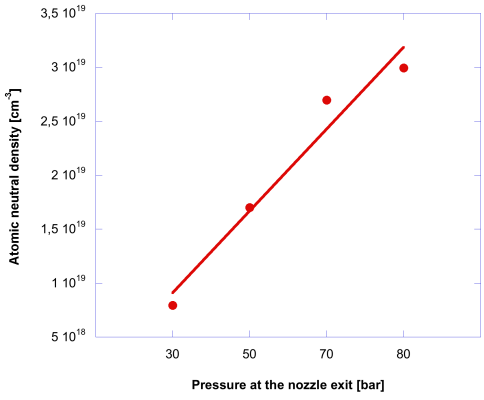

Figure A.9: Neutral density as a function of the backing pressure.

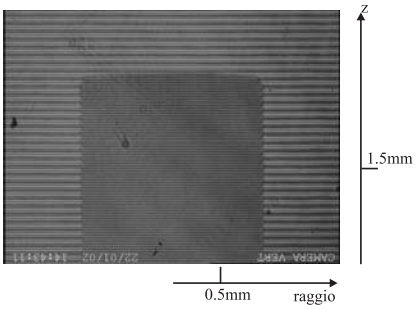

Figure A.10: Typical reference interferogram (i.e. without gas).

behavior which stay in the middle between a supersonic (density stays constant along the flow axis z) or a sonic (neutral density decreases along this z axis) expansion. In fact, the neutral density decreases along the z axis, but slower than a sonic gas jet.

Density profiles

In order to obtain a two-dimensional neutral density profile we made an Abel inversion for each line of the phase image. A two-dimensional neutral density profile, deduced from Figs. A.1.4, A.6, A.7, A.8, are presented in Fig. A.11.

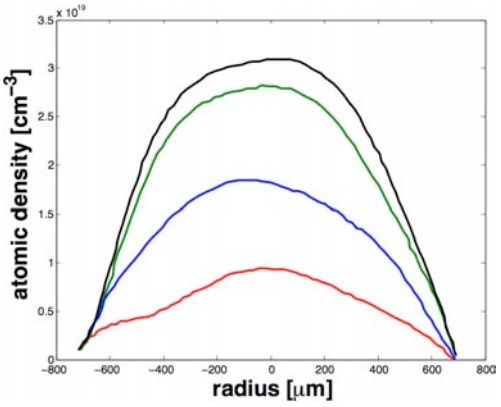

Figure A.11: Neutral density obtained with our cylindrical sonic nozzle with backing pressures of 30, 50, 70 and 80 bars, respectively.

The gas density changes from 0 (at the gas jet edge) to a peak value of 8×10^{18} cm^{-3}, 1.7×10^{19} cm^{-3}, 2.7×10^{19} cm^{-3}, 3×10^{19} cm^{-3}, for backing pressures of 30, 50, 70 and

80 bars, respectively. To define the symmetry axis we calculate for each z the integral of the phase along the radius.

Appendix B

PTRACE

This appendix describes the main features of the particle-tracing code PTRACE developed by A. Schiavi and used to shed light on the interaction of a proton beam with electromagnetic field structures. At the core of PTRACE there is a differential equation solver that computes the trajectory of a particle in presence of electromagnetic fields. The numerical algorithm chosen is a Runge-Kutta fourth-order algorithm coupled with an adaptive stepsize monitoring routine, as presented in the book Numerical Recipes in C [214]. The main advantage of such approach is that it offers a fast and reliable solution to the equation of motion with the possibility of prescribing the overall precision to which the trajectory is computed. The adaptive stepsize routine assures that the time steps at which the dynamics is sampled are smaller where the acting forces are larger, so that computational resources are well managed during the simulation. It was therefore possible to trace millions of particles per hour on a desktop workstation and simulate and resolve complex problems such as the charging-up and discharge of a micro-sphere on a picosecond timescale.

PTRACE is a C++ code divided into several objects that combine functions and routines with the data structures they are acting upon. Fig. B.1 shows a schematic diagram of the code.

Main loop is shown together with object components.

- Particle: specifies mass and charge of the particles to trace
- Source: geometric parameters of the particle source such as origin, direction, divergence
- Spectrum: extracts particles from an energy distribution according to parameters such as energy range, beam temperature, number of energy components

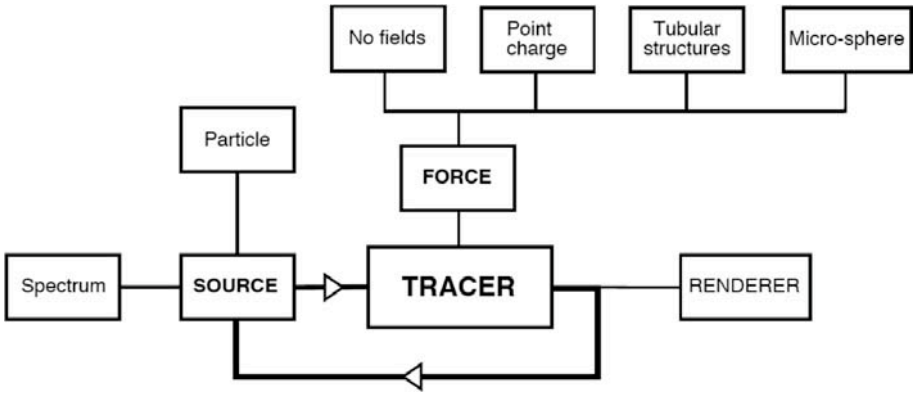

Figure B.1: PTRACE flow chart.

- Tracer: tracing engine that solves the equations of motion for one particle at a time
- Force: computes the force acting on a particle as a function of time and position

The relativistic equation of motion to be solved is

$$\frac{d\mathbf{p}}{dt} = \mathbf{F} = q(\mathbf{E} + \mathbf{v} \times \mathbf{B}), \tag{B.1}$$

which was implemented in the code as a system of six differential equations of the first order. The relativistic momentum $\mathbf{p} = \mathrm{m}\gamma\mathbf{v}$ was written as $\mathbf{p} = \mathrm{m}\mathbf{u}$, where $\mathbf{u} = \gamma\mathbf{v}$ (see [215]), and the system of equations in the variables ($\mathbf{x}$, $\mathbf{u}$) reads

$$\begin{cases} \frac{d\mathbf{x}}{dt} &= \mathbf{v} = \frac{\mathbf{u}}{\gamma} \\ \frac{d\mathbf{p}}{dt} = \frac{\mathbf{F}}{m} &= \frac{q}{m}(\mathbf{E} + \frac{\mathbf{v}}{\gamma} \times \mathbf{B}). \end{cases}$$

B.0.5 Uniformity check

Particles (or rays) were randomly generated and traced one at a time. A Sobol' sequence algorithm was used to place points on a sphere with a uniform areal density. The Sobol' sequence generates points that fill space in a way such that they tend to avoid each other. Filling a Cartesian grid to deeper and deeper levels assures a great uniformity, but requires each level to be fully completed in order to ensure a good uniformity. This way the number of points required for each resolution step increases exponentially. If we want to fill a square and the mesh size is halved at each step, the number of points to compute at each level of the grid forms the sequence $4, 12, 48, 192, ..., 3 \times 4^{N-1}$, where N is the grid level. A pseudo-random generator can

be used to bypass this problem, so that it is possible to stop the simulation at any time without affecting the overall uniformity of the points. Fig. B.2 presents a uniformity

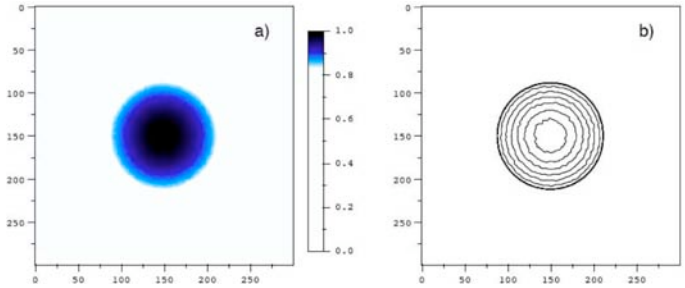

Figure B.2: Simulated cross-section of an unperturbed proton beam. Density and contour plots of the particle counts accumulated on the detector plane.

check for a proton beam generated by a point source. All particles had the same energy in this simulation, and they expanded freely in vacuum. Panel a) shows the particle counts accumulated on a plane orthogonal to the beam axis, just as in the experiments. The corresponding contour plot is shown in panel b). This represents the unperturbed cross-section of the simulated proton beam. The signal is more intense at the centre of the image than at the edge as a consequence of the curvature of the expanding shell of particles, as shown in Fig. B.3. It was found that a satisfactory

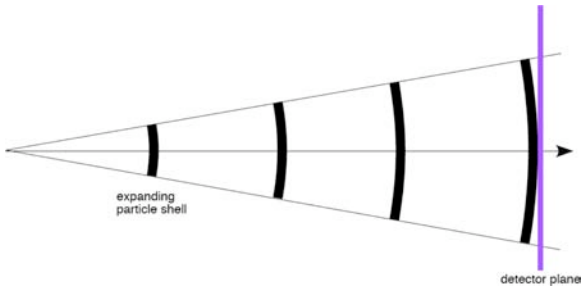

Figure B.3: Curvature effect of an expanding shell of particles.

uniformity was obtained when at least 5 particles per pixel were accumulated on the detector plane. The total number of particles to trace was computed for each run as a function of the divergence of the beam, the distance of the detector, the number of energy components included in the simulation, and the output resolution of the rendered image.

Appendix C

Transition radiation

In this appendix the theory of the transition radiation is briefly presented. It is the electromagnetic radiation emission produced by a charged particle during the crossing of the interface between two materials with different refraction indexes. The transition radiation was theoretically predicted by Franck and Ginzburg in 1945 [166] and experimentally observed by Goldsmith and Jelley in 1958 [216]. In particular, it was successfully used for the control of beams on high energy accelerators [217, 179] and on free electron lasers [218, 190, 191].

A charged particle can emit an electromagnetic radiation under two conditions: when its speed $\mathbf{v}$ exceeds the phase velocity of electromagnetic local waves $v_\phi = c/n$, where $n = \sqrt{\epsilon}$ is the index of the medium (Čerenkov radiation) or, when the ratio between these two velocities presents temporal or spatial variations. However, If only the speed $\mathbf{v}$ varies, one speaks of synchrotron radiation ($|\mathbf{v}| = const.$) or traditional *Bremsstrahlung* ($\mathbf{v}/|\mathbf{v}| = const.$). On the contrary, if $\mathbf{v}$ is constant and n varies, one speaks of transition radiation, for example when the particle crosses the interface between two different optical mediums.

From a qualitative point of view, before the interface, the radiated field is characteristic of the particle movement and the first medium. After having crossed the interface, the field is characteristic of the particle movement and the second medium. Even if the movement of the particle is uniform, the initial and final fields are different because of the distinct dielectric properties of the two mediums. The transition radiation results from the rearrangement of the fields in the vicinity of the discontinuity created by the interface [97].

Another phenomenologic description is based on the polarization and depolarization properties of the crossed mediums. During the propagation of a charged particle in a certain material, it occurs, in the vicinity of its trajectory and under the effect

of the associated field, a distortion of the electronic clouds of the atoms because the electrons are displaced in comparison of the presumed motionless cores. Each atom of the medium then behaves like an elementary dipole which radiates an electromagnetic wave when, the particle being moved, the electrons come back to their equilibrium position. The radiated fields, coming from several point-like sources in space, add in a coherent way in the vicinity of the particle trajectory and until a certain depth in the medium (called *coherence length*) and producing a *transition* radiation, characterized by specific spectral and angular distributions.

In the following, some expressions which describe the general properties of the transition radiation will be presented. We limit ourself to the case in which one of the mediums is vacuum ($\epsilon = 1$) and the other one is supposed to be non-magnetic ($\mu = 1$). We will follow the method introduced by Wartski [167, 169, 219] to obtain the expression of the angular distribution of the transition radiation.

C.1 Energy emitted by a moving charge

Let us consider a charged particle with a charge q, driven between times t_0 and t_1 along the trajectory $\mathbf{r}(t)$ with speed $\mathbf{v}$, in a homogeneous medium with a refraction index n. Let us also consider the vectors $\mathbf{R}_0$ and $\mathbf{R}$ which connects the origin of the trajectory (O in Fig. C.1) and the charge position at time t (O'), with, respectively, the observation point M (see figure C.1). The vector $\mathbf{n}$ is an unit vector in the vector direction $\mathbf{R}_0$, and θ is the angle between the vectors $\mathbf{n}$ (or $\mathbf{R}_0$) and $\mathbf{r}(t)$.

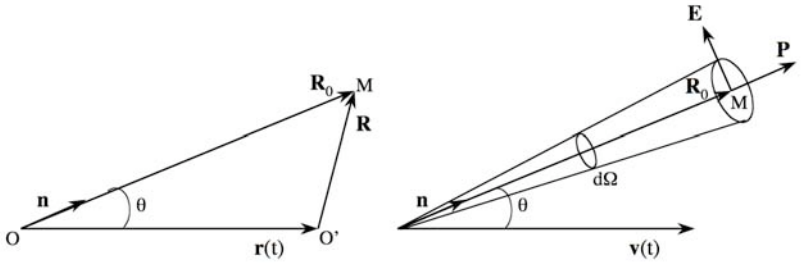

Figure C.1: Definition of the vectors $\mathbf{R}_0$, $\mathbf{R}$ and $\mathbf{n}$ and the angles θ and $d\Omega$.

The distance from the charge at the observation point, i.e. the absolute value of $\mathbf{r}$, can be expressed like

$$R = R_0 \left(1 - \frac{\mathbf{r}\cdot\mathbf{n}}{R_0} + \frac{\mathbf{r}^2}{2R_0^2} - \frac{(\mathbf{r}\cdot\mathbf{n})^2}{2R_0^2} + \cdots\right) \tag{C.1}$$

We supposed that the distance from the observation point to the impact point is large, if compared to the characteristic size of the region where the radiation is pro-

duced ($r(t) \ll R_0$), in order to use the far field approximation. At the observation point, the electric and magnetic fields are perpendicular between them and perpendicular to the wave vector $\mathbf{k} = (\omega\sqrt{\epsilon}/c)\mathbf{n}$. In the following only the first two terms of Eq. C.1 will be only considered.

By using the delayed potentials one obtains the electromagnetic field generated at the observation point by the current density associated with the moving charge. In this approximation the propagator is reduced to a function δ and the expression of the delayed potential vector becomes simpler.

Thus, knowing that the electromagnetic power which traverses a surface S is flux of the Poynting vector through this surface (in CGS units):

$$\mathbf{P} = \frac{c}{4\pi}\mathbf{E} \times \mathbf{H} = \frac{c}{4\pi\sqrt{\epsilon}}|\mathbf{H}|^2\mathbf{n} \ ,$$

one can calculate the flux of energy radiated per unit of time and solid angle:

$$\frac{d^2W}{d\Omega dt} = \frac{c}{4\pi\sqrt{\epsilon}}R_0^2|\mathbf{H}|^2$$

In order to obtain the spectral density, we use the Fourier development of the magnetic field and we integrate the energy flux over time, obtaining:

$$\frac{d^2W}{d\Omega d\omega} = \frac{c}{\sqrt{\epsilon}}R_0^2\left|\mathbf{H}_\omega\right|^2 = \frac{c}{\sqrt{\epsilon}}R_0^2\left|\nabla \times \mathbf{A}_\omega\right|^2 \ , \tag{C.2}$$

Here $\mathbf{a}_\omega$ is the potential delayed vector:

$$\mathbf{A}_\omega = \frac{1}{c}\int \frac{\mathbf{j}_\omega}{R}e^{ikR}dV \ , \tag{C.3}$$

where où $\mathbf{k} = \frac{\omega\sqrt{\epsilon}}{c}\mathbf{n}$ ($k = |\mathbf{k}|$) is the wave vector of the radiation and $\mathbf{j}_\omega$ is the current density of a concentrated charge q which is driven at the speed $\mathbf{v}(t)$:

$$\mathbf{j}_\omega = \frac{q}{2\pi}\int \mathbf{v}(t)\delta(\mathbf{r} - \mathbf{r}(t))e^{i\omega t}dt \tag{C.4}$$

Furthermore, taking $R \approx R_0 - \mathbf{r}\cdot\mathbf{n}$ in the phase factor of the equation C.3 and $R \approx R_0$ in the denominator of C.3 and C.4, follows, integrating over the space,

$$\mathbf{A}_\omega = \frac{q}{2\pi c}\frac{e^{ikR_0}}{R_0}\int \mathbf{v}(t)e^{i(\omega t - \mathbf{k}\cdot\mathbf{r}(t))}dt$$

Then, by injecting the rotational potential vector $\mathbf{A}_\omega$

$$\nabla \times \mathbf{A}_\omega = \frac{q}{2\pi c}\frac{e^{ikR_0}}{R_0}\frac{i\omega\sqrt{\epsilon}}{c}\int \mathbf{n}\times\mathbf{v}(t)e^{i(\omega t-\mathbf{k}\cdot\mathbf{r}(t))}dt$$

in Eq. C.2, one finally obtains the spectral energy density radiated per unit of solid angle:

$$\frac{d^2W}{d\Omega d\omega} = \frac{q^2\omega^2\sqrt{\epsilon}}{4\pi^2c^3}\left|\int \mathbf{n}\times\mathbf{v}(t)e^{i(\omega t-\mathbf{k}\cdot\mathbf{r}(t))}dt\right|^2 \tag{C.5}$$

Summarizing, in this expression (here in CGS units) ω represents the frequency of the emitted radiation, $\epsilon = \epsilon(\omega)$ the dielectric function of the medium, $\mathbf{n}$ the unit vector in the emission direction, and $\mathbf{k}$ the wave vector of the radiation. The radiation is linearly polarized in the $(\mathbf{k}, \mathbf{v})$ plane, called *observation plane*. The expression C.5 is of great importance in all the radiation problems mentioned in the introduction of this appendix. For example, let us consider the charge in uniform rectilinear motion, i.e., $\mathbf{v}(t) = \mathbf{v}$ et $\mathbf{r}(t) = \mathbf{v}t$. When the trajectory of the charge is infinite $t = -\infty \rightarrow \infty$), the integral of the eq. C.5 becomes 0, except when

$$\omega - \mathbf{k}\cdot\mathbf{v} = \omega(1-\beta\sqrt{\epsilon}\cos\theta) = 0 \quad \Rightarrow \quad \cos\theta = \frac{1}{\sqrt{\epsilon}\beta}\ ,$$

which is the condition for the Čerenkov radiation emission.

C.2 Transition radiation

Up to now, we considered a concentrated charge in rectilinear and uniform motion in a homogeneous medium. One now will introduce an inhomogeneity: the charge crosses the interface plane between two mediums of distinct dielectric properties. We will limit ourself to the case in which one of the mediums is the vacuum ($\epsilon = 1$), the transition will be in the direction medium $\rightarrow$ vacuum, the observation point is located in the vacuum. One can consider that the trajectory of the charge consists of two semi-infinite trajectories, that is to say, the charge emits a wave in the medium and suddenly stops at the interface. This wave (T) is refracted at the interface before emerging in vacuum. The charge immediately sets out again towards the vacuum with same speed, and emits two other waves, one (D) directly emitted in the vacuum, and the other one (R) reflected at the interface. Fig. C.2 sketched this mechanism in the general case of a charge in oblique incidence to the interface.

If the integration of the eq. C.5 is made over a semi-infinite trajectory $t = 0 \rightarrow \infty$ (case of a charge suddenly accelereted at $t = 0$) or $t = -\infty \rightarrow 0$ (case of a charge

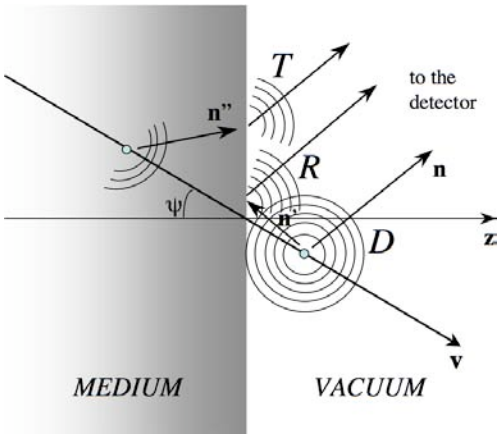

Figure C.2: Emission, for a charge in oblique incidence, of the three waves, direct (D), reflected (R) and refracted or transmitted (T) to the interface medium-vacuum.

suddenly stopped at $t = 0$), one obtains

$$\frac{d^2W}{d\Omega d\omega} = \frac{q^2\sqrt{\epsilon}}{4\pi^2c^3}\left|\frac{\mathbf{n}\times\mathbf{v}}{1-\sqrt{\epsilon}\beta\cdot\mathbf{n}}\right|^2, \tag{C.6}$$

where $\beta = \mathbf{v}/c$ is the normalized speed of the particle. In fact, this expression can be developed as a coherent sum of the three waves previously described (direct, reflected and refracted) by respecting the Fresnel laws for the refraction. The emitted electric field will have two components: one in the observation plan, i.e., the plan which contains the normal to the interface and to the observation direction, and the other one perpendicular to the first component (see Fig. C.3 a)). Under these conditions, it is convenient to decompose the velocity vector of the charge β in two components, one parallel to the observation plan $\beta_\parallel$ and the other one perpendicular to this last one $\beta_\perp$.

The calculation of the spectral density [167] leads to the following expressions for the spectral density of the radiation in two possible polarizations:

$$\frac{d^2W_\parallel}{d\Omega d\omega} = \frac{q^2}{4\pi^2c}\left|\underbrace{\frac{\beta_\parallel\times\mathbf{n}}{(1-\beta\cdot\mathbf{n})}}_{(D)} + r_\parallel\underbrace{\frac{\beta_\parallel\times\mathbf{n}'}{(1-\beta\cdot\mathbf{n}')}}_{(R)} - \underbrace{\frac{f_\parallel}{\sqrt{\epsilon}}\frac{\beta_\parallel\times\mathbf{n}''}{(1-\beta\cdot\mathbf{n}''\sqrt{\epsilon})}}_{(T)}\right|^2, \tag{C.7}$$

$$\frac{d^2W_\perp}{d\Omega d\omega} = \frac{q^2}{4\pi^2c}\beta_\perp^2\left|\overbrace{\frac{1}{(1-\beta\cdot\mathbf{n})}} + r_\perp\overbrace{\frac{1}{(1-\beta\cdot\mathbf{n}')}} - \overbrace{\frac{f_\perp}{\sqrt{\epsilon}}\frac{1}{(1-\beta\cdot\mathbf{n}''\sqrt{\epsilon})}}\right|^2, \tag{C.8}$$

where $\mathbf{n}$, $\mathbf{n}'$ and $\mathbf{n}''$ are the unit vectors respectively associated with the direct (D), reflected (R) and refracted (T) waves. Fig. C.3 b) indicates the positioning of these

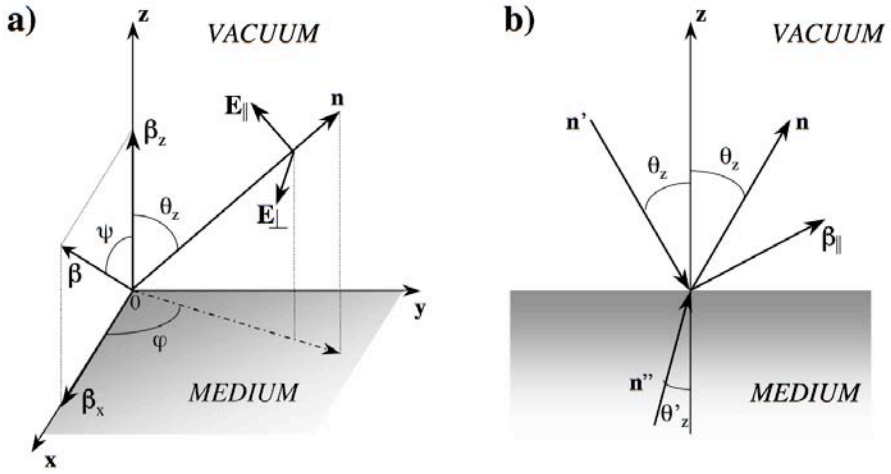

Figure C.3: a) Definition of the incidence and observation planes and the associated angles. The charge crosses the interface ($x - y$ plane) in 0, by forming an angle ψ with the normal to the interface (axis z). The incidence plane is defined by the speed of the charge $\mathbf{v}$ and the normal to the interface, and the observation plane by the observation direction $\mathbf{n}$ and the normal to the interface. **b)** Arrangement of the vectors $\mathbf{n}$, $\mathbf{n}'$, $\mathbf{n}''$ and β in the observation plane.

vectors in the observation plane. θ_z is the angle between the normal to the surface and the observation direction, θ'_z the related angle which satisfies the refraction law. $r_\parallel$ and $f_\parallel$ are the Fresnel coefficients of the wave polarized in the observation plane:

$$\begin{aligned} r_\parallel &= \frac{\epsilon\cos\theta_z - \sqrt{\epsilon - \sin^2\theta_z}}{\epsilon\cos\theta_z + \sqrt{\epsilon - \sin^2\theta_z}} \\ f_\parallel &= \frac{2\epsilon\cos\theta_z}{\epsilon\cos\theta_z + \sqrt{\epsilon - \sin^2\theta_z}} \end{aligned}$$

which satisfy the continuity relation $1 + r_\parallel = f_\parallel$ and also $r_\perp = \frac{f_\perp}{\sqrt{\epsilon}} - 1$; $r_\perp$ and $r_\perp$ are the Fresnel coefficients associated with the perpendicular component:

$$\begin{aligned} r_\perp &= \frac{\cos\theta_z - \sqrt{\epsilon - \sin^2\theta_z}}{\cos\theta_z + \sqrt{\epsilon - \sin^2\theta_z}} \\ f_\perp &= \frac{2\sqrt{\epsilon}\cos\theta_z}{\cos\theta_z + \sqrt{\epsilon - \sin^2\theta_z}} \end{aligned}$$

The total spectral density is given by the sum of the two components of the radiation C.8:

$$\frac{d^2W}{d\Omega d\omega} = \frac{d^2W_\parallel}{d\Omega d\omega} + \frac{d^2W_\perp}{d\Omega d\omega} \ , \tag{C.9}$$

with the two terms, after development, given by [167]:

$$\begin{aligned} \frac{d^2W_\parallel}{d\Omega d\omega} &= \frac{q^2}{\pi^2 c}\frac{\beta_z^2\cos^2\theta_z|1-\epsilon|^2}{[(1-\beta_x\cos\theta_x)^2 - \beta_z^2\cos^2\theta_z]^2\sin^2\theta_z} \\ &\times \left|\frac{(1-\beta_z\sqrt{\epsilon-\sin^2\theta_z} - \beta_z^2 - \beta_x\cos\theta_x)\sin^2\theta_z}{(1-\beta_x\cos\theta_x - \beta_z\sqrt{\epsilon-\sin^2\theta_z})(\sqrt{\epsilon-\sin^2\theta_z} + \epsilon\cos\theta_z)}\right. \\ &\left.\frac{-\beta_x\beta_z\cos\theta_x\sqrt{\epsilon-\sin^2\theta_z}}{}\right|^2 \ , \end{aligned} \tag{C.10}$$

$$\begin{aligned} \frac{d^2W_\perp}{d\Omega d\omega} &= \frac{q^2}{\pi^2 c}\frac{\beta_x^2\beta_z^4\cos^2\theta_y\cos^2\theta_z|1-\epsilon|^2}{[(1-\beta_x\cos\theta_x)^2 - \beta_z^2\cos^2\theta_z]^2\sin^2\theta_z} \\ &\times \frac{1}{\left|(1-\beta_x\cos\theta_x - \beta_z\sqrt{\epsilon-\sin^2\theta_z})(\sqrt{\epsilon-\sin^2\theta_z} + \cos\theta_z)\right|^2} \ , \end{aligned} \tag{C.11}$$

où $\beta_x = \sin\psi$, $\beta_z = \beta\cos\psi$, $\cos\theta_x = \sin\theta_z\cos\varphi$ et $\cos\theta_y = \sin\theta_z\sin\varphi$. ψ is the incidence angle in respect with the normal to the interface, and φ the angle between the incidence and observation planes (see fig. C.3).

Formulae corresponding to the transition vacuum $\rightarrow$ medium can be obtained simply by changing the sign of β_z in Eqs. C.10 and C.11.

Appendix D

Calculation of the coherent field radiated by a bunch of relativistic electrons

Let us consider a bunch of electrons injected in the front target surface, with an initial temporal profile $\propto e^{-(t/\tau)^2}$. The field radiated by the bunch at the target back side is written as:

$$E(t) = \frac{1}{\sqrt{\pi}\tau} \int_{-\infty}^{+\infty} \tilde{j}(t-t') \sqrt{\eta^*(t-t')} \, \exp\left(-\frac{t'^2}{\tau^2}\right) dt' \, , \tag{D.1}$$

In the integral, $\tilde{j}(t)$ is the electron flux at the rear side of a target with a given thickness z and represents the velocity modulation of the electronic population contained in the bunch. $\eta^*(t)$ is the energy radiated at the target/vacuum interface, by an electron with a given speed. The coherent electric field radiated at the frequency ω, $E(\omega)$, is calculated by making the Fourier transform of Eq. D.1. We deduce:

$$\begin{aligned} E(\omega) &\equiv \mathcal{F}\big[E(t)\big] \\ &= \frac{1}{\sqrt{\pi}\tau} \int_{-\infty}^{+\infty} \left[\int_{-\infty}^{+\infty} \tilde{j}(t-t') \sqrt{\eta^*(t-t')} \, \exp\left(-\big(t'/\tau\big)^2\right) dt' \right] e^{-i\omega t} \, dt \end{aligned}$$

By making the change of variables $x = t - t'$,

$$
\begin{aligned}
E(\omega) &= \frac{1}{\sqrt{\pi}\tau} \int_{-\infty}^{+\infty} \tilde{j}(x)\, \sqrt{\eta^*(x)}\, e^{-i\omega x}\, dx \int_{-\infty}^{+\infty} \exp\left(-\frac{t^2}{\tau^2} - i\omega t\right) dt \\
&= \frac{1}{\sqrt{\pi}\tau}\, \mathcal{F}\big[\tilde{j}(x)\sqrt{\eta^*(x)}\big](\omega)\, \exp\left(-\frac{\tau^2\omega^2}{4}\right) \int_{-\infty}^{+\infty} -\exp\left(\frac{t}{\tau} + i\frac{\omega\tau}{2}\right)^2 dt
\end{aligned}
$$

By transforming x into t in the Fourier transform (it does not depend on time) and with a new change of variables, $y = \frac{t}{\tau} + i\frac{\omega\tau}{2}$, calculation becomes

$$
E(\omega) = \frac{1}{\sqrt{\pi}\tau}\, \mathcal{F}\big[\tilde{j}(t)\sqrt{\eta^*(t)}\big](\omega)\, \exp\left(-\frac{\tau^2\omega^2}{4}\right) \tau \int_{-\infty}^{+\infty} e^{-y^2}\, dy
$$

The integral which persists in the equation is of Poisson type and its value is $\sqrt{\pi}$. We finally obtain

$$
E(\omega) = \mathcal{F}\big[\tilde{j}(t)\sqrt{\eta^*(t)}\big](\omega)\, \exp\left(-\frac{\tau^2\omega^2}{4}\right) . \tag{D.2}
$$

Appendix E

Trajectory of a relativistic electron in a uniform electrostatic field

Let us consider an electron in the position, in cylindrical coordinates, $(r_{0\perp}, 0)$ at the initial time $t = 0$ and in a uniform electrostatic field, parallel to the symmetry axis $\mathbf{E} = E\hat{\mathbf{z}}$. Its trajectory is given by motion equation $\mathbf{F} = \frac{d\mathbf{p}}{dt} = -eE\hat{\mathbf{z}}$, which further implies:

$$\left\{ \begin{array}{l} \dot{p_\perp} = 0 \\ \dot{p_z} = -eE \end{array} \right. \Rightarrow \left\{ \begin{array}{l} p_\perp = p_{0\perp} \\ p_z = p_{z0} - eEt \end{array} \right. \Rightarrow \left\{ \begin{array}{l} \dot{r} = \frac{p_{0\perp}}{\gamma m_e} \\ \dot{z} = \frac{p_{0z}}{\gamma m_e} - \frac{eE}{\gamma m_e} t \end{array} \right.$$

The relativistic factor $\gamma(t)$ and the momentum $p(t)$ of the electron are related by

$$\begin{aligned} \gamma(t) &= \sqrt{1 + \left(\frac{p(t)}{m_e c}\right)^2} \\ &= \sqrt{1 + \left(\frac{p_{0\perp}}{m_e c}\right)^2 + \left(\frac{p_{0z} - eEt}{m_e c}\right)^2} \end{aligned} \tag{E.1}$$

By changing the variables $\sigma = \left(\frac{p_{0\perp}}{m_e c}\right)^2 + \left(\frac{p_{0z} - eEt}{m_e c}\right)^2$ and $\tau = \frac{p_{0z} - eEt}{m_e c}$, one obtains the following system

$$\begin{cases} \dot{r} = \frac{cp_{0\perp}}{m_e c\sqrt{1+\sigma}} \\ \dot{z} = \frac{c\tau}{\sqrt{1+\left(\frac{p_{0\perp}}{mc}\right)^2+\tau^2}} \end{cases} \Rightarrow \begin{cases} r = r_0 - \frac{cp_{0\perp}}{eE} \int\limits_{\frac{p_{0\perp}^2+p_{0z}^2}{(m_e c)^2}}^{\frac{p_{0\perp}^2+(p_{0z}-eEt)^2}{(m_e c)^2}} \frac{d\sigma}{2\sqrt{1+\sigma}} \\ z = \frac{m_e c^2}{eE} \int\limits_{\frac{p_{0z}-eEt}{m_e c}}^{\frac{p_{0z}}{m_e c}} \frac{\tau\, d\tau}{\sqrt{1+\left(\frac{p_{0\perp}}{m_e c}\right)^2+\tau^2}} \end{cases}$$

After the integration and taking into account the Eq. E.1, the electron trajectory is finally given by:

$$\begin{aligned} r(t) &= r_0 + \frac{cp_{0\perp}}{eE}\left(\gamma_0 - \gamma(t)\right) \\ z(t) &= \frac{m_e c^2}{eE}\left(\gamma_0 - \gamma(t)\right) . \end{aligned} \tag{E.2}$$

Appendix F

Radiation by accelerated charges

F.1 Bremsstrahlung type radiation

In Sect. 5.2.3 we have presented the basic formulas for the Bremsstrahlung type emission, together with its main qualitative aspects. The qualitative arguments of Sect. 5.2.3 has shown that for relativistic motion the radiated energy is spread over a wide range of frequencies. The range of the frequency spectrum was estimated by appealing to properties of Fourier integrals. In the following, by using the Parseval's theorem of Fourier analysis, we will made the argument more precise, in order to quantify the linear braking radiation emitted per unit wavelength per unit solid angle, according to our experimental conditions. Let us to start from the Eq. 5.26. By substituting $\frac{dP}{dt}$ with eE, the total radiated power becomes:

$$P = \frac{2}{3}\frac{e^2}{m^2c^3}(eE)^2 \quad [\text{erg/s}] \quad (\text{c.g.s.}) \tag{F.1}$$

The general form of the radiated power is:

$$P(t) = |\mathbf{A}(t)|^2 \tag{F.2}$$

where

$$\mathbf{A}(t) = \sqrt{\frac{c}{4\pi}}\Re\{\mathbf{E}_{ret}\} \tag{F.3}$$

$\mathbf{E}_{ret}$ being the electric field of the emitted wave. The total energy radiated is the time integral of Eq. F.3:

$$W_{tot} = \int_0^{t_{max}} |\mathbf{A}(t)|^2 dt \tag{F.4}$$

This can be expressed alternatively as an integral over a frequency spectrum by use of Forrier transforms. We introduce the Fourier transform $\mathbf{A}(\omega)$ of $\mathbf{A}(t)$,

$$\mathbf{A}(\omega) = \frac{1}{\sqrt{2\pi}} \int_0^{t_{max}} \mathbf{A}(t) e^{\imath\omega\, t} dt \tag{F.5}$$

and its inverse,

$$\mathbf{A}(t) = \frac{1}{\sqrt{2\pi}} \int_{-\infty}^{t_{+\infty}} \mathbf{A}(\omega) e^{-\imath\omega\, t} d\omega \tag{F.6}$$

Then Eq. F.4 can be written

$$W_{tot} = \int_{-\infty}^{+\infty} |\mathbf{A}(\omega)|^2 d\omega \tag{F.7}$$

The equality of F.4 and F.8, with suitable mathematical restrictions on the function $\mathbf{A}(t)$, is a special case of Parseval's theorem. It is customary to integrate only over positive frequencies, since the sign of the frequency has no physical meaning. Then the relation,

$$\frac{dW_{tot}}{d\omega} = 2|\mathbf{A}(\omega)|^2 \tag{F.8}$$

defines a quantity which is the energy radiated per unit frequency interval in all the solid angle. This result relates in a quantitative way the behavior of the power radiated as a function of time to the frequency spectrum of the radiated energy. However at the observation point we have only a limited solid angle (experimentally the optical aperture of our detection system is $f/1 - f/2$). Moreover the emission is not isotropic, but with a typical angular dependency expressed in Eq. 5.24. Thus, by Eq. 5.24 and F.8 we obtain:

$$\frac{dW_{tot}}{d\omega} = const \int_0^{\frac{\pi}{2}} \frac{\sin^2\theta}{(1-\beta\cos\theta)^5} d\Omega = 2|\mathbf{A}(\omega)|^2 \tag{F.9}$$

giving:

$$const = \frac{2|\mathbf{A}(\omega)|^2}{\int_0^{\frac{\pi}{2}} \frac{\sin^2\theta}{(1-\beta\cos\theta)^5} d\Omega} \tag{F.10}$$

and finally:

$$\frac{dW_{tot}}{d\omega\, d\Omega} = \frac{2|\mathbf{A}(\omega)|^2}{\int_0^{\frac{\pi}{2}} \frac{\sin^2\theta}{(1-\beta\cos\theta)^5} d\Omega} \int_0^{\theta_{max}} \frac{\sin^2\theta}{(1-\beta\cos\theta)^5} d\Omega \tag{F.11}$$

where θ_{max} is the maximum detection angle.

Thanks to these analytical developments we have extimated, in Fig. 5.18, the energy radiated by the Bremsstrahlung type mechanism per unit wavelength interval, as a function of the electron energy, wavelength and electrostatic field. The solid angle corresponding to our optical experimental aperture has been taken into account. In Fig. 5.18 we can observe local very fast local variations of the energy radiated as a function of the wavelength and the electron energy. This is a direct consequence of the coherent superposition of the radiation emitted along all the braking process.

F.2 Radiation of a charge in arbitrary, extremely relativistic motion

For a charged particle undergoing arbitrary, extremely relativistic motion the radiation emitted at any instant can be thought of as a coherent superposition of contributions coming from the components of acceleration parallel to and perpendicular to the velocity. But we have seen in Sect. 5.2.3 that for comparable parallel and perpendicular forces the radiation from the parallel component is negligible (of order $1/\gamma^2$) to that from the perpendicular component. Consequently we may neglect the parallel component of acceleration and approximate the radiation intensity by that from the perpendicular component alone. In other words, the radiation emitted by a charged particle in arbitrary, extreme relativistic motion is approximatively the same as the emitted by a circular moving instantaneously along the arc of a circular path whose radius of curvature ρ is given by

$$\rho = \frac{v^2}{\dot{v}_\perp} \simeq \frac{c^2}{\dot{v}_\perp} \tag{F.12}$$

where $\dot{v}_\perp$ is the perpendicular component of acceleration. The form of the angular distribution of radiation is given by Eqs. 5.31 and 5.34. It corresponds to a narrow cone (of aperture $1/\gamma$) of searchlight beam of radiation directed along the instantaneous velocity vector of the charge. The radiation will be visible only when the particle's velocity is directed towards the observer. For a particle in arbitrary motion the observer will thus detect a pulse of radiation of very short time duration (or a succession of such burst if the particle is in periodic motion). Since the angular width

of the beam is of the order of γ^{-1}, during the detection time the particle will travel only a distance of the order of

$$d = \frac{\rho}{\gamma} \tag{F.13}$$

corresponding to a time,

$$\Delta t = \frac{\rho}{\gamma v} \tag{F.14}$$

while illuminating the observer. As we will see in the following paragraph, this time could be very short and allowing the emission of a wide spectrum of synchrotron type radiation. To make the argument conceptually simple neglect the curvature of the path during this time and suppose that a sharp rectangular pulse of radiation is emitted. In the time Δt the front edge of the pulse travels a distance,

$$\Delta t = c\Delta t = \frac{\rho}{\gamma\beta} \tag{F.15}$$

Since the particle is moving in the same direction with speed v and moves a distance d in the time Δt, the rear edge of the pulse will be only a distance

$$L = D - d = \left(\frac{1}{\beta} - 1\right)\frac{\rho}{\gamma} \simeq \frac{\rho}{2\gamma^3} \tag{F.16}$$

behind the front edge as the pulse moves off. The pulse length is thus L in space, or L/c in time. From general arguments about the Fourier decomposition of finite wave trains this implies that the spectrum of the radiation will contain appreciable frequency components up to a critical frequency,

$$\omega_c \sim \frac{c}{L} \simeq \left(\frac{c}{\rho}\right)\gamma^3 \tag{F.17}$$

For a circular motion c/ρ is the angular frequency of rotation ω_0 and even for arbitrary motion it plays the role of a fundamental frequency. Eq. F.17 show that a relativistic particle emits a broad spectrum of frequencies, up to γ^3 times the fundamental frequency.

F.3 Spectrum of relativistic charges in instantaneously circular motion

In Sect. F.3 we saw that the radiation emitted by an extremely relativistic particle subject to arbitrary accelerations is equivalent to that emitted by a particle moving

instantaneously at constant speed on an appropriate circular path. Moreover, the detector collect only the signal emitted by the particle when it moves in a narrow cone along the observation direction. Thus, in order to obtain the total energy radiated per unit solid angle per unit frequency interval, we need to integrate the relation F.5 over the the emission time Δt defined in Sect. F.3, taking into account the coherent superposition at each time. This implies a complicate Fourier analysis which we will not develop here. However, the result of this analysis is that the radiated energy radiated per unit frequency interval per unit solid angle can be finally written as [97]:

$$\frac{d^2W}{d\omega d\Omega} = \frac{e^2}{3\pi^2 c}\left(\frac{\omega\rho}{c}\right)^2\left(\frac{1}{\gamma^2}+\theta^2\right)^2\left[K_{2/3}^2(\xi)+\frac{\theta^2}{(1/\gamma^2)+\theta^2}K_{1/3}^2(\xi)\right] \tag{F.18}$$

where $K_{2/3}^2(\xi)$ and $K_{1/3}^2(\xi)$ are defined as modified Bessel functions:

$$\int_0^\infty x\sin\left[\frac{3}{2}\xi\left(x+\frac{1}{3}x^3\right)\right]dx = \frac{1}{\sqrt{3}}K_{2/3}(\xi) \tag{F.19}$$

$$\int_0^\infty \cos\left[\frac{3}{2}\xi\left(x+\frac{1}{3}x^3\right)\right]dx = \frac{1}{\sqrt{3}}K_{1/3}(\xi) \tag{F.20}$$

with

$$\xi = \frac{\omega\rho}{3c}\left(\frac{1}{\gamma^2}+\theta^2\right) \tag{F.21}$$

The first term in the square bracket to radiation polarized in the plane of the orbit, and the second to radiation polarized perpendicular to that plane. We now proceed to examine this somewhat complex result. First we integrate over all frequencies and find that the distribution of energy in angle is

$$\frac{dW}{d\Omega} = \frac{7}{16}\frac{e^2}{\rho}\frac{1}{\left(\frac{1}{\gamma^2}+\theta^2\right)^{5/2}}\left[1+\frac{5}{7}\frac{\theta^2}{(1/\gamma^2)+\theta^2}\right] \tag{F.22}$$

This shows the characteristic behaviour seen in Sect. 5.2.3. Eq. F.22 can be obtained directly, of course, by integrating a slight generalization of the circular-motion power formula (eq. F.22) over all times. As in Eq. F.18, the first term in Eq. F.22 corresponds to polarization parallel to the orbital plane, and the second to perpendicular polarization. Integrating over all angles, we find that seven times as much energy is radiated with parallel polarization as with perpendicular polarization. Thus, the radiation from a relativistically moving charge is very strongly, but not completely, polarized in the plane of motion.

Furthermore, the properties of the modified Bessel functions show that the intensity of radiation is negligible for $\xi \gg 1$. From Eq. F.21 we see that this will occur at large angles; the greater the frequency, the smaller the critical angle beyond which there will be negligible radiation. This show that the radiation is largely confined to the plane containing the motion, as shown by eq. F.22, being more so confined the higher the frequency relative to c/ρ. If ω gets too large, however, we see that ξ will be large at *all* angles. Then there will be negligible total energy emitted at that frequency. The critical frequency ω_c beyond which there is negligible radiation at any angle can be defined by $\xi = 1$ for $\theta = 0$. then we find

$$\omega_c = 3\gamma^3 \left(\frac{c}{\rho}\right) = 3 \left(\frac{E}{mc^2}\right)^3 \frac{c}{\rho} \tag{F.23}$$

This critical frequency is seen to agree with our qualitative estimate (see eq. F.17). Let us to notice that for our experimental conditions (wavelength $\lambda > 300$ nm, kinetic energies of the order of a few MeV and an electrostatic field of the order of ≈ 1 MV/μm) the critical wavelength $\lambda_c = 2\pi\, c/\omega_c$ is always between few ten's nm (for $E_k \sim 1$ MeV) and 1 nm (for $E_k \sim 10$ MeV) and thus largely shorter that our detection range. Since the radiation is predominantly in the orbital plane for $\gamma \gg 1$, it is instructive to evaluate the angular distribution (Eq. F.18) at $\theta = 0$. For frequencies well below the critical frequency ($\omega \ll \omega_c$), we find

$$\frac{d^2W}{d\omega d\Omega}\Big|_{\theta=0} \simeq \frac{e^2}{c} \left[\frac{\Gamma(\frac{2}{3})}{\pi} \left(\frac{3}{4}\right)^{\frac{1}{3}} \left(\frac{\omega\rho}{c}\right)^{\frac{2}{3}}\right] \tag{F.24}$$

For the opposite limit of $\omega \gg \omega_c$, the result is

$$\frac{d^2W}{d\omega d\Omega}\Big|_{\theta=0} \simeq \frac{3}{2\pi} \frac{e^2}{c} \Gamma^2 \frac{\omega}{\omega_c} e^{-2\frac{\omega}{\omega_c}} \tag{F.25}$$

These limiting forms show that the spectrum at $\theta = 0$ increases with frequency roughly as $\omega^{\frac{2}{3}}$ well below the critical frequency (which is our case), reaches a maximum in the neighborhood of ω_c, and then drops exponentially to zero above that frequency.

Furthermore, the spread in angle at a fixed frequency can be extimated by determining the angle θ_c at which $\xi(\theta_c) \simeq \xi(0) + 1$. In the low frequency range ($\omega \ll \omega_c$), $\xi(0)$ is very small, so that $\xi(\theta_c) \simeq 1$. This gives

$$\theta_c \simeq \left(\frac{3c}{\omega\rho}\right)^{\frac{1}{3}} = \frac{1}{\gamma} \left(\frac{\omega_c}{\omega}\right)^{\frac{1}{3}} \tag{F.26}$$

We can note that in our low frequency regime the radiation is emitted at much wider angles than the average, $\langle\theta^2\rangle \simeq \gamma^{-1}$. More in detail, for our experimental

conditions (wavelength $\lambda > 300$ nm, kinetic energies of the order of a few MeV and an electrostatic field of the order of ≈ 1 MV/μm) the critical angle is always between 15° (for $E_k \sim 10$ MeV and $\lambda \sim 400$ nm) and 35° (for $E_k \sim 1$ MeV and $\lambda \sim 500$ nm).

In the high-frequency limit ($\omega > \omega_c$), $\xi(0)$ is large compare to unity. then the intensity falls off in angle approximately as

$$\frac{d^2W}{d\omega d\Omega} \simeq \frac{d^2W}{d\omega d\Omega}\Big|_{\theta=0} e^{-3\frac{\omega\gamma^2\theta^2}{\omega_c}} \tag{F.27}$$

Thus the critical angle, defined by the $1/e$ point, is

$$\theta_c \simeq \frac{1}{\gamma}\left(\frac{\omega_c}{3\omega}\right)^{\frac{1}{2}} \tag{F.28}$$

The frequency distribution of the total energy emitted as the particle passes by can be found by integrating the eq. F.18 over all angles. We can extimate the integral for our low-frequency range by using the value of the angular distribution (eq. F.24) at $\theta = 0$ and the critical angle θ_c (eq. F.26). Then we obtain

$$\frac{dW}{d\omega} \sim 2\pi\theta_c \frac{d^2W}{d\omega d\Omega}\Big|_{\theta=0} \sim \frac{e^2}{c}\left(\frac{\omega\rho}{c}\right)^{\frac{1}{3}} \tag{F.29}$$

showing that the spectrum increases as $\sim \omega^{\frac{1}{3}}$ for $\omega \ll \omega_c$. This gives a very broad, flat spectrum at frequencies below ω_c. For the high-frequency limit where $\omega \gg \omega_c$ we can integrate Eq. F.27 over all angles to obtain the reasonably accurate result,

$$\frac{dW}{d\omega} \simeq \sqrt{3\pi}\frac{e^2}{c}\Gamma\frac{\omega}{\omega_c}e^{-2\frac{\omega}{\omega_c}} \tag{F.30}$$

The peak intensity is of the order of $e^2\gamma/c$, and the total energy is of the order of $e^2\gamma\omega_c/c = 3e^2\gamma^4/\rho$. This is in agreement with the value of $4\pi\, e^2\gamma^4/3\rho$ for the radiative loss per revolution in circular accelerators.

Appendix G

Diagnostic calibrations

G.1 Calibration of the spectral diagnostic

G.1.1 Dispersion and spectral resolution

Dispersion of our spectrometer was measured using a Mercury ORIEL lamp. The identification of the characteristic of the emission lines of this gas on the images produced on the CCD devices enabled us to obtain by a linear fit of the spectral dispersion $\delta\lambda$[nm/px] and a benchmark position $\lambda(px_{ref})$[nm]:

$$\lambda_{px} = \lambda(px_{ref}) + \Delta\lambda(px - px_{ref}) \tag{G.1}$$

where $px = 1, \ldots, 1024$

The minimal spectral resolution, which depends on the dispersion, is proportional to the aperture of the entry slit of of spectrometer h_{spec}:

$$res[\text{nm}] = h_{spec}[\mu\text{m}]\,\frac{\Delta\lambda[\text{nm/px}]}{\mathscr{M}_{exp}[\mu\text{m/px}]} \tag{G.2}$$

where $\mathscr{M}_{exp}[\mu\text{m/px}]$ is the intrinsic magnification of the system.

Dispersions and spectral resolutions obtained are:

Config. 2 Spectrometer Yobin-Yvon model HR2505, Czerny-Turner configuration with a focal length of 250 mm and grating of 150 lines/mm.

- Spectral dispersion: $\Delta\lambda = 0.677\,\text{nm/px}$ For all the images:

$$\lambda_{px}[\text{nm}] = 213.863 + 0.677\,px \qquad \text{for} \qquad px = 1, \ldots 1024\ .$$

- Spectral resolution: $res \approx 5\,\text{nm}$, obtained with a $h_{spec} = 100\,\mu\text{m}$ and $\mathscr{M}_{exp} \approx 1.6\,\mu\text{m/px}$.

G.1.2 Spectral response in energy

The response in energy of our detection system was performed by using a calibrated lamp. The calibration lamp was placed inside the interaction chamber so that the source is at the same position of the emitting region at the rear surface of the targets during a shoot. The radiation emitted by the lamp was thus collected in the same solid angle Ω and follows the same optical path until the detection system (lenses, beam splitters, filters) that the studied visible radiation. We used the calibration lamp *ORIEL Standard of Spectral Radiance 63355*. The manufacturer provides a table of its radiance [**?**] as a function of the energy E expressed in eV. From this table we obtained the fit

$$y = \frac{m_1 E^{m_3}}{e^{E/m_2} - 1}\ , \tag{G.3}$$

with the constants $m_1 = 150.19$, $m_2 = 0.27722$ and $m_3 = 4.9588$. y corresponds to a tenth of the radiance (in $\text{mWm}^{-2}\text{nm}^{-1}$) at 50 cm from the source and with a supplied power of 200 W. Energy E is related to the wavelength by the equation:

$$\lambda[\text{nm}] = \frac{hc}{e}\frac{10^9}{E[\text{eV}]} \approx \frac{1240}{E[\text{eV}]} \tag{G.4}$$

Thus the source is:

$$S_\lambda[\text{Jnm}^{-1}] = x^2\, 10y\,[\text{Wm}^{-2}\text{nm}^{-1}]\,\tau_{calib}[\text{s}]\,S\ , \tag{G.5}$$

where $x^{-1} = \frac{r}{R}$, with $R = 50$ cm, the distance for which the constructor give the value $10y[\text{Wm}^{-2}\text{nm}^{-1}]$ for the lamp radiance. Thus, by supposing an isotropic emissivity of the lamp, at a distance r from the source, we have x^2 times the radiance given by the constructor. $\tau_{calib} = 1\,\text{ms}$ is the acquisition time of the ICCD calibration. We placed the lamp at a distance $r = 1\,\text{cm}$ from a pin hole located at the target position and with an aperture of $S \approx 25\pi\,10^{-8}\ \text{m}^2$. After withdrawing the background noise, the signal is integrated in order to obtain the curve $C_{calib}(\lambda)$ in *counts* per nanometer of

the wavelength axis (see Fig. (b)). The spectral response of the acquisition system is thus given by (see Fig. G.1):

$$\eta(\lambda)[\text{counts/J}] = \frac{C_{calib}[\text{counts/px}]}{T_{calib}\, S_\lambda[\text{Jnm}^{-1}]} \frac{1}{\Delta\lambda[\text{nm/px}]} \tag{G.6}$$

where T_{calib} is related to transmission of the filters placed on the optical path during the calibration.

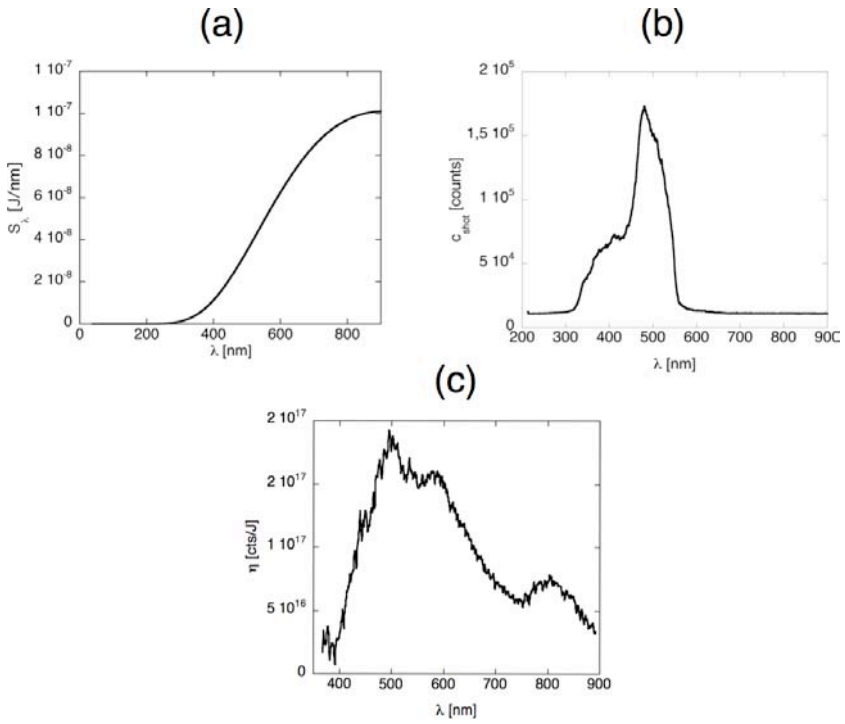

Figure G.1: (a) Emissivity of the lamp of calibration *ORIEL Standard of Spectral Radiance 63355*. **(b)** Signal of the lamp obtained by the experimental system. **(c)** Spectral response of the acquisition system.

G.2 ICCD camera energy calibration

G.2.1 ICCD camera absolute energy calibration

In order to measure the energy associated to each *count*, we used, as a source of calibration, a probe pulse of 40 fs at the fundamental laser wavelength (815 nm) which follows the same optical path of the recorded radiation during our experiment. The incidental beam was attenuated with several neutral densities placed in front of the

entry of the ICCD camera and was measured by a microjoulemeter Scientech 37 (model 280101 S/N 5449). The acquisition time of the camera was 2 ns with the Gain of 255, as during the experiment shots. The energy received by the device to be calibrated is then given by

$$Energy = E_{\mu J}\, T_{815\,\mathrm{nm}}$$

where $E_{\mu J}$ is the energy measured on the microjoulemeter, $T_{815\,\mathrm{nm}}$ the transmissivity of the optical ND densities used at the source wavelength (measured with a spectrophotometer). After the subtraction of the background noise, an integral of the signal provides the total number of *counts* corresponding to detected energy. By making a *fit* for various attenuations of the probe beam at the entry of the ICCD camera, we finally obtained the value:

$$\left(\frac{Counts}{Energy}\right)_{ICCD} = 10^{17}\,\mathrm{cts/J} \tag{G.7}$$

G.2.2 ICCD camera energy spectral response

The Andor camera response depends on the radiation wavelength. Thus, in order to obtain the camera response as function of the detected radiation wavelength, we use the spectral response of the acquisition system with the spectrometer (eq. G.6) weighted by the absolute energy calibration value of 10^{17} (cts/J) obtained for the detected radiation at 815 nm without the spectrometer. In this way, we finally get $\approx 5.6 \times 10^{16}$ (cts/J) and $\approx 2.25 \times 10^{17}$ (cts/J) for the signal recorded respectively at 405 and 546 nm (cf. Sect. 6.2).

Bibliography

[1] D. Strickland and G. Mourou. Compression of amplified chirped optical pulses. *Optics Communications*, 56(3):219, 1985.

[2] E. Lefebvre and G. Bonnaud. Transparency/Opacity of a Solid Target Illuminated by an Ultrahigh-Intensity Laser Pulse. *Physical Review Letters*, 74:2002–2005, March 1995.

[3] S. C. Wilks, W. L. Kruer, M. Tabak, and A. B. Langdon. Absorption of ultra-intense laser pulses. *Physical Review Letters*, 69:1383–1386, August 1992.

[4] M. Tabak, J. Hammer, M. E. Glinsky, W. L. Kruer, S. C. Wilks, J. Woodworth, E. M. Campbell, M. D. Perry, and R. J. Mason. Ignition and high gain with ultrapowerful lasers. *Physics of Plasmas*, 1:1626–1634, May 1994.

[5] C. Deutsch, H. Furukawa, K. Mima, M. Murakami, and K. Nishihara. Interaction Physics of the Fast Ignitor Concept. *Physical Review Letters*, 77:2483–2486, September 1996.

[6] J. Meyer-ter-Vehn. On energy gain of fusion targets: the model of Kidder and Bodner improved. *Nuclear Fusion*, 22(4):561–565, 1982.

[7] S. Atzeni and M. L. Ciampi. Presentation at *Pisa Easter Meetings on Plasma Physics*, 1996.

[8] L. Gremillet. étude d'un nouveau concept de Fusion par Confinement Inertiel : l'allumeur rapide. Rapport de stage long, CEA - École Nationale des Ponts et Chaussées, 1996.

[9] R. Wagner, S.-Y. Chen, A. Maksimchuk, and D. Umstadter. Electron Acceleration by a Laser Wakefield in a Relativistically Self-Guided Channel. *Physical Review Letters*, 78:3125–3128, April 1997.

[10] M. Borghesi, A. J. MacKinnon, L. Barringer, R. Gaillard, L. A. Gizzi, C. Meyer, O. Willi, A. Pukhov, and J. Meyer-Ter-Vehn. Relativistic Channeling of a Pi-

cosecond Laser Pulse in a Near-Critical Preformed Plasma. *Physical Review Letters*, 78:879–882, February 1997.

[11] M. Borghesi, A. J. MacKinnon, R. Gaillard, O. Willi, A. Pukhov, and J. Meyer-Ter-Vehn. Large Quasistatic Magnetic Fields Generated by a Relativistically Intense Laser Pulse Propagating in a Preionized Plasma. *Physical Review Letters*, 80:5137–5140, June 1998.

[12] J. Fuchs, G. Malka, J. C. Adam, F. Amiranoff, S. D. Baton, N. Blanchot, A. Héron, G. Laval, J. L. Miquel, P. Mora, H. Pépin, and C. Rousseaux. Dynamics of Subpicosecond Relativistic Laser Pulse Self-Channeling in an Underdense Preformed Plasma. *Physical Review Letters*, 80:1658–1661, February 1998.

[13] K. Krushelnick, A. Ting, C. I. Moore, H. R. Burris, E. Esarey, P. Sprangle, and M. Baine. Plasma Channel Formation and Guiding during High Intensity Short Pulse Laser Plasma Experiments. *Physical Review Letters*, 78:4047–4050, May 1997.

[14] A. J. MacKinnon, M. Borghesi, R. Gaillard, G. Malka, O. Willi, A. A. Offenberger, A. Pukhov, J. Meyer-Ter-Vehn, B. Canaud, J. L. Miquel, and N. Blanchot. Intense laser pulse propagation and channel formation through plasmas relevant for the fast ignitor scheme. *Physics of Plasmas*, 6:2185–2190, May 1999.

[15] E. L. Clark, K. Krushelnick, J. R. Davies, M. Zepf, M. Tatarakis, F. N. Beg, A. Machacek, P. A. Norreys, M. I. K. Santala, I. Watts, and A. E. Dangor. Measurements of Energetic Proton Transport through Magnetized Plasma from Intense Laser Interactions with Solids. *Physical Review Letters*, 84:670–673, January 2000.

[16] A. Maksimchuk, S. Gu, K. Flippo, D. Umstadter, and V. Y. Bychenkov. Forward Ion Acceleration in Thin Films Driven by a High-Intensity Laser. *Physical Review Letters*, 84:4108–4111, May 2000.

[17] K. Nemoto, A. Maksimchuk, S. Banerjee, K. Flippo, G. Mourou, D. Umstadter, and V. Y. Bychenkov. Laser-triggered ion acceleration and table top isotope production. *Applied Physics Letters*, 78:595–597, January 2001.

[18] S. P. Hatchett, C. G. Brown, T. E. Cowan, E. A. Henry, J. S. Johnson, M. H. Key, J. A. Koch, A. B. Langdon, B. F. Lasinski, R. W. Lee, A. J. MacKinnon, D. M. Pennington, M. D. Perry, T. W. Phillips, M. Roth, and et al. Electron, photon, and ion beams from the relativistic interaction of Petawatt laser pulses with solid targets. *Physics of Plasmas*, 7:2076–2082, May 2000.

[19] R. A. Snavely, M. H. Key, S. P. Hatchett, T. E. Cowan, M. Roth, T. W. Phillips, M. A. Stoyer, E. A. Henry, T. C. Sangster, M. S. Singh, S. C. Wilks, A. MacKinnon, A. Offenberger, D. M. Pennington, K. Yasuike, A. B. Langdon, B. F.

Lasinski, J. Johnson, M. D. Perry, and E. M. Campbell. Intense High-Energy Proton Beams from Petawatt-Laser Irradiation of Solids. *Physical Review Letters*, 85:2945–2948, October 2000.

[20] A. J. MacKinnon, Y. Sentoku, P. K. Patel, D. W. Price, S. Hatchett, M. H. Key, C. Andersen, R. Snavely, and R. R. Freeman. Enhancement of Proton Acceleration by Hot-Electron Recirculation in Thin Foils Irradiated by Ultraintense Laser Pulses. *Physical Review Letters*, 88(21):215006–+, May 2002.

[21] M. Hegelich, S. Karsch, G. Pretzler, D. Habs, K. Witte, W. Guenther, M. Allen, A. Blazevic, J. Fuchs, J. C. Gauthier, M. Geissel, P. Audebert, T. Cowan, and M. Roth. MeV Ion Jets from Short-Pulse-Laser Interaction with Thin Foils. *Physical Review Letters*, 89(8):085002–+, August 2002.

[22] M. Roth, A. Blazevic, M. Geissel, T. Schlegel, T. E. Cowan, M. Allen, J.-C. Gauthier, P. Audebert, J. Fuchs, J. Meyer-Ter-Vehn, M. Hegelich, S. Karsch, and A. Pukhov. Energetic ions generated by laser pulses: A detailed study on target properties. *Physical Review Special Topics Accelerators and Beams*, 5(6):061301–+, June 2002.

[23] M. Roth, M. Allen, P. Audebert, A. Blazevic, E. Brambrink, T. E. Cowan, J. Fuchs, J.-C. Gauthier, M. Geißel, M. Hegelich, S. Karsch, J. Meyer-ter-Vehn, H. Ruhl, T. Schlegel, and R. B. Stephens. The generation of high-quality, intense ion beams by ultra-intense lasers. *Plasma Physics and Controlled Fusion*, 44:B99+, December 2002.

[24] M. Borghesi, A. J. Mackinnon, A. Schiavi, D. H. Campbell, and Willi. Radiography of dense matter with laser-produced protons: preliminary tests. Annual report, RAL Central Laser Facility, 1999/2000.

[25] M. Borghesi, A. Schiavi, D. H. Campbell, M. G. Haines, O. Willi, A. J. MacKinnon, L. A. Gizzi, M. Galimberti, R. J. Clarke, and H. Ruhl. Proton imaging: a diagnostic for inertial confinement fusion/fast ignitor studies. *Plasma Physics and Controlled Fusion*, 43:A267+, December 2001.

[26] M. Borghesi, S. Bulanov, D. H. Campbell, R. J. Clarke, T. Z. Esirkepov, M. Galimberti, L. A. Gizzi, A. J. MacKinnon, N. M. Naumova, F. Pegoraro, H. Ruhl, A. Schiavi, and O. Willi. Macroscopic Evidence of Soliton Formation in Multiterawatt Laser-Plasma Interaction. *Physical Review Letters*, 88(13):135002–+, April 2002.

[27] M. Roth, T. E. Cowan, M. H. Key, S. P. Hatchett, C. Brown, W. Fountain, J. Johnson, D. M. Pennington, R. A. Snavely, S. C. Wilks, K. Yasuike, H. Ruhl, F. Pegoraro, S. V. Bulanov, E. M. Campbell, M. D. Perry, and H. Powell. Fast

Ignition by Intense Laser-Accelerated Proton Beams. *Physical Review Letters*, 86:436–439, January 2001.

[28] T. Tajima and J. M. Dawson. Laser electron accelerator. *Physical Review Letters*, 43:267–+, July 1979.

[29] H. Ruhl, Y. Sentoku, K. Mima, K. A. Tanaka, and R. Kodama. Collimated Electron Jets by Intense Laser-Beam-Plasma Surface Interaction under Oblique Incidence. *Physical Review Letters*, 82:743–746, January 1999.

[30] W. Yu, V. Bychenkov, Y. Sentoku, M. Y. Yu, Z. M. Sheng, and K. Mima. Electron Acceleration by a Short Relativistic Laser Pulse at the Front of Solid Targets. *Physical Review Letters*, 85:570–573, July 2000.

[31] A. Pukhov, Z.-M. Sheng, and J. Meyer-Ter-Vehn. Particle acceleration in relativistic laser channels. *Physics of Plasmas*, 6:2847–2854, July 1999.

[32] G. D. Tsakiris, C. Gahn, and V. K. Tripathi. Laser induced electron acceleration in the presence of static electric and magnetic fields in a plasma. *Physics of Plasmas*, 7:3017–3030, July 2000.

[33] F. Amiranoff, M. Laberge, J. R. Marquès, F. Moulin, E. Fabre, B. Cros, G. Matthieussent, P. Benkheiri, F. Jacquet, J. Meyer, P. Miné, C. Stenz, and P. Mora. Observation of modulational instability in Nd-laser beat-wave experiments. *Physical Review Letters*, 68:3710–3713, June 1992.

[34] C. E. Clayton, M. J. Everett, A. Lal, D. Gordon, K. A. Marsh, and C. Joshi. Acceleration and scattering of injected electrons in plasma beat wave accelerator experiments. *Physics of Plasmas*, 1:1753–1760, May 1994.

[35] F. Amiranoff, S. Baton, D. Bernard, B. Cros, D. Descamps, F. Dorchies, F. Jacquet, V. Malka, J. R. Marquès, G. Matthieussent, P. Miné, A. Modena, P. Mora, J. Morillo, and Z. Najmudin. Observation of Laser Wakefield Acceleration of Electrons. *Physical Review Letters*, 81:995–998, August 1998.

[36] A. Modena, Z. Najmudin, A. E. Dangor, C. E. Clayton, K. A. Marsh, C. Joshi, V. Malka, C. B. Darrow, C. Danson, D. Neely, and F. N. Walsh. Electron Acceleration from the Breaking of Relativistic Plasma Waves. *Nature*, 377:606 –+, October 1995.

[37] D. Umstadter, S.-Y. Chen, A. Maksimchuk, G. Mourou, and R. Wagner. Nonlinear Optics in Relativistic Plasmas and Laser Wake Field Acceleration of Electrons. *Science*, 273:472–475, July 1996.

[38] C. I. Moore, A. Ting, K. Krushelnick, E. Esarey, R. F. Hubbard, B. Hafizi, H. R. Burris, C. Manka, and P. Sprangle. Electron Trapping in Self-Modulated

Laser Wakefields by Raman Backscatter. *Physical Review Letters*, 79:3909–3912, November 1997.

[39] V. Malka, S. Fritzler, E. Lefebvre, M.-M. Aleonard, F. Burgy, J.-P. Chambaret, J.-F. Chemin, K. Krushelnick, G. Malka, S. P. D. Mangles, Z. Najmudin, M. Pittman, J.-P. Rousseau, J.-N. Scheurer, B. Walton, and A. E. Dangor. Electron Acceleration by a Wake Field Forced by an Intense Ultrashort Laser Pulse. *Science*, 298:1596–1600, November 2002.

[40] V. Malka, J. Faure, Y. Glinec, and A. F. Lifschitz. Laser-plasma accelerators: a new tool for science and for society. *Plasma Physics and Controlled Fusion*, 47:B481–B490, December 2005.

[41] J. Faure, Y. Glinec, A. Pukhov, S. Kiselev, S. Gordienko, E. Lefebvre, J.-P. Rousseau, F. Burgy, and V. Malka. A laser-plasma accelerator producing monoenergetic electron beams. *Nature*, 431:541–544, September 2004.

[42] T. Fuchs H. Szymanowski U. Oelfke Y. Glinec, J. Faure and V. Malka. *Medical Physics*, (33).

[43] Y. Glinec, J. Faure, L. L. Dain, S. Darbon, T. Hosokai, J. J. Santos, E. Lefebvre, J. P. Rousseau, F. Burgy, B. Mercier, and V. Malka. High-Resolution γ-Ray Radiography Produced by a Laser-Plasma Driven Electron Source. *Physical Review Letters*, 94(2):025003–+, January 2005.

[44] B. Brozek-Pluska, D. Gliger, A. Hallou, V. Malka, and Y. A. Gauduel. Direct observation of elementary radical events: low- and high-energy radiation femtochemistry in solutions. *Radiation Physics and Chemistry*, 72:149–157, February 2005.

[45] S. Jacquemot. Le laser à rayons x. In J. P. Watteau R. Dautray, editor, *La fusion thermonucléaire inertielle par laser, partie 1*, volume 2, page 1168. Eyrolles, Paris, 1993.

[46] E. S. Sarachik and G. T. Schappert. Classical Theory of the Scattering of Intense Laser Radiation by Free Electrons. *Physical Review D*, 1:2738–2752, May 1970.

[47] P. Gibbon. High-order harmonic generation in plasmas. *IEEE Journal of Quantum Electronics*, 33(11):1915–1924, 1997.

[48] I. Watts, M. Zepf, E. L. Clark, M. Tatarakis, K. Krushelnick, A. E. Dangor, R. M. Allott, R. J. Clarke, D. Neely, and P. A. Norreys. Dynamics of the Critical Surface in High-Intensity Laser-Solid Interactions: Modulation of the XUV Harmonic Spectra. *Physical Review Letters*, 88(15):155001–+, April 2002.

[49] M. D. Perry, J. A. Sefcik, T. Cowan, S. Hatchett, A. Hunt, M. Moran, D. Pennington, R. Snavely, and S. C. Wilks. Hard x-ray production from high intensity laser solid interactions (invited). *Review of Scientific Instruments*, 70:265–269, January 1999.

[50] P. A. Norreys, A. P. Fews, F. N. Beg, A. R. Bell, A. E. Dangor, P. Lee, M. B. Nelson, H. Schmidt, M. Tatarakis, and M. D. Cable. Neutron production from picosecond laser irradiation of deuterated targets at intensities of 10^{19} W cm^{-2}. *Plasma Physics and Controlled Fusion*, 40:175–182, February 1998.

[51] G. Pretzler, A. Saemann, A. Pukhov, D. Rudolph, T. Schätz, U. Schramm, P. Thirolf, D. Habs, K. Eidmann, G. D. Tsakiris, J. Meyer-Ter-Vehn, and K. J. Witte. Neutron production by 200 mJ ultrashort laser pulses. *Physical Review E*, 58:1165–1168, July 1998.

[52] L. Disdier, J.-P. Garçonnet, G. Malka, and J.-L. Miquel. Fast Neutron Emission from a High-Energy Ion Beam Produced by a High-Intensity Subpicosecond Laser Pulse. *Physical Review Letters*, 82:1454–1457, February 1999.

[53] R. Kodama, K. A. Tanaka, T. Yamanaka, Y. Kato, Y. Kitagawa, H. Fujita, T. Kanabe, N. Izumi, K. Takahashi, H. Habara, K. Okada, M. Iwata, T. Matsushita, and K. Mima. Studies of intense laser-plasma interactions for the fast ignitor concept at ILE, Osaka University. *Plasma Physics and Controlled Fusion*, 41:A419–A425, March 1999.

[54] M. H. Key, M. D. Cable, T. E. Cowan, K. G. Estabrook, B. A. Hammel, S. P. Hatchett, E. A. Henry, D. E. Hinkel, J. D. Kilkenny, J. A. Koch, W. L. Kruer, A. B. Langdon, B. F. Lasinski, R. W. Lee, B. J. MacGowan, and et al. Hot electron production and heating by hot electrons in fast ignitor research. *Physics of Plasmas*, 5:1966–1972, May 1998.

[55] G. Mourou. Ultrahigh-intensity lasers: Physics of the extreme on a tabletop. *Physics Today*, 22, 1998.

[56] S. Ichimaru and H. Kitamura. Ultradense hydrogen in astrophysics, high-pressure metal physics and fusion studies. In M. Lontano, G. Mourou, F. Pegoraro, and E. Sindoni, editors, *AIP Conf. Proc. 426: Superstrong Fields in Plasmas*, pages 541–+, 1998.

[57] L. Landau and E. Lifchitz. *The Classical Theory of Fields*. Pergamon, Oxford, 1975.

[58] P. Monot, T. Auguste, P. Gibbon, F. Jakober, G. Mainfray, A. Dulieu, M. Louis-Jacquet, G. Malka, and J. L. Miquel. Experimental Demonstration of Relativistic Self-Channeling of a Multiterawatt Laser Pulse in an Underdense Plasma. *Physical Review Letters*, 74:2953–2956, April 1995.

[59] C. E. Max, J. Arons, and A. B. Langdon. Self-Modulation and Self-Focusing of Electromagnetic Waves in Plasmas. *Physical Review Letters*, 33:209–212, July 1974.

[60] A. B. Borisov, O. B. Shiryaev, A. McPherson, K. Boyer, and C. K. Rhodes. Stability analysis of relativistic and charge-displacement self-channelling of intense laser pulses in underdense plasmas. *Plasma Physics and Controlled Fusion*, 37:569–597, May 1995.

[61] W. Rozmus and V. T. Tikhonchuk. Heating of solid targets by subpicosecond laser pulses. *Physical Review A: General Physics*, 46:7810–7814, December 1992.

[62] L. Spitzer and R. Härm. Transport Phenomena in a Completely Ionized Gas. *Physical Review*, 89:977–981, March 1953.

[63] W. Rozmus and V. T. Tikhonchuk. Skin effect and interaction of short laser pulses with dense plasmas. *Physical Review A: General Physics*, 42:7401–7412, December 1990.

[64] A. Ng, A. Forsman, and P. Celliers. Heat front propagation in femtosecond-laser-heated solids. *Physical Review E*, 51:5208–+, June 1995.

[65] D. Bauer, P. Mulser, and W.-H. Steeb. Relativistic ponderomotive force, Uphill acceleration, and transition to chaos. *Physical Review Letters*, 75:4622–4625, December 1995.

[66] F. V. Hartemann, S. N. Fochs, G. P. Le Sage, N. C. Luhmann, Jr., J. G. Woodworth, M. D. Perry, Y. J. Chen, and A. K. Kerman. Nonlinear ponderomotive scattering of relativistic electrons by an intense laser field at focus. *Physical Review E*, 51:4833–4843, May 1995.

[67] J. N. Bardsley, B. M. Penetrante, and M. H. Mittleman. Relativistic dynamics of electrons in intense laser fields. *Physical Review A: General Physics*, 40:3823–3835, October 1989.

[68] W. Rozmus, V. T. Tikhonchuk, and R. Cauble. A model of ultrashort laser pulse absorption in solid targets. *Physics of Plasmas*, 3:360–367, January 1996.

[69] W. L. Kruer. *The physics of laser plasma interactions.* Addison-Wesley, New-York, 1988.

[70] G. J. Pert. Inverse bremsstrahlung in strong radiation fields at low temperatures. *Physical Review E*, 51:4778–4789, May 1995.

[71] E. S. Weibel. Anomolous skin effect in a plasma. *Physics of Fluids*, 10:741, 1967.

[72] T.-Y. B. Yang, W. L. Kruer, R. M. More, and A. B. Langdon. Absorption of laser light in overdense plasmas by sheath inverse bremsstrahlung. *Physics of Plasmas*, 2:3146–3154, August 1995.

[73] J. P. Freidberg, R. W. Mitchell, R. L. Morse, and L. I. Rudsinski. Resonant Absorption of Laser Light by Plasma Targets. *Physical Review Letters*, 28:795–799, March 1972.

[74] K. G. Estabrook, E. J. Valeo, and W. L. Kruer. Two-dimensional relativistic simulations of resonance absorption. *Physics of Fluids*, 18:1151–1159, September 1975.

[75] D. W. Forslund, J. M. Kindel, K. Lee, E. L. Lindman, and R. L. Morse. Theory and simulation of resonant absorption in a hot plasma. *Physical Review A: General Physics*, 11:679–683, February 1975.

[76] J. M. Dawson. Nonlinear Electron Oscillations in a Cold Plasma. *Physical Review*, 113:383–387, January 1959.

[77] T. P. Coffey. Breaking of large amplitude plasma oscillations. *Physics of Fluids*, 14(7):1402, 1971.

[78] S. C. Wilks and W. L. Kruer. Absorption of ultrashort, ultra-intense laser light by solids and overdense plasmas. *IEEE Journal of Quantum Electronics*, 33(11):1954–1968, 1997.

[79] D. W. Forslund, J. M. Kindel, and K. Lee. Theory of hot-electron spectra at high laser intensity. *Physical Review Letters*, 39:284–288, August 1977.

[80] K. Estabrook and W. L. Kruer. Properties of resonantly heated electron distributions. *Physical Review Letters*, 40:42–45, January 1978.

[81] S. Bastiani, A. Rousse, J. P. Geindre, P. Audebert, C. Quoix, G. Hamoniaux, A. Antonetti, and J.-C. Gauthier. Experimental study of the interaction of subpicosecond laser pulses with solid targets of varying initial scale lengths. *Physical Review E*, 56:7179–7185, December 1997.

[82] P. Gibbon. Harmonic Generation by Femtosecond Laser-Solid Interaction: A Coherent "Water-Window" Light Source? *Physical Review Letters*, 76:50–53, January 1996.

[83] F. Brunel. Not-so-resonant, resonant absorption. *Physical Review Letters*, 59:52–55, July 1987.

[84] P. Gibbon and A. R. Bell. Collisionless absorption in sharp-edged plasmas. *Physical Review Letters*, 68:1535–1538, March 1992.

[85] W. L. Kruer. Ponderomotive and thermal filamentation of laser light. *Comments Plasma Physics and Controlled Fusion*, 9(2):63–72, 1985.

[86] C. J. McKinstrie and D. F. Dubois. A covariant formalism for wave propagation applied to stimulated Raman scattering. *Physics of Fluids*, 31:278–287, February 1988.

[87] A. Pukhov and J. Meyer-Ter-Vehn. Laser Hole Boring into Overdense Plasma and Relativistic Electron Currents for Fast Ignition of ICF Targets. *Physical Review Letters*, 79:2686–2689, October 1997.

[88] E. Lefebvre. *Mécanismes d'absorption et d'émission dans l'interaction d'une impulsion laser ultra-intense avec une cible surcritique.* Thèse de doctorat, Université Paris XI Orsay, 1996.

[89] B. F. Lasinski, A. B. Langdon, S. P. Hatchett, M. H. Key, and M. Tabak. Particle-in-cell simulations of ultra intense laser pulses propagating through overdense plasma for fast-ignitor and radiography applications. *Physics of Plasmas*, 6:2041–2047, May 1999.

[90] G. Malka and J. L. Miquel. Experimental Confirmation of Ponderomotive-Force Electrons Produced by an Ultrarelativistic Laser Pulse on a Solid Target. *Physical Review Letters*, 77:75–78, July 1996.

[91] P. Mora and F. Amiranoff. Electron acceleration in a relativistic electron plasma wave. *Journal of Applied Physics*, 66:3476–3481, October 1989.

[92] D. Gordon, K. C. Tzeng, C. E. Clayton, A. E. Dangor, V. Malka, K. A. Marsh, A. Modena, W. B. Mori, P. Muggli, Z. Najmudin, D. Neely, C. Danson, and C. Joshi. Observation of Electron Energies Beyond the Linear Dephasing Limit from a Laser-Excited Relativistic Plasma Wave. *Physical Review Letters*, 80:2133–2136, March 1998.

[93] S. Guérin. *Interaction d'une onde électromagnétique ultra-intense avec un plasma surdense.* Thèse de doctorat, Université Paris XI Orsay, 1996.

[94] C. Toupin. *Interaction d'une impusion laser ultra-intense avec un plasma dense: chauffage et transport électronique et ionique.* Thèse de doctorat, Université de Paris-Sud, 1999.

[95] F. N. Beg, A. R. Bell, A. E. Dangor, C. N. Danson, A. P. Fews, M. E. Glinsky, B. A. Hammel, P. Lee, P. A. Norreys, and M. Tatarakis. A study of picosecond laser-solid interactions up to 10^{19} Wcm^{-2}. *Physics of Plasmas*, 4:447–457, February 1997.

[96] V. T. Tikhonchuk. Interaction of a beam of fast electrons with solids. *Physics of Plasmas*, 9:1416–+, April 2002.

[97] J. D. Jackson. *Classical Electrodynamics*. John Wiley & Sons, New-York, 1975.

[98] P. H. Rutherford R. J. Golston. *Introduction to Plasma Physics*. Institute of Physics Publishing, Bristol and Philadelphia, 1995.

[99] H. A. Bethe. Molière's Theory of Multiple Scattering. *Physical Review*, 89:1256–1266, March 1953.

[100] L. Reimer. *Scanning electron microscopy*. Springer, Berlin, 1985.

[101] F. Rohrlich and B. C. Carlson. Positron-Electron Differences in Energy Loss and Multiple Scattering. *Physical Review*, 93:38–44, January 1954.

[102] R. M. Sternheimer. Density Effect for the Ionization Loss of Charged Particles. *Physical Review*, 145:247–250, May 1966.

[103] ICRU. Stopping powers for electrons and positrons. Technical Report ICRU Report 37, International Commission on Radiation Units and Measurements, 1984.

[104] E. Fermi. The Ionization Loss of Energy in Gases and in Condensed Materials. *Physical Review*, 57:485–493, March 1940.

[105] R. M. Sternheimer. The density effect for the ionization loss in various materials. *Physical Review*, 88(4):851–859, 1952.

[106] R. R. Warnecke. *Introduction à l'étude des accélérateurs de particules - Tome 2*. Masson/Seditas, Paris, 1976.

[107] R. M. More. Pressure ionization, resonances, and the continuity of bound and free states. *Advances in Atomic and Molecular Physics*, 21:305–356, 1985.

[108] E. Nardi and Z. Zinamon. Energy deposition by relativistic electrons in high-temperature targets. *Physical Review A: General Physics*, 18:1246–1249, September 1978.

[109] H. Alfven. On the motion of cosmic rays in interstellar space. *Physical Review*, 55(5):425, 1939.

[110] A. R. Bell, J. R. Davies, S. Guerin, and H. Ruhl. Fast-electron transport in high-intensity short-pulse laser - solid experiments. *Plasma Physics and Controlled Fusion*, 39:653–659, May 1997.

[111] J. R. Davies, A. R. Bell, M. G. Haines, and S. M. Guérin. Short-pulse high-intensity laser-generated fast electron transport into thick solid targets. *Physical Review E*, 56:7193–7203, December 1997.

[112] O. Buneman. Dissipation of Currents in Ionized Media. *Physical Review*, 115:503–517, August 1959.

[113] E. S. Weibel. Spontaneously Growing Transverse Waves in a Plasma Due to an Anisotropic Velocity Distribution. *Physical Review Letters*, 2:83–84, February 1959.

[114] S. I. Krasheninnikov, A. V. Kim, B. K. Frolov, and R. Stephens. Intense electron beam propagation through insulators: Ionization front structure and stability. *Physics of Plasmas*, 12:3105–+, July 2005.

[115] M. Manclossi, J. J. Santos, D. Batani, J. Faure, A. Debayle, V.T. Tikhonchuk, and V. Malka. Study of ultra intense laser-produced fast-electron propagation and filamentation in insulators and metal foils targets by optical emission diagnostics. *Physical Review Letters*, 12(96):125002, 2006.

[116] J. R. Davies. Electric and magnetic field generation and target heating by laser-generated fast electrons. *Physical Review E*, 68(5):056404–+, November 2003.

[117] R. V. Lovelace and R. N. Sudan. Plasma Heating by High-Current Relativistic Electron Beams. *Physical Review Letters*, 27:1256–1259, November 1971.

[118] L. Gremillet. *Étude théorique et expérimentale du transport des électrons rapides dans l'interaction laser-solide à très haut flux*. Thèse de doctorat, École Polytechnique, 2001.

[119] T. Ditmire, E. T. Gumbrell, R. A. Smith, L. Mountford, and M. H. R. Hutchinson. Supersonic Ionization Wave Driven by Radiation Transport in a Short-Pulse Laser-Produced Plasma. *Physical Review Letters*, 77:498–501, July 1996.

[120] E. T. Gumbrell, R. A. Smith, T. Ditmire, A. Djaoui, S. J. Rose, and M. H. R. Hutchinson. Picosecond optical probing of ultrafast energy transport in short pulse laser solid target interaction experiments. *Physics of Plasmas*, 5:3714–3721, October 1998.

[121] B.-T. V. Vu, O. L. Landen, and A. Szoke. Time-resolved probing of femtosecond-laser-produced plasmas in transparent solids by electron thermal transport. *Physics of Plasmas*, 2:476–485, February 1995.

[122] L. Gremillet, F. Amiranoff, S. D. Baton, J.-C. Gauthier, M. Koenig, E. Martinolli, F. Pisani, G. Bonnaud, C. Lebourg, C. Rousseaux, C. Toupin, A. Antonicci, D. Batani, A. Bernardinello, T. Hall, D. Scott, P. Norreys, H. Bandulet,

and H. Pépin. Time-Resolved Observation of Ultrahigh Intensity Laser-Produced Electron Jets Propagating through Transparent Solid Targets. *Physical Review Letters*, 83:5015–5018, December 1999.

[123] M. Borghesi, A. J. MacKinnon, A. R. Bell, G. Malka, C. Vickers, O. Willi, J. R. Davies, A. Pukhov, and J. Meyer-Ter-Vehn. Observations of Collimated Ionization Channels in Aluminum-Coated Glass Targets Irradiated by Ultraintense Laser Pulses. *Physical Review Letters*, 83:4309–4312, November 1999.

[124] D. Batani, A. Antonicci, F. Pisani, T. A. Hall, D. Scott, F. Amiranoff, M. Koenig, L. Gremillet, S. Baton, E. Martinolli, C. Rousseaux, and W. Nazarov. Inhibition in the propagation of fast electrons in plastic foams by resistive electric fields. *Physical Review E*, 65(6):066409–+, June 2002.

[125] L. Gremillet, G. Bonnaud, and F. Amiranoff. Filamented transport of laser-generated relativistic electrons penetrating a solid target. *Physics of Plasmas*, 9:941–948, March 2002.

[126] J. J. Honrubia, A. Antonicci, and D. Moreno. Hybrid simulations of fast electron transport in conducting media. *Laser Particle Beams*, 22:129–135, june 2004.

[127] M. Tatarakis, M. Zepf, F. N. Beg, E. L. Clark, A. E. Dangor, K. Krushelnick, K.W.D. Lendigham, I Spencer, P. A. Norreys, and R. J. Clarke. *CLF-Rutherford Appleton Laboratory Annual Report 2000/2001*, pages 23–24, 2001.

[128] M. Zepf, E. L. Clark, K. Krushelnick, F. N. Beg, C. Escoda, A. E. Dangor, M. I. K. Santala, M. Tatarakis, I. F. Watts, P. A. Norreys, R. J. Clarke, J. R. Davies, M. A. Sinclair, R. D. Edwards, T. J. Goldsack, and et al. Fast particle generation and energy transport in laser-solid interactions. *Physics of Plasmas*, 8:2323–2330, May 2001.

[129] F. Pisani, A. Bernardinello, D. Batani, A. Antonicci, E. Martinolli, M. Koenig, L. Gremillet, F. Amiranoff, S. Baton, J. Davies, T. Hall, D. Scott, P. Norreys, A. Djaoui, C. Rousseaux, P. Fews, H. Bandulet, and H. Pepin. Experimental evidence of electric inhibition in fast electron penetration and of electric-field-limited fast electron transport in dense matter. *Physical Review E*, 62:5927–+, November 2000.

[130] D. Batani, S. D. Baton, M. Manclossi, J. J. Santos, F. Amiranoff, M. Koenig, E. Martinolli, A. Antonicci, C. Rousseaux, M. R. Le Gloahec, T. Hall, V. Malka, T. E. Cowan, J. King, R. R. Freeman, M. Key, and R. Stephens. Ultraintense Laser-Produced Fast-Electron Propagation in Gas Jets. *Physical Review Letters*, 94(5):055004–+, February 2005.

[131] A. Benuzzi-Mounaix, M. Koenig, J. M. Boudenne, T. A. Hall, D. Batani, F. Scianitti, A. Masini, and D. Di Santo. Chirped pulse reflectivity and frequency domain interferometry in laser driven shock experiments. *Physical Review E*, 60(3):R2488–R2491, September 1999.

[132] M. Borghesi, D. H. Campbell, A. Schiavi, M. G. Haines, O. Willi, A. J. MacKinnon, P. Patel, L. A. Gizzi, M. Galimberti, R. J. Clarke, F. Pegoraro, H. Ruhl, and S. Bulanov. Electric field detection in laser-plasma interaction experiments via the proton imaging technique. *Physics of Plasmas*, 9:2214–+, May 2002.

[133] J. J. Santos, F. Amiranoff, S. D. Baton, L. Gremillet, M. Koenig, E. Martinolli, M. Rabec Le Gloahec, C. Rousseaux, D. Batani, A. Bernardinello, G. Greison, and T. Hall. Fast Electron Transport in Ultraintense Laser Pulse Interaction with Solid Targets by Rear-Side Self-Radiation Diagnostics. *Physical Review Letters*, 89(2):025001–+, June 2002.

[134] S. D. Baton, J. J. Santos, F. Amiranoff, H. Popescu, L. Gremillet, M. Koenig, E. Martinolli, O. Guilbaud, C. Rousseaux, M. Rabec Le Gloahec, T. Hall, D. Batani, E. Perelli, F. Scianitti, and T. E. Cowan. Evidence of Ultrashort Electron Bunches in Laser-Plasma Interactions at Relativistic Intensities. *Physical Review Letters*, 91(10):105001–+, September 2003.

[135] J. P. Geindre, P. Audebert, S. Rebibo, and J.-C. Gauthier. *Rapport LULI*, page E1, 1998.

[136] L. Rovagnani. *Laser-plasma investigations employing laser-driven proton probes.* PhD thesis, Department of Physics and Astronomy, The Queen's University of Belfast, September 2005.

[137] www.srim.org, 2005.

[138] www.ispcorp.com, 2005.

[139] W. L. McLaughlin, C. Yun-Dong, C. G. Soares, A. Miller, G. van Dyk, and D. F. Lewis. Sensitometry of the response of a new radiochromic film dosimeter to gamma radiation and electron beams. *Nuclear Instruments and Methods in Physics Research A*, 302:165–176, April 1991.

[140] A.Z. Jones, C. D. Bloch, E.R. Hall, S.B Klein, R. Hashemian, B. von Przewoski, K.M. Murray, and C.C. Foster. Comparison of Indiana University Cyclotron Facility Faraday cup proton dosimetry with radiochromic films, a calorimeter, and acalibrated ion chamber. *IEEE Transactions on Nuclear Science*, 46(1762), 1999.

[141] R. B. Stephens, R. A. Snavely, Y. Aglitskiy, F. Amiranoff, C. Andersen, D. Batani, S. D. Baton, T. Cowan, R. R. Freeman, T. Hall, S. P. Hatchett, J. M. Hill, M. H. Key, J. A. King, J. A. Koch, M. Koenig, A. J. MacKinnon, K. L. Lancaster, E. Martinolli, P. Norreys, E. Perelli-Cippo, M. Rabec Le Gloahec, C. Rousseaux, J. J. Santos, and F. Scianitti. Kα fluorescence measurement of relativistic electron transport in the context of fast ignition. *Physical Review E*, 69(6):066414–+, June 2004.

[142] D. J. Bond, J. D. Hares, and J. D. Kilkenny. Demonstration of Resistive Inhibition of Fast Electrons from Laser-Produced Plasmas in Low-Density Gold Targets. *Physical Review Letters*, 45:252–255, July 1980.

[143] Y.-K. Kim and M. E. Rudd. Binary-encounter-dipole model for electron-impact ionization. *Physical Review A*, 50:3954–3967, November 1994.

[144] M. V. Ammosov, N. B. Delone, and V. P. Krainov. *Soviet Physics JETP*, 64:1186–1191, 1986.

[145] D. R. Welch, D. V. Rose, B. V. Oliver, E. Schamiloglu, K. Hahn, and J. E. Maenchen. Transport of a relativistic electron beam in gas and plasma-filled focusing cells for X-ray radiography. *Physics of Plasmas*, 11:751–+, February 2004.

[146] S. Strasburg, D. D. Hinshelwood, J. W. Schumer, D. Mosher, P. F. Ottinger, R. F. Fernsler, and S. P. Slinker. Intense electron-beam ionization physics in air. *Physics of Plasmas*, 10:3758–+, September 2003.

[147] S. K. Iyyengar and V. K. Rohatgi. Effect of rise time and pulse width on the transport and interaction of a 1 MeV, 15 kA relativistic electron beam in low pressure argon and hydrogen. *Physics of Fluids B*, 1:1860–1865, September 1989.

[148] T. W. L. Sanford. High-power electron-beam transport in long gas cells from 10^{-3} to 10^{3} Torr nitrogen. *Physics of Plasmas*, 2:2539–2546, june 1995.

[149] A. A. Rukhadze and J. Kistemaker. About the possibility of existence of current-convective instability in REB-neutral gas injection experiments. *Plasma Physics*, 23:979–984, October 1981.

[150] A. J. Kemp, R. E. W. Pfund, and J. Meyer-Ter-Vehn. Modeling ultrafast laser-driven ionization dynamics with Monte Carlo collisional particle-in-cell simulations. *Physics of Plasmas*, 11:5648–+, December 2004.

[151] A. Schiavi. PhD thesis, Imperial College of Science, Technology and Medecine, London (UK), 2003.

[152] K. B. Wharton, S. P. Hatchett, S. C. Wilks, M. H. Key, J. D. Moody, V. Yanovsky, A. A. Offenberger, B. A. Hammel, M. D. Perry, and C. Joshi. Experimental Measurements of Hot Electrons Generated by Ultraintense (10^{19} W/cm^2) Laser-Plasma Interactions on Solid-Density Targets. *Physical Review Letters*, 81:822–825, July 1998.

[153] P. A. Norreys, M. Santala, E. Clark, M. Zepf, I. Watts, F. N. Beg, K. Krushelnick, M. Tatarakis, A. E. Dangor, X. Fang, P. Graham, T. McCanny, R. P. Singhal, K. W. D. Ledingham, A. Creswell, and et al. Observation of a highly directional γ-ray beam from ultrashort, ultraintense laser pulse interactions with solids. *Physics of Plasmas*, 6:2150–2156, May 1999.

[154] R. Kodama, P. A. Norreys, K. Mima, A. E. Dangor, R. G. Evans, H. Fujita, Y. Kitagawa, K. Krushelnick, T. Miyakoshi, N. Miyanaga, T. Norimatsu, S. J. Rose, T. Shozaki, K. Shigemori, A. Sunahara, M. Tampo, K. A. Tanaka, Y. Toyama, T. Yamanaka, and M. Zepf. Fast heating of ultrahigh-density plasma as a step towards laser fusion ignition. *Nature*, 412(6849):798–802, 2001.

[155] H. Popescu, S. D. Baton, F. Amiranoff, C. Rousseaux, M. Rabec Le Gloahec, J. J. Santos, L. Gremillet, M. Koenig, E. Martinolli, T. Hall, J. C. Adam, A. Heron, and D. Batani. Subfemtosecond, coherent, relativistic, and ballistic electron bunches generated at ω_0 and $2\omega_0$ in high intensity laser-matter interaction. *Physics of Plasmas*, 12(6):063106, 2005.

[156] J. A. Koch, C. A. Back, C. Brown, K. Estabrook, B. A. Hammel, S. P. Hatchett, M. H. Key, J. D. Kilkenny, O. L. Landen, R. W. Lee, J. D. Moody, A. A. Offenberger, D. Pennington, M. D. Perry, M. Tabak, V. Yanovsky, R. J. Vallace, K. B. Wharton, and S. C. Wilks. Time-resolved X-ray spectroscopy of deeply buried tracer layers as a density and temperature diagnostic for the fast ignitor. *Laser and Particle Beams*, 16(1):225–232, 1998.

[157] F. Califano, T. Cecchi, and C. Chiuderi. Nonlinear kinetic regime of the Weibel instability in an electron-ion plasma. *Physics of Plasmas*, 9:451–457, February 2002.

[158] T. A. Hall, S. Ellwi, D. Batani, A. Bernardinello, V. Masella, M. Koenig, A. Benuzzi, J. Krishnan, F. Pisani, A. Djaoui, P. Norreys, D. Neely, S. Rose, M. H. Key, and P. Fews. Fast Electron Deposition in Laser Shock Compressed Plastic Targets. *Physical Review Letters*, 81:1003–1006, August 1998.

[159] M. Tatarakis, F. N. Beg, E. L. Clark, A. E. Dangor, R. D. Edwards, R. G. Evans, T. J. Goldsack, K. W. Ledingham, P. A. Norreys, M. A. Sinclair, M.-S. Wei, M. Zepf, and K. Krushelnick. Propagation Instabilities of High-Intensity Laser-Produced Electron Beams. *Physical Review Letters*, 90(17):175001–+, April 2003.

[160] J. Fuchs, T. E. Cowan, P. Audebert, H. Ruhl, L. Gremillet, A. Kemp, M. Allen, A. Blazevic, J.-C. Gauthier, M. Geissel, M. Hegelich, S. Karsch, P. Parks, M. Roth, Y. Sentoku, R. Stephens, and E. M. Campbell. Spatial Uniformity of Laser-Accelerated Ultrahigh-Current MeV Electron Propagation in Metals and Insulators. *Physical Review Letters*, 91(25):255002–+, December 2003.

[161] H. Teng, J. Zhang, Z. L. Chen, Y. T. Li, K. Li, X. Y. Peng, and J. X. Ma. Propagation of hot electrons through high-density plasmas. *Physical Review E*, 67(2):026408–+, February 2003.

[162] F. Brandl, G. Pretzler, D. Habs, and E. Fill. Čerenkov radiation diagnostics of hot electrons generated by fs-laser interaction with solid targets. *Europhysics Letters*, 61:632–638, March 2003.

[163] M. S. Wei, F. N. Beg, E. L. Clark, A. E. Dangor, R. G. Evans, A. Gopal, K. W. Ledingham, P. McKenna, P. A. Norreys, M. Tatarakis, M. Zepf, and K. Krushelnick. Observations of the filamentation of high-intensity laser-produced electron beams. *Physical Review E*, 70(5):056412–+, November 2004.

[164] Ya. B. Zel'dovich and Yu. P. Raizer. *Physics of Shock Waves and High-Temperature Hydrodynamic Phenomena*. Academic Press, Inc., London, 1966.

[165] E. Martinolli, M. Koenig, F. Amiranoff, S. D. Baton, L. Gremillet, J. J. Santos, T. A. Hall, M. Rabec-Le-Gloahec, C. Rousseaux, and D. Batani. Fast electron heating of a solid target in ultrahigh-intensity laser pulse interaction. *Physical Review E*, 70(5):055402–+, November 2004.

[166] I. Frank and V. Ginzburg. *Journal of Physics-USSR*, 9:353, 1945.

[167] L. W. Wartski. *Étude du rayonnement de transition optique produit par des électrons d'énergie 30 à 70 MeV. Application aux diagnostics de faisceaux de particules chargées*. Thèse de doctorat, Université de Paris-Sud, 1976.

[168] D. E. Gray (ed.). *American Institute of Physics Handbook*. McGraw-Hill, 1972.

[169] K. Honkavaara. *Optical Transition Radiation in High Energy Beam Diagnostics*. Phd thesis, Université de Paris-Sud and University of Helsinki, 1999.

[170] D. W. Rule and R. B. Fiorito. Beam profiling with optical transition radiation. In *Proccedings of the 1993 Particle Accelerator Conference*, volume 3, pages 2453–2455, Washignton DC, 1993. IEEE / APS.

[171] X. Artru, R. Chehab, K. Honkavaara, and A. Variola. Resolution power of optical transition radiation: Theoretical considerations. *Nuclear Instruments and Methods in Physics Research B*, 145:160–168, October 1998.

[172] M. Abramowitz and I.A. Stegun. *Handbook of mathematical functions.* Dover Publications, Inc., New York, 9th edition, 1972.

[173] J. A. Koch, M. H. Key, R. R. Freeman, S. P. Hatchett, R. W. Lee, D. Pennington, R. B. Stephens, and M. Tabak. Experimental measurements of deep directional columnar heating by laser-generated relativistic electrons at near-solid density. *Physical Review E*, 65(1):016410, December 2001.

[174] F. F. Chen. *Introduction to Plasma Physics and Controlled Fusion*, volume 1. Plenum Press, New York, 1984.

[175] M. H. Key, F. Amiranoff, C. Andersen, D. Batani, S. Baton, T. E. Cowan, T. Jitsuno, N. Nisch, R. R. Freeman, L. Gremillet, T. A. Hall, S. J. Hatchett, J. M. Hill, J. King, J. A. Koch, M. Koenig, B. F. Lasinski, A. B. Langdon, A. J. MacKinnon, E. Martinolli, P. Norreys, P. B. Parks, E. Perelii-Cippo, M. Rabec Le Gloahec, M. N. Rosenbluth, C. Rousseaux, J. J. Santos, F. Scianitti, R. A. Snavely, and R. B. Stephens. Studies of energy transport by relativistic electrons in the context of fast ignition. In *Proc. 2nd Int. Conf. on Inertial Fusion Sciences and Applications (IFSA2001)*, Kyoto, Japan, 2001.

[176] E. Martinolli, D. Batani, E. Perelli-Cippo, F. Scianitti, M. Koenig, J. J. Santos, F. Amiranoff, S. D. Baton, T. Hall, M. Key, A. MacKinnon, R. Snavely, R. Freeman, C. Andersen, J. King, R. Stephens, M. Rabec Le Gloahec, C. Rousseaux, and T. E. Cowan. Fast electron transport and heating in solid-density matter. *Laser and Particle Beams*, 20:171–175, April 2002.

[177] E. Martinolli. *Transport d'électrons relativistes dans une cible solide. Étude du chauffage dans le cadre de l'Allumage Rapide.* Thèse de doctorat, École Polytechnique, 2003.

[178] L. Wartski, S. Roland, J. Lasalle, M. Bolore, and G. Filippi. Interference phenomenon in optical transition radiation and its application to particle beam diagnostics and multiple-scattering measurements. *Journal of Applied Physics*, 46:3644–3653, August 1975.

[179] Y. Shibata, T. Takahashi, T. Kanai, K. Ishi, M. Ikezawa, J. Ohkuma, S. Okuda, and T. Okada. Diagnostics of an electron beam of a linear accelerator using coherent transition radiation. *Physical Review E*, 50:1479–1484, August 1994.

[180] M. Pittman, S. Ferré, J. P. Rousseau, L. Notebaert, J. P. Chambaret, and G. Chériaux. Design and characterization of a near-diffraction-limited femtosecond 100-TW 10-Hz high-intensity laser system. *Applied Physics B: Lasers and Optics*, 74:529–535, 2002.

[181] R. Ramis, R. Schmalz, and J. Meyer-Ter-Vehn. MULTI - A computer code for one-dimensional multigroup radiation hydrodynamics. *Computer Physics Communications*, 49:475–505, June 1988.

[182] J. Zheng, K. A. Tanaka, T. Sato, T. Yabuuchi, T. Kurahashi, Y. Kitagawa, R. Kodama, T. Norimatsu, and T. Yamanaka. Study of Hot Electrons by Measurement of Optical Emission from the Rear Surface of a Metallic Foil Irradiated with Ultraintense Laser Pulse. *Physical Review Letters*, 92(16):165001–+, April 2004.

[183] H. Popescu, S. Baton, F. Amiranoff, C. Rousseaux, M. Rabec Le Gloahec, J. J. Santos, L. Gremillet, T. Hall, J. Fuchs, P. Antici, N. Le Galloudec, and T. Cowan. Generation and ballistic transport of ultra-short high energy electron bunches in laser-matter interaction at high intensities. *APS Meeting Abstracts*, pages 1004–+, November 2004.

[184] K. Eidmann, J. Meyer-Ter-Vehn, T. Schlegel, and S. Hüller. Hydrodynamic simulation of subpicosecond laser interaction with solid-density matter. *Physical Review E*, 62:1202–1214, July 2000.

[185] D. Batani, H. Stabile, A. Ravasio, G. Lucchini, F. Strati, T. Desai, J. Ullschmied, E. Krousky, J. Skala, L. Juha, B. Kralikova, M. Pfeifer, C. Kadlec, T. Mocek, A. Präg, H. Nishimura, and Y. Ochi. Ablation pressure scaling at short laser wavelength. *Physical Review E*, 68(6):067403–+, December 2003.

[186] S. Atzeni. 2-D Lagrangian studies of symmetry and stability of laser fusion targets. *Computer Physics Communications*, 43:107–124, December 1986.

[187] M. Temporal, S. Atzeni, D. Batani, M. Koenig, A. Benuzzi, and B. Faral. Numerical simulations for the design of absolute equation-of-state measurements by laser-driven shock waves. *Nuovo Cimento D Serie*, 19:1839–+, December 1997.

[188] M. Borghesi, D. H. Campbell, M. G. Haines, A. Schiavi, O. Willi, A. J. Mackinnon, M. Galimberti, L. A. Gizzi, R. J. Clarke, S. Hawkes, and H. Ruhl. Detection of highly transient electric fields following ultra-intense laser interaction with solid targets. Annual report, RAL Central Laser Facility, 2000/2001.

[189] J. Rosenzweig, G. Travish, and A. Tremaine. Coherent transition radiation diagnosis of electron beam microbunching. *Nuclear Instruments and Methods in Physics Research A*, 365:255–259, February 1995.

[190] A. Tremaine, J. B. Rosenzweig, S. Anderson, P. Frigola, M. Hogan, A. Murokh, C. Pellegrini, D. C. Nguyen, and R. L. Sheffield. Observation of Self-Amplified Spontaneous-Emission-Induced Electron-Beam Microbunching Using Coherent Transition Radiation. *Physical Review Letters*, 81:5816–5819, December 1998.

[191] A. H. Lumpkin, R. Dejus, W. J. Berg, M. Borland, Y. C. Chae, E. Moog, N. S. Sereno, and B. X. Yang. First Observation of z-Dependent Electron-Beam Microbunching Using Coherent Transition Radiation. *Physical Review Letters*, 86:79–82, January 2001.

[192] A. H. Lumpkin, R. Dejus, J. W. Lewellen, W. Berg, S. Biedron, M. Borland, Y. C. Chae, M. Erdmann, Z. Huang, K.-J. Kim, Y. Li, S. V. Milton, E. Moog, D. W. Rule, V. Sajaev, and B. X. Yang. Evidence for Microbunching "Sidebands" in a Saturated Free-Electron Laser Using Coherent Optical Transition Radiation. *Physical Review Letters*, 88(23):234801–+, June 2002.

[193] K. Yasuike, M. H. Key, S. P. Hatchett, R. A. Snavely, and K. B. Wharton. Hot electron diagnostic in a solid laser target by K-shell lines measurement from ultraintense laser-plasma interactions (3×10^{20} W/cm^2, $\leqslant 400$ J). *Review of Scientific Instruments*, 72:1236–1240, January 2001.

[194] J. J. Honrubia, M. Kaluza, J. Schreiber, G. D. Tsakiris, and J. Meyer ter Vehn. Laser-driven fast-electron transport in preheated foil targets. *Physics of Plasmas*, 12(5):052708, 2005.

[195] E. Martinolli, M. Koenig, S. D. Baton, J. J. Santos, F. Amiranoff, D. Batani, E. Perelli-Cippo, F. Scianitti, L. Gremillet, R. Mélizzi, A. Decoster, C. Rousseaux, T. A. Hall, M. H. Key, R. Snavely, A. J. MacKinnon, R. R. Freeman, J. A. King, R. Stephens, D. Neely, and R. J. Clarke. Fast-electron transport and heating of solid targets in high-intensity laser interactions measured by Kα fluorescence. *Physical Review E*, 73(4):046402–+, April 2006.

[196] P. Nicolaï. private communication, 2006.

[197] J. J. Santos, M. Manclossi, D. Batani, A. Guemnie-Tafo, J. Faure, V. Malka, A. Debayle, Ph. Nicolaı, V. Tikhonchuck, and J. J. Honrubia. Study of ultra intense laser-produced fast-electron propagation and filamentation in insulators and metal foils targets by optical emission diagnostics. submitted to Physics of Plasmas, 2006.

[198] G. Malka, J. Fuchs, F. Amiranoff, S. D. Baton, R. Gaillard, J. L. Miquel, H. Pépin, C. Rousseaux, G. Bonnaud, M. Busquet, and L. Lours. Suprathermal Electron Generation and Channel Formation by an Ultrarelativistic Laser Pulse in an Underdense Preformed Plasma. *Physical Review Letters*, 79:2053–2056, September 1997.

[199] J. J. Honrubia. private communication, 2005.

[200] M. Honda, J. Meyer-Ter-Vehn, and A. Pukhov. Two-dimensional particle-in-cell simulation for magnetized transport of ultra-high relativistic currents in plasma. *Physics of Plasmas*, 7:1302–1308, April 2000.

[201] F. Pisani. *Étude expérimentale de la propagation et du dépôt d'énergie d'électrons rapides dans une cible solide ou comprimée par choc laser : application à l'allumeur rapide*. Thèse de doctorat, École Polytechnique, 2000.

[202] T. E. Cowan, J. Fuchs, H. Ruhl, A. Kemp, P. Audebert, M. Roth, R. Stephens, I. Barton, A. Blazevic, E. Brambrink, J. Cobble, J. Fernández, J.-C. Gauthier, M. Geissel, M. Hegelich, J. Kaae, S. Karsch, G. P. Le Sage, S. Letzring, M. Manclossi, S. Meyroneinc, A. Newkirk, H. Pépin, and N. Renard-Legalloudec. Ultralow Emittance, Multi-MeV Proton Beams from a Laser Virtual-Cathode Plasma Accelerator. *Physical Review Letters*, 92(20):204801–+, May 2004.

[203] J. C. Kieffer, J. P. Matte, M. Chaker, Y. Beaudoin, C. Y. Chien, S. Coe, G. Mourou, J. Dubau, and M. K. Inal. X-ray-line polarization spectroscopy in laser-produced plasmas. *Physical Review E*, 48:4648–4658, December 1993.

[204] Y. Inubushi, H. Nishimura, M. Ochiai, S. Fujioka, Y. Izawa, T. Kawamura, S. Shimizu, M. Hashida, and S. Sakabe. X-ray polarization spectroscopy for measurement of anisotropy of hot electrons generated with ultraintense laser pulse. *Review of Scientific Instruments*, 75:3699–3701, October 2004.

[205] R. Kodama, H. Shiraga, K. Shigemori, Y. Toyama, S. Fujioka, H. Azechi, H. Fujita, H. Habara, T. Hall, Y. Izawa, T. Jitsuno, Y. Kitagawa, K. M. Krushelnick, K. L. Lancaster, K. Mima, K. Nagai, M. Nakai, H. Nishimura, T. Norimatsu, P. A. Norreys, S. Sakabe, K. A. Tanaka, A. Youssef, M. Zepf, and T. Yamanaka. Nuclear fusion: Fast heating scalable to laser fusion ignition. *Nature*, 418:933–934, August 2002.

[206] Y. Sentoku, K. Mima, P. Kaw, and K. Nishikawa. Anomalous Resistivity Resulting from MeV-Electron Transport in Overdense Plasma. *Physical Review Letters*, 90(15):155001–+, April 2003.

[207] H. Ruhl, A. Macchi, P. Mulser, F. Cornolti, and S. Hain. Collective Dynamics and Enhancement of Absorption in Deformed Targets. *Physical Review Letters*, 82:2095–2098, March 1999.

[208] S. D. Baton, D. Batani, M. Manclossi, A. Morace, D. Piazza, A. Benuzzi-Mounaix, M. Koenig, P. Guillou, B. Loupias, J. Fuchs, F. Amiranoff, M. Rabec LeGloahec, H. Popescu, C. Rousseaux, M. Borghesi, C. Cecchetti, R. Kodama, T. Norimatsu, M. Nakatsutsumi, and Y. Aglitskiy. Recent experiments on electron transport in high-intensity laser matter interaction. *Plasma Physics and Controlled Fusion*, 47:B777–B789, December 2005.

[209] W. L. Kruer and K. Estabrook. $\mathbf{J} \times \mathbf{B}$ heating by very intense laser light. *Physics of Fluids*, 28(1):430–432, 1985.

[210] R. Ramis, R. Schmalz, and J. Meyer-Ter-Vehn. MULTI A computer code for one-dimensional multigroup radiation hydrodynamics. *Computer Physics Communications*, 49:475–505, june 1988.

[211] V. Malka, C. Coulaud, J. P. Geindre, V. Lopez, Z. Najmudin, D. Neely, and F. Amiranoff. Characterization of neutral density profile in a wide range of pressure of cylindrical pulsed gas jets. *Review of Scientific Instruments*, 71:2329–2333, june 2000.

[212] C. A. Coverdale, C. B. Darrow, C. D. Decker, W. B. Mori, K.-C. Tzeng, K. A. Marsh, C. E. Clayton, and C. Joshi. Propagation of Intense Subpicosecond Laser Pulses through Underdense Plasmas. *Physical Review Letters*, 74:4659–4662, june 1995.

[213] K. A. Nugent. Interferogram analysis using an accurate fully automatic algorithm. *Applied Optics*, 24:3101–3105, September 1985.

[214] William H. Press, Saul A. Teukolsky, William T. Vetterling, and Brian P. Flannery. *Numerical Recipes in FORTRAN; The Art of Scientific Computing*. Cambridge University Press, New York, NY, USA, 1993.

[215] C. K. Birdsall and A. B. Langdon. *Plasma Physics Via Computer Simulation*. McGraw-Hill, New York, NY, USA, 1985.

[216] P. Goldsmith and J. V. Jelley. *Philosophical Magazine*, 4:1915–1924, 1959.

[217] J. Bosser, J. Mann, G. Ferioli, and L. Warts. Optical transition radiation proton beam profile monitor. *Nuclear Instruments and Methods in Physics Research A*, 238:45–52, July 1985.

[218] X. K. Maruyama, R. B. Fiorito, and D. W. Rule. Optical transition radiation as a real-time, on-line diagnostic for free electron laser systems. *Nuclear Instruments and Methods in Physics Research A*, 272:237–240, October 1988.

[219] A. Specka. *Expérience d'acceleration d'électrons à l'aide d'une onde plasma créée pare le battement de deux impulsions laser. Étude du moniteur de faisceau d'électrons de 3 MeV utilisant le rayonnement de transition optique et du spectrographe magnétique*. Thèse de doctorat, École Polytechnique, 1994.

Publication list

[1] D. Batani, S. D. Baton, M. Manclossi, F. Amiranoff, M. Koenig, J. J. Santos, E. Martinolli, L. Gremillet, H. Popescu, A. Antonicci, C. Rousseaux, M. Rabec Le Gloahec, T. Hall, V. Malka, T. E. Cowan, R. Stephens, M. Key, J. King, and R. Freeman. Propagation In Matter Of Currents Of Relativistic Electrons Beyond The Alfven Limit, Produced In Ultra-High-Intensity Short-Pulse Laser-Matter Interactions. In L. Hadžievski, T. Grozdanov, and N. Bibic, editors, *American Institute of Physics Conference Series*, pages 446–457, December 2004.

[2] D. Batani, S. D. Baton, M. Manclossi, J. J. Santos, F. Amiranoff, M. Koenig, E. Martinolli, A. Antonicci, C. Rousseaux, M. R. Le Gloahec, T. Hall, V. Malka, T. E. Cowan, J. King, R. R. Freeman, M. Key, and R. Stephens. Ultraintense Laser-Produced Fast-Electron Propagation in Gas Jets. *Physical Review Letters*, 94(5):055004–+, February 2005.

[3] D. Batani, M. Manclossi, D. Piazza, S. D. Baton, A. Benuzzi-Mounaix, M. Koenig, H. Popescu, F. Amiranoff, M. Rabec Le Gloahec, C. Rousseaux, M. Borghesi, and C. Cecchetti. Study of the propagation of ultra-intense laser-produced fast electrons in gas jets. *Journal de Physique IV*, 133:367–370, June 2006.

[4] D. Batani, M. Manclossi, J. J. Santos, V. T. Tikhonchuk, J. Faure, A. Guemnie-Tafo, and V. Malka. Transport of intense laser-produced electron beams in matter. *Plasma Physics and Controlled Fusion*, 48:B211–B220, December 2006.

[5] S. D. Baton, D. Batani, M. Manclossi, A. Morace, D. Piazza, A. Benuzzi-Mounaix, M. Koenig, P. Guillou, B. Loupias, J. Fuchs, F. Amiranoff, M. Rabec LeGloahec, H. Popescu, C. Rousseaux, M. Borghesi, C. Cecchetti, R. Kodama, T. Norimatsu, M. Nakatsutsumi, and Y. Aglitskiy. Recent experiments on electron transport in high-intensity laser matter interaction. *Plasma Physics and Controlled Fusion*, 47:B777–B789, December 2005.

[6] T. E. Cowan, J. Fuchs, H. Ruhl, A. Kemp, P. Audebert, M. Roth, R. Stephens, I. Barton, A. Blazevic, E. Brambrink, J. Cobble, J. Fernández, J.-C. Gauthier,

M. Geissel, M. Hegelich, J. Kaae, S. Karsch, G. P. Le Sage, S. Letzring, M. Manclossi, S. Meyroneinc, A. Newkirk, H. Pépin, and N. Renard-Legalloudec. Ultralow Emittance, Multi-MeV Proton Beams from a Laser Virtual-Cathode Plasma Accelerator. *Physical Review Letters*, 92(20):204801–+, May 2004.

[7] T. E. Cowan, J. Fuchs, H. Ruhl, Y. Sentoku, A. Kemp, P. Audebert, M. Roth, R. Stephens, I. Barton, A. Blazevic, E. Brambrink, J. Cobble, J. C. Fernández, J.-C. Gauthier, M. Geissel, M. Hegelich, J. Kaae, S. Karsch, G. P. Le Sage, S. Letzring, M. Manclossi, S. Meyroneinc, A. Newkirk, H. Pépin, and N. Renard-Legalloudec. Ultra-low emittance, high current proton beams produced with a laser-virtual cathode sheath accelerator. *Nuclear Instruments and Methods in Physics Research A*, 544:277–284, May 2005.

[8] E. D'Humières, J. Fuchs, P. Antici, P. Audebert, M. Borghesi, E. Brambrink, C. A. Cecchetti, M. Kaluza, E. Lefebvre, V. Malka, M. Manclossi, S. Meyroneinc, P. Mora, H. Pépin, A. Pipahl, L. Romagnani, Y. Sentoku, J. Schreiber, T. Toncian, and O. Willi. Proton Acceleration: New Developments in Energy Increase, Focusing and Energy Selection. In *AIP Conf. Proc. 877: Advanced Accelerator Concepts: 12th Advanced Accelerator Concepts Workshop*, pages 41–50, November 2006.

[9] J. Fuchs, P. Antici, E. D'Humières, E. Lefebvre, M. Borghesi, E. Brambrink, C. A. Cecchetti, M. Kaluza, V. Malka, M. Manclossi, S. Meyroneinc, P. Mora, J. Schreiber, T. Toncian, H. Pépin, and P. Audebert. Laser-driven proton scaling laws and new paths towards energy increase. *Nature Physics*, 2:48–54, January 2006.

[10] J. Fuchs, P. Antici, E. D'Humières, E. Lefebvre, M. Borghesi, E. Brambrink, C. A. Cecchetti, M. Kaluza, V. Malka, M. Manclossi, S. Meyroneinc, P. Mora, J. Schreiber, T. Toncian, H. Pépin, and P. Audebert. Scaling Laws for Proton Acceleration from the Rear Surface of Laser-Irradiated Thin Foils. In M. Lontano and D. Batani, editors, *AIP Conf. Proc. 827: Superstrong Fields in Plasmas*, pages 237–247, April 2006.

[11] J. Fuchs, T. E. Cowan, H. Ruhl, Y. Sentoku, A. Kemp, P. Audebert, M. Roth, R. Stephens, I. Barton, A. Blazevic, E. Brambrink, J. Cobble, J. C. Fernández, J.-C. Gauthier, M. Geissel, M. Hegelich, J. Kaae, S. Karsch, G. P. Le Sage, S. Letzring, M. Manclossi, S. Meyroneinc, A. Newkirk, H. Pépin, and N. Renard-Legalloudec. Ultra-Low Emittance Proton Beams From A Laser-Virtual Cathode Plasma Accelerator. In V. Yakimenko, editor, *American Institute of Physics Conference Series*, pages 942–948, December 2004.

[12] M. Gerbaux, M. M. Aléonard, G. Claverie, F. Gobet, F. Hannachi, G. Malka, J. N. Scheurer, M. Tarisien, V. Méot, P. Morel, J. Faure, Y. Glinec, A. Guemnie-

Tafo, V. Malka, M. Manclossi, and J. Santos. Multi-MeV laser-produced particle sources: Characterization by activation techniques. *Journal de Physique IV*, 133:1139–1141, June 2006.

[13] G. Malka, M. M. Aleonard, G. Claverie, M. Gerbaux, F. Gobet, F. Hannachi, J. N. Scheurer, M. Tarisien, S. Fritzler, J. Faure, Y. Glinec, V. Malka, M. Manclossi, L. Notebaert, J. Santos, A. Tafo, N. Cochet, E. Lefebvre, V. Meot, P. Morel, and V. Tikhonchuk. Energetic electrons generation in high intensity and ultra-short laser pulse interactions with thin foil or low density gas jet targets. In G. A. Kyrala, J.-C. J. Gauthier, C. A. MacDonald, and A. M. Khounsary, editors, *Laser-Generated, Synchrotron, and Other Laboratory X-Ray and EUV Sources, Optics, and Applications II. Proceedings of the SPIE*, volume 5918, pages 246–252, August 2005.

[14] V. Malka, J. Faure, S. Fritzler, M. Manclossi, A. Guemnie-Tafo, E. D'Humières, E. Lefebvre, and D. Batani. Production of energetic proton beams with lasers. *Review of Scientific Instruments*, 77:302–+, March 2006.

[15] M. Manclossi, D. Batani, D. Piazza, S. Baton, F. Amiranoff, M. Koenig, H. Popescu, P. Audebert, J. J. Santos, E. Martinolli, A. Benuzzi-Mounaix, M. R. Le Gloahec, A. Antonicci, C. Rousseaux, M. Borghesi, C. Cecchetti, V. Malka, and T. Hall. Optical shadowgraphy and proton imaging as diagnostics tools for fast electron propagation in ultrahigh-intensity laser-matter interaction. *Radiation Effects and Defects in Solids*, 160:575–585, October 2005.

[16] M. Manclossi, A. Guemnie-Tafo, D. Batani, V. Malka, S. Fritzler, E. Lefebvre, and E. D'Humieres. Proton beam generation by ultra-high intensity laser-solid interaction. *Radiation Effects and Defects in Solids*, 160:631–637, October 2005.

[17] M. Manclossi, J. J. Santos, D. Batani, J. Faure, A. Debayle, V. T. Tikhonchuk, and V. Malka. Study of Ultraintense Laser-Produced Fast-Electron Propagation and Filamentation in Insulator and Metal Foil Targets by Optical Emission Diagnostics. *Physical Review Letters*, 96(12):125002–+, March 2006.

[18] M. Manclossi, J. J. Santos, D. Batani, J. Faure, V. Tikhonchuk, A. Debayle, and V. Malka. Ultra Intense Laser Produced Fast Electron Propagation and Filamentation in Insulators vs Conductors by Optical Emission Diagnostics. In M. Lontano and D. Batani, editors, *AIP Conf. Proc. 827: Superstrong Fields in Plasmas*, pages 534–539, April 2006.

[19] M. Manclossi, J. J. Santos, J. Faure, A. Guenmie-Tafo, D. Batani, V. Tikhonchuk, A. Debayle, and V. Malka. Characterization of ultraintense laser produced fast electron propagation in insulators vs. conductors by optical emission diagnostics. *Journal de Physique IV*, 133:499–502, June 2006.